

DEVELOPMENT OF SPECTRAL-SPATIAL STRATEGIES FOR DETECTION OF ENGINEERED OBJECTS USING HYPERSPECTRAL DATA

A Thesis Submitted to

Delhi Technological University

For the Award of Degree of

Doctor of Philosophy

In

Information Technology

By

SHALINI GAKHAR

(2K17/PhD/IT/09)

Under the Supervision of

Dr K. C. Tiwari

Professor, Multidisciplinary Centre for Geoinformatics



Department of Information Technology (IT)

Delhi Technological University

(Formerly Delhi college of Engineering)

Delhi-110042, India

SEPTEMBER-2021



©DELHI TECHNOLOGICAL UNIVERSITY-2021
ALL RIGHTS RESERVED

DECLARATION

I declare that the research work reported in the thesis entitled "**Development of spectral-spatial strategies for detection of engineered objects using hyperspectral data**" for the award of the degree of *Doctor of Philosophy* in the *Department of Information Technology (IT)* has been carried out by me under the supervision of *Dr K. C. Tiwari*, Professor in Multidisciplinary Centre for Geoinformatics (MCG), Delhi Technological University (DTU), Delhi, India.

The research work embodied in this thesis, except where otherwise indicated, is my original research. This thesis has not been submitted earlier in part or full to any other University or Institute for the award of any degree or diploma. This thesis does not contain other person's data, graphs or other information, unless specifically acknowledged.

Date: 20th September 2021



Shalini Gakhar
20th Sep 2021

(Shalini Gakhar)

2K17/PhD/IT/09

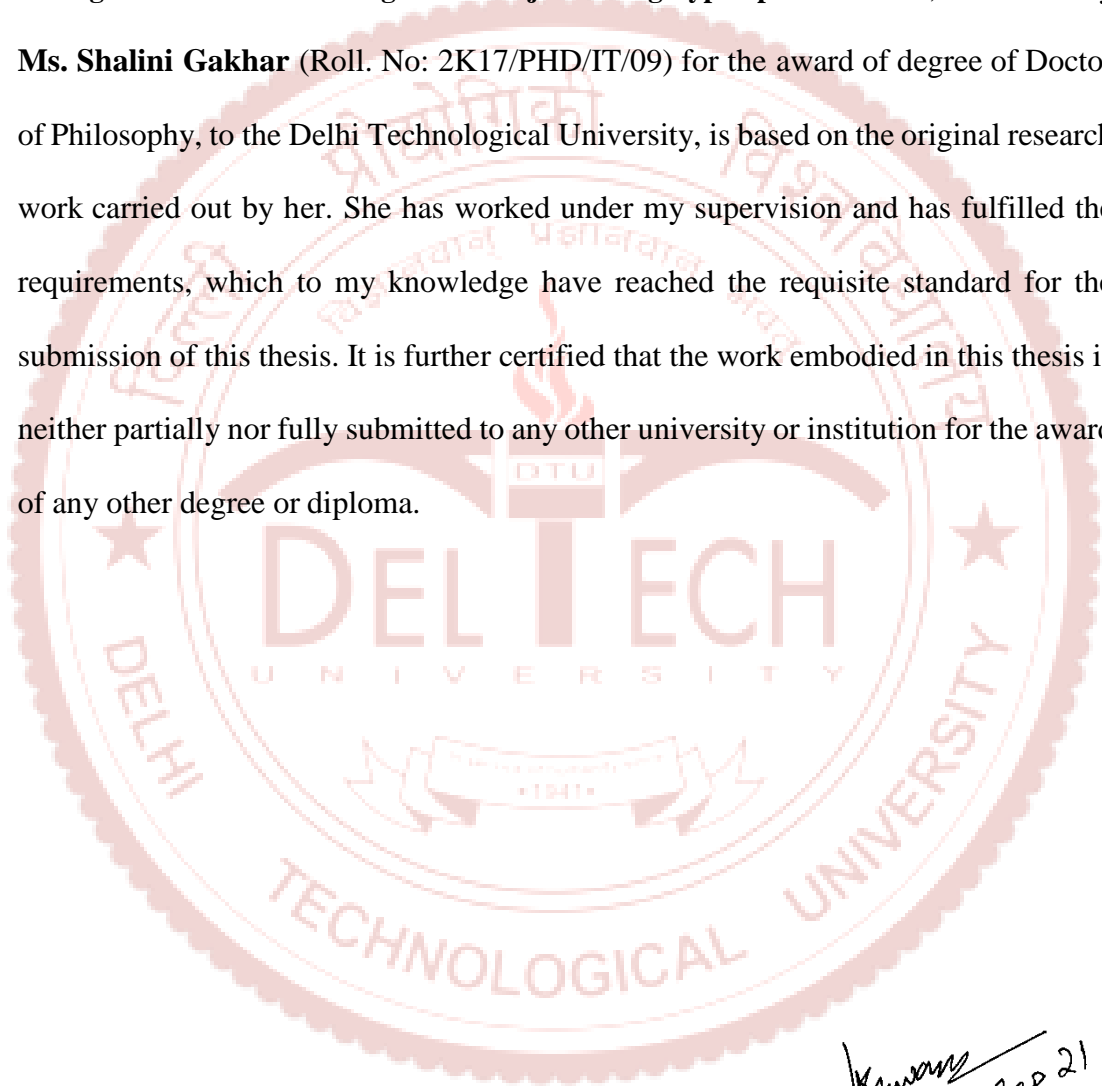
Department of IT

Delhi Technological University,

Delhi-110042, India

CERTIFICATE

This is to certify that the thesis entitled “**Development of spectral-spatial strategies for detection of engineered objects using hyperspectral data**”, submitted by **Ms. Shalini Gakhar** (Roll. No: 2K17/PHD/IT/09) for the award of degree of Doctor of Philosophy, to the Delhi Technological University, is based on the original research work carried out by her. She has worked under my supervision and has fulfilled the requirements, which to my knowledge have reached the requisite standard for the submission of this thesis. It is further certified that the work embodied in this thesis is neither partially nor fully submitted to any other university or institution for the award of any other degree or diploma.



[Signature]
20 Sep 21

Dr K. C. Tiwari

Professor,
Multidisciplinary Centre for Geoinformatics
Delhi Technological University,
Delhi- 110042, India

ACKNOWLEDGMENTS

I would like to extend my sincere thanks to **Dr K.C. Tiwari**, Professor, Multidisciplinary Centre for Geoinformatics (MCG), Delhi Technological University (DTU), Delhi for his invaluable advice, continuous support, and patience during my PhD study. His immense knowledge and plenteous experience have encouraged me in over the time to pursue academic research. He has widened the horizons of my thinking and promoted independent learning and research skills. He is an extra-ordinary mentor to share his wisdom and knowledge and putting his tireless efforts to support me through out.

I am deeply grateful to DRC chairman, *Dr. Kapil Sharma*, my SRC members; *Dr. L.K. Sinha*, Director, DTRL, DRDO; *Dr. R.D. Gupta*, Professor, MNNIT, Allahabad, Uttar Pradesh; *Dr. Seba Susan*, Professor, IT, DTU for evaluating the performance and giving their valuable feedback frequently to improve the work. I would also like to thank Professor *Nirendra Dev*, HOD, CE, DTU, Delhi for providing all the essential facilities in the department and the Centre.

I would like to offer my sincere thanks to the team of DTRL, DRDO for helping in field data collection and successfully carrying out the campaign twice in the project duration. Also, the instruments provided by the organization, helped in smooth data acquisition and maintaining the ground reference for the study. I extend my gratitude to *Indian Space and Research Organization (ISRO)* for supporting the project in airborne data collection, its pre-processing and its timely dissemination. This research is funded by *Department of Science and Technology (DST)*, under the grant number BDID/01/23/2014-HSRS.

I am also extremely grateful to the team members of *Networked Programme on Imaging Spectroscopy and Applications* (NISA) project especially *Dr. R.N. Sahu* for constantly motivating me and his insightful feedback pushed me to sharpen my thinking and brought my work to a higher level.

I would like to devote a special vote of acknowledgement to my all the fellow colleagues, *Dr. Deepti Soni, Dr. Amrita Bhandari, Dr. Rubeena Vohra, Dr. Dwijendra Pandey, Mr. Anupam Srivastava, Mr. Sanjay, Ms. Vaishnavi, Ms Princy*, for constantly encouraging me to widen my research from various perspectives. Further, I am also thankful to project staff associated with the MCG Centre, *Mr. Gopinadh* and *Ms. Rimjhim, Mr. Vijay* and *Ms. Tanisha* for not only devoting their time in fruitful discussions but performing administrative responsibilities. They have been a constant source to brim me with enthusiasm and carrying out the research.

Words cannot completely express my love and gratitude towards my family members who have supported and encouraged me through this journey. I owe a lot to my parents, who encouraged and helped me at every stage of my personal and academic life, and longed to see this achievement come true. I would like to thank my husband *Mr. Smit Chhabra* for his support, everlasting love, and sacrifices, which sustained my interest in research and motivated me towards the successful completion of this study. Finally, I would like to express my gratitude to my friends *Mr. Shivam Mahendru, Ms. Manisha Saini, Ms. Ranu, Ms. Shilpi* and *Ms. Sonia*. Without their tremendous understanding and encouragement in the past few years, it would be impossible for me to complete my study. Lastly, I thank the almighty God for the passion, strength, perseverance, and the resources to complete this study.

Date: 20th September 2021

Place: Delhi



(Shalini Gakhar)

2K17/PhD/IT/09

**Department of IT, DTU
Delhi-110042, India**

ABSTRACT

Humans all across the globe migrate to cities/urban areas in search of better livelihood. In India alone, the migrant population moving to cities is likely to rise to 40% by 2030. Urbanization takes a heavy toll of the scarce resources. Besides, there are many adverse environmental effects of rapid urbanization. Urban planners, therefore, have to continuously control and monitor the urban expansion, plan amenities, make judicious allocation of lands for industries, residences and agriculture, ensure low environmental pollution and simultaneously also address several other challenges of urban planning.

Remote sensing in general has been a very important supporting tool in the hands of urban planners in assessment of existing urban growth particularly in extraction of different levels of urban engineered surfaces such as roads and roofs *etc.* and its interpolation to assess future urban growth. The development in the field of remote sensing has therefore always been of interest to urban planners. The development of Hyperspectral Remote Sensing has further enabled urban planners in better assessment of urban expanse. However, though hyperspectral data is significantly more useful to the urban planners, it comes with its own set of challenges such as spectral variability, mixed pixel problems, accuracy requirements, requirement of recovery shape for correct identification of urban engineered surfaces (roads and roofs), selection of an appropriate approach such as target detection/classification/machine learning approach for information extraction providing better accuracy *etc.*

The present Thesis explores one of the relevant problems useful for urban planners *i.e* development of spectral-spatial strategies for detection of engineered objects using hyperspectral data. This problem has been explored under three

objectives. The first objective deals with an exhaustive comparative assessment of standard spectral target detection algorithms for engineered objects using hyperspectral data, under four categories. Various algorithms reported in literature have been considered for comparison. The second objective involves, development of different strategies for detection of engineered objects. It has been performed under two sub-objectives. In the first part, spectral - spatial urban target detection using Artificial Neural Network (ANN) has been explored. The second part explores, detection of the engineered surfaces (roads and roofs) using deep learning approach. The last objective expounds mixed pixel analysis and shape identification of engineered objects using hyperspectral data. This is also done in two parts, the first part deals with extraction of urban targets using fusion of spectral and shape features, and the second part deals with urban target detection using super-resolution mapping approach by recovery of shape.

The data for the research is Airborne Visible and Infrared Imaging Spectrometer – Next Generation (AVIRIS-NG) hyperspectral data collected during a joint ISRO-NASA campaign held during 2016-2017. For the present study, urban hyperspectral data for Udaipur, Rajasthan captured during February 2016 has been used.

For comparative assessment, different categories of target detection algorithms have been considered for extraction of roads and roofs. This has been implemented using reference spectra using both the in-scene (derived from image) and in-field (collected while ground data campaign) spectra. One of the findings of the results suggests that, Mahanalobis angle measure may be one of the robust angle measures for detection of roads and roofs. Besides in general, it is found that machine learning based methods such as ANN and ELM perform better amongst all the measures.

Associating spatial information such as morphological attribute profiles along with spectral signatures of labelled pixels of targets have yielded higher accuracy as

compared to standard target detection methods. The approach seems to perform better when targets of interests are composed of similar materials. For instance, roads and roofs are often made up of concrete, asphalt etc. and therefore purely spectra-based delineation of these two surfaces is challenging. Further, CNN based measures appear to provide higher accuracy in automated feature extraction of complex urban targets with minimal human intervention.

Spectral similarity of urban targets and coarse resolution of the sensor poses multiple challenges in their detection. Extraction of shape of urban engineered surfaces is an important part in urban planning. Therefore, two shape based features, exploiting the spatial aspect of hyperspectral data are proposed. Additionally, the shape of urban engineered surfaces (roads and roofs) is enhanced using unmixing based super resolution approach by taking the neighbouring pixels into account.

The study, however, restricts itself in terms of extraction of different levels of roads and roofs. Besides, the study does not link up with extraction of road and roof surfaces with different urban applications such as determination of road and roof conditions and aging. These and several other relevant issues may be explored in future.

TABLE OF CONTENTS

ABSTRACT	iii
LIST OF PUBLICATIONS	x
LIST OF FIGURES	xii
LIST OF TABLES	xvii
Chapter 1	1
Introduction	1
1.1. Problem Statement	5
1.2. Research Gaps	7
1.3. Research Objectives	10
1.4. Thesis Overview	10
Chapter 2	13
Theoretical Background	13
2.1. Hyperspectral remote sensing	13
2.2. Dimensionality Reduction	16
2.2.1. Principal Component Analysis (PCA)	17
2.3. Image Classification	17
2.4. Target Detection	19
2.4.1. Spectral target detection algorithms	21
2.4.2. Spectral-spatial target detection strategies	21
2.4.3. Mixed Pixel Analysis	22
2.4.4. Shape Identification	23
2.5. Classification vs Target detection: A comparison	24
2.6. Approaches to Target Detection and Enhancement	26
2.6.1. Spectral Target detection algorithms	27
2.6.1.1. Distance Measures	27
2.6.1.2. Angle Measures	28
2.6.1.3. Information Measures	28
2.6.1.4. Machine Learning Measures	29
2.6.2. Spectral-spatial target detection strategies	31
2.6.2.1. Dilation	32
2.6.2.2. Erosion	32
2.6.2.3. Opening	32

2.6.2.4. Closing.....	33
2.6.3. Machine Learning Approaches	33
2.6.3.1. Artificial Neural Networks (ANN).....	34
2.6.3.2. Extreme Learning Machine (ELM).....	37
2.6.3.3. Support Vector Machines (SVM).....	39
2.6.4. Deep Learning Methods.....	42
2.6.4.1. Convolution Neural Network (CNN)	43
2.6.5. Spectral Unmixing	45
2.6.5.1. Linear Spectral Unmixing	46
2.6.5.2. Vertex Component Analysis.....	47
2.6.6. Super resolution techniques	48
2.6.6.1. Pixel Swap	50
2.6.6.2. Inverse Euclidian Distance	51
Chapter 3	53
Data and Software.....	53
3.1. Data	53
3.1.1. Airborne Data Collection	53
3.1.1.1. AVIRIS-NG Phase 1	56
3.1.1.2. AVIRIS-NG Phase 2	57
3.1.2. Ground Data Collection	57
3.2. Software	60
3.2.1. Environment for Visualizing Images (ENVI).....	60
3.2.2. Matrix Laboratory (MATLAB).....	60
3.2.3. Jupyter Notebook using Python	61
Chapter 4	62
Comparative assessment of detection algorithms for engineered objects	62
4.1. Introduction	62
4.2. Problem Statement	66
4.3. Study Area and Data	66
4.4. Methodology and Implementation	68
4.5. Results and Discussion.....	71
4.5.1. Target detection using ground reference spectra	72
4.5.1.1. Distance Measures	72
4.5.1.2. Angle Measures	74
4.5.1.3. Information Measures	77

4.5.1.4. Machine Learning Measures	80
4.5.2. Target detection using image reference spectra	82
4.5.2.1. Distance Measures	82
4.5.2.2. Angle measures.....	84
4.5.2.3. Information Measures	87
4.5.2.4. Machine Learning Measures.....	89
4.5.3. Analysis of threshold for different algorithms	90
4.5.4. Performance Analysis	92
4.6. Summary	94
Chapter 5	97
Development of spectral-spatial strategies for detection of engineered objects.....	97
5.1. Introduction.....	97
5.2. Problem Statement	98
5.3. Study Area and Data	99
5.4. Methodology and Implementation	99
5.5. Results and Discussion	103
5.5.1. Detection using Dilation Operator	103
5.5.2. Detection of Erosion Operator	106
5.5.3. Detection using Opening operator	108
5.5.4. Detection using Closing Operator	111
5.6. Summary	113
Chapter 6	114
Deep learning strategy for detection of engineered objects	114
6.1. Introduction	114
6.2. Problem Statement	115
6.3. Study Area and Data	116
6.4. Methodology and Implementation	117
6.5. Results and Discussion.....	122
6.5.1. Detection of Roads.....	123
6.5.2. Detection of Roofs	126
6.6. Summary	128
Chapter 7	130
Shape Identification of engineered objects using spectral and shape-based features ...	130
7.1. Introduction	130
7.2. Problem Statement	135

7.3. Study area and data	136
7.4. Methodology and Implementation	136
7.5. Results and Discussion.....	138
7.5.1. Urban target detection using spectral features	139
7.5.2. Urban target detection using shape features.....	141
7.5.3. Urban Target detection using fusion of spectral and shape features.....	142
7.6. Summary	144
Chapter 8	146
Shape enhancement using spatial super-resolution	146
8.1. Introduction	146
8.2. Problem Statement	147
8.3. Study area and data	148
8.3.1. Synthetic Data	148
8.3.2. AVIRIS-NG Data.....	149
8.4. Methodology and Implementation	150
8.5. Results and Discussion.....	153
8.5.1. Super-resolution using synthetic data	153
8.4.2. Super-resolution using hyperspectral data	158
8.6. Summary	161
Chapter 9	163
Conclusions and Contributions	163
9.1. Conclusions	163
9.2. Research Contributions	166
9.3. Future Scope.....	166
References	168
Author's Biography	193

LIST OF PUBLICATIONS

International Journals (Published/Accepted)

- i. Gakhar, Shalini, and Kailash Chandra Tiwari. "Spectral–spatial urban target detection for hyperspectral remote sensing data using artificial neural network." **The Egyptian Journal of Remote Sensing and Space Science** 24, no. 2 (2021): 173-180.
- ii. Gakhar, Shalini, and K. C. Tiwari. "Comparative Assessment of Target-Detection Algorithms for Urban Targets Using Hyperspectral Data." **Photogrammetric Engineering & Remote Sensing** 87, no. 5 (2021): 349-362.
- iii. Gakhar, Shalini, and Kailash Chandra Tiwari. "Detection of engineered surfaces using deep learning approach in AVIRIS-NG hyperspectral data." **Geocarto International** just-accepted (2021): 1-20.
- iv. Shalini Gakhar & K. C. Tiwari, "Urban target detection using super-resolution mapping for AVIRIS-NG hyperspectral data." In Special issue on AVIRIS-NG, **Journal of Applied Remote Sensing**. (Accepted)

Papers in International Journal (Under Publication/Review)

- i. Shalini Gakhar & K. C. Tiwari, "Extraction of urban targets using fusion of spectral and shape features in AVIRIS-NG Hyperspectral Data" in **Journal of Applied Remote Sensing**. (Under Review)

Papers in International Conference

- i. Shalini Gakhar, K C Tiwari "Analysis of data collection parameters for urban engineered surfaces and objects", 38th Asian Conference on Remote Sensing (ACRS 2017), to be held during October 23-27, 2017 at Hotel, The Ashok, New Delhi, India.

- ii. Shalini Gakhar, K C Tiwari “Visual Image Interpretation of remote sensing images” in Space Technology for sustainable development. ISG Chapter, presented on 21-22 March 2017.

LIST OF FIGURES

Figure 1.1: Types of Roads and Roofs as engineered objects -----	6
Figure 1.2: Flow chart of Thesis organization-----	12
Figure 2.1: Components of Remote Sensing System-----	14
Figure 2.2: Principle of Hyperspectral remote sensing-----	14
Figure 2.3: Pre-processing steps for hyperspectral data exploitation-----	15
Figure 2.4: Types of Classification Approaches-----	18
Figure 2.5: Relationship between a traditional single-stage hard (crisp) classification using supervised or unsupervised classification logic and a classification based on the use of soft (fuzzy) logic-----	19
Figure 2.6: Artificial Neural Network Architecture-----	35
Figure 2.7: Single layer perceptron-----	37
Figure 2.8: Architecture of Extreme Learning Machine-----	38
Figure 2.9: Concept of SVM-----	40
Figure 2.10: General Architecture of Convolution Neural Network-----	45
Figure 2.11: (a) $m \times n$ array to super resolve (b) 3×3 window size and 8 neighbours (c) Super resolution mapping of all 8 neighbours-----	51
Figure 2.12: Abundance fractions layout in 3×3 -pixel array-----	52
Figure 3.1: Airborne campaign team and science field campaign team with B200 aircraft and AVIRIS-NG instrument-----	54
Figure 3.2: Three-dimensional image of (a) Forestry (b) Geology (c) Coastal Oceans (d) Snow/Ice-----	55
Figure 3.3: Multiple scan lines captured during the airborne data campaign Phase-1-----	56
Figure 3.4: Multiple scan lines captured during the airborne data campaign Phase-2-----	57

Figure 3.5: Flight paths of airborne campaign for field data collection-----	58
Figure 3.6: (a) Spectral signatures of concrete road (b) Railway tracks (Iron) (c) Tennis court (d) Bitumen roof-----	59
Figure 4.1: Airborne hyperspectral Data Experimental Site-----	67
Figure 4.2: Square window of size 60×60 considered for accuracy assessment-----	70
Figure 4.3: Flowchart of methodology-----	71
Figure 4.4: Detection of roads and roofs using Distance Measures considering ground reference spectra-----	74
Figure 4.5: Detection of roads and roofs using Angle Measures considering ground reference spectra-----	76
Figure 4.6: Detection of roads and roofs using Information Measures considering ground reference spectra-----	79
Figure 4.7: Detection of roads and roofs using Machine Learning Measures considering ground reference spectra-----	81
Figure 4.8: Detection of roads and roofs using Distance Measures considering image reference spectra-----	84
Figure 4.9: Detection of roads and roofs using Angle Measures considering image reference spectra-----	86
Figure 4.10: Detection of roads and roofs using Information Measures considering image reference spectra-----	88
Figure 4.11: Detection of roads and roofs using Machine Learning Measures considering image reference spectra-----	90
Figure 4.12: Threshold values for detection of Road and Roof targets using Ground Reference Spectra-----	91

Figure 4.13: Threshold values for detection of Road and Roof targets using Image Reference Spectra-----	91
Figure 4.14: Road detection accuracy using ground reference spectra and image reference spectra-----	93
Figure 4.15: Roof detection accuracy using ground reference spectra and image reference spectra-----	93
Figure 5.1(a): Line structuring element of length 5 angle 45° and neighbourhood 5×5 --	100
Figure 5.1(b): Rectangle structuring element of size 3×5 and neighbourhood 5×5 ---	100
Figure 5.1(c): Disk structuring element of radius 3 and neighbourhood 7×7 -----	100
Figure 5.2: Flowchart of the proposed approach-----	102
Figure 5.3: Road Detection using Dilation (a) disk (b) line and (c) rectangle-----	104
Figure 5.4: Roof Detection using Dilation (a) disk (b) line and (c) rectangle-----	105
Figure 5.5: Road Detection using Erosion (a) disk (b) line and (c) rectangle-----	107
Figure 5.6: Roof Detection using Erosion (a) disk (b) line and (c) rectangle-----	108
Figure 5.7: Road Detection using Opening (a) disk (b) line and (c) rectangle-----	109
Figure 5.8: Roof Detection using Opening (a) disk (b) line and (c) rectangle-----	110
Figure 5.9: Road Detection using Closing (a) disk (b) line and (c) rectangle-----	111
Figure 5.10: Roof Detection using Closing (a) disk (b) line and (c) rectangle-----	112
Figure 6.1: (a) Ground Reference generated using VCA for road, roof, vegetation and soil (b) Ground Reference for engineered surfaces (roads and roofs)-----	119
Figure 6.2: CNN Architecture for the proposed approach-----	121
Figure 6.3: Block Diagram of Methodology-----	122
Figure 6.4: Detection of Roads using proposed approach-----	125
Figure 6.5: Detection of roof using proposed approach-----	127

Figure 7.1: Three-dimensional hyperspectral data cube depicting pixel vector-----	131
Figure 7.2: Fusion of spectral and spatial features-----	137
Figure 7.3: Flow chart of the proposed Approach-----	138
Figure 7.4: Spectral Approach (a) Detection of Roads (b) Detection of Roofs (c) Scatter plot for both urban targets-----	140
Figure 7.5: Standard Deviation (a) Detection of Roads (b) Detection of Roofs (c) Scatter plot for both urban targets-----	141
Figure 7.6: Range (a) Detection of Roads (b) Detection of Roofs (c) Scatter plot for both urban targets-----	141
Figure 7.7: Spectral features and Standard deviation (a) Detection of Roads (b) Detection of Roofs (c) Scatter plot for both urban targets-----	143
Figure 7.8: Spectral features and Range (a) Detection of Roads (b) Detection of Roofs (c) Scatter plot for both urban targets-----	143
Figure 8.1: Synthetic data for road targets-----	149
Figure 8.2: Synthetic data for roof targets-----	149
Figure 8.3: Road and Roof targets identified for super-resolution-----	149
Figure 8.4: Abundance maps of (a) road and (b) roof surfaces generated using spectral linear unmixing-----	151
Figure 8.5: Flow chart of the proposed Approach-----	153
Figure 8.6: Detection of Synthetic Road Targets using Pixel Swapping and Inverse Euclidean Distance Method-----	155
Figure 8.7: Detection of Synthetic Roof Targets using Pixel Swapping and Inverse Euclidean Distance Method-----	157
Figure 8.8: Detection of AVIRIS-NG Road Targets using Pixel Swapping and Inverse Euclidean Distance Method-----	159

Figure 8.9: Detection of AVIRIS-NG Roof Targets using Pixel Swapping and Inverse	
Euclidean Distance Method-----	161

LIST OF TABLES

Table 2.1. Difference between Target detection and Classification approach-----	25
Table 2.2: Data collection parameters for target detection-----	26
Table 2.3. Descriptive Assessment of Target Detection algorithms-----	30
Table 3.1: Science themes and study sites for airborne data collection-----	54
Table 3.2: Specifications of the AVIRIS-NG Sensor/Data-----	54
Table 3.3: Level details of the airborne data collected-----	56
Table 3.4: Science themes and study sites for airborne data collection Phase 2-----	57
Table 3.5: AVIRIS-NG Airborne hyperspectral Phase-1 Flight Planning-----	58
Table 3.6: Spectral signatures collected for engineered objects-----	59
Table 4.1: Mathematical Formulas for Target Detection Algorithms-----	64
Table 4.2: Description of Image and Ground Data Collection-----	68
Table 4.3: Accuracy assessment for Distance measures using ground reference spectra- -----	74
Table 4.4: Accuracy assessment for Angle measures using ground reference spectra-	76
Table 4.5: Accuracy assessment for Information measures using ground reference spectra-----	79
Table 4.6: Accuracy assessment for Machine learning measures using ground reference spectra-----	81
Table 4.7: Accuracy assessment for Distance measures using image reference spectra- -----	84
Table 4.8: Accuracy assessment for Angle measures using image reference spectra--	86
Table 4.9: Accuracy assessment for Information measures using image reference spectra-----	88

Table 4.10: Accuracy assessment for Machine Learning measures using image reference spectra-----	90
Table 4.11: Threshold values considered for detection of road and roof targets-----	92
Table 5.1: Accuracy assessment of Roads using Dilation-----	105
Table 5.2: Accuracy assessment of Roofs using Dilation-----	106
Table 5.3: Accuracy assessment of Roads using erosion-----	107
Table 5.4: Accuracy assessment of Roofs using erosion-----	108
Table 5.5: Accuracy assessment of Roads using Opening-----	109
Table 5.6: Accuracy assessment of Roofs using Opening-----	110
Table 5.7: Accuracy assessment of Roads using Closing-----	112
Table 5.8: Accuracy assessment of Roofs using Closing-----	112
Table 6.1: Challenges and research gaps-----	116
Table 6.2: Accuracy assessment for road detection using proposed approach-----	125
Table 6.3: Accuracy Assessment of roof detection using proposed approach-----	127
Table 7.1: Shape extraction features used-----	132
Table 7.2: SVM and its variants with kernel functions-----	135
Table 7.3: Accuracy Assessment using spectral features-----	139
Table 7.4: Accuracy Assessment using shape features-----	141
Table 7.5: Accuracy assessment using spectral and shape features-----	143
Table 8.1: Description of road and roof targets selected from AVIRIS-NG hyperspectral Dataset-----	149
Table 8.2: Accuracy Assessment of Synthetic Road Targets using Pixel Swapping and Inverse Euclidean Distance Method-----	153
Table 8.3: Accuracy Assessment of Synthetic Roof Targets using Pixel Swapping and Inverse Euclidean Distance Method-----	155

Chapter 1

Introduction

The urban population is growing due to expansion of cities and migration of people in search of better opportunities (Storper and Scott 2009). According to a survey of Ministry of Housing and Urban Affairs, Government of India; the percentage of urban population to total population stands at 31.6 with a continuous increase in its proportion since the previous decade (Chandramouli 2011). This population living in urban areas, in India, is further estimated to increase approximately to 40% by 2030 (United Nations 2015). The major reasons attributed for increase in urban trends are industrialization, commercial opportunities, socio-economic benefits, occupational prospects and modernization (Ershad 2020). Numerous challenges associated with urbanization include, increasing population density and its impact on urban architecture (housing, roads, hospitals, schools *etc.*). The direct consequences of urbanization are changes in land quality, pollution, degraded water quality, atmospheric and climatic changes *etc.* In emerging economies, urbanization is one of the major parameters in assessment of multiple socio-economic issues. Growth in urban population plays a havoc on urban necessities like water, housing, transport, health and many more.

For sustainable development, preparation of strategic city plans are necessary which involve delineation of probable growth areas followed by delineation of city-level infrastructure (roads, roofs, drainage *etc.*). Alteration in vegetative cover, water and air quality, surface temperature is induced by urban expansion, which in turn influence the microclimate of the human habitat and degrades the environment (Shafri, *et al.* 2012). All these issues necessitate automated, time and cost-efficient techniques for urban planning and management. Social activist and urban writer Jane Jacobs once

quoted, “*Cities have the capability of providing something for everybody, only because, and only when, they are created by everybody.* (Jacobs 2016)”

With the development in space-borne and air-borne technologies, mapping the urban areas has become easier, less time and effort consuming, giving a bird’s eye view of larger area at the same time. However, due to miscellaneous material composition and levels of classification (Anderson and James 1976) of urban features, multitudes of challenges are encountered in extraction of urban information such as, small size/width of urban targets, for example, street roads and pavements, heterogeneity, higher within class variability and lower intra class variability (Chen, *et al.* 2018) *etc.* Certain urban built-up surfaces such as asphalt roofs and roads may also be confused with bare soil surfaces due to their spectral similarity (Herold, *et al.* 2004).

Therefore, in addition to standard statistical classification techniques, several new AI based techniques are being explored for mapping of urban targets consisting of different material composition and land cover types. Satellite remote sensing has also dramatically improved Earth observation and our capability to understand different land cover types and atmosphere. Most of the space borne sensors, so far, have been multispectral with a few wavebands tailored for specific observational requirements. It is now well established that information derived from multiple narrow contiguous bands known as hyperspectral may be far more suitable than a few discrete multispectral wavebands (S. B. Li 2009) (Pandey and Tiwari 2020) (Hegde, *et al.* 2014).

Hyperspectral Remote Sensing enables the study of the properties of in-scene materials remotely for the purpose of detection, identification, and composition analysis of objects present in the environment. It is expansively used for urban forestry

monitoring (Zhang, Song and Yu 2011) , agriculture (Teng and Gao 2009) , marine research (Lou, *et al.* 2008) , mineralogy (Pei and Fu. 2007) and many more.

Hyperspectral data is extensively used for multiple land use and land cover classification (Hegde, *et al.* 2014) and target detection applications (Li, *et al.* 2009) in urban areas. Urban land covers are complex in nature comprising of impervious surfaces which further consist of roads, roofs, parking lots and other infrastructure (Schueler, Fraley-McNeal and Cappiella 2009). The reflecting characteristics of roof materials modify the incident energy absorbed by them and has a direct impact on local climate (Oke and Cleugh 1987). The aging of roads also affects the trafficability, imposition of safety rules and regulations with an added cost of construction or maintenance. Improvement in mapping of roads and roofs has a capability of reframing current scenario of urban planning and development (Herold 2003). Susceptibility towards disaster, climatic changes is also mounting with rapid urban growth; influencing classification and target detection studies via remote sensing technology (Mourshed, Bucchiarone and Khandokar 2016).

With the availability of high spatial satellite and airborne data, *per-pixel* based algorithms are often considered for extraction of useful information from the data (Peña-Barragán, *et al.* 2011). As urban areas are an amalgamation of various heterogeneous surfaces such as roads, roofs, parking lots *etc.*; their spectral complexity may result in various challenges while using per-pixel analysis (Herold, *et al.* 2004). One of the significant challenges is that, substantial amount of signal captured at the sensor apparently comes from the pixel background (Townshend, *et al.* 2000). Therefore, the algorithms that incorporate both spectral and spatial aspect of the remote sensing data are useful for better classification. The spatial features may include

individual areas with a definite shape and spectral homogeneity, also referred as *image objects* (Blaschke, *et al.* 2014).

Target detection is a binary hypothesis to check whether a ‘rare’ object of known spectra is present or not in the area of interest. The ‘rare object’ often termed as target is relatively present in a small number in contrast with the total number of pixels in a hyperspectral image. As the number of pixels considered to be a target is comparatively low, therefore estimation of statistical properties of target class is difficult. Also, the targets may not be resolved clearly due to sensor spatial properties. The targets appearing in few pixels are termed as *pure-pixel* or *full-pixel* targets or else if they exist as part of a single pixel, they are called *subpixel* targets. Thus, key to target detection problem lies in making *target present* or *target absent* decision for every pixel in hyperspectral image (Manolakis, Lockwood and Cooley 2016). The target detection approach is therefore significantly different from conventional classification approach. Many urban surfaces may lend themselves to better extraction using target detection approach rather than through classification approach. However, there is lack of literature exploring the utility of target detection approach in extraction of urban surfaces.

Recent field campaign of Airborne Very High-Resolution Imaging Spectrometer -Next Generation, (AVIRIS-NG) conducted by ISRO and NASA during 2016-2017 has provided an opportunity to explore the potential applications of hyperspectral data in various thematic areas. Considering the potential of this emerging technology, the Interdisciplinary Cyber Physical Systems, Division of Department of Science & Technology, Government of India evolved a cluster based multidisciplinary Networked project on “Imaging Spectroscopy and Applications (NISA)” to promote

research in this area. This data provides an opportunity to explore hyperspectral data for various urban related studies.

The work presented in this thesis undertakes development of spectral-spatial strategies for detection of engineered objects using hyperspectral data collected during this campaign.

1.1. Problem Statement

Extraction of meaningful information from remote sensing data is a highly challenging task. Engineered objects or urban built-up surfaces are considered as anthropogenic features by which water cannot penetrate (Weng 2012). An engineered object can be regarded as a surface which is created artificially with less thickness. It can be composed of either single component or multiple components preferably three-dimension in nature. Furthermore, it has a well- defined boundary which is visible or tangible surface of object. Roads, rooftops, parking lots, sports infrastructure are examples of engineered objects or surfaces.

Detection and identification of engineered objects become complicated due to their different atomic structures, variant response to different parts of electromagnetic spectrum and molecular interaction between particles. Objects are complicated because of different base material used, variety of coatings/paintings on the surfaces or the series of steps involved in its development. Besides extraction of urban information may involve extraction at different levels. One such classification scheme is suggested by Anderson *et al* (Anderson and James 1976). It may not be possible to extract all types of engineered surfaces present in urban land covers at different levels; therefore, it is proposed to study and detect only two major target classes belonging to Roads and Roofs only up to first few levels. *Figure 1.1.* shows some examples of engineered objects collected during ground data collection.

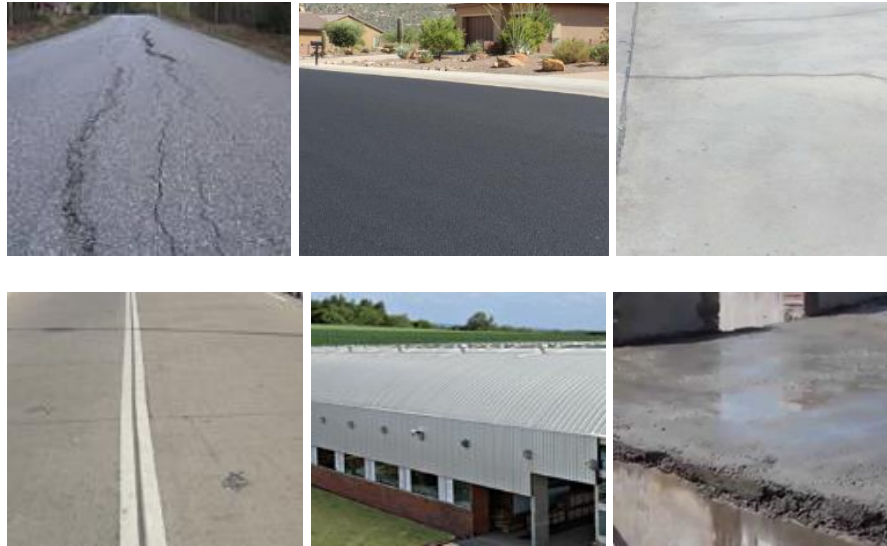


Figure 1.1. Types of Roads and Roofs as engineered objects

The unplanned increase in construction of engineered surfaces might lead to increase in volume, duration and intensity of urban runoff (Weng 2012). The urban stretch could experience a decrease in groundwater recharge with increased risk to stormflow and flood (Brun and Band 2000). Also, it has a direct impact on water quality and air quality. Till now, many researchers have explored detection and analysis related to natural targets such as vegetation (Farooq, Jia and Zhou 2019), forests (Kumar 2013), waterbodies (Igamberdiev 2011), and soil (Peng 2013), but applications within the urban domain have to explore newer challenges and complexities.

Spectral signatures of built-up materials in urban areas show similarities in terms of material composition, like asphalt and concrete are used for making roads and roofs, which make it difficult to spectrally discriminate these materials. Depending upon the spectral and spatial resolution, which are based on sensor characteristics, a lot of within-class-variability is also observed. Furthermore, due to heterogeneous and complex attributes of urban built-up mixed pixel pattern is also pragmatic. The signal reaching the sensor is a combination of multiple other features, in the background.

No standard approach for mapping road surfaces and identifying the condition of road is available. Though some researchers have emphasized extraction of road

centreline, but still, it is difficult to differentiate dark new roads and dark tile roofs (K. U. Segl 2003), (Mohammadi 2012).

Segl *et al* extended the reflective hyperspectral data till thermal bands to improve the detection of buildings to increase the reliability of differentiation between buildings and open spaces leading to more accurate results. Researchers have also tried to classify different roof materials using hyperspectral data by creating spectral library of various materials used for urban roofs followed by their detection using multiple supervised approaches (Chisense 2012). However, there is yet no standard approach for extraction of urban roads and roofs.

The issue of spectral similarity between roads and roofs has been addressed by associating spatial information with spectral features by researchers (Dalla Mura, *et al.* 2010), (Gu, Zhang and Zhang 2008) (Khodadadzadeh, *et al.* 2014). The spatial aspect from hyperspectral data often aids in correct detection of targets having similar composition, therefore spatial features such as morphological attributes, shape and unmixing based super-resolution may be used to delineate the urban engineered surfaces.

Huge volumes of real-time data processing pose a computational burden and increases the time complexity. With the introduction of machine and deep learning approaches the target detection can be done for larger areas with less human intervention and prediction capabilities of these algorithms can be exploited for unknown data (Bhangale, *et al.* 2016) (Dora, Francisco and Pablo 2014) (Chi, *et al.* 2009) (Kuo, *et al.* 2013).

1.2. Research Gaps

After extensive literature survey, following research gaps with respect to urban applications have been observed:

- i. Though a lot of work has been directed towards mapping of various urban surfaces and lot of studies have been carried out to understand the effects of urbanisation (Maktav, Erbek and Jürgens 2005) (Patino and Duque 2013) (Nada, Mourshed and Bray 2016), (Gamba, Dell'Acqua and Dasarathy 2005) limited work appears to have been directed towards extraction of different levels of engineered surfaces such as, roads, roofs *etc.*, particularly using hyperspectral data.
- ii. Though the multispectral data has been well explored in various types of urban studies (Guo, *et al.* 2011), (Dengsheng and Qihao 2005), (Lynch, Leonhard and Ellen 2020), (Shackelford and Davis 2003) the different aspects of hyperspectral data such as, spectral properties of urban materials, effect of spectral variability, study of urban spectral characteristics, quantitative assessment of spectral separability *etc.* appear to not have been explored well.
- iii. Airborne and space-borne observations contain higher within class variability that is dependent upon sensor characteristics (observed area, object geometry, illumination effects, atmospheric interactions, spectral resolution as well as spectral mixing effects) (Tiwari, *et al.* 2013). Most of the spectral studies have not considered the scale of analysis (Stefanou and Kerekes 2009). Laboratory spectra commonly consist of single material illuminated under specific conditions and is therefore significantly different from field spectra. A comparative investigation in extraction of urban engineered surfaces using both lab and field spectra may therefore be useful.
- iv. Target detection technique in comparison to conventional classification techniques has not been explored much with respect to urban surface extraction which needs to be examined.

- v. The current unsupervised, semi-supervised and active learning algorithms may not be able to handle huge volume of data, so there is a necessity of development of algorithms that can utilize unlabelled images. Further, most target detection algorithms for full pixel and subpixel targets have been obtained by describing spectral variability using multivariate normal distribution or subspace model. Machine and deep learning-based algorithms are being investigated in different types of urban applications (Kuras, *et al.* 2021), (Li, *et al.* 2020), (Senchuri 2021), (Tamilarasi and Prabu 2021), (Zhao and Du 2016) however, these need further investigations in extraction of urban engineered surfaces.
- vi. Most of the research with hyperspectral data in urban studies appear to be focused on utilisation of material spectra only (Zhao and Shihong 2016), (Bubner, Kempinger and Shettigara 2001), (Carvalho, Abilio and Meneses 2000), (Homayouni and Roux 2004), (Maryam 2019). This may be a limiting factor in extraction of some of the urban engineered surfaces such as roads and roofs *etc.* it is therefore important to explore the benefits of incorporating spatial-contextual information.
- vii. Multiple endmember extraction methods suffer from spectral confusion and computational complexity induced by numerous endmember combinations (Plaza, *et al.* 2004), (Zhang, Gao, *et al.* 2013), (Du, *et al.* 2008), (Plaza and Chang 2006). Incorporation of spatial information in the selection of endmember combination can reduce spectral confusion and improve computational efficiency. Identification of shape of urban targets using various methods may aid extraction process, therefore morphological operators, attribute profiles and spectral unmixing based super resolution methods need further investigations.

1.3. Research Objectives

The cumulative objectives derived from above mentioned research gaps are:

- i. Comparative assessment of spectral target detection algorithms for engineered objects using hyperspectral data.
- ii. Development of strategies for detection of engineered objects.
 - a. Spectral - Spatial Urban Target Detection for Hyperspectral Remote Sensing Data using Artificial Neural Network
 - b. Detection of engineered surfaces using deep learning approach
- iii. Mixed pixel analysis and shape identification of engineered objects using hyperspectral data.
 - a. Extraction of urban targets using fusion of spectral and shape features by Support Vector Machine
 - b. Shape enhancement using super-resolution mapping

1.4. Thesis Overview

The Thesis contains *nine* descriptive chapters, aligned in accordance with the objectives.

Chapter 1 gives Introduction to the area of research. Beginning from the motivation behind the work, the problem formulation has been discussed in detail. This chapter also discusses significance of the study along with research gaps and objectives.

Chapter 2 involves detailed study of the concepts required for understanding the work done with supporting literature including different approaches for urban information extraction, such as classification and target detection approaches. This chapter presents a comparative assessment between the traditional approaches used for detection of urban targets in recent scenarios.

Chapter 3 explains about the data and software used. It includes the AVIRIS-NG airborne data collection campaign in two phases along with its detailed specifications. The particulars about simultaneous ground data collection are also mentioned.

Chapter 4 to 8 involves individual discussions about each objective and their sub objectives. Each chapter includes, a brief discussion about the work, associated literature, the problem statement, the dataset used, results and discussion section followed by a summary.

Chapter 4 describes the work done under Objective 1, that is, comparative assessment of existing spectral target detection algorithms used for detection of engineered objects. This chapter examines the ground and image-based reference spectral signatures using various algorithms.

Chapter 5 is about the part of work done for Objective 2: development of spectral-spatial strategies for detection of urban targets, in which the morphological attributes derived from hyperspectral data are combined with the spectral knowledge for better detection.

Chapter 6 is an extension of work done in Objective 2 which focuses on deep learning approach that appears to be effective in this domain. Roads and roofs are extracted using automated features for the area under consideration.

Chapter 7 explains methodology, implementation details and result analysis for shape identification of engineered objects in order to determine their fine edges and boundaries, as one of the subtasks of Objective 3.

Chapter 8 addresses the problem of mixed pixel analysis in urban land covers using super-resolution approach by further fine tuning the coarse resolution of the sensor. This work is done to optimise the shape detected for urban engineered surfaces

as remaining part of Objective 3. The proposed approach is validated on synthetic dataset followed by analysis on hyperspectral data.

Chapter 9 provides the Conclusions derived from the study done and also enlists the set of contributions made. This section also discusses the future scope which may be considered for future exploration.

The flow chart for the Thesis orientation is illustrated in *Figure 1.2*.

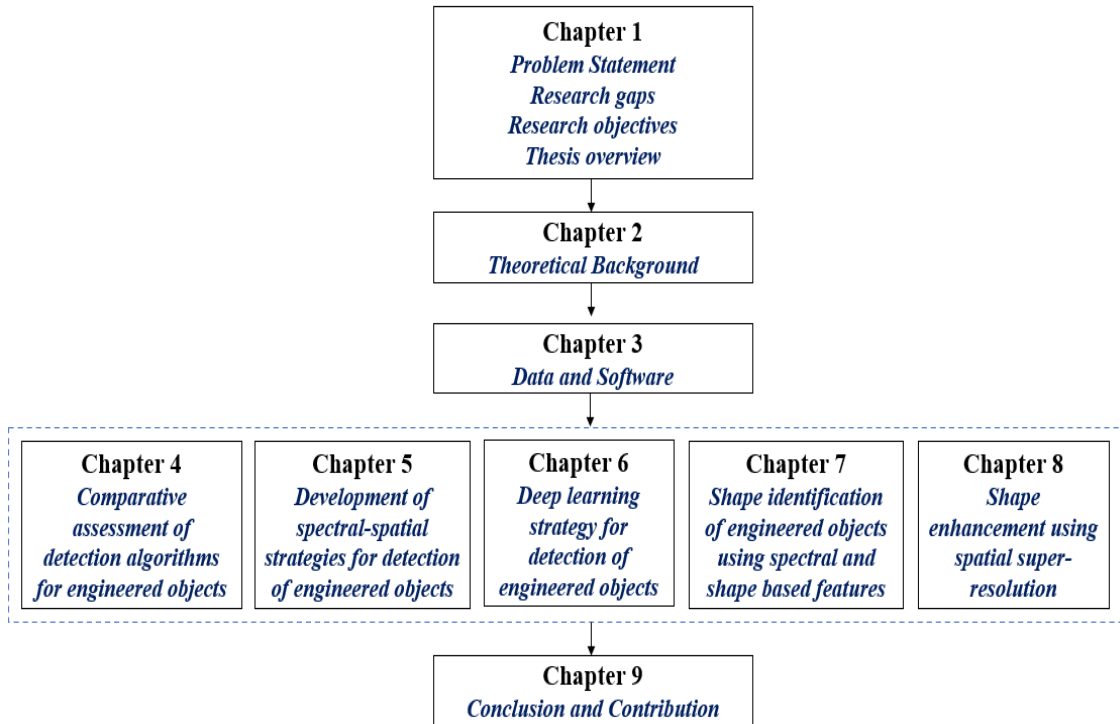


Figure 1.2. Flow chart of Thesis organisation

Chapter 2

Theoretical Background

This chapter deals with the theoretical background of the various remote sensing methods used in this work. The subsections traverse through the basic concepts that have been further explored in this research work.

2.1. Hyperspectral remote sensing

Hyperspectral remote sensing emphasizes extraction of useful information from Earth's surface by radiance values acquired by means of airborne or space borne sensors (Manolakis, Lockwood and Cooley 2016). Interaction of electromagnetic radiation with earth's surface causes fraction of energy to reflect, absorb and/or transmit. These fractions are dependent upon the type and condition of the target material. These variations describe the behavior of the different materials which is exploited by hyperspectral imaging.

The source of radiation is required to illuminate the target of interest. Multiple energy interactions take place while the radiations are travelling from source to target, which in turn are captured by the sensor. The energy makes its way through the intervening atmosphere and interacts with the target based upon its characteristics. The radiation may be *transmitted* (passes through the target), *absorbed* (results in target heating), *emitted* (based on temperature), *scattered* (in multiple directions) and *reflected*. For sensing the amount of energy released, several sensors are required to be mounted on various platforms, such as, ground based (spectroradiometer), airborne (AVIRIS-NG by NASA and ISRO) and space borne. *Figure 2.1* shows components of a remote sensing system with energy interactions.

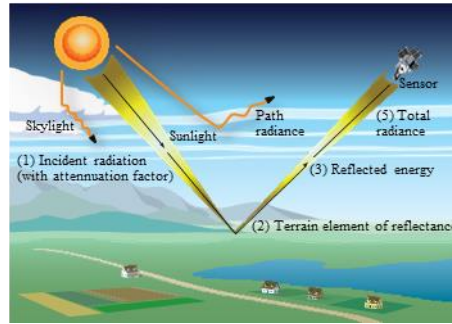


Figure 2.1 Components of Remote Sensing System
(Source: (Manolakis, Lockwood and Cooley 2016))

Hyperspectral imaging spans throughout ultraviolet (UV), visible and infrared (IR) regions of electromagnetic spectrum producing co-aligned images in hundreds of narrow bands. Hyperspectral data encapsulates rich spatial and spectral content formulated into a three-dimensional structure known as *hypercube*. The spatial aspect corresponds to the arrangement of pixels giving the geolocation whereas the spectral aspect deals with the radiation received by the sensor corresponding to different bands. Therefore, a pixel corresponds to a high-resolution spectral signature that uniquely identifies the target material. For a particular spatial sample, the radiance or reflectance measurement at different wavelengths are arranged in form of a vector (Refer *Figure 2.2*).

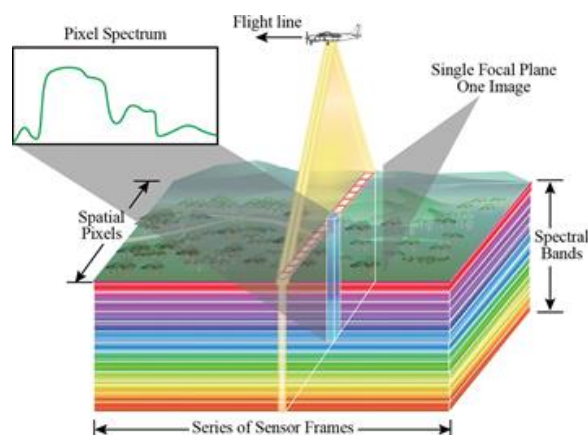


Figure 2.2 Principle of Hyperspectral remote sensing
(Source: (Manolakis, Lockwood and Cooley 2016))

Due to high spatial and spectral information condensed in hyperspectral data, its analysis entails use of sophisticated image processing software. As the raw radiance

data needs to be calibrated to scaled reflectance before interpretation. The calibration of the data, for an imaging spectrometer with a linear response, is the simple ratio of the value from a known radiometric source in the appropriate units, averaged over each spectral band, divided by the dark-subtracted raw signal in digital numbers (Manolakis, Lockwood and Cooley 2016). Further, the image is processed for removal of atmospheric hindrances, topographic effects (with respect to slope, altitude, roll, pitch and yaw) and any sensor related correction. *Figure 2.3.* shows the various steps involved in hyperspectral data pre-processing.

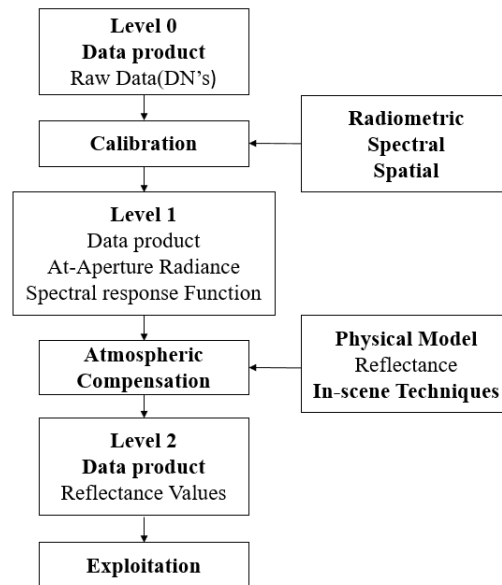


Figure 2.3. Pre-processing steps for hyperspectral data exploitation

Hyperspectral data have taken a leap over multispectral data, paving way for multiple applications such as soil mapping (Hively, *et al.* 2011), wildlife and forest mitigation (Hycza, *et al.* 2018), water body management (Pu, *et al.* 2017), disaster prediction (Bhangale, *et al.* 2016), mineral exploration (Arindam 2020), urban land-use classification (Fen, *et al.* 2018) and many more.

2.2. Dimensionality Reduction

The process deals with the computationally intensive image datasets to reduce its complexity, thereby capturing only the required significant details. Enormous amount of data is stored by the sensors, demanding dimensionality reduction to reduce the ambiguity in data. Dimensionality reduction techniques enable us to transform hyperspectral data to a lower dimension and are applicable for data visualization. Being lossy in nature, these operations may affect detection and classification accuracy, wherein hyperspectral data imbibe a significant amount of spectral redundancy so some amount of dimensional reduction is appropriate. Spectral transformation models enable the representation of vector data without any significant loss of information.

Large dimensionality of hyperspectral data has two implications: (i) Huge volume of data requires tremendous storage and processing resources; (ii) A large increase in amount of data required for statistically oriented detection (Manolakis, Lockwood and Cooley 2016). The most popular spectral transformation models include principal component analysis (PCA) (Farrell and Mersereau 2005), vertex component analysis (VCA) (Nidamanuri and Zbell 2010), independent component analysis (ICA) (Wang and Chang 2006) and linear discriminate analysis (LDA). Researchers have also tried sparse (Shao and Zhang. 2014) and locality preserving dimensionality reduction (Li, *et al.* 2011) for hyperspectral image analysis followed by the detection process.

Initially, an increase in dimensionality of remote sensing images favours the classification accuracy but it declines when number of training samples are less. This problem is referred to as Hughes phenomenon or Bellman's curse of dimensionality (Hughes 1968). Dimensionality reduction (DR) is mentioned as part of pre-processing/the general approach for carrying out target detection. Since high-

dimensional spaces have a huge volume, data tend to occupy a very small subspace; in essence, high-dimensional spaces are mostly empty. As a consequence, high-dimensional data can be projected to a lower dimensional subspace without losing significant information. For target detection applications, dimensionality reduction must be avoided or has to be used with extreme care (Manolakis, Lockwood and Cooley 2016).

2.2.1. Principal Component Analysis (PCA)

Principal Component Analysis (PCA) is the most common technique used for dimensionality reduction and feature extraction for hyperspectral data (Huang, *et al.* 2019), (Farrell and Mersereau 2005). A probable group of correlated features are projected to a new space based upon the eigen values and the new generated vectors are known as Principal Components (PCs), arranged in descending order of variance. If x is vector of d random variables, C_x is the covariance matrix then PCA constructs an orthogonal transformation $y = Ax$, where $A = [u_1^T; \dots; u_d^T]$, where u_k 's with $k \in [1, d]$ are the unit orthogonal eigenvectors of matrix C_x satisfying equation (2.1)

$$C_x u_k = \lambda_k u_k \quad (2.1)$$

Where λ_k 's are the eigen values of matrix C_x , satisfying $\lambda_1 \geq \dots \geq \lambda_d$. It can be shown that u_k 's can maximally explain the variance $Var(u_k^T x) = u_k^T C_x u_k$ with maxima λ_k (Su, *et al.* 2017).

2.3. Image Classification

Classification algorithms can be broadly grouped as *parametric* or *non-parametric*; *supervised* or *unsupervised*; *hard* or *soft*; *per-pixel* or *object-based* classification logic and *hybrid* approaches (Jensen 1996). Figure 2.4 shows types of classification algorithms.

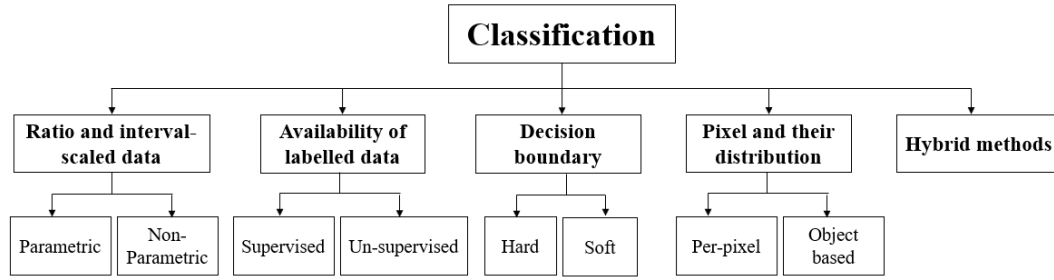


Figure 2.4 Types of Classification Approaches

Classification methods that follow normally distributed remotely sensed data of underlying class density functions fall under *parametric* methods. For example: maximum likelihood classifier and clustering methods (Buddenbaum, Schlerf and Hill 2005). When the data do not hold normal distribution then *non-parametric* methods such as fuzzy classifiers (Lemp and Weidner 2005), nearest neighbor (Thanh Noi and Kappas 2018) and artificial neural networks (Gakhar and Tiwari 2021) can be applied.

In case of *supervised* classification, *a priori* knowledge about the classes is already known through combination of training data, field analysis, visual image interpretation and previous experience. This kind of classification generally involves an analyst with prudent knowledge in the domain. In order to implement supervised approaches, a rich feature set derived from multivariate statistical parameters (correlation, covariance, mean *etc.*) is required to train the classifier. Each and every pixel of the unknown data or test data is assigned the class based on maximum similarity. Minimum distance, Mahalanobis distance, Support Vector machine are examples of supervised approaches (Huqqani and Khurshid 2014).

Unsupervised classification algorithms (or Clustering) are used when no labelled data is available and the data is grouped based on similar features. This approach requires minimal input from the analyst, as the process involves numerical operations which works on natural grouping of spectral features. Unlike supervised classification, here *a posteriori* knowledge is used to transform the input data into

classified thematic map. K-means (Ranjan, *et al.* 2017) and Iso-data (Duran and Petrou 2005) are the most commonly used clustering algorithms for initial analysis of remotely sensed data.

Hard or *Crisp* classification strictly considers the pixel to be part of an individual class whereas, *Soft* or *Fuzzy* classification assigns more than one class to a particular pixel (Figure 2.5). Hard classifiers are more suitable for homogeneous areas such as vegetation covers or water bodies but for complex heterogeneous areas like urban land covers, fuzzy approach may be considered. Fuzzy classifiers determine the membership grades for each class and generates classification certainty. Fuzzy learning vector quantization (FLVQ) approach (Koltunov and Ben- Dor 2001), fuzzy-clustering algorithms (Bilgin, Erturk and Yildirim 2008), Gaussian fuzzy self-organizing map (GFSOM) approach (Zhang and Qiu 2012) are some of the developments mentioned in the literature.

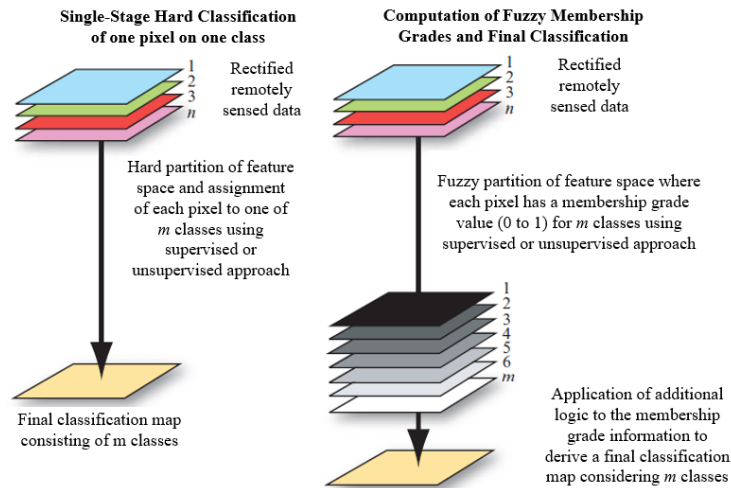


Figure 2.5. Relationship between a traditional single-stage hard (crisp) classification using supervised or unsupervised classification logic and a classification based on the use of soft (fuzzy) logic (Jensen 1996).

2.4. Target Detection

Target detection problem is also regarded as a problem of binary classification in which targets that lie within the circumference of region of interest are extracted from

the background (non-target class). Data and the detection algorithms are the two important aspects of target detection. As data apprehends the variations, while the algorithms provide suitable method for extraction of appropriate information. These algorithms can be categorized into two types, algorithms that are based upon utilisation of spectra in some form and the other which are independent of spectra. Spectral-matching and anomaly detection are examples of the first type which are dependent upon the availability of labelled data (Burgers, *et al.* 2009). Independent Component Analysis (ICA) is an example of the second type (Tiwari, *et al.* 2013). Techniques for which, the spectral signature along with additional details are already known from standard spectral libraries, ground truth, in-situ analysis or from the image itself, comes under the group of spectral matching. These include algorithms like Spectral Angle Mapper (SAM) (James and Richard 2005), Spectral Correlation Measure (SCM) (Robila 2005) *etc.* In anomaly detection, no *a priori* knowledge about the target is available, therefore incongruities are detected assuming their exceptional behaviour with respect to the background. Orthogonal Subspace Projection (OSP), Reed-Xiaoli (RX) are some algorithms belonging to this category (Tiwari, *et al.* 2013).

Depending upon the complexities of urban targets, only spectral component is not sufficient to extract them, because spatial neighbours always affect the measured signal (Da and Jianxun 2018). Either contextual, textural or morphological information is often required for detection of urban built-up surfaces. Thus, a detailed review of the approaches mentioned in the literature is carried out and target detection approaches are grouped addressing, (i) *spectral target detection methods*; (ii) *spectral-spatial target detection methods*; (iii) *Mixed Pixel Analysis* and (iv) *Shape based target detection*.

2.4.1. Spectral target detection algorithms

Target detection distinguishes objects of interest with background features. Its objective is to assign logical labels to every particular pixel vector in hyperspectral image based on prior knowledge of reference spectra, where value 1 signifies the presence of target and 0 represents non-target or background. The targets of interest usually dwell in a few pixels and the mentioned algorithms determine a high possibility to effectively characterize them by high-order statistics.

Spectral matching algorithms, ranging from the traditional clustering techniques to the advanced automated matching models, have evolved, recently. These algorithms include search-and-match strategy which use spectral libraries of materials to be detected. Automation of spectral matching algorithms perform well due to search of specific and spectrally defined targets (D. Manolakis, *et al.* 2009). In order to utilise the information derived from *a priori* knowledge and spectral libraries, various basic algorithms were evolved using deterministic approach, such as SAM and its variants (Kruse, *et al.* 1993) (Zhang and L. 2014) (Carvalho, Abilio and Meneses 2000). Spectral matching algorithms are often influenced by certain factors such as availability or creation of spectral libraries, illumination factors, setting of threshold values, mixed pixels, environmental factors (Shanmugam and SrinivasaPerumal. 2014). These parameters not only pose difficulty in the matching process but also tend to decrease the detection accuracy of the targets.

2.4.2. Spectral-spatial target detection strategies

Recent studies have shown the importance of exploitation of spatial information for classification and target detection applications (L. I. Da 2018) (Fauvel, *et al.* 2012). When two targets have similarities in their spectral properties then spatial component accommodating shape, texture, contextual information helps in detecting the target of

interest. For instance, roads and roofs both contain concrete, they both may behave spectrally similar but can be distinguished on spatial grounds. Unlike spectral approaches which are evaluated pixel-wise, spatial approaches involve transformation of image data using details of neighbouring pixels.

Spectral-spatial target detection algorithms involve local image descriptors which works on every pixel spatially in each spectral band (Shi, *et al.* 2013). The spatial and spectral components can be combined together by concatenation or other transformation and later fed to a target detection algorithm such as Artificial Neural Network (ANN). Texture features are widely used for target detection and provide appropriate information about degree of smoothness or roughness of surface including its granularity. Li *et al.* considered textural features to enhance the detection capabilities of hyperspectral data using deep belief network (Li, *et al.* 2018). In other work, multiple spatial features like Local Binary Patterns (LBP), Gabor features along with spectral features are used on the basis of weighted residual fusion using Support Vector Machine (SVM) (Peng, *et al.* 2015).

2.4.3. Mixed Pixel Analysis

Extraction of mixed pixels is relevant for delineating the targets from the background pixels in case of hyperspectral imagery. Mixed pixels constitute more than one distinct substance which persist due to coarse spatial resolution of the sensor or when endmembers combine to form a homogeneous mixture, for instance, a road is constructed with materials like asphalt, coal tar, bitumen, and cement (Keshava and Mustard 2002). To resolve this, spectral mixture analysis (SMA) is a commonly used method which partially overcomes the drawbacks of full pixel approaches by estimating the fractional abundances of endmembers within a mixed pixel. But deriving of abundance maps prefaced by endmember extraction along with their abundance values

is tedious task. However, hyperspectral data acquired from a high-altitude sensor unavoidably shows the occurrence of mixed pixels.

Endmembers can be extracted by multiple methods mentioned in the literature, such as pixel purity index (PPI) (Boardman, Kruse and Green 1995) which includes minimum noise fraction (MNF) as a dimensionality reduction process which further continues for calculation of a purity score for each pixel labeling them as pure depending upon threshold value. N-FINDR is another technique used for endmember extraction, which define a simplex that inscribes the set of pixels within the dataset having maximum volume (Winter 1999). Both PPI and N-FINDR consider only spectral attributes thereby ignoring the spatial properties imbibed in the hyperspectral data cube.

2.4.4. Shape Identification

Shape features are part of the spatial component in hyperspectral imagery, which further includes texture, size, morphological operators calculated with respect to the neighboring pixels. Han *et al.* proposed shape-size index (SSI) which combines homogeneous areas between one central pixel and its neighboring pixels using spectral similarity for multispectral images (Han, *et al.* 2012). Grey level co-occurrence matrix (GLCM) (Haralick, Shanmugam and Dinstein. 1973) is one of the common spatial texture extraction approaches which transforms the grey scale value of an image by various statistical measures like homogeneity, energy, entropy and contrast. Another technique mentioned in literature for performing shape-based analysis is Histogram of Oriented Gradient (HoG) (Dalal and Triggs 2005). Farooq *et al.* used HOG features for automatic grass weed detection and classification in hyperspectral data (Farooq, Jia and Zhou 2019).

Fauvel *et al.* proposed a method based on fusion of morphological information and original hyperspectral data by concatenating the two vectors into single feature vector followed by classification of urban data using SVM (Mathieu, *et al.* 2008). Fusing spectral and spatial aspect of hyperspectral data is not only limited to classification but mixed pixel characterization is also addressed in the literature (Khodadadzadeh, *et al.* 2014). Recently deep learning approaches have also been presented for better classification accuracies as they automatically learn high level features from the image itself (Zhao and Du 2016).

2.5. Classification vs Target detection: A comparison

Classification of remotely sensed data enables to identify the features and associated information present on earth's surface. The classification algorithms used for multispectral data are widely explored and experimentally implemented on hyperspectral data for improvement in terms of accuracy and performance (Q, *et al.* 2014) (Lu and Qihao 2007). In hyperspectral remote sensing, classification criteria forms groups based on similar properties by comparing the spectra with one another. The analyst chooses a reference spectrum from a single pixel or group of pixels and the classification algorithm finds the alike pixels by associating the similarity function and class (Manolakis, Lockwood and Cooley 2016) . The classifiers are capable of interpreting a scene and are evaluated based on probabilistic approach of assigning pixels to a particular class.

The other category is Target detection, where 'rare objects' are termed as targets and are identified using known spectral signature. These objects are moderately distributed in the scene as compared to the background or non-target pixels. This approach is used when, (i) labelled data is less and to derive statistical properties of targets and (ii) targets are not resolved due to spatial resolution of the sensor used.

Therefore, the target detection algorithms use statistical decision theory in which the probability of error is minimised by classifying every pixel as non-target (D. Manolakis, R. Lockwood, *et al.* 2009). When viewed in spectral subspace, different targets can be represented in form of a spectral vectors which may occupy different or overlapping spectral subspace depending upon their spectral variability.

Classifiers are highly dependent upon the number of classes which are assumed to be known by the analyst in case of supervised or unsupervised methods. In classification approach, increasing the number of features or classes cannot keep up with available observations for statistical estimation, therefore not necessarily leading to better performance (Svensén and Bishop 2007). For classification, each component is modelled using a normal distribution whereas in target detection approach, multivariate t-distribution is used to apprehend the behaviour of natural hyperspectral backgrounds (Landgrebe 2003). The performance of the classification algorithms is highly dependent on factors like, data, class distributions, labelling of training and testing data. However, detection assumes probabilistic modelling for solving decision problem and detection of targets. In most applications each target is characterized by its spectral signature and detection algorithms make decisions using the target signature and the data cube of the imaged scene. *Table 2.1* shows a contrast between target detection and classification approach.

Table 2.1. Difference between Target detection and Classification approach		
Features	Target Detection	Classification
Objective	Provide target detection map	Provide classification map
Theory	Binary hypothesis testing	M-ary hypothesis testing
Performance	ROC Curves	Confusion matrix
Application	Search for rare targets	Generate thematic maps for ground cover classes
Prerequisite	Target signature	Training data for each class

2.6. Approaches to Target Detection and Enhancement

The spectral signature along with additional details are already known by means of standard spectral libraries, ground truth, and laboratory analysis or from the image itself. Detection and identification of targets involve gathering of spectral signatures, which can uniquely determine the surface properties of the target or object under consideration. The spectra of a particular pixel is influenced by certain parameters such as illumination effects, height and background material, colour, material composition, surface geometry of object (slope, orientation and texture), age of material as well as atmospheric interactions. *Table 2.2.* shows a brief introduction of factors that influence the profile of spectral signature of a material.

Table 2.2: Data collection parameters for target detection

S No.	Factors	Description of Factors	Parameters
1.	Sensor Related Factors	Sensors record the amount of light reflected from the surface of target corresponding to numerous wavelength intervals. The efficacy of the response depends upon following the necessary protocols of Field Spectroscopy. These factors can be taken care at the time of pre-processing, as few instruments allow to configure them according to the requirement.	Aperture size, focal length, focal plane array size, spatial resolution, spectral resolution, signal-to-noise ratio, radiometric resolution, calibration, Height and altitude of the instrument, calibration (Kerekes and Goldberg 2013).
2.	Scene Related Factors	Targets confined to very small number of pixels in a scene, therefore content of the spectra is under influence of certain background features.	Material Composition, Color, scene complexity, (number of distinct surface classes) (Kerekes and Goldberg 2013) Target Condition (open/ hidden/ camouflaged/ buried) (Tiwari, et al. 2013)
3.	Atmosphere Related Factors	The behaviour of electromagnetic radiation falling on a target is altered by absorption and scattering mechanisms of atmosphere, simultaneous corrections are required for correcting the distortions caused by atmospheric interactions.	Illumination, presence of haze, fog or clouds, Temperature, Moisture content (Kerekes and Goldberg 2013)
4.	Spatial Factors	The spectral signature of a surface is highly dependent upon spatial features such as location and size of the target.	Target Location involves Surface, subsurface or Air whereas Target size includes Single pixel, a group of pixels or subpixel (Tiwari, et al. 2013)
5.	Morphological Factors	Morphological features give a glimpse about the shape, boundaries, convex hull of a specific target.	Point, linear (line), Area (polygon).
6.	Processing Factors	These factors encompass their domain over the selectable attributes which can be varied in order to increase the accuracy of unmixing, detection, identification and classification of objects.	Threshold values, number of iterations, number of bands (Kerekes and Goldberg 2013)

Literature involves a collection of supervised, semi-supervised and unsupervised detection approaches to detect targets. In context of supervised approach,

various distance, angle, information and machine learning measures are defined in the following subsections.

2.6.1. Spectral Target detection algorithms

2.6.1.1. Distance Measures

The idea of spectral distance originates the need of many hyperspectral applications to use measures for assessing the similarity (or distance) between spectra, or between a spectrum and a group of spectra. Distance measures are frequently used in classification as well as in target detection (S. A. Robila 2005). Distance measures are widely used to measure similarity of shapes of two spectral signatures. Nirmal used distance matrices for band selection in hyperspectral processing for material identification (Nirmal 2004). In this work, the band selection approach was applied to data for two spectrally similar classes, and, minimum distance method succeeded in correctly discriminating pixels that were misclassified by other techniques such as Euclidian minimum distance and least square projection. Mahalanobis metric is considered to be superior to Euclidian distance and is capable of exploiting correlation between hyperspectral data. It has recently been used by Maryam (Imani 2019) as a difference-based target detection technique where output is generated by calculating the difference between the distance of testing pixel with background and distance of testing pixel with target. Normalization of image values is necessary, especially when distance classifiers are used. These methods aim at normalizing each feature of the image in multiple ranges, thereby assigning equal weights to different features and reducing computational load (Naeini, Babadi and Homayouni 2017). The distance values computed for the entire dataset are normalized between 0 and 1 by using the mentioned formula in *Equation 2.2*, where l is lower bound, u is upper bound, x_i is

vector at particular pixel, i accounts to total number of pixels and xn_i is normalized matrix ranging from 0 to 1.

$$xn_i = \frac{x_i - l}{u - l} \quad (2.2)$$

2.6.1.2. Angle Measures

Robila in 2005 investigated the efficiency of various angular measures namely, spectral angle (SA), spectral correlation angle (SCA) and spectral gradient angle (SGA) when used with spectral screening of hyperspectral data (S. Robila 2005). Concluding that, implemented algorithms provided results that matched closely the processing on full data and may be considered as a substitute for the spectral angle. Angle measures have been used for target detection, spectral angle mapper (SAM) being the simplest one. The algorithm determines the spectral similarity between two spectra by calculating the angle between them, treating them as vectors in a space with dimensionality equal to the number of bands (Kruse, *et al.* 1993). Most recently, Imani proposed two difference-based target detection methods in contrast with standard detection algorithms. The first approach used the Mahalanobis distance whereas the second used the kernel-based spectral angle mapper (SAM) utilizing the difference between target and background computed distances (Imani 2019).

2.6.1.3. Information Measures

Work done by Adam Cisz *et al.* evaluated performance of hyperspectral target detection algorithms in altitude varying scenes (Cisz and Schott 2005). Hyperspectral data were examined at three different altitudes (5000, 10000 and 20000 feet) for multiple targets and backgrounds particularly using CEM and ACE. Forest Radiance I data was collected with the HYDICE sensor, detecting grass, tree and road as targets. With the increase in availability of high-resolution data, it is important to have reliable

and robust mechanisms to predict the performance of target detection systems for real-time applications. For this purpose, performance prediction model for the widely used matched filter (MF) and adaptive cosine estimator (ACE) detectors is presented using signal modelling (Truslow 2013). Apart from these measures, spectral information divergence (SID) has equivalently been used for spectral characterization (Chang 2000). Generally, statistical models use estimated parameter values which are optimum for observed data, hence, maximum likelihood parameter estimation sets up a base for most of the target detection algorithms such as MF, CEM and ACE (Dimitris, David and Gary 2003).

2.6.1.4. Machine Learning Measures

More recently machine learning algorithms have shown remarkable results in the very same field having exceptional capabilities to automatically learn the relationship between the data (here, spectra captured) and predict accordingly. These methods help in extracting useful information from raw data by generalizing the unknown facts. There are numerous algorithms that exploit the concepts of machine learning for analysis of hyperspectral data. Plaza *et al.* used neural network-based models for hyperspectral image spectra separation (Plaza, *et al.* 2009). The focus of the work is on selecting small training sets as input to the network for characterization of mixed pixels. Recently a new learning technique with single layer feed-forward network has been developed by Huang *et al.* known as extreme learning machine (ELM) (Huang, Zhu and Siew 2006). Heras considered two ELM-based techniques integrating spectral and spatial information of the image (Heras, Argüello and Quesada-Barriuso 2014). The first is a scheme used a majority vote approach in order to combine the results of a pixel-wise spectral classification by while the second introduced spatial

information from a small spatial neighbourhood after the classification by ELM. *Table*

2.3 gives descriptive assessment of target detection algorithms.

Table 2.3. Descriptive Assessment of Target Detection algorithms

S No.	Algorithm	Approach	Advantages	Limitations	Dataset Used
Distance Measures					
1.	<i>Euclidean Distance</i> (S. A. Robila 2005)	Distance metric provides a quantitative measure of the distance between the reference and unknown test spectra.	<ul style="list-style-type: none"> - Computationally simple - Time efficient - Suitable for a smaller number of bands 	<ul style="list-style-type: none"> - Values are positively defined and are not within a set interval - Distance increases with increase in number of bands 	<ul style="list-style-type: none"> - HYDICE Data, - Hyperion Data, - AVIRIS Data
2.	<i>Dot Product</i> (Stein and Scott 1994)	It provides the cosine angle between the target and test spectra	<ul style="list-style-type: none"> - Treats difference in peak intensities of reference and target spectra continuously to determine identical spectra 	<ul style="list-style-type: none"> - More computational time for evaluation - Relative intensities of neighboring peaks are not considered 	<ul style="list-style-type: none"> - NIST mass spectral database
3.	<i>Z-Score</i> (Parshakov, Coburn and Staenz 2014)	A distance measure that calculates the number of standard deviations a spectral signature is away from population or sample mean (spectral class)	<ul style="list-style-type: none"> - Takes into account the variation of pixel spectra within classes - Uses both mean and standard deviation as compared to other spectral matching algorithms that use only mean. 	<ul style="list-style-type: none"> - Generate lower accuracy if not used with land cover types having lower intra and higher inter class spectral variability 	<ul style="list-style-type: none"> - Landsat 5 TM image of an agricultural area
4.	<i>Mahalanobis Distance</i> (Maryam 2019)	It is based on correlation which takes mean and covariance of reference and test sample into account.	<ul style="list-style-type: none"> - Efficient for unprocessed data 	<ul style="list-style-type: none"> - Scene variability introduces substantial error in estimating the parameters that describe heavy-tailed distributions - Making decisions by comparing the Mahalanobis distance which is lower or higher than the fixed threshold is insufficient. 	<ul style="list-style-type: none"> - AVIRIS Data
Angle measures					
5.	<i>Spectral angle mapper (SAM)</i> (Falcone and Gomez 2005)	Supervised classification technique based on the computation of spectral angle similarity between a reference source and the target spectra	<ul style="list-style-type: none"> - Advantageous in situations where target materials have different spectra. 	<ul style="list-style-type: none"> - Measures the angular direction of data points and not their magnitude - Relatively insensitive to illumination and albedo effects. - Cannot distinguish negative and positive correlations because only the absolute value is considered 	<ul style="list-style-type: none"> - NASA EO-1 Hyperion, Level 1 Radiance
6.	<i>Spectral correlation angle (SCA)</i> (S. Robila 2005)	The angle between correlation vector of reference spectra and test spectra.	<ul style="list-style-type: none"> - Allows detection of targets with negative correlation - Eliminates shading effect 	<ul style="list-style-type: none"> - Evaluate the match based on the spectral shape while ignoring the amplitude of the spectra 	<ul style="list-style-type: none"> - AVIRIS Data set, Indian Pines test site
7.	<i>Spectral gradient angle (SGA)</i> (Angelopoulou, Lee and Bajcsy 1999)	The angle between the absolute values of gradient vectors of test and reference spectra.	<ul style="list-style-type: none"> - Invariant to surface geometry, viewpoint and illumination effects - Suitable for depicting shape of spectral curve 	<ul style="list-style-type: none"> - Unable to handle noise in data 	-
8.	<i>Mahalanobis Angle</i> (Manolakis, Lockwood and Cooley 2016)	The angle between the test and the reference vector after applying the whitening transformation.	<ul style="list-style-type: none"> - Invariant under all non-singular transformations 	<ul style="list-style-type: none"> - Inverse of the correlation matrix can't be calculated if the variables are highly correlated 	-
Information Measures					
9.	<i>Constrained Energy minimization (CEM)</i> (Dimitris, David and Gary 2003)	It constrains the energy of desired spectral signature of the target by minimizing	<ul style="list-style-type: none"> - Performs better with a greater number of bands 	<ul style="list-style-type: none"> - Energy of the desired target level is lower than the energy of undesired 	

		the output energy from background.		pixels, resulting into false alarms	
10.	<i>Matched filter (MF)</i> (West, et al. 2005)	A weighted inner product between the test pixel's spectrum and the target spectrum	-Not requires knowledge of all the end-members in the scene	-Higher false alarms	HYDICE data cubes from the Forest Radiance I & Desert Radiance II
11.	<i>Adaptive cosine estimator (ACE)</i> (Truslow 2013)	A measure of the cosine of the angle between the normalized test and target vector	-Invariant to scaling of input data -Constant False alarm rate.	-Nonlinear in nature which complicates statistical analysis.	Real time dataset containing urban features
12.	<i>Spectral Information Divergence (SID)</i> (Chang 2000)	A measure of divergence, if smaller the target spectra belong to the reference class.	-Efficient in preserving spectral properties as compared to angular measures	-Pixels greater than threshold value remains unclassified	AVIRIS and HYDICE data
13.	<i>Maximum likelihood algorithm</i>	Calculates the probability of a pixel belonging to a specific class	-Gives good results when number of bands are less	-A band with no variance at all, leads to singularity problem -Assumes the statistics for each class in each band are normally distributed	
Machine Learning Measures					
14.	<i>Artificial neural network (ANN)</i> (Peña, Crespo and Duro 2009)	Approach which uses standard back-propagation algorithm applied to set of input, hidden and output layers	-Predict the results for unknown datasets	-Requires labeled data for training process. -Training of the network takes time.	Indian Pines data
15.	<i>Extreme learning machine (ELM)</i> (Heras, Argüello and Quesada-Barriuso 2014)	Learning algorithm for single layered feed-forward neural network	-Higher accuracy as compared to SVM and neural networks -Fast learning -Computationally scalable -Independent of tuning process	-Evaluation speed is low -Require astronomically high hidden layer neurons -Cannot encode more than one layer of abstraction	-University of Pavia image (Rosis 2013) -Indian Pines image (AVIRIS 2013)

2.6.2. Spectral-spatial target detection strategies

One of the methods incorporating the spatial information with the spectral details involves Morphological operators to enhance the desired response from the target by suppressing the intervening background. Mathematical morphological operators use certain reference shapes, referred as *Structuring Element (SE)* to locally compare the known structures present in the scene. Some of the primary operators used for morphological analysis are dilation, erosion, opening and closing. The major advantage of morphology is to preserve the shape of the targets of interest. Also, they take neighbouring pixels into account unlike spectral matching algorithms that work at pixel level.

2.6.2.1. Dilation

Replace every pixel by the maximum value computed over the neighbourhood defined by the structuring element. Features that are brighter than their immediate surroundings are enlarged. Features that are darker than their immediate surroundings are suppressed.

$$\delta_E(X) = \{x \in R^D \mid E_x \cap X \neq \emptyset\} \quad (2.3)$$

Where, δ_E is Dilation with respect to Structuring Element E, X is the Image on which dilation is performed and x Origin where the locus of points is taken.

2.6.2.2. Erosion

Replace every pixel by the minimum value computed over the neighbourhood defined by the structuring element. Features that are darker than their immediate surroundings are enlarged. Features that are brighter than their immediate surroundings are suppressed.

$$\varepsilon_E(X) = \{x \in R^D \mid E_x \subseteq X\} \quad (2.4)$$

Where, ε_E – Erosion with respect to Structuring Element E, X – Image on which erosion is performed and x – Origin where the locus of points is taken.

2.6.2.3. Opening

Erosion followed by dilation with the symmetrical structuring element. Features that are brighter than their immediate surroundings and smaller than the SE disappear. Other features (dark, or bright and large) remain unchanged.

$$Y_E(X) = \delta_{\tilde{E}}[\varepsilon_E(X)] \quad (2.5)$$

Where, Y_E – Opening with respect to Structuring Element E, X – Image on which opening is performed; δ_E – Dilation and ε_E – Erosion

2.6.2.4. Closing

Dilation followed by an erosion with the symmetrical structuring element. Features that are darker than their immediate surroundings and smaller than the SE disappear. Other features (bright, or dark and large) remain unchanged.

$$\varphi_E(X) = \varepsilon_E[\delta_E(X)] \quad (2.6)$$

Where, φ_E – Closing with respect to Structuring Element E, X – Image on which dilation is performed, δ_E – Dilation and ε_E – Erosion.

2.6.3. Machine Learning Approaches

Machine learning algorithms have exceptional capabilities to automatically learn the relationship between the data and predict accordingly (Mas and Flores 2008). There are numerous algorithms that exploit the concepts of machine learning for analysis of hyperspectral data like Laplacian methods, graph-based methods (Gómez-Chova, *et al.* 2008), active learning methods (Jun and Ghosh 2008). Hyperspectral images encompass unique specifications such as, geographic content, spatial information and spectral correlation of the area under investigation. Therefore, in order to establish synergies between high dimensional data and machine learning methods, it is necessary to discover alternative approach. Recent research work in this field have contributed in recognition of specific non-intuitive properties of hyperspectral data.

Machine learning and pattern recognition algorithms have been successfully used for learning the relationships between captured spectra and the information derived from hyperspectral images. Gaussian models, being extensively used in target and anomaly detection are the foundation for many standard algorithms such as Mahalanobis distance (Zhang, *et al.* 2015), spectral matching filter (Homayouni and Roux 2004), and adaptive cosine detector (Huqqani and Khurshid 2014) also assume Gaussian distribution. Ensemble learning is a supervised learning technique of merging

the results from multiple base predictors to produce a more accurate result (Su, *et al.* 2020). Three type of ensemble learning approaches: bagging, boosting and random forest has been applied for hyperspectral imaging applications and attracted the interest of many researchers (Chi, *et al.* 2009). AdaBoost technique with association with SVMs has been used for band selection process (Kawaguchi and Nishii 2007). Random forest classifier applied to identify anomaly from synthetic dataset by training a binary classifier and using training dataset for anomaly and non-anomaly class (Cheung-Wai and Paelinckx 2008).

Apart from this, other classifiers such as Extreme learning machine (ELM) (Dora, Francisco and Pablo 2014), that is, a feed forward neural network (FNN) (Lulla 2010) like learning system whose connections with output neurons are adjustable, while the connections with and within hidden neurons are randomly fixed; has also being explored for classification of various features. Various directed and undirected graphical models are primarily implemented for hyperspectral unmixing, where each node represents a variable and edges signify interdependency among the nodes. However, three machine learning methods are selected from the literature, to be used for the analysis and are explained in detail, in following subsection.

2.6.3.1. Artificial Neural Networks (ANN)

Machine-learning algorithms are generally able to model complex class signatures, can accept a variety of input predictor data, and do not make assumptions about the data distribution (J. Plaza, *et al.* 2009). The technique has already been used successfully with the fusion of spectral and edge information also with spectral and textural information (Ko 1996). A wide range of studies has generally found that these methods tend to produce higher accuracy compared to traditional parametric classifiers, especially for complex data with a high-dimensional feature space (Maxwell, Warner

and Fang 2018). Artificial Neural Network is designed to mimic human brain containing neurons as their fundamental and functional unit. These architectures contain a fully connected network of input, hidden and output layers with weight on the intermediate connections and a non-linear activation function for input to output mapping.

Neurons or ‘computing elements’, communicate with each other through a complex network. They have an ability to derive useful information, extract patterns, predict trends from the imprecise data. A single fundamental unit is called a neuron. The input neurons in the input layer receives raw information as inputs. Then the data traverses between the hidden unit which transforms the data into a usable form to generate the output. The basic architecture of the neural network is shown in *Figure 2.6*.

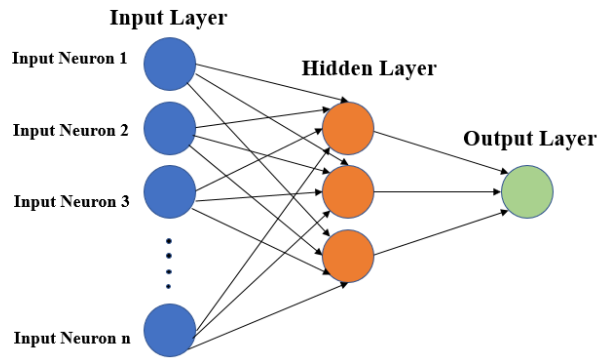


Figure 2.6: Artificial Neural Network Architecture

The data is passed through feed-forward technique through the perceptron which is replicated at every neuron. The steps involved are given below and the detailed process is shown in *Figure 2.7*.

- For every input x_i the corresponding weight value w_i is multiplied. The weights indicate the strength of the connection between the input layer's neuron and the hidden layer's neuron. The one with higher influence on the output value is triggered.

$$\Sigma = (x_1 \times w_1) + (x_2 \times w_2) + \dots (x_n \times w_n) \quad (2.7)$$

Where, $x = [x_1, x_2, x_3 \dots x_n]$ and $w = [w_1, w_2, w_3 \dots w_n]$ are the row vectors belonging to input and the corresponding weights. Therefore, the dot product is given by:

$$x \cdot w = (x_1 \times w_1) + (x_2 \times w_2) + \dots (x_n \times w_n) \quad (2.8)$$

Which turns out to be,

$$\Sigma = x \cdot w \quad (2.9)$$

- Bias plays a major role in balancing the complete architecture, it often acts as an offset to move the activation function and produce the output value.

$$z = x \cdot w + b \quad (2.10)$$

- This intermediate value generated is passed to an activation function which is non-linear in nature which influence the learning speed of the network. There is multiple activation function used, depending upon the application. One of the simplest one is sigmoid activation function, \hat{y} gives the predicted value and σ is the activation function, and it is computed as,

$$\hat{y} = \sigma(z) = \frac{1}{1+e^{-z}} \quad (2.11)$$

- The training mechanism includes backpropagating the error by computing the gradient values with respect to the weight. The mean square error is calculated by the difference between the actual values (y_i) and the predicted values (\hat{y}_i) of error,

$$MSI_i = (y_i - \hat{y}_i)^2 \quad (2.12)$$

The cumulative error for entire training set is termed as loss function, which is calculated as,

$$MSE = \frac{1}{n} \sum_{i=1}^n (y_i - \hat{y}_i)^2 \quad (2.13)$$

Later, the weights can be optimised and hyper-parameters such as the minimum error, number of epochs, learning rates can be fixed.

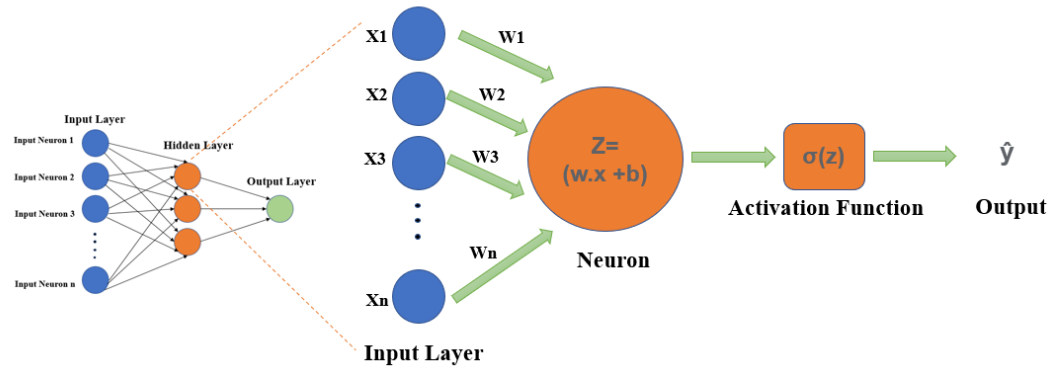


Figure 2.7: Single layer perceptron

2.6.3.2. Extreme Learning Machine (ELM)

ELM is a kind of feedforward neural network (FNN) whose connections with the output neurons are adjustable while with and within hidden neurons are randomly fixed. Unlike ANN, the output is determined using norm least-square solution and Moore-Penrose inverse of general linear system. It utilizes any non-linear activation function such as sigmoid, sine, tan, gaussian *etc.* for hidden layer and a linear activation function for output layer. G.B Huang in 1994 coined ELM that a single hidden layer can overcome some major bottlenecks of traditional gradient methods, such as ANN (Guang-Bin, Qin-Yu and Chee-Kheong 2006). The drawbacks are, slow learning process and all parameters are tuned iteratively whereas ELM has the following characteristics:

- The learning speed of ELM is extremely fast with an advantage of less training time (Bazi, *et al.* 2013).
- ELM has better generalization performance than the gradient-based learning such as back propagation in most cases (Chen, *et al.* 2014).
- The traditional classic gradient-based learning algorithms may face several issues like local minima, improper learning rate and over fitting, *etc.* The ELM

tends to reach the solutions straightforward without such trivial issues (Pal 2009).

- Gradient-based learning algorithms which only work for differentiable activation functions, ELM learning algorithm could be used to train Single Layer Feedforward Networks with many non-differentiable activation functions (Jiaojiao, *et al.* 2015).

Figure 2.8. shows the architecture of single layer feedforward network, often termed as ELM.

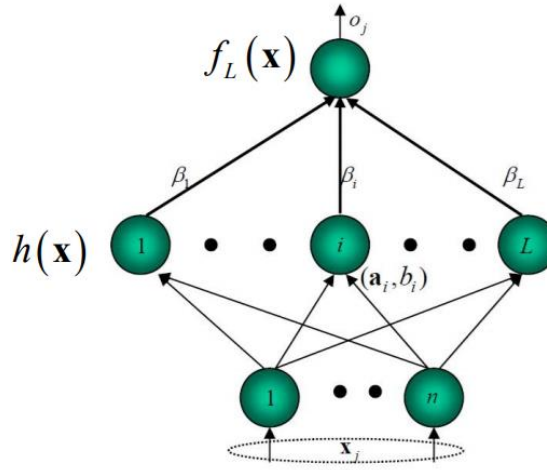


Figure 2.8: Architecture of Extreme Learning Machine (Source: (Guang-Bin, Qin-Yu and Chee-Kheong 2006))

The output function is given by Equation 2.14 followed by the hidden layer output function in Equation 2.15,

$$f_L(x) = \sum_{i=1}^L \beta_i G(a_i, b_i, x) \quad (2.14)$$

$$h(x) = [G(a_1, b_1, x), \dots, G(a_L, b_L, x)] \quad (2.15)$$

The training of the ELM happens by,

$$f_L(x) = \sum_{i=1}^L \beta_i G(a_i, b_i, x) = H\beta \quad (2.16)$$

Where H is a column vector given by,

$$H = \begin{bmatrix} h(x_1) \\ \vdots \\ h(x_N) \end{bmatrix} = \begin{bmatrix} h_1(x_1) & \cdots & h_L(x_1) \\ \vdots & \vdots & \vdots \\ h_1(x_N) & \cdots & h_L(x_N) \end{bmatrix}$$

Here, the training set is $\{(x_i, t_i) | x_i \in R^d, t_i \in R^m, i = 1, \dots, N\}$, hidden node output function $G(a, b, x)$, and the number of hidden nodes L . The value of β is computed as,

$$\beta = H^T T \quad (2.17)$$

$$\begin{aligned} H &= (w_1, \dots, w_N, b_1, \dots, b_N, x_1, \dots, x_N) \\ &= \begin{bmatrix} g(w_1 \cdot x_1 + b_1) & \cdots & g(w_N \cdot x_1 + b_N) \\ \vdots & \vdots & \vdots \\ g(w_1 \cdot x_N + b_1) & \cdots & g(w_N \cdot x_N + b_N) \end{bmatrix} \\ \beta &= \begin{bmatrix} \beta_1^T \\ \vdots \\ \beta_N^T \end{bmatrix} \quad T = \begin{bmatrix} t_1^T \\ \vdots \\ t_N^T \end{bmatrix} \end{aligned}$$

Many researchers have tried to exploit the advantage of fast learning process and higher training accuracy with low error percentage. As hyperspectral dataset is voluminous in nature, the traditional gradient based methods take an additional computation effort for performing classification or target detection problem (Mahesh, Aaron and Timothy 2013) (Faxian, *et al.* 2019) (Ramón, *et al.* 2014).

2.6.3.3. Support Vector Machines (SVM)

Support Vector Machine (SVM) by Vapnik (Corinna and Vapnik 1995) is an extensively used method for hyperspectral data analysis. The method works on the concept of maximizing the margins and generating a decision boundary with maximum separation between the data points of these classes. The decision boundary may be linear or non-linear depending upon the separability analysis of the data used. SVMs perform better and yield higher classification accuracies in contrast to other pattern recognition techniques such as, maximum likelihood and multilayer neural networks.

SVMs may prove helpful when multiple heterogeneous classes are available with few training samples in a scene (Farid and Bruzzone 2004).

In case of SVM, if the data is linearly separable then a hyperplane can be used to separate the considered classes, otherwise the algorithm maximizes the margin adjusting few misclassifications (Kuo, *et al.* 2013). SVM deals with two classes at a time, therefore real-time problems are transformed to series of binary ones. It is a machine learning algorithm that utilizes labelled data, trains the associated model and predicts for unlabelled data. *Figure 2.9.* illustrates the basics of SVM. The key advantage that SVM has over other machine learning algorithms is that the features can be transfigured using multiple kernel functions. The kernel enables to data to be mapped (dot product of two vectors) in preferably higher dimension where it is assumed that, the features may be separated by a linear boundary. This technique enhances the capability of SVM and makes it feasible for multi-class problems also.

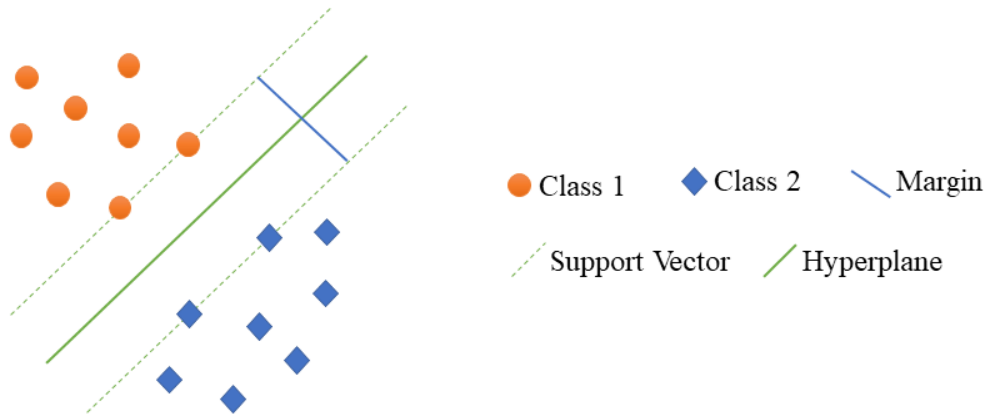


Figure 2.9: Concept of SVM

The mathematical formulation of SVM includes, formulas of line in two-dimension and hyperplane in multi-dimension, represented by,

$$y = mx + b \quad (2.18)$$

$$\vec{w} \cdot \vec{x} + b = 0 \quad (2.19)$$

Where, x is sample dataset, for which SVM finds weights w such that, the data points in the dataset are separated using the most optimum hyperplane. Assuming a two-class problem, decision rules are established to generate a margin that is as wide as possible. Therefore, the width is calculated by taking the dot product of distance vector and perpendicular vector w , then dividing by the magnitude of w .

$$width = \frac{1}{2} \cdot \frac{w^2}{||w||} \quad (2.20)$$

Since the width needs to be maximised, LaGrange multipliers are used (Shirish, *et al.* 2000). Further L is differentiated with respect to w ,

$$L = \frac{1}{2} \cdot \frac{w^2}{||w||} - \sum_i^n [y_i(\vec{w} \cdot \vec{x}_i + 1) - 1] \quad (2.21)$$

$$\vec{w} = \sum_i^n a_i \cdot y_i \cdot \vec{x}_i \quad (2.22)$$

And differentiating L with respect to b gives,

$$b = \sum_i^n a_i \cdot y_i = 0 \quad (2.23)$$

Substituting value of w from Equation 2.22 in Equation 2.21, then

$$L = \frac{1}{2} (\sum_i^n a_i \cdot y_i \cdot \vec{x}_i) (\sum_j^n a_j \cdot y_j \cdot \vec{x}_j) - (\sum_i^n a_i \cdot y_i \cdot \vec{x}_i) (\sum_j^n a_j \cdot j \cdot \vec{x}_j) - b(\sum_i^n a_i \cdot y_i) + \sum_i^n a_i \quad (2.24)$$

Which further reduces to Equation 2.25,

$$L = \sum_i^n a_i - \frac{1}{2} \sum_i^n \sum_j^n a_i a_j y_i y_j \vec{x}_i \cdot \vec{x}_j \quad (2.25)$$

Since, the above derivation deals with linearly separable data points, but the practical problems involve non-linear boundaries to establish separation, therefore kernel trick is required, and the general equation is,

$$k(x, y) = x^T y + c \quad (2.26)$$

SVM has already proved its efficacy for hyperspectral data, which is evident from the literature also. Pal in year 2006 did an extensive case study for the use of SVM for landcover classification (M. Pal 2006). Dealing with the problem of limited training

set, Junshi *et al.* examined rotation based SVM for hyperspectral classification (Junshi, *et al.* 2015). Some of the other studies which explore SVM include (Anita, Raczko and Zagajewski 2020), (Zhilei and Yan 2016), (Peijun, Tan and Xing 2012).

2.6.4. Deep Learning Methods

The theoretical idea of deep learning transformed into implementation in 2006 by Hinton (Geoffrey and Salakhutdinov 2006). Derived from machine learning, the deep learning models try to learn features in a hierarchical fashion, beginning from low level to high level. The idea involves derivation of features in an unsupervised manner followed by supervised approach to reach the output (Yushi, *et al.* 2014). Therefore, the initial layers are assigned for automated feature extraction, which acts as an input for further layers, and at last pattern recognition is performed by supervised means. The lower-level features involve points *etc*, mid-level may include lines and higher-level features learn about contours and more complex shapes. These features are associated to generate better approximation to non-linear activation functions, unlike machine learning models (Nicolas and Bengio 2010).

Some of the standard deep learning architectures involve, CNN (Khan, *et al.* 2017), deep belief networks (DBN) (Xiaoai, *et al.* 2020), Auto-encoders (Yanzi, *et al.* 2019), Restricted Boltzmann machine (RBM) (Roux and Yoshua 2008). The mentioned deep learning methods are successfully implemented for hyperspectral data in multiple application areas. The most common one is CNN, explained in the following subsection.

Deep learning works on automated extraction of features needed for mining useful information from raw data. High dimensionality of hyperspectral data affects supervised methods in terms of accurate derivation of statistical parameters leading to overfitting of network, in case of supervised approach (Paoletti, *et al.* 2019). Large

number of calculations resulting from deep architectures involve high computational load in terms of time and storage for parallel computing (Cheng, *et al.* 2017). Learning rate, number of epochs, activation function are some of the additional parameters to be tuned for an optimized network and better detection rate, thereby adding dispensable trial runs for training the deep architecture. The “black-box” conduct of deep learning models may hinder to visualize the parameters, optimise the model and make it hard to interpret the training procedure (Shwartz-Ziv and Tishby 2017).

2.6.4.1. Convolution Neural Network (CNN)

In recent years, various deep learning architectures have been proposed by researchers and CNN being employed as feature extractor and classifier for spectral, spatial and spectral-spatial configurations. In spectral models, the data is exploited pixel wise by extracting spectra of individual pixels or a particular class in the scene, therefore a priori information is necessary to identify the pixels belonging to target of interest (W. Y. Hu 2015). Spatial features may also be derived from the complete spectral data by applying dimensionality reduction or cropping spatial patches of a particular window size (Zhao 2015), (Haut 2019). In the third approach, the complete three-dimensional data is utilized for extraction of sub-volumes in terms of spectral and spatial knowledge because of flexible architecture of CNN (Mei 2017).

CNN is a multi-layer architecture to process different features where each layer has decisive impact on the model. Apart from input and output layer, the most common layers comprised in CNN are convolution layer, activation layer, down sampling layer and a fully connected layer.

- **Convolution Layer:** This layer contains a set of neurons acting as linear kernels to analyse the statistical characteristics of a hypercube ($lines \times samples \times bands$) in which data features are equally distributed with respect to spatial

positions. Therefore, the features learned for a particular target can be applied to other regions to locate the same target. Fix sized filters are convolved by sliding-window mechanism overlapping the input data at certain interval called stride. For computation dot product of weights and input layer is performed with an added bias (*Equation 2.27*)

$$X^{(l)} = (W^{(l)} \times X^{(l-1)} + b^{(l)})_{K^{(l)} \times k^{(l)} \times k^{(l)} \times q^{(l)}} \quad (2.27)$$

Output volume $X^{(l)}$ is generated when l^{th} convolution layer applies $K^{(l)}$ linear 3D kernels over the input layer $X^{(l-1)}$ which performs a dot product between weights $W^{(l)}$ and biases $b^{(l)}$ respectively, and small fragments of input data. The general feature calculation is done using *Equation 2.28* (Paoletti, *et al.* 2019).

$$x_{i,j,t}^{l(z)} = \sum_{i=0}^{k^{(l)}-1} \sum_{j=0}^{k^{(l)}-1} \sum_{t=0}^{q^{(l)}-1} (w_{i,j,t}^{(l)} \cdot x_{(i \cdot s^l + i), (j \cdot s^l + j), (t \cdot s^l + t)}^{(l-1)}) + b^{(l)} \quad (2.28)$$

- **Activation Layer:** Activation functions are mathematical equations which are the decisive to fire an input neuron relevant for model prediction. Computational efficiency of an activation function is equally important because it is calculated for a lot of neurons iteratively. They are linear (behaves like simple linear regression model) or non-linear (for complex data and mapping between input and output layer with stack of hidden layers) in nature. The result of this layer constitutes of output volume containing the activation values from the previous layer, as shown in *Equation 2.29*.

$$X^{(l)} = f(X^{(l-1)}) \quad (2.29)$$

$f(\cdot)$ can be varied as linear or non-linear manner. The common activation functions are linear, sigmoid, tanh and ReLU. Depending upon the application, the activation functions may be chosen wisely.

- **Down Sampling Layer:** Time and space complexity for implementation of deep neural networks is quite high, therefore to reduce the size of feature maps generated by the previous layers down-sampling is used. Down-sampling can be attained by varying the stride of convolution or by pooling layer. In all cases, pooling helps to make the representation become approximately invariant to small translations of the input. Invariance to translation means that if we translate the input by a small amount, the values of most of the pooled outputs do not change (Goodfellow 2016). The objective of the pooling is to, (i) reduce the spatial dimensions and volume, (ii) contribute the data with certain invariance to small transformations, (iii) reduce computation time and space (Paoletti, *et al.* 2019).
- **Fully Connected Layer:** In this layer, each node of a layer is connected to all the nodes in the following layer which is required for end-to-end training. The architecture of CNN is shown with respect to hyperspectral image processing in *Figure 2.10*.

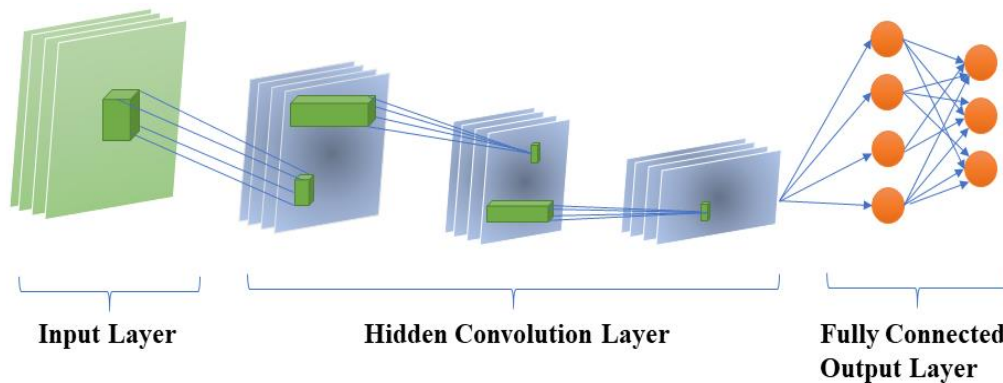


Figure 2.10: General Architecture of Convolution Neural Network

2.6.5. Spectral Unmixing

Urban targets may be confined to multiple pixels (full pixel) or are part of fraction of pixel (subpixel), which result in a mixed signal to the sensor. Mixed pixel detection is a challenging task for delineating the targets from the background class.

Mixed Pixel analysis techniques can be linear or non-linear in nature. In former, pure spectral constituents (endmembers) are assumed to have a constant reflectance across the scene followed by calculation of their abundance values by solving constrained linear equations, while in latter multiple scattering between components within instantaneous field of view are considered with respect to photon's interaction (*Fan, et al. 2009*). Apart from these, coarse spatial resolution is also one of the major challenges faced while extraction of urban built-up surfaces using remote sensing methods.

Traditional approaches for determination of endmembers were predominantly based on manual efforts (*Ann and Curtiss 1996*). But modern techniques of endmember extraction are based on automated methods, catalysing the process. Due to within-class variability, multiple endmembers belong to one class, leading to spectral variation (*Philip and Roberts 2003*). In such cases, pure spectra is representative of all spectral signatures in modelled pure class. But assuming that hyperspectral data acquired remotely contain pure observations for every material present in the scene eases the process of validation with ground data (*Jin, et al. 2009*), for instance, N-FINDR. Incorporation of other methods such as, spatial information (*Shaohui, et al. 2011*), (Huali and Zhang 2011) sparse regression (*Castrodad, et al. 2011*), (*Charles, Olshausen and Rozell 2011*) deep learning (*Boyu and Wang 2018*) have enhanced the results obtained by spectral unmixing. Linear spectral unmixing and Vertex Component Analysis (VCA), being the simplest one, are explained in the upcoming subsection.

2.6.5.1. Linear Spectral Unmixing

After extraction of pure endmembers, spectral unmixing is performed to determine the abundance values associated with each pixel and corresponding abundance maps are generated. Linear mixture model (LMM) is extensively used for modeling the spectral signature of a pixel as linear combination of its individual

constituents and its abundance fractions. The algorithm is based on two assumptions, (i) the sum of abundance of each member is equal to one (additive constraint) (ii) the abundance value of each endmember cannot be less than zero (non-negativity constraint) (Manolakis, Siracusa and Shaw 2001). The mathematical formulation of linear mixture model is shown in *Equation 2.30*. Considering L spectral bands, the spectral signature of every endmember can be represented by $L - dimensional vector$, then the general formulation of LMM is illustrated as:

$$x = \sum_{k=1}^M a_k s_k + w \triangleq Sa + w \quad (2.30)$$

$$S \triangleq [s_1 \ s_2 \ \cdots \ s_M]$$

$$a \triangleq [a_1 a_2 \cdots a_M]^T$$

Where, x is the spectrum of the mixed pixel, s_k is spectrum of the considered endmembers, a_k are their respective abundance values, M is the number of endmembers and W accomodates the L -dimensional error vector accounting for noise.

2.6.5.2. Vertex Component Analysis

VCA is used to derive ground reference data for the proposed study, as it exploits two facts: the endmembers are the vertices of a simplex (can be broken down into constituent n -dimensional elements) and the affine transformation of simplex is also simplex. (MP and Dias 2005). The mathematical interpretation of VCA involves observed spectral vector, given by *Equation 2.31*.

$$r = x + n = M \gamma \alpha + n \quad (2.31)$$

Where r is an L -vector (L is the number of bands), $M \equiv [m_1, m_2, \dots \dots m_p]$ is the mixing matrix (m_i denotes the i^{th} endmember signature and p is the number of endmembers present in the covered area), $S \equiv \gamma \alpha$ (γ is the scale factor modelling illumination variability due to surface topography), $\alpha = [\alpha_1, \alpha_2, \dots \dots \alpha_p]^T$ is the

abundance vector containing the fractions of each endmember. Here $(.)^T$ stands for transpose and n is the additive noise. The abundance fraction always satisfies the physical constraints of non-negativity ($\alpha \geq 0$) and the positivity constraint $1^T \alpha = 1$, where 1 is a $p \times 1$ vector of ones.

The spectral signatures of the endmembers may be chosen from the standard digital spectral libraries, (such as USGS), captured from the field, processed in laboratory or derived from the imagery. The abundance fractions are generated using Dirichlet distribution (Nascimento and Bioucas-Dias 2011), given by *Equation 2.32*:

$$p(\alpha_1, \alpha_2, \dots, \alpha_p) = \frac{\tau(\mu_1 + \mu_2 + \dots + \mu_p)}{\tau(\mu_1)\tau(\mu_2)\dots\tau(\mu_p)} \times \alpha_1^{\mu_1-1} \alpha_2^{\mu_2-1} \dots \alpha_p^{\mu_p-1} \quad (2.32)$$

Where $0 \leq \alpha_i \leq 1$, $\sum_{i=1}^p \alpha_i = 1$, $E[\alpha_i] = \mu_i / \sum_{k=1}^p \mu_k$ is the expected value of the i^{th} endmember fraction, and $\tau(.)$ denotes the gamma function. Parameter γ is Beta (β_1, β_2) distributed, constructing *Equation 2.33*,

$$p(\gamma) = \left(\frac{\tau(\beta_1 + \beta_2)}{\tau(\beta_1)\tau(\beta_2)} \right) \gamma^{\beta_1-1} (1-\gamma)^{\beta_2-1} \quad (2.33)$$

2.6.6. Super resolution techniques

Researchers are continuously working to improve spatial resolutions using super resolution techniques which make use of estimated abundance fractions in different pixels or any other such similar parameter/value. Use of abundance fractions leads to consideration of subpixel components of a class and helps in development of maps with higher accuracy. Elbakary and Alam proposed a method to produce high resolution bands from low resolution imagery based on local correlation values using super resolution reconstruction (Elbakary and Alam 2007). Models that enable to represent hyperspectral data as linear combination of small image planes to reconstruct spectrum of observed scene is also another approach mentioned in literature (Akgun, Altunbasak and Mersereau 2005).

When the targets are embedded within a pixel, target detection approach deals with pixel-wise comparison neglecting the partial target details in the surrounding pixels (mixed pixels). Spectral unmixing mentioned in the previous section is one of the solution to accommodate the complete abundance information about the target, however it lacks spatial distribution of subpixel of target with respect to surrounding pixels (Muad and Foody 2012) . Bridging this gap, super-resolution is capable of optimising the spatial distribution of subpixels within a pixel on the basis of available abundance fractions (Gu, Zhang and Zhang 2008).

Scale factor governs the number of subpixels into which a mixed pixel is supposed to be sub-divided. Literature is still restricted in terms of urban target detection using super-resolution mapping techniques, though applications primarily emphasising on wetland inundation (Li, *et al.* 2015), lakes (Qin, *et al.* 2020), land use and land cover map generation (Kasetkasem, Arora and Varshney 2005) (Ma, Hong and Song 2020) have extensively applied this concept. Super resolution based methods can be broadly grouped in three categories, (i) interpolation, (ii) learning and (iii) reconstruction wherein, the first approach uses interpolation to determine the high resolution image through low resolution image assumming the high correlation between the neighboring pixels. Learning based methods require training the network with known information followed by its validation and testing it over unknown dataset. In third technique, the original image is downscaled as a priliminary step and then further analysis is carried out in terms of super-resolution (Dixit and Agarwal 2020) .

Extracting full pixels of targets along with its fractions or endmember abundance values using the concept of spectral unmixing is often followed by super-resolution techniques in order to locate correct spatial distribution . Therefore this category of target detection lies unexplored as most of the approaches reported here,

use random allocation of location to subpixels of different endmembers. This recursive procedure not only increases the computational complexity but adds on to CPU time as well, for instance, Pixel Swap Algorithm. Algorithms like Inverse Euclidean Distance Approach are based on a non-random, non-recursive assignment of subpixels to binary end members. Both of these approaches are explained in upcoming section.

2.6.6.1. Pixel Swap

This algorithm alters the spatial arrangement of subpixels to maximise the correlation between the neighboring pixels (P. M. Atkinson 2005). At first iteration, the spatial arrangement of subpixels is done randomly subsequently their correct allocation is done by finding the maximum spatial correlation value. Since the algorithm is capable of working on a two-class problem, therefore the results from spectral unmixing are required as input. After setting the scale factor, the number of sub-pixels in a pixel remains fixed throughout the implementation and each subpixel is assigned to single landcover class maintaining the original class fractions in coarse resolution image. For every subpixel in pixel i , attractiveness A_i is calculated corresponding to every neighboring pixel ($q = 1, 2, 3 \dots q$) within a window as a distance weighted function, given in *Equation 2.34*,

$$A_i = \sum_{q=1}^q \lambda_{iq} z(y_q) \quad (2.34)$$

Where, $z(y_q)$ is the binary target/class of the q^{th} pixel at location y_q and λ_{iq} is given by *Equation 2.35*,

$$\lambda_{iq} = \exp\left(\frac{-h_{iq}}{a}\right) \quad (2.35)$$

h_{iq} denotes the distance between the location y_i of pixel i and location of y_q of neighboring pixel q , and a is a non-linear parameter. Later, minimum (A_i) and maximum (A_q) attractiveness is calculated for all subpixels currently allocated to 1

and 0 respectively. If $A_i < A_q$, then pixel swapping takes place and continues till the threshold value is achieved and no more swaps are possible.

2.6.6.2. Inverse Euclidian Distance

Pixel-swap algorithm is based on random allocation and an iterative mechanism making it computationally intensive. As the technique is dependent upon a non-linear parameter a given in *Equation 2.35* which adds uncertainty in terms of achieving convergence at a given threshold. Therefore, Euclidean distance algorithm is a non-random and non-iteartive method for assignment of subpixels to the binary endmembers (Arora and Tiwari 2013). The algorithm is explained here in brief. Consider an image array of size $m \times n$ (*Figure 2.11a*) and an pixel of size 3×3 is extracted for super resolution (*Figure 2.11b*). Let super resolution is performed at a scale factor of 5, giving 25 subpixels to be predicted using inverse Euclidean distance (*Figure 2.11c*). The neighborhood of the central pixel P5 shown is denoted from P1 to P9. The abundance fractions of these subpixels is identified from the soft classification or unmixing methods, so the corresponding abundances are denoted from a1 to a9, required for each binary class calculation (*Figure 2.12*). If the abundance value of the central pixel is 0.6 then $0.6 \times 25 = 15$ subpixels out of 25 belong to this class and rest of the 10 pixels are allocated to the other class.

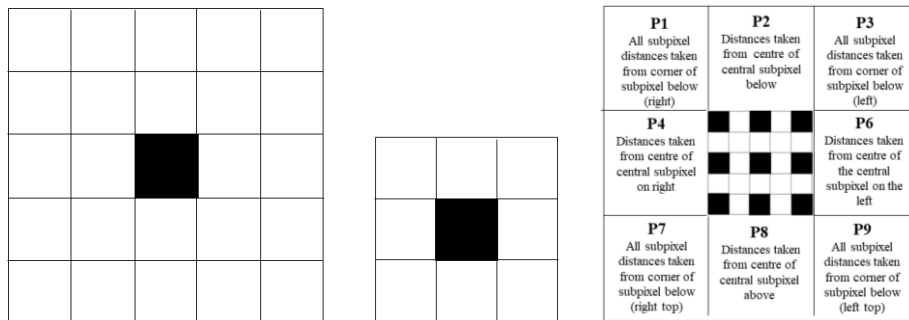


Figure 2.11: (a) $m \times n$ array to super resolve (b) 3×3 window size and 8 neighbours (c) Super resolution mapping of all 8 neighbours (Source: (Arora and Tiwari 2013))

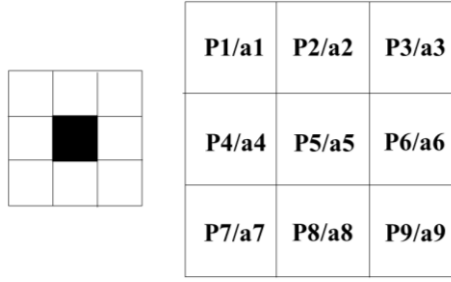


Figure 2.12: Abundance fractions layout in 3×3 pixel array (Source: (Arora and Tiwari 2013))

The attractiveness for the neighborhood subpixels with respect to the central pixel is calculated as a function of inverse Euclidean distance and is given by *Equation 2.36*.

$$A_{ij} = \frac{1}{d_{ij}} \quad (2.36)$$

$$d_{ij} = \sqrt{(i - x_c)^2 + (j - y_c)^2}$$

Where i and j are row and column coordinate of the central subpixel, x_c and y_c are the centers of subpixels within the super-resolved pixel and d_{ij} is Euclidean distance. The super resolution is initiated with the very first pixel in the image, later the highest abundance fraction is obtained in the corresponding neighbourhood, known as endmember centre. Attractiveness ranked in decreasing order is determined immediately after this step, assigning logical 1 value to the endmember subpixel and rest are assigned as 0. The same process continues till all the pixels are super-resolved.

Chapter 3

Data and Software

The data for this research work has been provided under the Airborne Visible InfraRed Imaging Spectrometer - Next Generation (AVIRIS-NG) mission. The campaign is part of “*Big Data Initiatives*” by Department of Science and Technology (DST), Government of India, which was initiated in 2015. This ISRO-NASA joint airborne hyperspectral campaign is a development towards exploring the future potential of hyperspectral remote sensing in earth observation.

3.1. Data

3.1.1. Airborne Data Collection

The broad objectives of the campaign include (Bimal, *et al.* 2019):

- i. To harness the benefits of unique and advanced remote sensing measurements for society by bringing together important talents and expertise in instrumentation, science and applications of both ISRO and NASA.
- ii. To jointly develop advanced science understanding, models, algorithms and techniques through knowledge sharing and to open up new avenues of collaboration.
- iii. To provide the required precursor ground truth data and science and application research demonstrations for present and future ISRO space imaging spectrometer missions.

The data introduces about 430 narrow spectral bands concatenated together in Very Near Infrared (VNIR) and Short-Wave Infrared (SWIR) regions ranging from 380 nm to 2500 nm. The spectral interval is 5 nm with an accuracy of 95% having Field of View (FOV) of 34° and Instantaneous FOV of 1 mrad. The Ground Sampling Distance (GSD)

varies between 4 to 8 m. The major themes for the campaign include, Agriculture and Ecosystem; Geology; Ocean and coastal areas; Rivers and water quality; Urban; Snow-ice and atmosphere. *Table 3.1.* gives the broad science themes along with the sub-themes. *Figure 3.1* shows the photographs of the airborne campaign.

Table 3.1: Science themes and study sites for airborne data collection

S. No.	Broad Science Themes	Sub-themes	Number of Study sites
1.	Agriculture and Ecosystem Crop	Soil, Mangrove, Wetland	21
2.	Geology	-	11
3.	Ocean & coastal	Coastal zone, biological oceanography, coral reef	11
4.	Rivers and water quality	-	5
5.	Urban		2
6.	Snow and ice		2
7.	Atmosphere	Air quality, cloud microphysics	3



Figure 3.1: Airborne campaign team and science field campaign team with B200 aircraft and AVIRIS-NG instrument

The specifications of the AVIRIS-NG sensor/data are summarised in Table 3.2.

Table 3.2: Specifications of the AVIRIS-NG Sensor/Data

S. No.	Parameter	Value
1.	Wavelength	380 nm to 2510 nm
2.	Spectral Resolution (FWHM, minimum)	5nm \pm 0.5 nm
3.	Field of View	36 \pm 2 degrees with 600 resolved elements
4.	Instantaneous Field of View	1.0 1.4 mrad \pm mrad
5.	Spatial Sampling (maximum observed at resolved elements)	1.0 mrad \pm 0.1 mrad
6.	Spectral Distortion (smile)	Uniformity > 97%
7.	Spectral Distortion (keystone)	Uniformity >97%
8.	Frame Rate	10 - 100 frames per second
9.	Pixel Size	27 microns x 27 microns
10.	Calibration	On-board calibrator
11.	Data Resolution	14 bits
12.	Data Rate	Up to 74 MB/s of throughput
13.	Data Volume	Up to 1.0 TB of raw data before disk swap
14.	Physical Volume	83 cm (H) x 57 cm (Dia.) plus electronics boxes
15.	Mass	465kg
16.	Vacuum Requirement	10-4 torr
17.	Ambient Operating Temperature	-40 to +50C

18.	Maximum Altitude	18 km
19.	Cool-Down Time	< 48 hours
20.	Operational Time / Mission	14 days
21.	FPA	480 (spectral direction) X 640 (cross track)

Exceptional volumes of high-quality data were collected for multiple themes. Imaging spectroscopy data sets acquired by AVIRIS-NG gives a three-dimensional hypercube which can be viewed in two-dimension in form of True Colour Composite (TCC) or False Colour Composite (FCC). The three-dimensional image of some of the themes are shown in *Figure 3.2*.

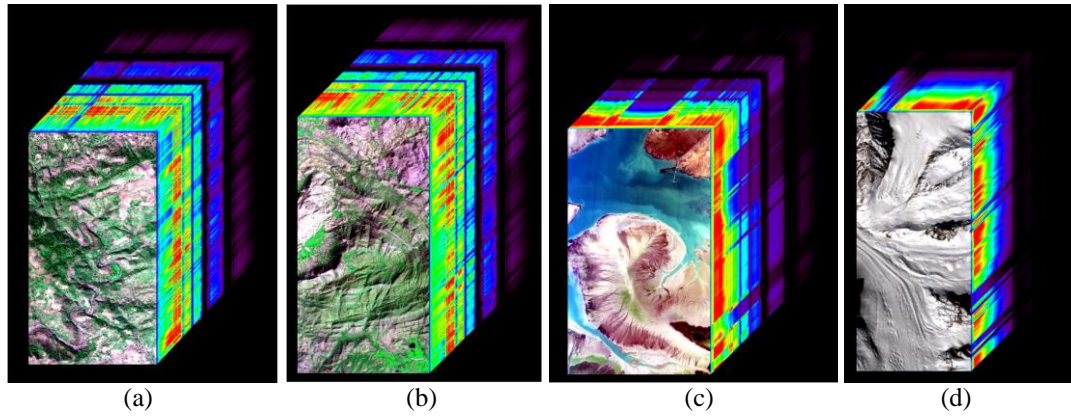


Figure 3.2: Three-dimensional image of (a) Forestry (b) Geology (c) Coastal Oceans (d) Snow/Ice

Three levels of products, that is, L0, L1 and L2 have been derived from AVIRIS-NG data. The L0 and L1 data represent raw data, calibrated and ortho-rectified top-of-radiance (TOA), respectively which were generated on-board the aircraft. The L2 data represent surface reflectance products in all the bands after atmospheric correction. Two types of prototype models viz. point-based and pixel-based, have been developed. The former is useful for a sub-scene where atmosphere is assumed spatially invariant and point-measured aerosol optical depth and water vapour can be used for generating surface reflectance. Pixel-based approach first derives atmospheric water vapour and aerosol optical depth at pixel-level from TOA radiance itself, which serve as input to atmospheric correction models. The product levels are given in *Table 3.3*.

Table 3.3: Level details of the airborne data collected

Product Type	Product Definition	Data Content
Level-0	Raw	Raw data captured by the sensor
Level-1	Calibrated Radiance	Radiance image cube
Level-2	Atmospherically corrected surface reflectance	Reflectance Image Cube

The social benefit areas are, food security, mineral exploration, water and air quality assessment, mapping forest tree species with medical benefits, urban development and planning, climatic changes and many more.

3.1.1.1. AVIRIS-NG Phase 1

About 230 AVIRIS-NG scenes collected over 57 sites in the first phase of campaign have been archived in VEDAS portal. In addition to that, ground-truth data and field campaign reports are also archived in VEDAS. Data are being disseminated to interested researchers of different Indian Academia based on certain guidelines. The flight paths of phase 1 are shown in *Figure 3.3*.

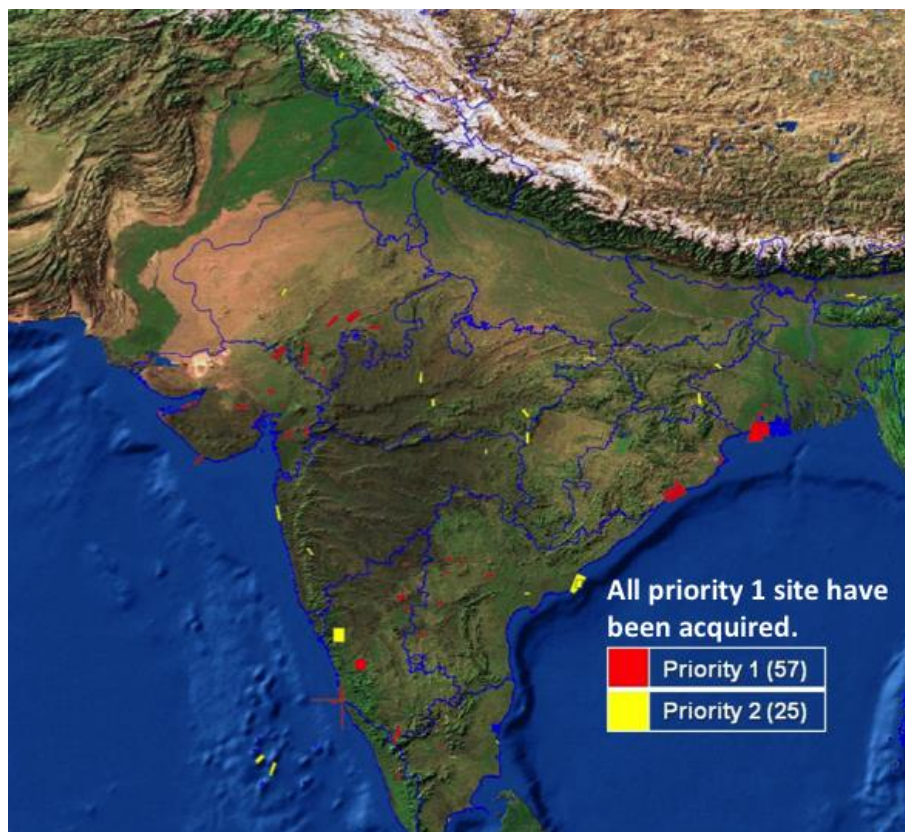


Figure 3.3: Multiple scan lines captured during the Airborne data campaign Phase-1

3.1.1.2. AVIRIS-NG Phase 2

A total of 100 sites distributed over India have been covered in Phase – 2 airborne hyperspectral campaign with AVIRIS-NG. Phase – 2 is divided into two parts, Phase – 2A and Phase – 2B. The Phase – 2A covered 50 sites during 21 February – 30 April 2018 from seven airbases (*Figure 3.4*) in India covering the themes shown in *Table 3.4*

Table 3.4: Science themes and study sites for airborne data collection Phase 2

S. No.	Broad Science Themes	Sub-themes	Number of Study sites
1.	Agriculture and Ecosystem Crop	Soil, Mangrove, Wetland	10
2.	Geology	-	10
3.	Ocean & coastal	Coastal zone, biological oceanography, coral reef	5
4.	Rivers and water quality	-	7
5.	Urban		3
6.	Forest/Mangrooves		10
7.	Atmosphere	Air quality, cloud microphysics	3

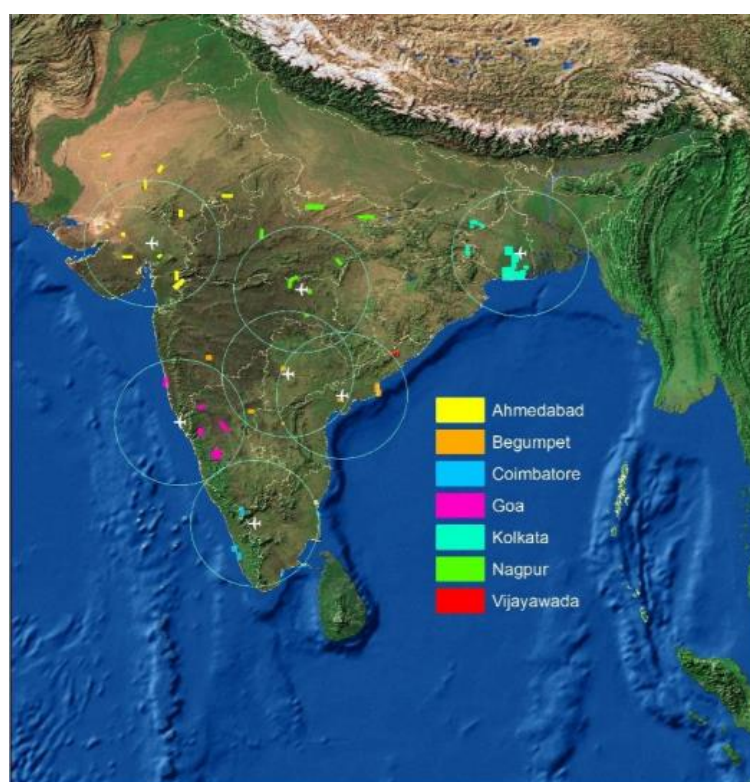


Figure 3.4: Multiple scan lines captured during the Airborne data campaign Phase-2A

3.1.2. Ground Data Collection

The pre-campaign meeting held at Space Application Centre (SAC), Ahmedabad, India in September 2015. Parameters like, sampling plans, points, time

and other field data equipment were decided. Other protocols such as biochemical, geochemical analysis, laboratory analysis was also planned and the detailed Performa is placed in *Annexure I*. Teams of researchers from multiple institutions were formed to carry out simultaneous process of field data acquisition. The radiometric calibration was carried out at SAC before the Phase 1 of the airborne campaign which started on 19th December 2015 and continued till 8th March 2016. The campaign was organised from nine airport bases mentioned in *Table 3.5*. Approximately 200 people were part of the complete program who managed on-site permissions, air traffic control, weather conditions and flight planning. The corresponding flight paths are shown in *Figure 3.5* along which the simultaneous ground data collection was done.

Table 3.5: AVIRIS-NG Airborne hyperspectral Phase-1 Flight Planning

S. No.	Airports (As per flight schedule)	Duration	Number of Sites	Area (km ²)
1.	Begumpet	16 to 21 December 2015 25 to 29 January 2016	12	2650
2.	Bhubaneswar	22 to 28 December 2015	6	3780
3.	Mangalore	29 December 2015 to 2 January 2016	5	3491
4.	Coimbatore	3 to 8 January 2016	5	1416
<i>Phase Inspection of aircraft</i>				
5.	Udaipur	31 January to 5 February 2016	8	3697
6.	Ahmedabad	6 to 16 February 2016 6 to 9 March 2016	10	2788
7.	Chandigarh	17 to 21 February 2016	4	835
8.	Patna	22 to 24 February 2016	3	396
9.	Kolkata	24 February to 6 March 2016	4	3787
<i>Total Number of Days = 84</i>		<i>Total area imaged = 22840 km2 over 57 sites</i>		

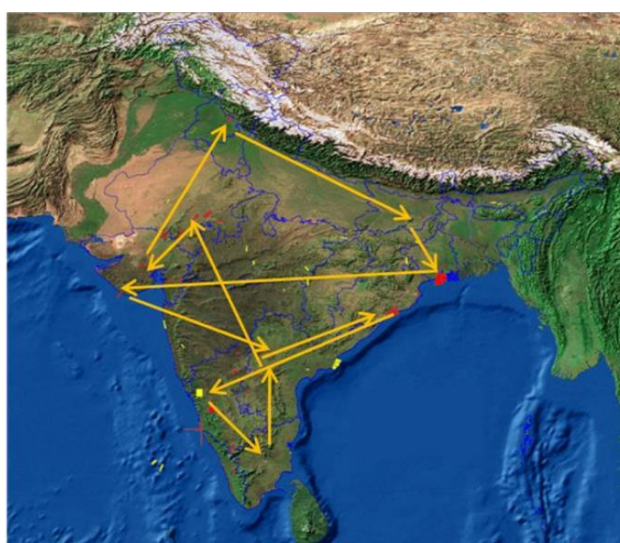


Figure 3.5: Flight paths of airborne campaign for field data collection

Multiple engineered objects listed in *Table 3.6*. were acquired as part of the campaign covering the spectral range over the interval of 350 – 2500 nm with 2151 channels. The field spectroscopy data was captured during high exposure and minimum cloud coverage. The spectroradiometer used for the study spanned over visible to short infrared region with a spectral resolution of 1.5 nm at 350 – 1000 nm, 3.0 nm at 1500 nm and 3.8 nm at 2100 nm, respectively. Over 1000 spectral signatures under multiple categories such as roads, roofs, sports infrastructure, vehicles *etc* were collected and some of them are shown in *Figure 3.6*.

Table 3.6: Spectral signatures collected for engineered objects

1. Bitumen	9. Railway tracks	17. Pebble Road
2. Concrete roof	10. Floor tiles	18. Unmetalled road
3. PCC roof	11. Polished marble	19. Tennis court
4. Sandstone roof	12. Concrete Road	20. Mica sheet
5. Iron	13. Cement Roof	21. CGI Sheet
6. Red Brick	14. PVC Pipe	22. Granite
7. Rubble Road	15. Tiled roof	23. Basketball pitch
8. Asbestos	16. Walkway tile	24. Asphalt Road

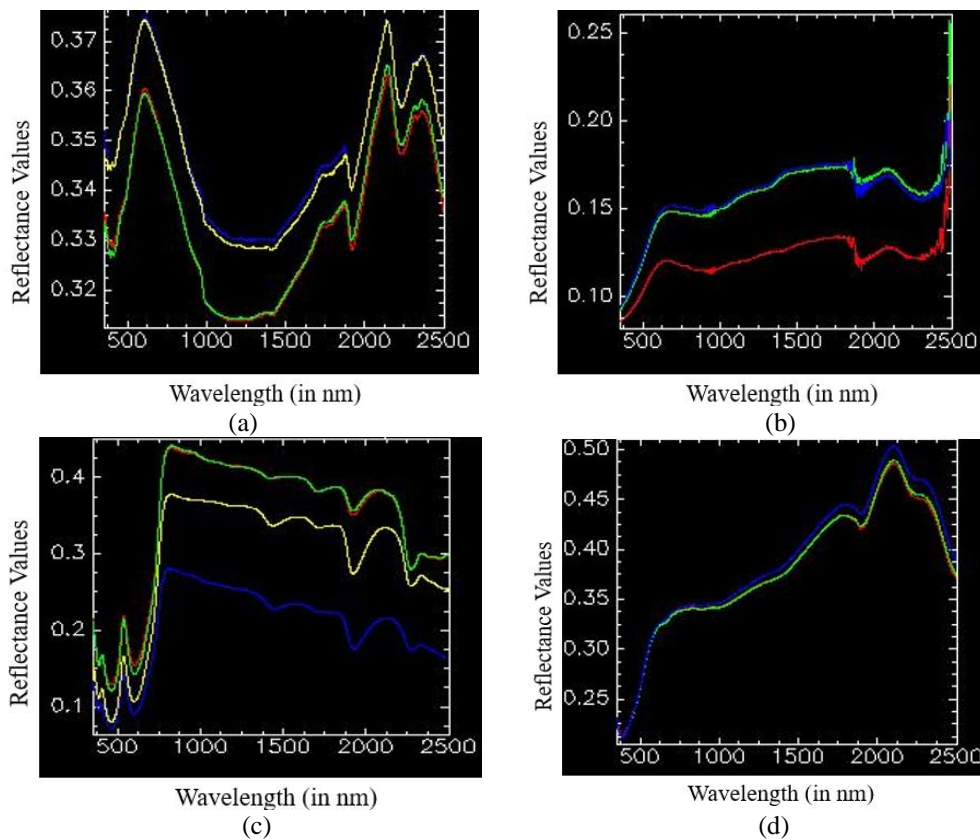


Figure 3.6: (a) Spectral signatures of concrete road (b) Railway tracks (Iron) (c) Tennis court (d) Bitumen roof

3.2. Software

For the implementation of the approaches developed for identification and detection of desired targets, different software tools have been used are detailed here.

3.2.1. Environment for Visualizing Images (ENVI)

ENVI software version 4.8, developed by ITT Visual Information Solutions, has been used for visualizing, processing and analyzing remotely sensed data. Some of these used in the present research work include,

- Pre-processing of hyperspectral data, such as removal of bad bands, spectral and spatial sampling.
- Viewing hyperspectral data
- Dynamic image display, histogram and spectral library building
- Automatic and manual contrast stretching
- Spectra extraction using Region of interest (ROI) generation
- Interactive scatter plot generation
- Classification, Target detection *etc.*

3.2.2. Matrix Laboratory (MATLAB)

MATLAB version R2018b is a fourth-generation programming language which provides efficient environment for numerical computing. It allows plotting of data, matrix operations, creation of user interfaces *etc.* it has numerous libraries for supporting wide range of applications such as control systems, image processing, neural networks, fuzzy logic, statistics *etc.* in this study, MATLAB has been used for,

- Implementation of various algorithms in the study
- Plotting of data for computing the algorithms
- Statistics computation (mean, standard deviation, correlation *etc.*)

- Neural network for analyzing target spectral behavior
- Visualizing the images
- Matrix computation for performing operations on images
- Morphological analysis

3.2.3. Jupyter Notebook using Python

The Jupyter Notebook is an open-source web application that helps to create and share live codes, equations, visualizations, and narrative text. It includes data cleaning and transformation, numerical simulation, statistical modeling, data visualization, machine learning, and much more. It is a web-based interactive computational environment for creating codes. In this work, Python is used for,

- Training the deep neural network using libraries
- Implementation of CNN
- Finding out accuracy assessment parameters
- Plotting curves

Chapter 4

Comparative Assessment of detection algorithms for engineered objects

Hyperspectral data facilitates exploration of treasure of spectral information that lie within multitudes of its spectral bands. Hyperspectral data is being analysed to explore levels of urbanization due to its competence to address spectral variability in urban environment. Literature reports use of a variety of algorithms for extraction of urban information from any given data with varying accuracies.

4.1. Introduction

This work aims to explore target detection approach, a binary classifier, to extract certain features. Roads and roofs are the most common features present in any urban scene and have been considered as targets. These experiments have been conducted on a subset of AVIRIS-NG hyperspectral data set of Udaipur region (India) with roads and roofs as targets. This section also presents a brief taxonomy of algorithms selected for the work, explores methods like Mahalanobis angle, which has been reported in the literature as being effective in extraction of urban targets, implementation of machine learning algorithms for increasing the accuracy. The work is likely to aid in city planning, sustainable development and various other governmental and non-governmental works related with urbanisation.

The objective of this work is to study an alternative approach for extraction of urban targets and treat it as a binary hypothesis and make use of various target detection algorithms for their extraction. The novelty of the work lies in the idea of dealing the problem of detecting urban targets by target detection approach rather than classification. Classification deals with multiple land cover classes at a time and

generates the corresponding thematic map, while target detection searches for some specific objects producing a binary image. Therefore, the process is well suited for detection of roads and roofs in urban areas.

A summary of various available target detection algorithms is abridged in *Table 4.1* along with its mathematical details. The work being done sums up certain standard spectral matching algorithms and performs an extensive comparative assessment for detection of urban targets (particularly road and roof). For this, all the spectral matching algorithms listed in Table 4.1 have been implemented followed by accuracy assessment. Also, the work done provides a review about conventional and modern target detection techniques adopted in hyperspectral remote sensing in past years.

In Distance measures, Euclidean distance is calculated as square root of sum of squared distances between the reference spectral signature y_i and the test spectral signature x_i . Dot product gives the scalar product of magnitude of y_i and x_i . Z-score is derived by the number of standard deviations between y_i and x_i . Lastly, Mahalanobis distance uses covariance matrix and mean of class with respect to the test spectrum x_i .

For angle measures, SAM directly compares the angle between y_i and x_i determining the similarity between them. SCM method is a derivative of Pearsonian Correlation Coefficient and calculated in similar manner like SAM. SGA is a descriptive measure to analyse the trend between two adjacent bands. Mahalanobis angle makes use of covariance matrix and then calculates the angle between y_i and x_i .

In Information measures, CEM is designed with perspective, when signature of endmember to be extracted is only available as compared to other measures. MF assumes that the target and background classes follow multivariate normal distributions with the same covariance matrix and then find the mutual information. ACE performs detection solely on the basis of spectral shape on the other hand SID works on

divergence to match pixels with y_i . Maximum likelihood algorithm calculates discriminant functions for each x_i using probabilistic approach.

Using machine learning technique, ANN and ELM are implemented that work on handcrafted features, extracted from the image and ground data. ELM tends to perform by giving extremely fast training speed as compared to ANN. ANN uses gradient descent method that takes longer than matrix invert used by ELM.

Detailed theoretical background in respect of the algorithms discussed above has been provided in *Section 2.4.1*.

Table 4.1: Mathematical Formulas for Target Detection Algorithms

S No.	Algorithm	Formula	Description
Distance Measures			
1.	Euclidean Distance	$e(x, y) = \sqrt{\sum_{i=1}^n (x_i - y_i)^2}$	$e(x, y)$ – Euclidean distance x_i – Test spectra y_i – Reference spectra n – Total number of pixels
2.	Dot Product	$x \cdot y = \sum_{i=1}^n x_i y_i = x_1 y_1 + x_2 y_2 \dots + x_n y_n$	$x \cdot y$ – Dot product x_i – Test spectra y_i – Reference spectra n – Total number of pixels
3.	Z-Score	$ZSD = \sqrt{\sum_{b=1}^n (r_b - t_b)^2 / \sigma t_b^2}$	ZSD – Z-Score Distance r_b – Reflectance amplitude of n band resampled reference spectrum at band b t_b – Mean reference of n band class spectrum at band b σt_b – Class standard deviation at band b
4.	Mahalanobis Distance	$(S_i, S_j) = \sqrt{(s_i - s_j)^T Q^{-1} (s_i - s_j)}$ $Q = \frac{1}{n-1} \sum_{x=1}^n (s_x - \bar{s})(s_x - \bar{s})^T, \bar{s} = \frac{1}{n} \sum_{x=1}^n S_x$	MD – Mahalanobis Distance S_i, S_j – Spectral vectors Q – Estimated covariance matrix computed with n data training samples
Angle Measures			
5.	Spectral angle mapper (SAM)	$SAM(s_i, s_j) = \cos^{-1} \left(\frac{\sum_{l=1}^N s_{il}}{\sqrt{\sum_{l=1}^N s_{il}^2} \sqrt{\sum_{l=1}^N s_{jl}^2}} \right)$	S_i, S_j – Spectral vectors
6.	Spectral correlation angle (SCA)	$c(x, y) = \frac{\langle x - \bar{x}, y - \bar{y} \rangle}{\ x - \bar{x}\ _2 \ y - \bar{y}\ _2}$ $SCA(x, y) = \arccos \left(\frac{c(x, y) + 1}{2} \right)$	x, y – n dimensional vectors \bar{x}, \bar{y} – Expected values of vectors

7.	Spectral gradient angle (SGA)	$SG(x) = (x_2 - x_1, x_3 - x_2, x_4 - x_3 \dots \dots x_n - x_{n-1})$ $SGA(x, y) = SA(abs(SG(x)), abs(SG(y)))$	SG – Spectral Gradient x, y – n dimensional vectors $abs(x)$ – Vectors whose components are absolute values of components of x .
8.	Mahalanobis Angle	$cos\theta_{ij} = \frac{(x_i - m)^T C^{-1} (x_j - m)}{[(x_i - m)^T C^{-1} (x_i - m)]^{1/2} [(x_j - m)^T C^{-1} (x_j - m)]^{1/2}}$	x_i, x_j – Spectral vectors C – Covariance matrix m – Mean spectra of class
Information Measures			
9.	Constrained Energy minimization (CEM)	$y_i = w^t r_j$ $t^t w = 1$ $w = \frac{R^{-1} t}{t^t R^{-1} t}$	t – Known target spectra R – Auto correlation matrix w – Coefficient vector
10.	Matched filter (MF)	$x = x_o - m_b$ $s = s_o - m_b$ $MF = \frac{x^T C_b^{-1} s}{\sqrt{s^T C_b^{-1} s}}$	x, s – Spectral vectors m_b – Background mean vector c_b – Covariance matrix
11.	Adaptive cosine estimator (ACE)	$ACE: \frac{x^T C_b^{-1} s}{\sqrt{s^T C_b^{-1} s} \sqrt{x^T C_b^{-1} x}}$	x, s – Spectral vectors m_b – Background mean vector c_b – Covariance matrix
12.	Spectral Information Divergence (SID)	$SID(r_1, r_2) = D(r_1 \ r_2) + D(r_2 \ r_1)$ $I_i(r_1) = \log(p_i) \text{ and } I_i(r_2) = -\log(q_i)$	r_1, r_2 – Pixels with spectral signatures s_1 and s_2 p, q – Probability functions generated by spectra s_1 and s_2 .
13.	Maximum likelihood algorithm	$g_i(x) = \ln p(w_i) - \frac{1}{2} \ln \epsilon_i $ $- \frac{1}{2} (x - m_i)^T \sum_i^{-1} (x - m_i)$	x – n dimensional data i – class $p(w_i)$ – probability of class w_i , assumed to be same for every class $\sum i$ – Covariance matrix
Machine learning Measures			
14.	Artificial neural network (ANN)	$y_i = g_i = g(\sum_{j=1}^K w_{ji} x_j + \theta_i)$ $E = \frac{1}{2} \sum_{j=1}^k (y_j - t_j)$	y – output x – input g – activation function w – weight θ – bias E – error t – ground truth for instance
15.	Extreme learning machine (ELM)	$\sum_{i=1}^L \beta_i G(a_i, b_i, x), x \in R^d, \beta_i \in R^m$ $G(a_i, b_i, x) = g(a_i \cdot x + b_i), a_i \in R^d, b_i \in R$ $\sum_{j=1}^N \ f_L(x_j) - t_j\ = 0$ $\sum_{i=1}^L \beta_i G(a_i, b_i, x) = t_j, j = 1, 2 \dots \dots N$ $H\beta = T$	L – Hidden nodes $G(a_i, b_i, x)$ – Output function at i^{th} hidden node a_i, b_i – hidden node parameters β_i – weight vector g – activation function H – hidden layer output matrix

4.2. Problem Statement

In the present work, it is proposed to explore target detection algorithms for extraction of urban targets. The two specific urban targets selected for this study are road and roof surfaces. The literature provides a large number of different types of algorithms for target detection as discussed briefly in *Section 2.4* and in detail in *Chapter 2*.

There are however, very little literature available to support such kinds of studies where target detection methods have been used for extraction of urban targets (road and roof surfaces). Since a lot of variation in performance of different algorithms for extraction of urban targets can be expected, in the first stage, it has been considered to carry out a comparative assessment of different types of target detection algorithms for detection of urban targets using hyperspectral data. Therefore, a set of target detection algorithms in four categories have been identified from literature survey viz distance measures, angle-based measures, information measures and machine learning measures. Target detection is followed by performance evaluation. Due to constraints such as, unavailability of ground reference data, locational variability *etc.* researchers have also used image derived spectral signatures for analysis (Zhang, *et al.* 2012) (Ren, *et al.* 2006). Hence, in this work also, reference spectra derived from the field as well as from the image have been considered. Further the results from the field and the image spectra have been used for a comparative assessment of various algorithms for detection of urban targets (roads and roofs).

4.3. Study Area and Data

The Hyperspectral data for the purpose of analysis is acquired as part of Airborne Visible and Infrared Imaging Spectrometer – Next Generation (AVIRIS-NG) data collection campaign held in February 2016 (Refer *Section 3.1* for details). The area

being considered for investigation is Udaipur, Rajasthan, India scene having 1295×388 pixels with 425 bands in the range of 376 nm to 2500 nm, with 5 nm spectral resolution and 8.1 m spatial resolution. Level 2 (derived geospatial variables at same resolution and location as Level 1 source data) spatial subset of 394 lines and 385 samples, which constitutes maximum urban area has been selected manually for conducting the set of experiments.

The spectroradiometer used for ground spectra collection for the very same region spans its range over 2151 channels with 1nm spectral sampling. Figure 4.1, shows the RGB (R=54, G=36, B=18) representation of subset of size 394×385 of the complete Udaipur image. The rectangle in the top middle represents the target roof, which is easily distinguishable from the background. The second rectangle in the bottom left is an enlargement of highway road whereas the third rectangle at the bottom right depicts another type of roof. Table 4.2 provides a brief introduction about the image and ground data collection parameters considered for the study.

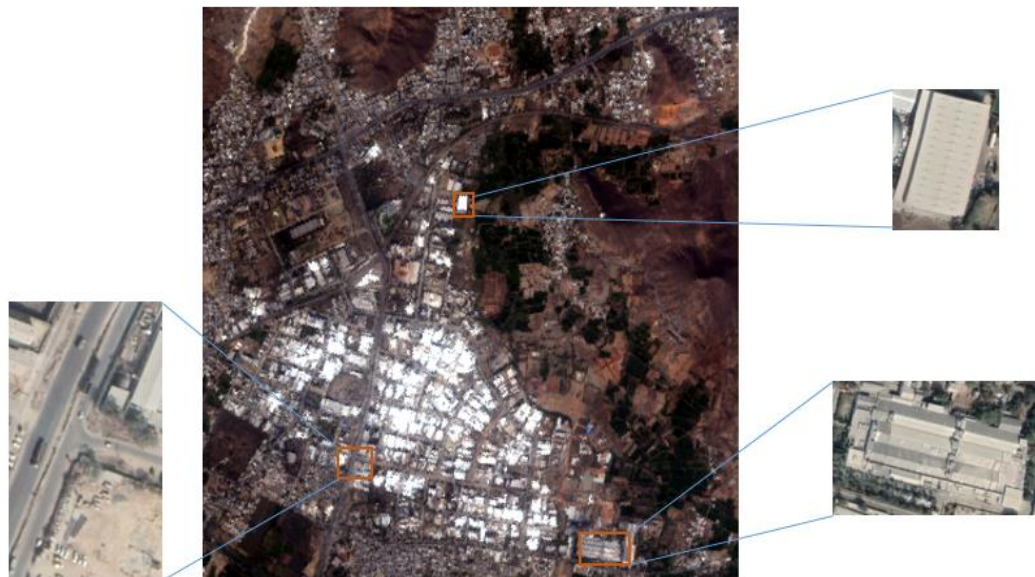


Figure 4.1: Airborne hyperspectral Data Experimental Site

Table 4.2: Description of Image and Ground Data Collection

S No.	Parameters	Image Data Description	Ground Data Description
1.	Location	Udaipur, Rajasthan, India	
2.	Date of Data acquisition	02/02/2016	16/07/2017 – 21/07/2017

3.	Spatial Resolution	8.1 meter	-
4.	Spectral Resolution	5 nm	3nm(700nm),8nm(1500nm) 6nm(2100nm)
5.	Channels	425	2151
6.	Level of data	Level 1 and Level 2	
7.	Main features in the images	Urban features such as roads, bridges, different types of roofs (Concrete, bitumen, sandstone, CGI sheet), vehicles, railway tracks <i>etc.</i>	
8.	Targets in image	High road made of concrete and asphalt, concrete roofs	

4.4. Methodology and Implementation

Pre-processing: As part of pre-processing, Level 2 (derived geospatial variables at same resolution and location as Level 1 source data) AVIRIS-NG data having 425 bands is processed and bands severely affected by atmospheric gases and water vapours are removed. After removal of bad bands, the implementation is carried out on 387 bands.

Target Detection: The reference spectra for implemented algorithms is derived in two ways: (i) from ground data collection and (ii) from the image itself. In first method, resampling of ground spectra (2151 channels) with respect to the image subset by reducing them to 387 bands has been done. As part of field data collection campaign multiple spectral signatures of urban targets were collected, such as, road (bitumen, concrete), roof (concrete, bitumen, CGI sheets, and sandstone), vehicles, railway tracks *etc.* Out of these spectral signatures, spectra of concrete road and concrete roof were selected as reference in order to distinguish between them on spectral grounds. Mean spectra of 9 road samples and 6 roof samples respectively are considered as per the availability for evaluation. Whereas in second method, mean spectra of both targets are computed by considering hundred pixels each from hyperspectral image which serves as reference spectra in each algorithm. The geographic locations of the targets are also validated using Google Earth imagery and ground spectral data collected. Various target detection algorithms are implemented and the results corresponding to them are

generated in *Section 4.5, Results and Discussion*. Each algorithm produces a pair of output comprising of extracted road and roof pixels.

Thresholding: Multi-thresholding technique as an extension to Otsu's method (Nobuyuki 1979) is used for applying threshold to the resultant image based on minimizing the within class variance in all implemented methods. The resultant image prior to thresholding can be represented in L levels ranging from 0 to 1. The number of pixels at level i is denoted by f_i , then total number of pixels sums to $N = f_0 + f_1 + \dots + f_{L-1}$. For the resultant image, the occurrence of probability of threshold i is given by:

$$p_i = \frac{f_i}{N} \quad p_i \geq 0 \quad \sum_{i=1}^L p_i = 1 \quad (4.1)$$

If an image is segmented in K clusters (C_0, C_1, \dots, C_{K-1}), $K - 1$ thresholds (t_0, t_1, \dots, t_{K-2}) must be selected. The cumulative probability w_k and mean grey level μ_k for each cluster C_k are respectively given by:

$$w_k = \sum_{i \in C_k} p_i \quad \text{And } u_k = \sum_{i \in C_k} i \cdot p_i / w_k \quad k \in \{0, 1, \dots, K - 1\} \quad (4.2)$$

Therefore, mean intensity of whole image μ_T and between-class variance σ_B^2 are respectively determined by:

$$\mu_T = \sum_{i=0}^{L-1} i \cdot p_i = \sum_{k=0}^{K-1} \mu_k w_k \quad (4.3)$$

$$\sigma_B^2 = \sum_{k=0}^{K-1} w_k (\mu_k - \mu_T)^2 = \sum_{k=0}^{K-1} w_k \mu_k^2 - \mu_T^2 \quad (4.4)$$

Performance Evaluation: A window size of 60×60 has been selected containing road and roof as targets as shown in *Figure 4.2*. Two binary images have been created having 1 as target and 0 as background, for ground truth image of road and roof. The spatial locations have been validated by the field data taken and Google Earth coordinates. The known set of road pixels calculated are 33 with 42 pixels of roof as ground truth data. The same region as of the reference window was extracted from the output subset of

size 394×385 after applying thresholding. Based on these values detection rate is evaluated according to the following equation

$$\text{Detection Rate} = (\text{Pixels detected} / \text{Total Pixels}) * 100 \quad (4.5)$$



Figure 4.2: Square window of size 60×60 considered for accuracy assessment

Comparative Assessment: A detailed comparative study has been carried out to explore the suitable algorithm for urban target detection. The contrast has been made at two levels, (i) Comparison between accuracies computed by ground-based and image-based reference spectra; (ii) Comparison among the various measures of target detection (distance, angle, information and machine learning). A comprehensive bar graph comparing these measures is plotted to depict a peculiarity between them. Also, a line diagram illustrating the threshold value range used for extraction of roads and roofs by considering ground-based and image-based reference spectra is made.

Implementation: For implementation, various spectral matching algorithms are used for detection and identification of urban targets considered, that is, road and roof. The software used to carry out the analysis are MATLAB 2018b and ENVI 5.0. The flow chart of the implementation is shown in *Figure 4.3*.

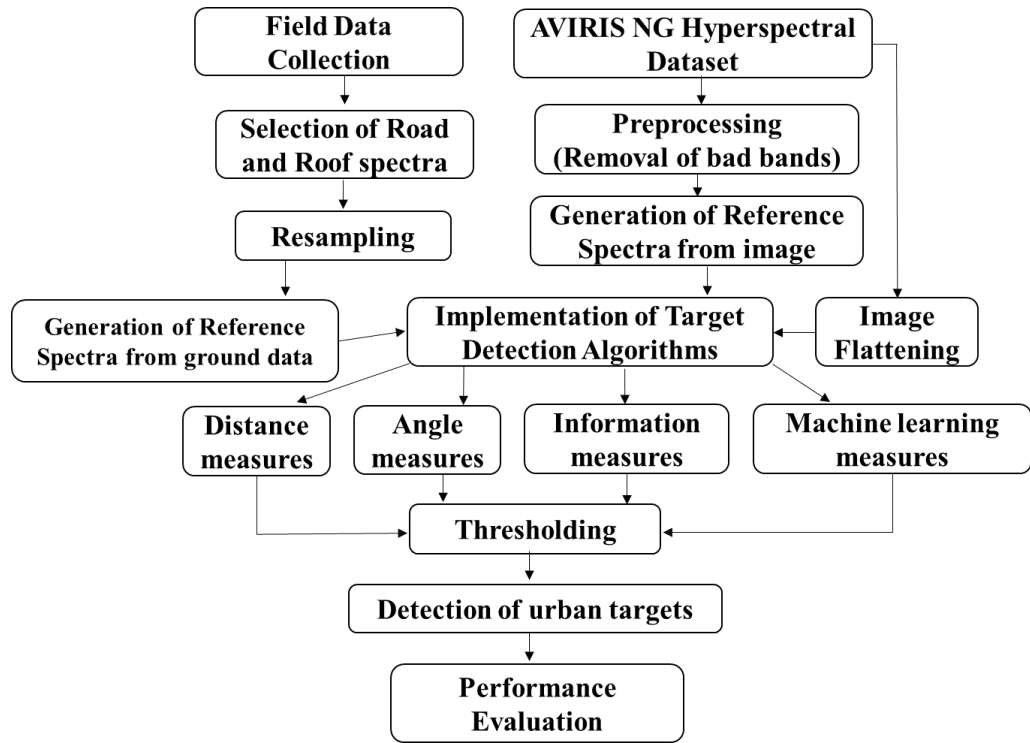


Figure 4.3: Flowchart of methodology

4.5. Results and Discussion

This work presents an alternative approach of target detection for extraction of urban targets rather than conventional classification method. For this, a series of target detection algorithms specified in *Table 4.1* have been implemented and a comparative assessment has also been carried out.

The dataset used for this study is already discussed in *Section 4.3*. A set of experiments have been conducted based on the measures used for their evaluation, namely (i) Distance measures (Euclidean distance, Dot Product, Z-Score, Mahalanobis distance) (ii) Angle measures (SAM, SGA, SCA, Mahalanobis angle) (iii) Information measures (CEM, MF, ACE, SID, Maximum likelihood estimation) and (iv) Machine learning measures (ANN, ELM), in order to detect the road and roof as targets.

4.5.1. Target detection using ground reference spectra

4.5.1.1. Distance Measures

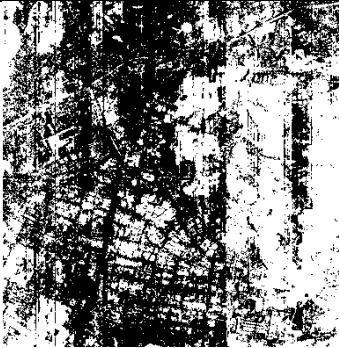
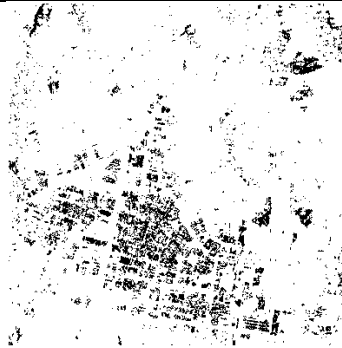


The results obtained after implementation of various distance measures are shown in *Figure 4.4 (i-viii)* and *Table 4.3*. Distance between the spectra to be classified is calculated corresponding to all the representatives of the class and the one with minimum distance based upon the threshold value is selected as the member of the class. The analysis with respect to the reference spectra taken for experiments is shown as follows:

- i. **Euclidean Distance:** The accuracies for detection of road and roof are listed in *Table 4.3* give satisfactory accuracies for roads and roofs, in case of Euclidean distance. An accuracy of 51.51% and 52.38% is achieved for roads and roofs respectively. However, a visual analysis of the corresponding resultant images shown in *Figure 4.4 (i-ii)* do not highlight road/roofs. A major limitation is that the values between reference and test spectral signatures are positively defined and indeterminately distributed. Higher values of spectral bands lead to a large value for Euclidean distance, and the threshold becomes hard to set (Wenzheng, *et al.* 2019).
- ii. **Dot Product:** Dot product being square root of Euclidian distance shows similar results for road and roof detection. The images in *Figure 4.4 (iii-iv)* depict scarcely detected road and roof surfaces with comparatively lesser accuracies for both surfaces (*Table 4.3*).
- iii. **Z-Score:** This measure is generally used for spectral library creation, but here it has been used to extract the considered urban targets. A visual examination of the resultant images produced using Z-Score appears to be incapable of

separating roads and roofs (*Figure 4.4 (v-vi)*). But as compared to Euclidean distance and dot product, it performs slightly better, refer *Table 4.3*.

- iv. ***Mahalanobis Distance:*** Unlike Euclidean distance, Mahalanobis distance accounts for how correlated the variables are to one another. This method uses the Mahalanobis distance and benefits the valuable information contained in the statistics of targets and background. The algorithm has attained maximum detection in distance measures for extraction of roads and roofs, refer *Figure 4.4 (vii-viii)* and *Table 4.3*.

The observations listed above indicate relatively poor performance of various distance measures. All these distance measures are based upon a simple linear modelling of the spectra which however is non-linear in nature. This appears to be the reason for poor performance of distance measures. Besides, a reference spectrum obtained in field is often influenced by factors such as sensor related parameters, atmospheric intervention *etc.*

S No.	Algorithm	Detection of Roads	Detection of Roofs
<i>Distance Measures</i>			
1.	Euclidean Distance		
2.	Dot Product		

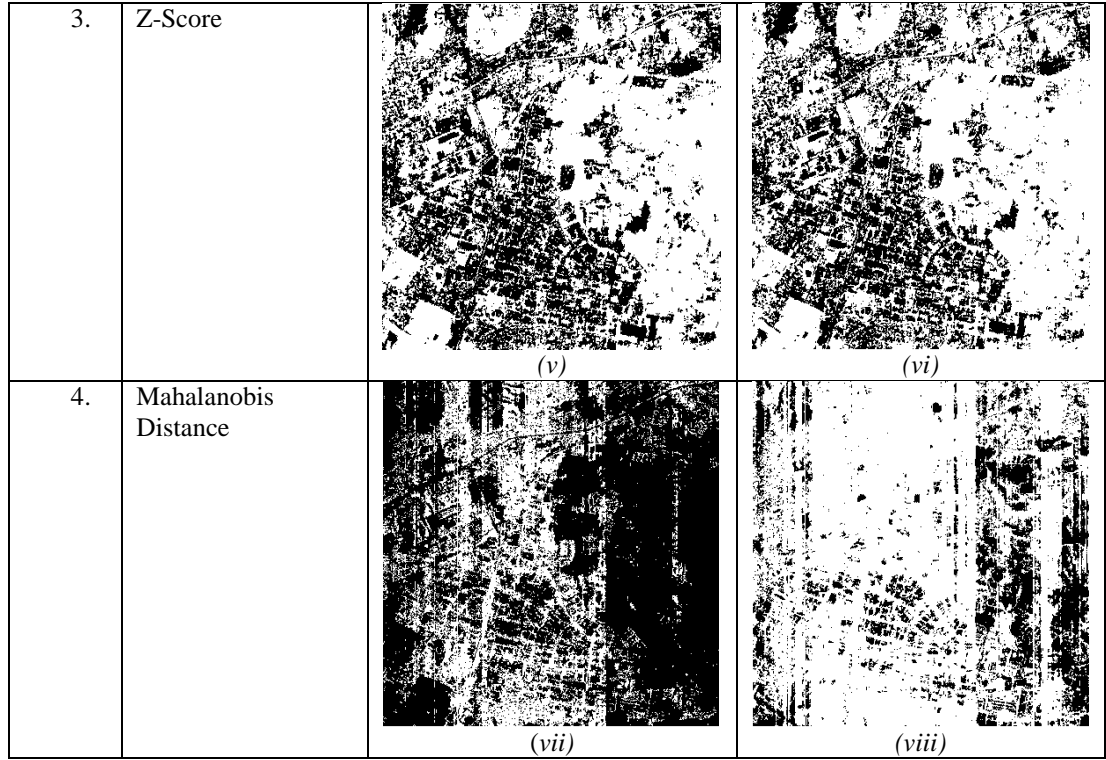


Figure 4.4: Detection of roads and roofs using Distance Measures considering ground reference spectra

Table 4.3: Accuracy assessment for Distance measures using ground reference spectra

TARGETS	Road			Roof		
ALGORITHMS	Total Pixels	Pixels Detected	Detection Percentage	Total Pixels	Pixels Detected	Detection Percentage
Distance Measures						
1. Euclidean Distance	33	17	51.51 %	42	22	52.38 %
2. Dot Product	33	18	54.54 %	42	18	42.86 %
3. Z-Score	33	19	57.57 %	42	22	52.38 %
4. Mahalanobis Distance	33	23	69.69 %	42	30	71.43 %

4.5.1.2. Angle Measures

In comparison to the distance algorithms, angular measures have performed well and the corresponding results are shown in *Figure 4.5 (i-viii)* and *Table 4.4*. Pixel vectors of class making small angles with the reference spectra often belong to the same class.

- i. **SAM:** It has shown consistent performance but have confused few pixels of roads and roofs at certain positions as illustrated in *Figure 4.5 (i-ii)*. SAM has satisfactory ability to delineate different materials, but it often yields unsatisfactory results for detecting target with similar composition and material type (Wenzheng, *et al.* 2019). Moreover, there is no optimality properties

associated with the SAM algorithm, even for multivariate normally distributed classes (F. A. Kruse, A. B. Lefkoff, *et al.* 1993). As perceived from *Table 4.4*, SAM gives an accuracy of 72.73% for roads and 73.8% for roofs.

- ii. **SCA:** On visual examination, SCA appears to detect patches of soil along with extraction of roads and roofs on the top-right side of *Figure 4.5 (iii-iv)*. Though SCA considers negative correlation as well, presenting wide variation in data leading to less detection rate of 66.67% and 57.14% for roads and roofs respectively.
- iii. **SGA:** On the other hand, SGA has shown no results contributing to extraction of roads and roofs (*Figure 4.5 (v – vi)*). The detection rate has dropped at a high scale, making it least effective in detection process with 66.67% for roads and 57.14% in roofs, refer *Table 4.4*.
- iv. **Mahalanobis angle:** Mahalanobis angle outperformed with an accuracy of 81.82% for road detection and 83.33% for roof detection (*Figure 4.5 (vii – viii) and Table 4.4*). This measure has not been considered yet for extraction of targets using hyperspectral data, but has yielded promising results after implementation.

The comments stated above show the efficiency of angular measures, as the detection rate is higher as compared to distance measures implemented. On experimentation, these measures took more computation time with complex calculations. Loosely derived from distance measures, angle measures are combination of dot products, difference *etc.* leading to a better detection of targets. SAM has given a steady performance as compared to SCM. Loss of spectral property while calculation of gradient might be a reason for degraded performance of SGA. Mahalanobis angle has outdid due to consideration covariance between neighbouring bands.




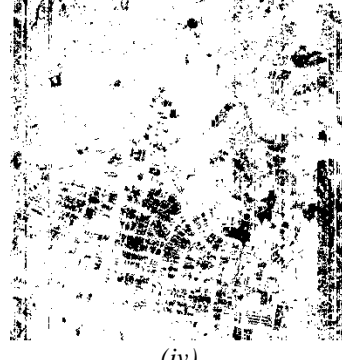

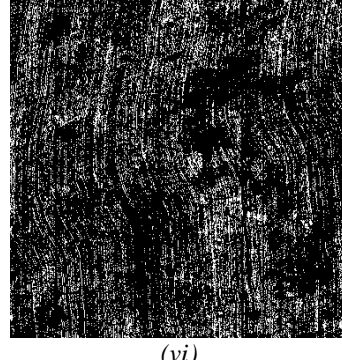


S No.	Algorithm	Detection of Roads	Detection of Roofs
<i>Angle Measures</i>			
1.	Spectral angle mapper (SAM)	 (i)	 (ii)
2.	Spectral correlation angle(SCA)	 (iii)	 (iv)
3.	Spectral gradient angle (SGA)	 (v)	 (vi)
4.	Mahalanobis Angle	 (vii)	 (viii)

Figure 4.5: Detection of roads and roofs using Angle Measures considering ground reference spectra

Table 4.4: Accuracy assessment for Angle measures using ground reference spectra

TARGETS	Road			Roof		
ALGORITHMS	Total Pixels	Pixels Detected	Detection Percentage	Total Pixels	Pixels Detected	Detection Percentage
<i>Angle Measures</i>						
1. SAM	33	24	72.73 %	42	31	73.81 %
2. SCA	33	22	66.67 %	42	24	57.14 %



3. SGA	33	16	48.48 %	42	22	52.38 %
4. Mahalanobis Angle	33	27	81.82 %	42	35	83.33%

4.5.1.3. Information Measures

In the next group information measures namely, CEM, MF, ACE, SID and maximum likelihood algorithms have been analysed for target detection. All the mentioned algorithms are implemented with an intention to examine the influence of image dataset as input on the different techniques used for processing the data. Covariance matrix of background is required for implementation of these algorithms and is calculated using the entire image, assuming the target occupies a very small fraction of the complete image (Manolakis, Siracusa, *et al.* 2001). Considering the V-I-S (Vegetation, impervious surface, soil) model, vegetation and soil are considered as background whereas road and roofs are considered as targets (Merrill 1995). *Figure 4.6 (i-x)* and *Table 4.5* show the consequent images and accuracy assessment table respectively.

- i. **CEM:** CEM is not able to detect any traces of road and roof pixels, on visual analysis and thus fails as target detector (*Figure 4.6 (i-ii)*). In road detection, it gives highly confused results with soil whereas for roof detection it generates unclear resultant image. The performance of CEM is highly dependent on the information used to describe the desired target signature, also it is very sensitive towards noise (Ren, Du and Chang, *et al.* 2003).
- ii. **MF:** MF is also highly jumbled with pixels of bare soil and is unable to produce satisfactory results by viewing the output images (*Figure 4.6 (iii-iv)*). MF takes only magnitude and direction of the considered target spectral signature. It is then possible for a pixel that is very far from any mixture of mean of target and background to still receive a high matched filter response which is a potential cause for high false alarms (DiPietro, *et al.* 2010).

- iii. **ACE:** Visually, this algorithm has shown results in this category but in detection of roofs, pixels of road are wrongly detected as part of roof (*Figure 4.6 (v-vi)*). Though the algorithm performs better as compared to other angle measures with an accuracy of 78.79% for roads and 73.81% for roofs. The major challenge in case of adaptive detection is that the number of pixels in the target class is very small, making the estimation of target density parameters extremely difficult, unlike classification (Manolakis, Marden and Shaw, Hyperspectral image processing for automatic target detection applications 2003).
- iv. **SID:** The results of SID are average and are not able to separate between roads and roofs, also shown in *Figure 4.6 (vii-viii)* and *Table 4.5*. SID is self-information, discrimination measure which models the spectral signature as a probability distribution, to capture spectral variations among various bands in a stochastic manner (Du, *et al.* 2004).
- v. **Maximum Likelihood Algorithm:** On implementation, this algorithm is able to detect roof but has not performed well for extraction of road surfaces, as also evident from *Figure 4.6 (ix-x)* and *Table 4.5* giving the lowest detection percentage. Based on pixel-by-pixel approach, it individual pixels are assigned as targets; maximising the likelihood function of the dataset.

S No.	Algorithm	Detection of Roads	Detection of Roofs
Information Measures			
1.	Constrained Energy minimization (CEM)	 (i)	 (ii)






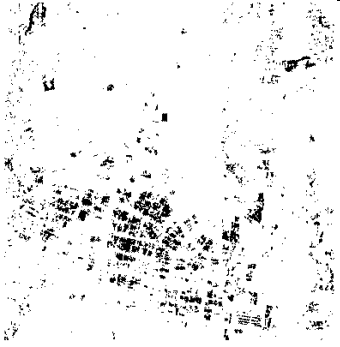
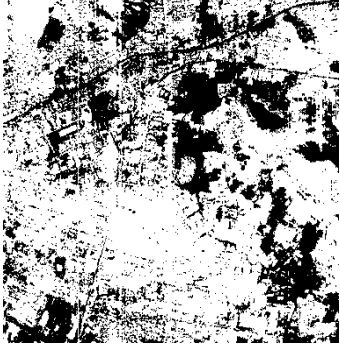
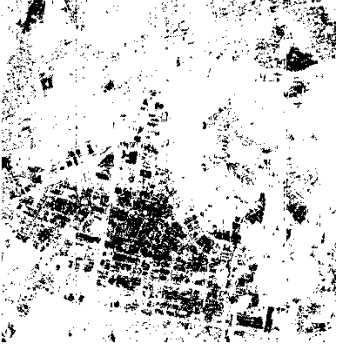
2.	Matched filter (MF)		
3.	Adaptive cosine estimator (ACE)		
4.	Spectral Information Divergence (SID)		
5.	Maximum likelihood algorithm		

Figure 4.6: Detection of roads and roofs using Information Measures considering ground reference spectra

Table 4.5: Accuracy assessment for Information measures using ground reference spectra

TARGETS	Road			Roof		
ALGORITHMS	Total Pixels	Pixels Detected	Detection Percentage	Total Pixels	Pixels Detected	Detection Percentage
Information Measures						
1. CEM	33	20	60.61 %	42	27	64.28 %
2. MF	33	21	63.64 %	42	28	66.67 %

3. ACE	33	26	78.79 %	42	31	73.81 %
4. SID	33	19	57.57 %	42	30	71.43 %
5. Maximum Likelihood	33	17	51.51 %	42	26	61.90%

The information measures work on an assumption of considering vegetation, impervious surface and soil for computation of covariance matrix, but the scene may constitute of other urban features as well. Since the material used for construction of roads and roofs may be same, most of the algorithms appear to be confused in between road and bare soil also road and roof.

4.5.1.4. Machine Learning Measures

A good generalization potential of detecting the urban targets is observed by using machine learning approaches. Machine learning algorithms have exceptional capabilities to automatically learn the relationship between the data and predict the desired results. In this work, ANN and ELM are exploited for analysis of hyperspectral data. A training file of size 2000 samples derived from ground data and image is employed for making the two networks to learn. Wherein, 500 spectra each constitute the reflectance values of road, roof, vegetation and soil respectively. While implementing the algorithm for a particular target (road or roof), all pixels belonging to other category are treated as background or non-target. Training function using is backpropagation method for ANN and positive hard limit transfer function for ELM. The hidden neurons have been varied from the range of 20 to 50 for ANN and 950 to 1000. Training parameters like performance error, epochs, momentum, learning rate, *etc.* have been tuned by trial and error in order to improve accuracy of the network. The images are shown in *Figure 4.7 (i-iv)* with corresponding detection percentage in *Table 4.6*.

- i. **ANN:** ANN having competence over learning from given data has produced good results with an accuracy of 84.84 % for roads and 88.09 % for roofs

(Figure 4.7 (i – ii)). ANN being a non-parametric method aids unique detection of the target with its capability to learn from nonlinear relationship of the data appears to be a promising approach.

- ii. **ELM:** Similarly for ELM, detection of road and roof is prominent, as illustrated in Figure 4.7 (iii - iv) and Table 4.6. A well-defined boundary of road and roof can be visualized in the output images highlighting the urban targets.

Despite of data complexity of hyperspectral imagery, machine learning measures gave best results out of all measures. With an added advantage of prediction on unknown dataset, these algorithms produce higher detection rate.

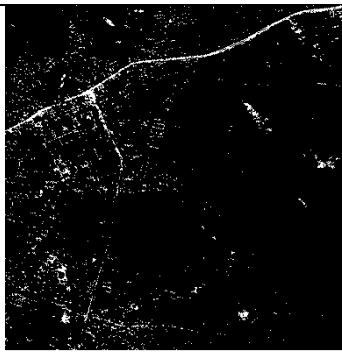
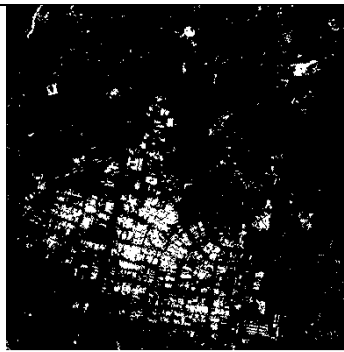

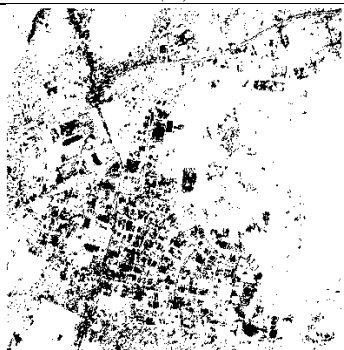
S No.	Algorithm	Detection of Roads	Detection of Roofs
Machine learning Measures			
1.	Artificial neural network (ANN)		
		(i)	(ii)
2.	Extreme learning machine (ELM)		
		(iii)	(iv)

Figure 4.7: Detection of roads and roofs using Machine Learning Measures considering ground reference spectra

Table 4.6: Accuracy assessment for Machine learning measures using ground reference spectra

TARGETS IDENTIFIED	Road			Roof		
ALGORITHMS	Total Pixels	Pixels Detected	Detection Percentage	Total Pixels	Pixels Detected	Detection Percentage
Machine Learning Measures						
1. ANN	33	28	84.84 %	42	37	88.09 %
2. ELM	33	29	87.87 %	42	36	85.71 %

The algorithms have been implemented by considering ground reflectance spectra as reference. Due to lack of knowledge about composition of material, sufficient target data is not available on ground. The reference spectra obtained in the field has been taken under different atmospheric conditions and is highly influenced by background. Also, the test spectra to be compared for target detection process are derived from hyperspectral imagery. Despite of resampling the target spectra with respect to the image test spectra mismatch between the two persists. As already discussed, distance, angle, information and machine learning measures have been implemented using ground-based reference signature and the results has been shown above. In distance measures particularly Mahalanobis distance has performed well. Similarly in angle measures, Mahalanobis angle performs well for delineating road and roof surfaces. While for information measures, ACE algorithm has given promising results. Out of four categories, machine learning algorithms, namely ANN and ELM have shown remarkable detection rate. Overcoming the drawback of extensive training time in ANN, ELM has performed well for this hyperspectral data.

4.5.2. Target detection using image reference spectra



4.5.2.1. Distance Measures

The resultant output images of road and roof are shown in *Figure 4.8 (i-viii)* and their detection accuracies are listed in *Table 4.7*.

- i. **Euclidean distance:*** It has detected road and roof surfaces with an accuracy of 63.64 % and 69.05% respectively, refer *Table 4.7*. While extraction of roof, it has highlighted the bare soil area on the right bottom part of the image, as shown in *Figure 4.8 (i-ii)*.

- ii. **Dot Product:** Dot product is not able to produce significant results neither for road nor roof extraction. In both the cases it is producing similar result on visually examining the output images in *Figure 4.8 (iii-iv)*.
- iii. **Z-Score:** This measure appears to detect road with an accuracy of 66.67% but has not proved to be equally efficient for roof detection as can be seen from *Figure 4.8(v-vi)* and the detection percentage with respect to this measure is listed in *Table 4.7*.
- iv. **Mahalanobis Distance:** Mahalanobis distance excels in determination of roof surfaces, even a small target is also detected as projected from *Figure 4.8 (viii)* but in case of road detection the algorithm detects surfaces covered with bare soil also *Figure 4.8 (vii)*.

The reason for this may be attributed to confusion between the similar materials used for construction of roads and roof such as concrete, bitumen *etc.* leading to false alarms. Apart from this, an additional step of data normalization added up to the computation time as the computed values did not fall within a set interval. Consequently, the distance values increase with an increase in number of bands (Nirmal 2004).

S No.	Algorithm	Detection of Roads	Detection of Roofs
Distance Measures			
1.	Euclidean Distance		
		(i)	(ii)

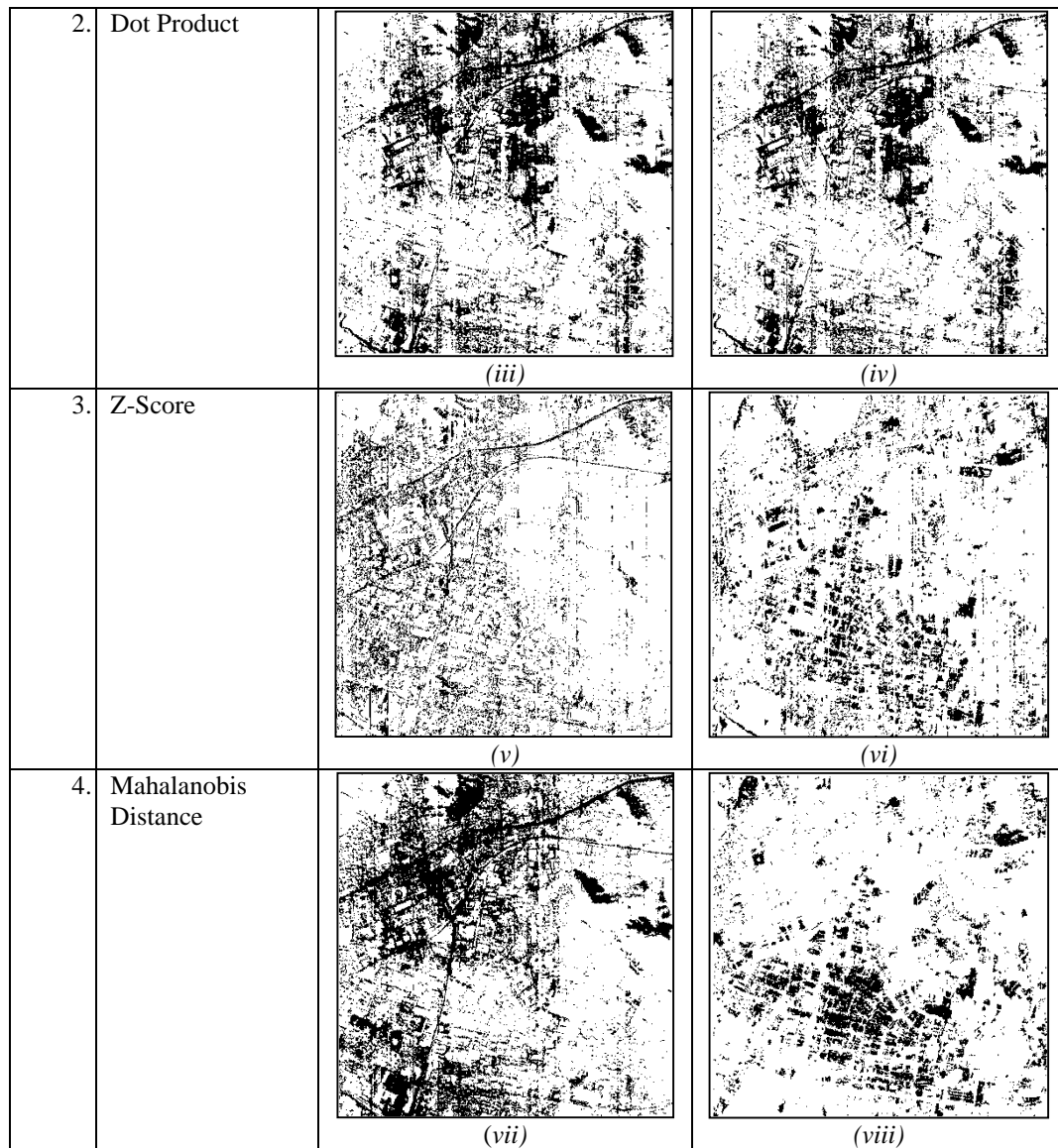


Figure 4.8: Detection of roads and roofs using Distance Measures considering image reference spectra

Table 4.7: Accuracy assessment for Distance measures using image reference spectra

TARGETS	Road			Roof		
	Total Pixels	Pixels Detected	Detection Percentage	Total Pixels	Pixels Detected	Detection Percentage
Distance Measures						
1. Euclidean Distance	33	21	63.64 %	42	29	69.05 %
2. Dot Product	33	23	69.70 %	42	27	64.28 %
3. Z-Score	33	22	66.67 %	42	26	61.90 %
4. Mahalanobis Distance	33	25	75.76 %	42	33	78.57 %

4.5.2.2. Angle measures

Figure 4.9 and Table 4.8 illustrate the experimentation results of SAM, SCA, SGA and Mahalanobis Angle. Following are the observations documented after careful examination of results obtained.

- i. **SAM:** On visual examination, SAM is able to highlight difference between road and roof surfaces precisely, refer *Figure 4.9 (i-ii)* with detection rate of 75.76% for roads and 73.81% for roofs.
- ii. **SCA:** The algorithm partly recognizes the considered targets as shown in *Figure 4.9 (iii – iv)* making it least efficient for detection of urban surfaces, in angle measure category.
- iii. **SGA:** Implementation of SGA did not show good results even after contemplation of slope changes within a vector (*Figure 4.9 (v – vi)*).
- iv. **Mahalanobis angle:** This measure is explored for detection of roads and roofs, which generated effective detection accuracy, so far it has not been productively used for hyperspectral target detection applications (*Figure 4.9 (vii-viii)* and *Table 4.8*).

Despite having an added advantage of being insensitive to illumination changes, SAM is unable to perceive difference in intensities of spectral reflectance of broadly similar materials and yields alike spectral angles for road and roof detection. SCA performs well when number of similar spectra are less but considers negative correlations (Nidamanuri and Zbell 2010). SGA is not able to distinguish between road and roof and the reason may be highly redundant band information. Mahalanobis angle has achieved highest detection and is successful in extraction of urban targets considered. In terms of detection rate, for distance measures the maximum accuracy obtained is 75.76% for roads and 78.57% for roofs whereas taking a leap, angle measures give a maximum accuracy of 87.88% for roads and 85.71% for roofs.





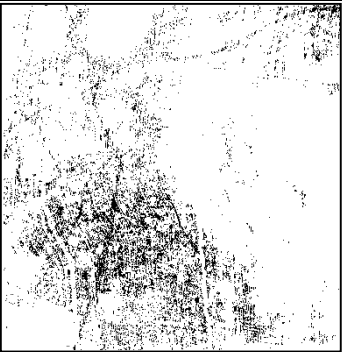



S No.	Algorithm	Detection of Roads	Detection of Roofs
Angle Measures			
1.	Spectral angle mapper (SAM)	 (i)	 (ii)
2.	Spectral correlation angle (SCA)	 (iii)	 (iv)
3.	Spectral gradient angle (SGA)	 (v)	 (vi)
4.	Mahalanobis Angle	 (vii)	 (viii)

Figure 4.9: Detection of roads and roofs using Angle Measures considering image reference spectra

Table 4.8: Accuracy assessment for Angle measures using image reference spectra						
TARGETS	Road			Roof		
ALGORITHMS	Total Pixels	Pixels Detected	Detection Percentage	Total Pixels	Pixels Detected	Detection Percentage
Angle Measures						
1. SAM	33	25	75.76 %	42	31	73.81 %


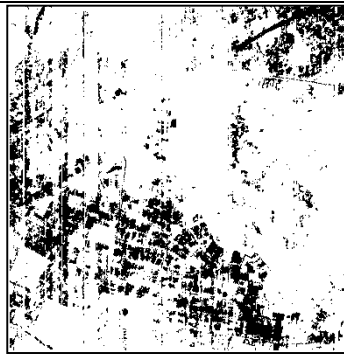
2. SCA	33	19	57.57 %	42	20	47.62 %
3. SGA	33	20	60.61 %	42	27	64.28 %
4. Mahalanobis Angle	33	29	87.88 %	42	36	85.71 %

4.5.2.3. Information Measures

The result images are shown in *Figure 4.10 (i – x)* and the corresponding accuracies are listed in *Table 4.9*.

- i. CEM: It detects pixels of roof while de2tection of road, leading to very less accuracy as shown in (*Figure 4.10 (i – ii)*) and *Table 4.9*.
- ii. ACE: ACE performed equally well for both roads and roofs, giving an accuracy of 81.82% for roads and 83.33% for roofs (*Figure 4.10 (v-vi)* and *Table 4.9*).
- iii. SID: It has shown remarkable results for detection of roofs with an accuracy of 78.57 %, thereby preserving the spectral characteristics of a class (*Figure 4.10 (vii-viii)*, *Table 4.9*).
- iv. MF and maximum likelihood algorithm: These algorithms were successful in partially detecting the roads and roofs. Some part of soil was also detected as target by these algorithms (*Figure 4.10 (iii-iv and ix-x)*).

On visual examination, information measures have produced satisfactory results and are able to extract road and roof as urban targets. ACE has surpassed the detection accuracies of other algorithms in this category whereas maximum likelihood algorithm has been able to detect traces of targets.

S No.	Algorithm	Detection of Roads	Detection of Roofs
Information Measures			
1.	Constrained Energy minimization (CEM)		
		(i)	(ii)




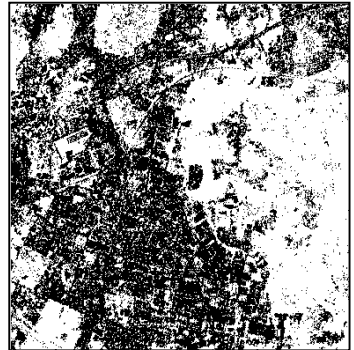

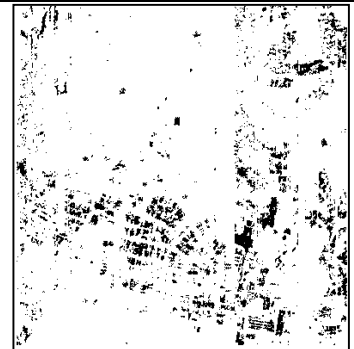
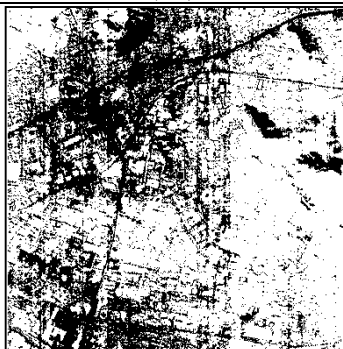
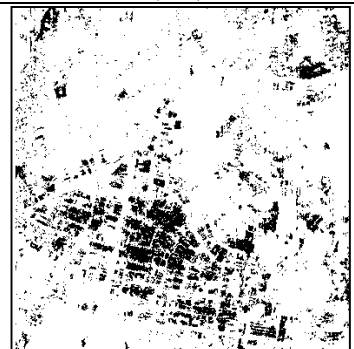
2.	Matched filter (MF)		
		(iii)	(iv)
3.	Adaptive cosine estimator (ACE)		
		(v)	(vi)
4.	Spectral Information Divergence (SID)		
		(vii)	(viii)
5.	Maximum likelihood algorithm		
		(ix)	(x)

Figure 4.10: Detection of roads and roofs using Information Measures considering image reference spectra

Table 4.9: Accuracy assessment for Information measures using image reference spectra

TARGETS	Road			Roof		
ALGORITHMS	Total Pixels	Pixels Detected	Detection Percentage	Total Pixels	Pixels Detected	Detection Percentage
Information Measures						
1. CEM	33	24	72.73 %	42	29	69.05 %
2. ACE	33	27	81.82 %	42	35	83.33 %



3. SID	33	24	72.73 %	42	33	78.57 %
4. MF	33	23	69.70 %	42	23	54.76 %
5. Maximum Likelihood	33	15	45.45 %	42	29	69.05 %

4.5.2.4. Machine Learning Measures

The results for both the algorithms are described in *Figure 4.11 (i – iv)* and *Table 4.10*.

- i. ANN: ANN has given a remarkable accuracy of 87.87% for roads and 90.48% for roofs.
- ii. ELM: It has been recently explored for hyperspectral data with ease of implementation, less training time, preferred for large datasets, minimal human intervention generates high accuracy.

Large amount of data leads to better accuracy for machine learning methods. The only challenge is availability of labelled data. With known data, both the algorithms considered under this category perform well and are able to detect the targets. The range of values considered for feature vectors of roads and roofs overlap due to which derivation of discriminative features is difficult to attain.

S No.	Name of Algorithm	Detection of Roads	Detection of Roofs
Machine learning Measures			
1.	Artificial neural network (ANN)	 (i)	 (ii)

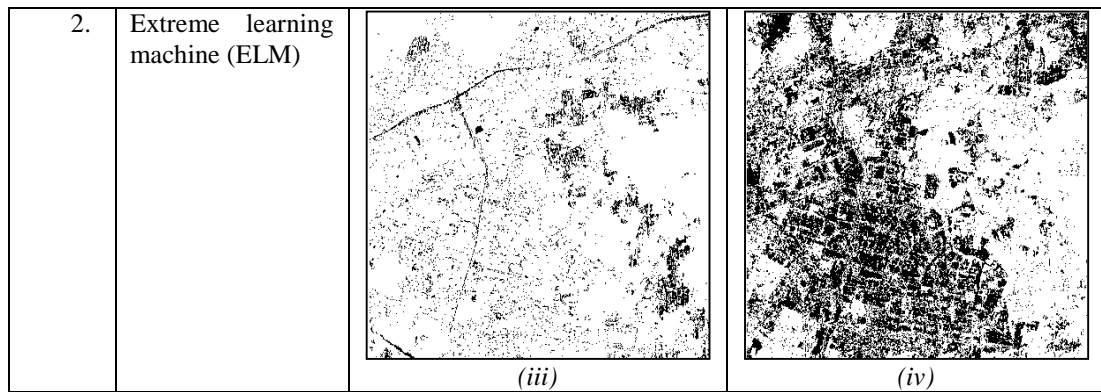


Figure 4.11: Detection of roads and roofs using Machine Learning Measures considering image reference spectra

Table 4.10: Accuracy assessment for Machine Learning measures using image reference spectra

TARGETS		Road		Roof		
ALGORITHMS	Total Pixels	Pixels Detected	Detection Percentage	Total Pixels	Pixels Detected	Detection Percentage
Machine Learning Measures						
1. ANN	33	29	87.87 %	42	38	90.48 %
2. ELM	33	30	90.9 %	42	35	83.33 %

The measures in this stage make use of reference signature derived from the scene and then comparing it to the test spectra from the image itself. The detection percentage is higher as compared to the algorithms which took field reference spectra in account. As reference signature in this case is exceedingly related to the imagery and variability encountered is only in terms of spectral range of values of a particular class. Also, no such problem of insufficient spectral signatures arises in this case. Therefore, a large set of spectra combines to give an optimal reference spectrum. The common observation in both the scenarios mentioned is the high performance of machine learning algorithms which are considered more suitable for this data.

4.5.3. Analysis of threshold for different algorithms

The results produced are binary images after thresholding process, black pixels referring to 0 as absence of target and 1 indicating target detected. Once the detections were made using all fifteen target detection algorithms mentioned, detected pixels per image were compared to the ground truth images. Two ground truth images were

generated for road and roof respectively, mapping with the locations of ground spectra collection and validating the same with Google Earth coordinates.

A set of variable thresholds has been generated by Otsu's method while the minimum value was used and the area of the false-alarm and target histograms to the right of the threshold was measured. The result map has been thresholded to distinguish likely targets and backgrounds creating a binary image which was compared to the ground truth image to evaluate the performance of the target detector. *Table 4.11* lists the threshold values used for detecting roads and roofs using ground and in scene reference spectra respectively. *Figure 4.12* and *Figure 4.13* depicts a line chart corresponding these values.

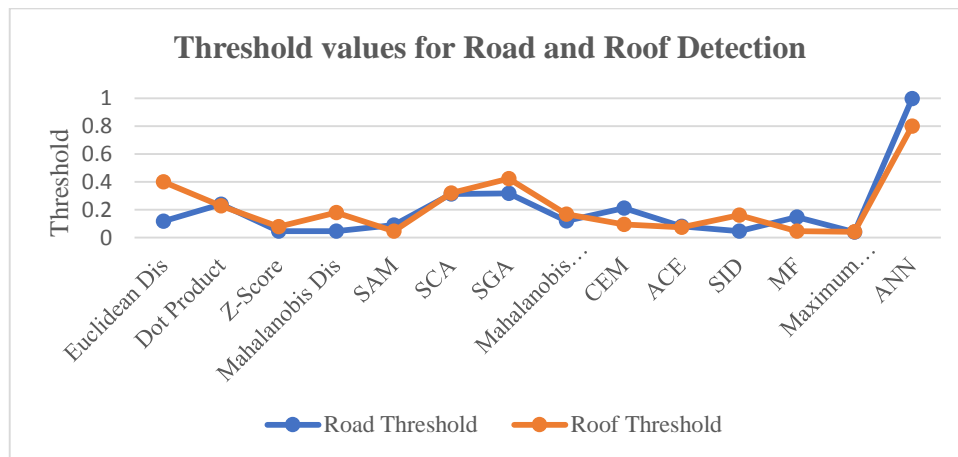


Figure 4.12: Threshold values for detection of Road and Roof targets using Ground Reference Spectra

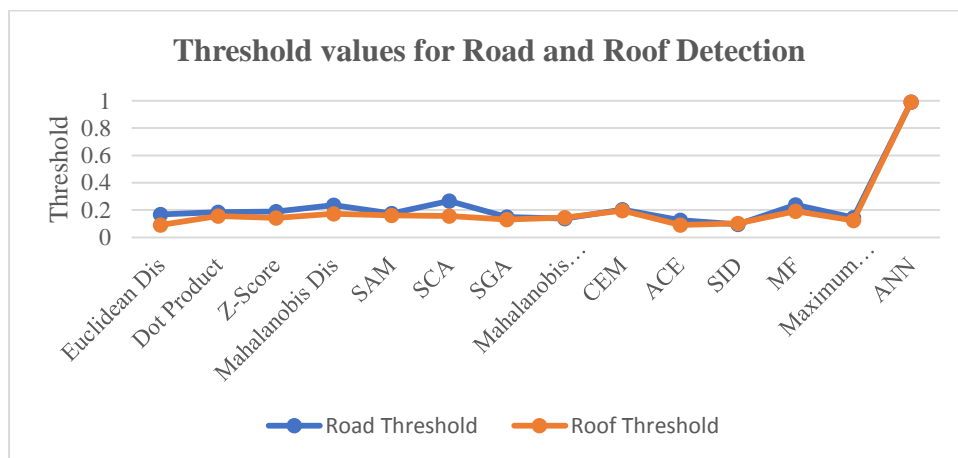


Figure 4.13: Threshold values for detection of Road and Roof targets using Image Reference Spectra

Table 4.11: Threshold values considered for detection of road and roof targets

S No.	Algorithms	Ground Reference Spectra		Image Reference Spectra	
		Road	Roof	Road	Roof
Distance Measures					
1.	Euclidean Distance	0.1686	0.0902	0.1176	0.4
2.	Dot Product	0.1843	0.1569	0.2392	0.2275
3.	Z-Score	0.1882	0.1411	0.0471	0.0784
4.	Mahalanobis Distance	0.2353	0.1725	0.0471	0.1804
Angle Measures					
5.	Spectral Angle mapper (SAM)	0.1757	0.1608	0.0901	0.0478
6.	Spectral Correlation Mapper (SCA)	0.2666	0.1568	0.3137	0.3216
7.	Spectral Gradient Angle (SGA)	0.149	0.1294	0.3172	0.4246
8.	Mahalanobis Angle	0.1372	0.1448	0.1213	0.1683
Information Measures					
9.	Constrained Energy Minimization (CEM)	0.2039	0.1965	0.2135	0.0941
10.	Adaptive Cosine Estimator (ACE)	0.1255	0.0915	0.0818	0.0743
11.	Spectral Information Divergence (SID)	0.09411	0.1019	0.0471	0.1608
12.	Matched Filter (MF)	0.2392	0.1921	0.149	0.0471
13.	Maximum likelihood Algorithm	0.1451	0.1243	0.0392	0.0431
Machine Learning Measures					
14.	1. Artificial Neural Network (ANN)	0.999	0.998	0.999	0.8
15.	2. Extreme Learning Machine (ELM)	-	-	-	-

4.5.4. Performance Analysis

The results obtained after applying the target detection algorithms have been analysed in a histogram. *Figure 4.14 and 4.15* evidently discerns the effectiveness of machine learning algorithms which perform well for AVIRIS- NG hyperspectral data. The other observation is that, when reference spectra is field based, the accuracies of all the algorithms decline by certain amount whereas if the reference spectra is derived from the scene itself the resultant accuracies increase significantly. The reason enunciated for this may be the influence of parameters like background, moisture content, temperature and many more while capturing the spectra in field. Also, distance measures have performed consistent as they are based on simple statistical computations followed by angle measures which takes minimum angles in account, to assign test pixel to target class giving reasonable detection rate. Information measures extract the mutual information between test and the target spectral signature, making them less effective in case of spectrally similar targets. Lastly, Machine learning

methods have considered that spectrally similar targets may have analogous statistical measurements, hence making them difficult to be discriminated parametrically. A non-parametric approach such as ANN and ELM have helped to extract the considered targets by learning from nonlinear relationship of the data.

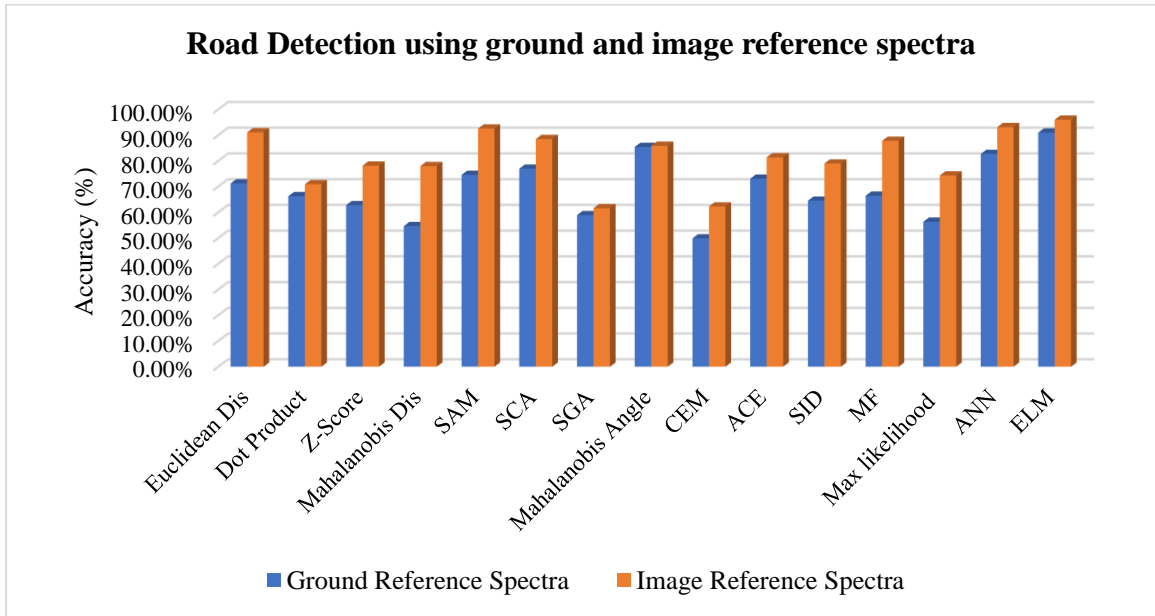


Figure 4.14: Road detection accuracy using ground reference spectra and image reference spectra

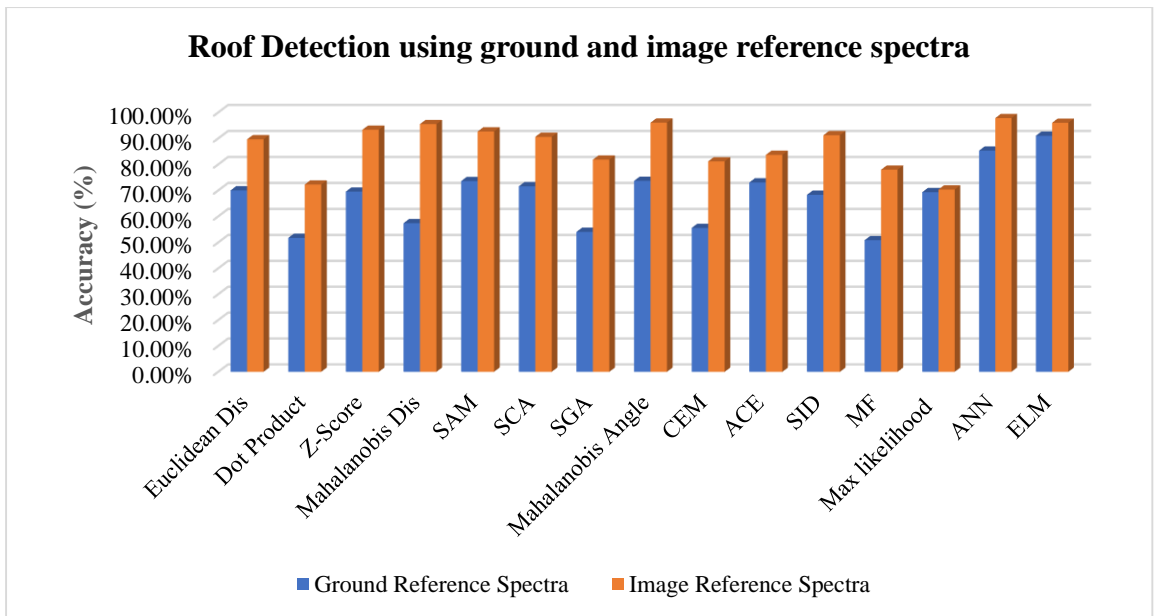


Figure 4.15: Roof detection accuracy using ground reference spectra and image reference spectra

4.6. Summary

The problem of extraction of urban targets *i.e* roads and roofs has been successfully dealt as a target detection problem and studied in detail. A comprehensive taxonomy of target detection methods using hyperspectral remote sensing data has also been presented. Several algorithms which though reported in the literature but not implemented such as Mahalanobis angle for target detection have also been used in this study. In this work, several target detection algorithms have been implemented using recently acquired hyperspectral AVIRIS- NG data of Udaipur region in India.

The algorithms have been compared under four categories, namely, (i) Distance measures: Euclidean distance, dot product, Z-score, Mahalanobis distance; (ii) Angle measures: SAM, SCA, SGA, Mahalanobis angle; (iii) Information measures: CEM, MF, ACE, SID, maximum likelihood and (iv) Machine learning measures: ANN and ELM. Road and roofs have been treated as urban targets.

The work has been implemented in different stages, primarily, using reference spectra acquired from field in Stage -1 and spectra drawn from the scene itself in Stage-2. The experiments conducted for target detection show that roads and roofs can be effectively extracted from the hyperspectral data using both the field reference spectra as well as the scene drawn spectra. However, in all the target detection implementations, it is seen that the reference signature drawn from the image produces higher detection rate, thereby increasing the accuracy of the algorithm used whereas the field reference spectra due to prevailing effects of background, illumination and resolution yields low detection. The reason for this difference could be the fact that down-sampling of ground data with respect to image data degrades the performance of the target detector. Besides, the spatial resolution of data used in these experiments is 8.1 meters and this might be insufficient for detection of urban targets as their scale is much smaller. A sharp

delineating boundary between roads and roofs is therefore not seen/detected in the resultant images.

Machine learning methods appear to be more attractive and show their tremendous potential in detecting targets with less execution time and high accuracy rate. Their learning capability from known data and prediction for unknown data make them outperform among all the algorithms. Distance measures are less effective and insensitive to spectral properties of roads and roofs with less accuracy. Information measures lead to partial detection of roads and roofs as all the techniques depend upon calculation of background covariance matrix. Mahalanobis angle target detection performed well in comparison to other angle measures and distance measures but did not outperform machine learning methods. Overall, machine learning algorithms appear to perform high uniformly, various target detection algorithms in other categories produce mixed results, and some perform well for roads while others perform well for roofs.

Target detection exceedingly depends upon the threshold value. Here, Otsu's method for generating multiple thresholds was explored for generating binary output maps containing target and background values. The threshold values vary with the material composition, image dataset and algorithm used. Another important observation is that class distributions of the hyperspectral imagery are non-Gaussian, thus a class may not be defined by a single component. Because of this it is difficult to map urban targets using ground or image reference signature. Apart from this, material used for construction of roads and roofs is also similar, such as concrete, asphalt, bitumen which could be regarded as another reason for lesser detection rate.

In summary, target detection approach appears to yield effective results in extraction of roads and roofs using hyperspectral data. Further the success of target

detection approach also suggests that this approach can be further extended for next level of detection/delineation of roads and roof surfaces into its various types. For example, roads can be further detected/delineated into concrete roads, coal tar roads *etc.* and roofs can be detected/delineated into metallic, concrete roof *etc.*

Chapter 5

Development of spectral-spatial strategies for detection of engineered objects

The results of the comparative assessment carried out in previous chapter indicate that while target detection approach in extraction of urban targets (roads and roofs) performs satisfactorily, however, there are two observations, (i) image/scene-based reference spectra give higher accuracy than the field/ground reference spectra (ii) the spectral based detection appears to have an upper limit of performance which may be improved by including certain spatial component/feature.

In the present work, therefore, extraction of urban objects that is, roads and roofs is proposed to be extracted using a hybrid approach of the spectral and spatial components of hyperspectral data. It utilizes morphological operators namely, Dilation, Erosion, Opening and Closing with fused spectral signatures of urban targets considered. Artificial neural network (ANN) has been used as a machine learning measure due to its high prediction capability and its effectiveness over other conventional target detection approaches, as determined from the previous chapter. This approach can be implemented either by supervised extraction of spectral-spatial features or by automated extraction. In this chapter the focus will be on supervised extraction of spectral-spatial features and in the next chapter, using automated extraction.

5.1. Introduction

Detection of roads and roofs hold an utmost importance for mapping the urbanisation trends. Road network acts as a major parameter for applications in city planning, transportation, traffic management, GPS Navigation (Shi, Miao and Debayle 2013) *etc.* Also, detection of roofs aids in population prediction, temperature

distribution, and reconstruction of a particular area (Bannehr, *et al.* 2011). High resolution remotely sensed images such as IKONOS, MODIS *etc.* have been already explored in different applications involving spectral-spatial fusion by various researchers. It is therefore considered to extend similar spectral-spatial fusion approach to AVIRIS-NG hyperspectral data.

In order to increase the detection accuracy, the work emphasizes on exploiting the spatial and spectral component of the data by fusing them together. Surfaces like roads and roofs may be constructed out of the similar materials, then extracting them spatially increases the probability of the detection process.

5.2. Problem Statement

In previous objective, a comparative assessment of large number of different target detection algorithms such as distance, angle, information and machine learning based approaches have been carried out. Several limitations in extraction of urban targets (roads and roof surfaces) using hyperspectral data have been observed. These limitation include, inability to separate spectrally similar engineered objects, inability to detect sharp boundaries of urban targets. Though, literature provides a remarkable insight into the spectral properties of built-up materials but a comprehensive analysis of separability of different spectrally similar urban targets is yet to be addressed. Since the acquired signal is composed of multiple land surface targets; it is difficult to distinguish them based on spectral properties alone. It is therefore considered to explore and develop spectral-spatial strategies to improve the detection of urban targets (roads and roof surfaces).

5.3. Study Area and Data

The study area considered is same as mentioned in *Chapter 4, Section 4.3*. The spatial subset of 394 lines and 385 samples, covered maximum with urban landcover is selected manually for experimentation.

5.4. Methodology and Implementation

Pre-processing: In the pre-processing phase, available reflectance airborne data containing 425 spectral bands is reduced to 387 in number, thereby removing the bad bands affected by atmospheric hindrances.

Selection of Structuring Element: Depending upon the variability encountered in terms of different roads (linear structures) and roofs (clusters), three structuring elements are chosen, namely line, disc and rectangle for analysis. Structuring element is a matrix which recognises the pixel and defines the neighbourhood used in its processing in the input image. Generally, it is chosen depending upon the shape and size of the targets to be detected. The three types of structuring elements are explained as under:

Line: It creates a two-dimensional, linear structuring element, of a given length, and degree which specifies the angle of the line, as measured in a counter clockwise direction from the horizontal axis. Length is measured as the distance between the centres of the structuring element members at opposite ends of the line. For instance, *Figure 5.1(a)* shows line structuring element of length 5 at an angle of 45° in a neighbourhood of 5×5 .

Rectangle: It creates a rectangle-shaped structuring element, which takes rows and columns as input, together they form the size of it. Rows and columns must be non-negative to create a flat rectangle structuring element. *Figure 5.1(b)* shows a rectangle structuring element of size $m = 3$ and $n = 5$.

Disc: It forms a disk-shaped structuring element, with a specific non-negative radius value. It is approximated by a sequence of N periodic-line structuring elements. *Figure 5.1(c)* shows a disk structuring element of radius 3.

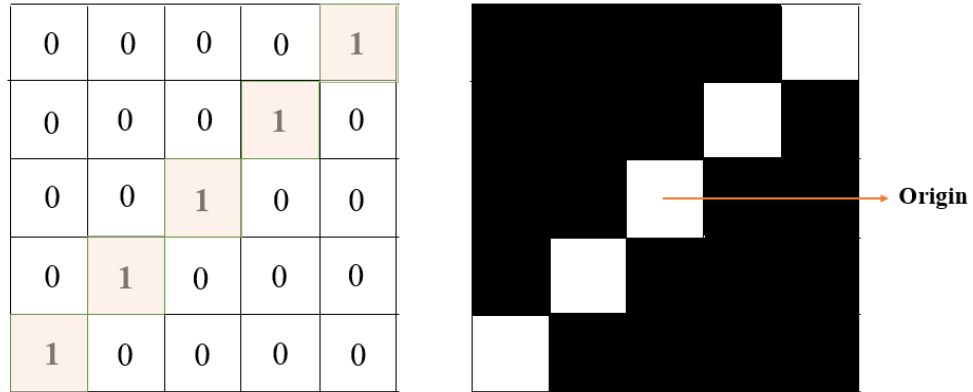


Figure 5.1(a): Line structuring element of length 5 angle 45° and neighbourhood 5×5

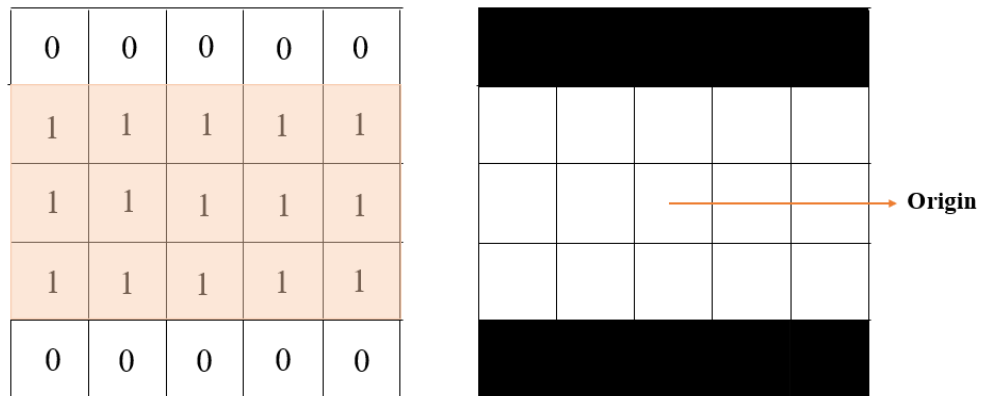


Figure 5.1(b): Rectangle structuring element of size 3×5 and neighbourhood 5×5

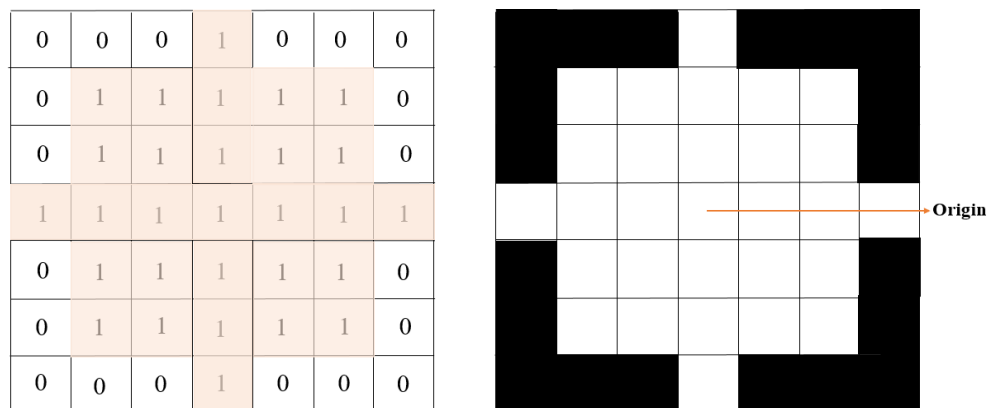


Figure 5.1(c): Disk structuring element of radius 3 and neighbourhood 7×7

Morphological Operators: As already stated that, urban features are heterogeneous in nature and detecting them based on spectral characteristics

may lead to confusion between spectrally similar materials. Consequently, there is an increased interest in developing advanced image-processing algorithms to incorporate spatial information for reliable detection process (Liao 2017). Four morphological operators, Dilation, Erosion, Opening and Closing are chosen for carrying out the work.

Generation of Training File: The labelled data is required for training of the network, so 2000 known samples of roads, roofs, vegetation and soil are considered. Where 500 samples belong to every feature individually. One vs Many approaches is chosen, for instance, to extract the pixels of road, pixels other than road, that is, roofs, vegetation and soil are masked. Other urban features like water, bare land is already masked out by physical field examination, visual image interpretation and deriving geo-locations from Google Earth. This gives a feature vector of size 1×387 constituted by average of spectral signature and corresponding morphological operator. So, in total four training files are generated as input to the ANN architecture.

Implementation of ANN: The training files are passed through ANN and output image is generated as a binary image highlighting the presence of the considered target. The learning algorithm used for implementing the model is backpropagation with random sets of training: validation: testing as 70:15:15. Backpropagation ensures the error minimisation with every iteration. The number of neurons has been varied from the range of 20-50. Other hyper-parameters like performance error, epochs, momentum, learning rate *etc.* are tuned by trial and error to improve the accuracy of the network. After completion of the learning process, training, validation and testing accuracies are computed followed by generation of optimized weight file, which is further

used for labelling the unknown data. Mathematical framework of ANN is already explained in *Chapter 2, Subsection 2.6.3.1*.

Performance Evaluation: Set of experiments are conducted in order to analyse the results from multiple combinations of different types of structuring elements (disc, line, rectangle) with morphological operators (Dilation, Erosion, Opening and Closing). A detailed comparative study has been carried out to explore the suitable spatial-spectral algorithm for urban target detection. The number of pixels detected in respect to the total pixels gives the detection accuracy which is calculated by Equation 5.1.

$$\text{Detection Rate} = \frac{\text{Pixels detected}}{\text{Total pixels}} \times 100 \quad (5.1)$$

The flow chart of the implementation steps is given in *Figure 5.2*.

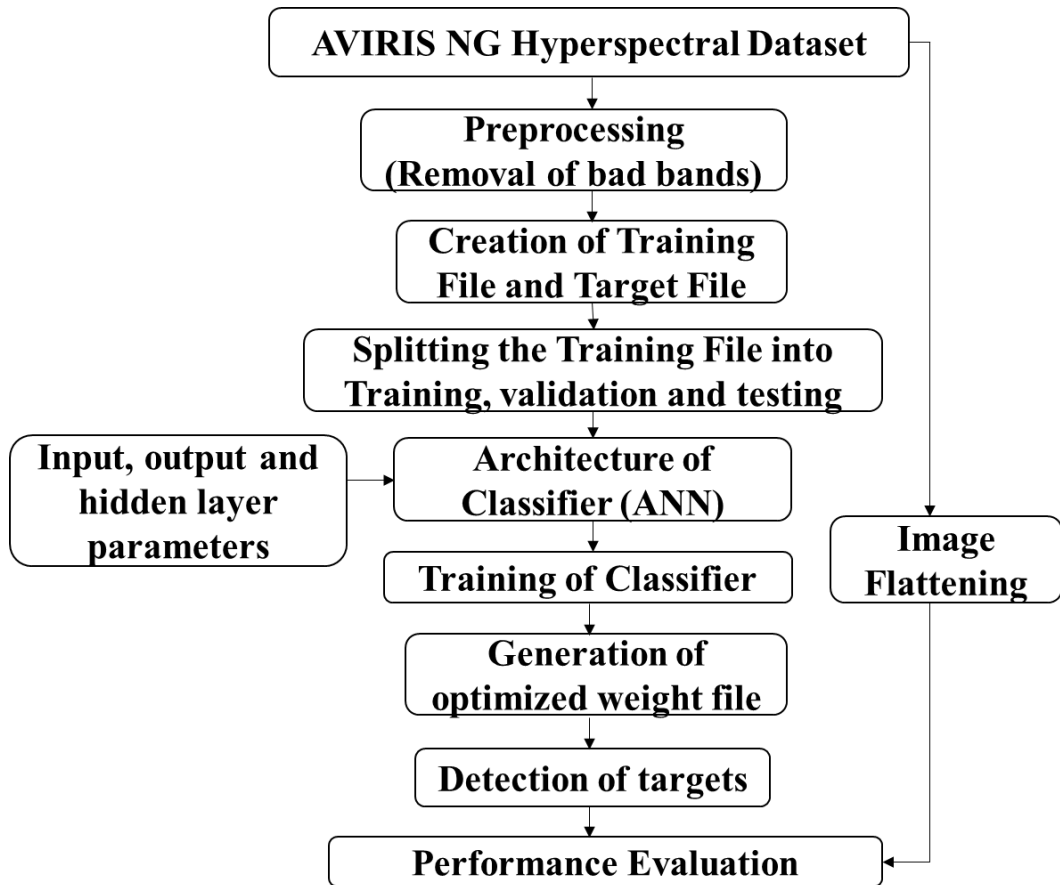


Figure 5.2: Flowchart of the proposed approach

5.5. Results and Discussion

A series of experiments are conducted after combining the spectral and spatial features derived from the hyperspectral data considered, also comparative assessment is carried out. After atmospheric corrections and bad band removal, the data was made ready for extraction of urban targets. Acquisition of field data was also synchronized with AVIRIS-NG airborne data collection. The four morphological operators implemented for detection of roads and roofs along with their accuracy table and resultant imagery are shown in this section. The resultant images are binary in nature, where bright or white pixels indicate the presence of target whereas the dark or black pixels marks the background region.

5.5.1. Detection using Dilation Operator

In case of Dilation, holes smaller than the structuring element are filled and close shapes are connected. The shapes aligning with the structuring element are expanded as the operation behaves like local maximum filter. Pixels are added at inner and outer side of the edges. The value of output calculated is the maximum amongst the considered neighbourhood pixels. *Figure 5.3 and Figure 5.4* show results of detection of roads and roofs respectively with the disk, line, rectangle as structuring element. *Table 5.1 and Table 5.2* shows the accuracy assessment of the same when computed with dilation.

5.5.1.1. Road Detection

By visually interpreting the morphology of roads, they appear to be linear in nature, therefore their extraction is done using three structuring elements. The advantage of using line instead over other structuring elements is reduced computational complexity. Also, morphological operations such as, dilation or erosion

by a line under an arbitrary angle takes only three comparisons per pixel, irrespective of the length of the line, using a recursive algorithm (Hendriks, Luengo and Vliet 2003). A simple structuring element line is selected, but due to curves, variation in height and other parameters, road is not detected with high percentage. The maximum accuracy attained by rectangle of size 2×3 (Refer Figure 5c). It is recommended, to use square or rectangle structuring element to extract shapes from geographic aerial images of a city, which aids in extraction of angular features from the image. Several different elements or different rotations of a singular element in order to extract the desired shapes from the image may be considered. For instance, in order to extract the rectangular roads from remotely sensed data, the rectangular structuring element may be rotated in multiple orientations of the roads within the image (Gumley 2001). The shape and size of the structuring element is defined by the targets to be detected. Further, disk structuring element is readily used to eliminate noise from the image (Maher, *et al.* 2015). Disk as structuring element gave promising results but detection of part of bare soil in the upper right side of Figure 5.3(a) is prominent. Line is not able to detect the cross-section of road properly as compared to other two structuring elements, as shown in Figure 5.3(b).

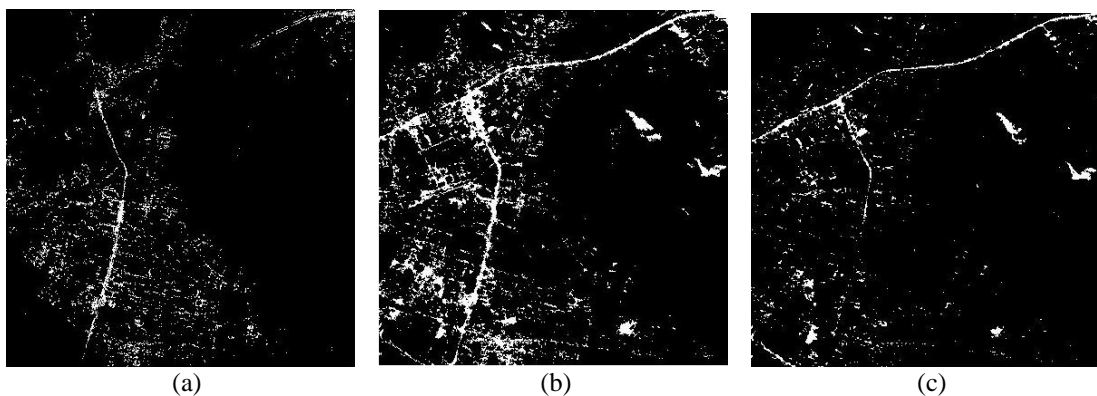


Figure 5.3: Road Detection using Dilation (a) disk (b) line and (c) rectangle

Table 5.1: Accuracy assessment of Roads using Dilation

Target	Spatial Operation	DILATION			
	Structuring Element	Training	Validation	Testing	Overall
Road	Disk	89.20%	85.70%	91.00%	88.63%
	Line	92.80%	70.60%	89.40%	84.27%
	Rectangle	86.90%	94.40%	89.90%	90.40%

Comparing the overall accuracy of detection of roads with reference to disc, line and rectangle structuring elements, the range varies from 84.27% to 90.40%. Rectangle yields the maximum accuracy as it appears to fit the most with linear roads in the considered dataset. Whereas disc and line, gave better training accuracy but the overall accuracy is 88.63% and 84.27% respectively.

5.5.1.2. Roof Detection

Roofs may be of different shapes and sizes, making it difficult to detect. As they are man-made urban surfaces therefore, they have a well-defined boundary which can be extracted using dilation operator which works well with the edges. Here, due to the coarse spatial resolution of the sensor, the roofs appear to be mingled together in *Figure 5.4*. Disk structuring element is able to detect large roofs whereas leaving the smaller ones (*Figure 5.4a*). But in contrast, line structuring element not only is able to differ in between the roof boundaries but is detecting small sized roofs also, as clearly visible in *Figure 5.4(b)*. Rectangle as a reference structure is able to extract the least roof area as compared to other two, as shown in *Figure 5.4(c)*.

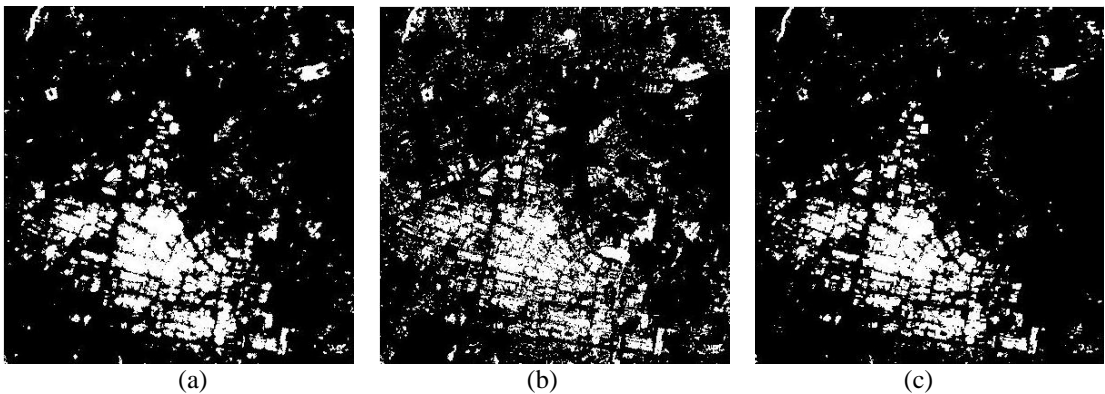
**Figure 5.4:** Roof Detection using Dilation (a) disk (b) line and (c) rectangle

Table 5.2: Accuracy assessment of Roofs using Dilation

Target	Spatial Operation	DILATION			
	Structuring Element	Training	Validation	Testing	Overall
Roof	Disk	77.30%	84.20%	75.90%	79.13%
	Line	85.20%	83.30%	85.40%	84.63%
	Rectangle	80.20%	81.80%	78.80%	80.27%

Table 5.1. and 5.2 evaluates the performance of dilation morphological operator when used with spectral features. The training file formed by their fusion is supplied to ANN to generate the detection accuracy. In case of roads, the maximum detection is given by rectangle operator. The reason may be, the size of this structuring element is taken as 2×3 , which detects the cross-section of roads along with its linear construction. For detection of roofs, the maximum accuracy of 84.63% is given by line. Also, disk and rectangle perform almost similar with an overall accuracy of 79.13% and 80.27% respectively.

5.5.2. Detection of Erosion Operator

Erosion operation is opposite to dilation. Unlike dilation, erosion is used to reduce the size of target objects probed by the selected structuring element. It behaves like a local minimum filter, by shrinking the pixels on the inner and outer boundaries of the target. It enlarges the holes and eliminates connected components smaller than the structuring element. *Figure 5.5 and Figure 5.6* illustrate detection of roads and roofs respectively with the disk, line, rectangle as structuring element. *Table 5.3 and Table 5.4* gives the accuracy assessment chart for erosion operator.

5.5.2.1. Road Detection

The maximum extraction of roads is achieved when disk is used as a structuring element. As seen from *Figure 5.5(a)*, disc can detect street roads as well apart from the highway road which is appearing prominently. Line and rectangle SE's have performed equally well but are not able to highlight the road boundaries in the lower and upper

part of *Figure 5.5(b and c)* respectively. Line structuring element is confusing the part of road with bare soil and is not able to detect roads with smaller width. Since erosion shrinks the target to be detected, therefore a structuring element like disk has performed well in contrast with the other two.

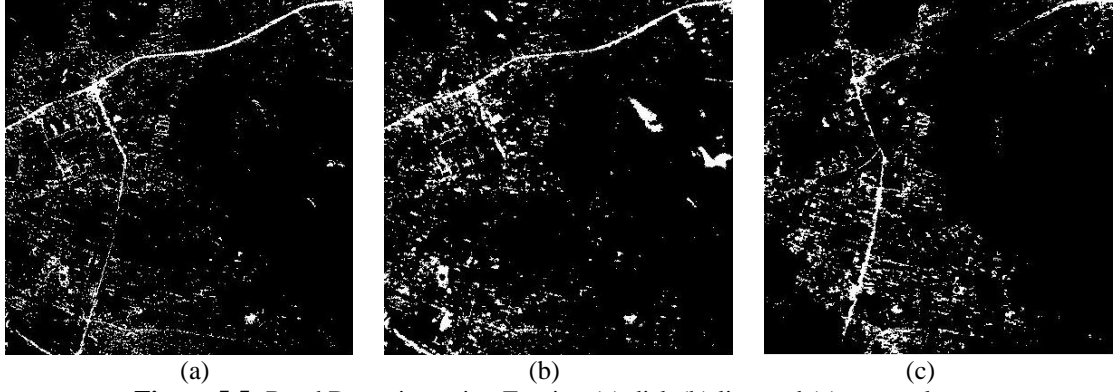


Figure 5.5: Road Detection using Erosion (a) disk (b) line and (c) rectangle

Table 5.3: Accuracy assessment of Roads using erosion

Target	Spatial Operation	EROSION			
	Structuring Element	Training	Validation	Testing	Overall
Road	Disk	92.70%	83.30%	87.60%	87.87%
	Line	87.00%	87.50%	85.10%	86.53%
	Rectangle	87.40%	81.50%	90.70%	86.53%

5.5.2.2. Roof Detection

A portion of small roofs is detected by every structuring element, as they are able to fit with the varying shape and sizes of the roofs present in the scene. By visual examination, disk seems to delineate defined boundaries of roofs but line and rectangle structuring elements are unable to do so, as in *Figure 5.6(a, b, c)*. Erosion operation removes the boundary of the target objects, assigning the minimum value to the central pixel out of all neighbouring pixels. In case of roofs, disk structuring element appears to be suitable to detect them, due to the irregular shape and features.

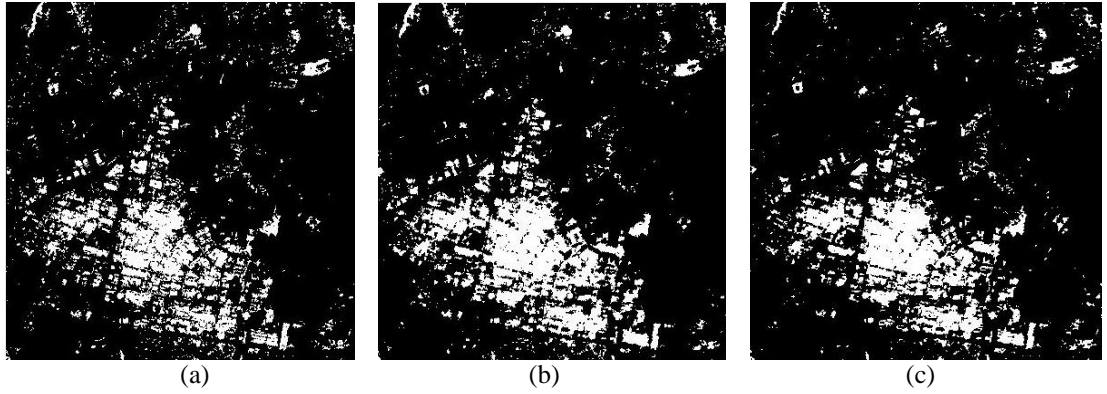


Figure 5.6: Roof Detection using Erosion (a) disk (b) line and (c) rectangle

Table 5.4: Accuracy assessment of Roads and Roofs using erosion

Target	Spatial Operation	EROSION			
	Structuring Element	Training	Validation	Testing	Overall
Roof	Disk	94.40%	94.70%	91.20%	93.43%
	Line	85.60%	85.70%	81.50%	84.27%
	Rectangle	86.50%	91.70%	87.00%	88.40%

The training, validation and testing accuracy for road and roof detection is well distributed and balanced. In case of road the maximum accuracy reaches to 87.87% and for roofs the maximum overall accuracy is 93.43% using disk structuring element. Line and rectangle structuring element ranges between 84.27% to 88.40%. Erosion appears to give better accuracy as compared to dilation operator as it removes the small anomalies. It helps in isolation of individual targets and joining disparate targets in an aerial image.

5.5.3. Detection using Opening operator

Opening is a compound morphological operation in which targets smaller than the structuring element disappear and rest remain unchanged. It combines erosion and dilation in same order, so narrow connections between connected components are removed. This parameter preserves the shape of the target to be detected, therefore useful for detecting the urban targets. This operator erodes an image and then dilates the eroded image using the same structuring element. That is, all foreground image structures that do not contain the structuring element are removed by the opening

morphological operator. The response for a particular target depends upon its interaction with the size of the structuring element. As the size of the considered targets for detection is not exactly known, it is advised to use a multiscale approach based on a range of different sizes of structuring elements instead of using a single size. It helps in building a morphological profile to explore spatial features (Dalla Mura, *et al.* 2010). *Figure 5.7 and 5.8* demonstrates the output of opening operator on roads and roofs separately, followed by the accuracy assessment in *Table 5.5 and 5.6*.

5.5.3.1. Road Detection

Opening operator is known for preserving the shape of the object to be detected. In case of road, a linear structure is extracted in top, but roads with less girth are not highlighted in *Figure 5.7*. Though this operator is successful in not sensing bare soil, as viewed from the previous results. Disk structuring element offers maximum accuracy and a fine centreline of highway in top-most part of *Figure 5.7(a)*. In *Figure 5.7(b,c)* breaks in detection of roads are visible, so narrow roads are not highlighted. Therefore, this operator may be useful in detecting the centreline of roads and not the complete pixels, thereby keeping the shape of the object intact.

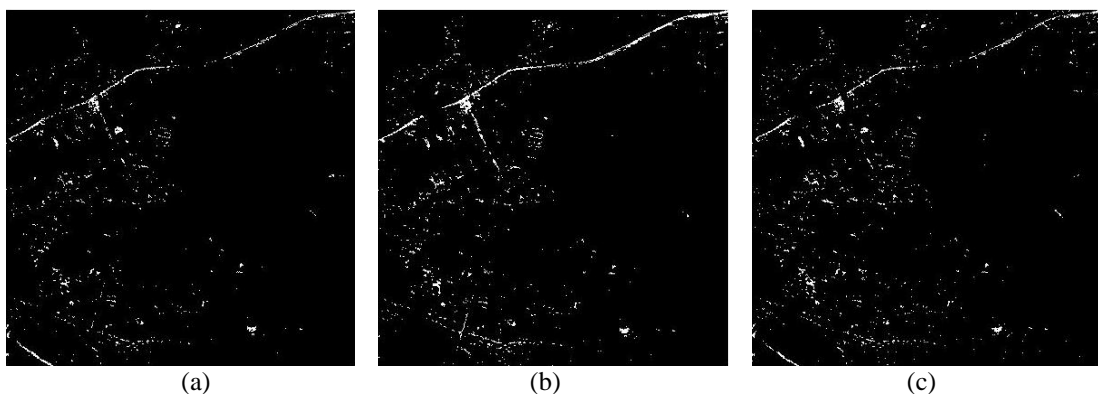


Figure 5.7: Road Detection using Opening (a) disk (b) line and (c) rectangle

Table 5.5: Accuracy assessment of Roads using Opening

Target	Spatial Operation	OPENING			
	Structuring Element	Training	Validation	Testing	Overall
Road	Disk	92.80%	83.30%	92.20%	89.43%
	Line	83.60%	86.70%	88.50%	86.27%

Rectangle	90.10%	73.30%	91.80%	85.07%
------------------	--------	--------	--------	--------

In *Table 5.5*, the overall accuracy using disc structuring element is computed to be maximum, in case of opening. As disc operator fits well for the roads structures for recovering the eroded image and hence yields better accuracy than line and rectangle.

5.5.3.2. Roof Detection

Fusion of spectral signatures with opening morphological operator detected major portions of roof areas in the considered scene. Three variants of structuring elements used, namely disk, line and rectangle gave sufficient accuracy with less false alarms. The first observation is that roofs smaller than the considered structuring elements are not detected. This behaviour is observed due to filtering properties of the opening operator in which the targets are selectively filtered out depending on the selection of the shape and size of structuring element used. Again, disk is able to determine the maximum of roof surfaces with a clear distinction of its boundaries as in *Figure 5.8(a)*. Line and rectangle give reasonable accuracy for roofs (*Figure 5.8a and Figure 5.8b*).

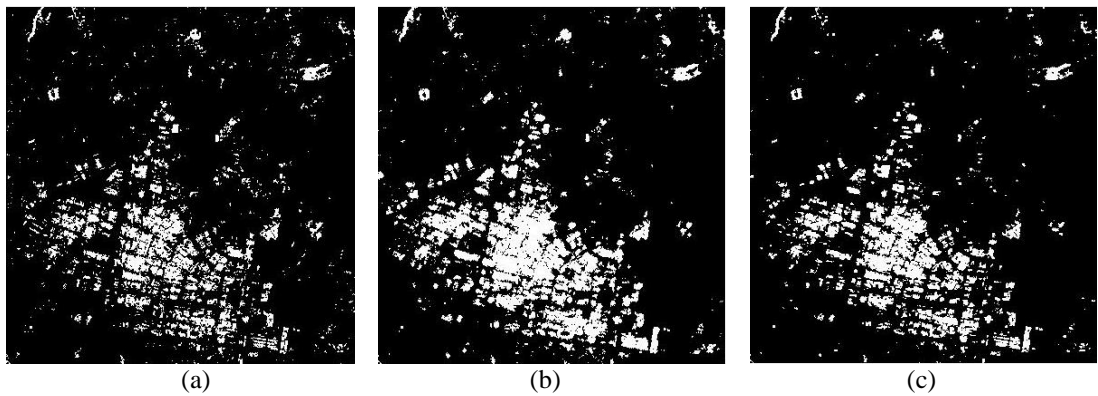


Figure 5.8: Roof Detection using Opening (a) disk (b) line and (c) rectangle

Table 5.6: Accuracy assessment of Roofs using Opening

Target	Spatial Operation	OPENING			
	Structuring Element	Training	Validation	Testing	Overall
Roof	Disk	86.10%	100%	91.30%	92.47%
	Line	83.70%	91.70%	83.70%	86.37%
	Rectangle	85%	100%	87.40%	90.80%

On evaluating the performance of opening morphological operator, roads and roofs give an accuracy range of 86.27% to 92.47%. In both cases, disk structuring element gives the maximum accuracy for the extraction process. This reference shape is able to detect the shape of roads and roofs present in the scene in a precise manner.

5.5.4. Detection using Closing Operator

Here dilation operation is followed by erosion. The operation fills the holes in the regions while keeping the initial region sizes. *Figure 5.9 and Figure 5.10* show detection of roads and roofs respectively with the disk, line, rectangle as structuring element. *Table 5.7 and 5.8* gives road and road detection accuracies when different combinations of morphological operators and structuring elements are applied.

5.5.4.1. Road Detection

Bare soil is detected using disk and rectangle structuring elements on the top right corner of *Figure 5.9(a and c)*. as part of road. But on contrary, line structuring element is able to distinguish road and soil but complete cross-section of road on the left side of the image is not extracted as shown in *Figure 5.8 (b)*. Street roads with narrower boundaries are also detected using disk and rectangle but line structuring element is able to work with this part.

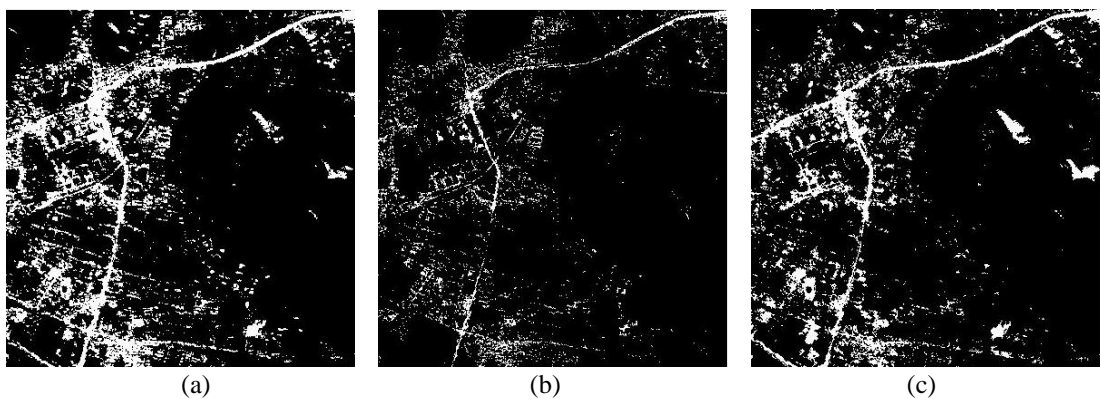


Figure 5.9: Road Detection using Closing (a) disk (b) line and (c) rectangle

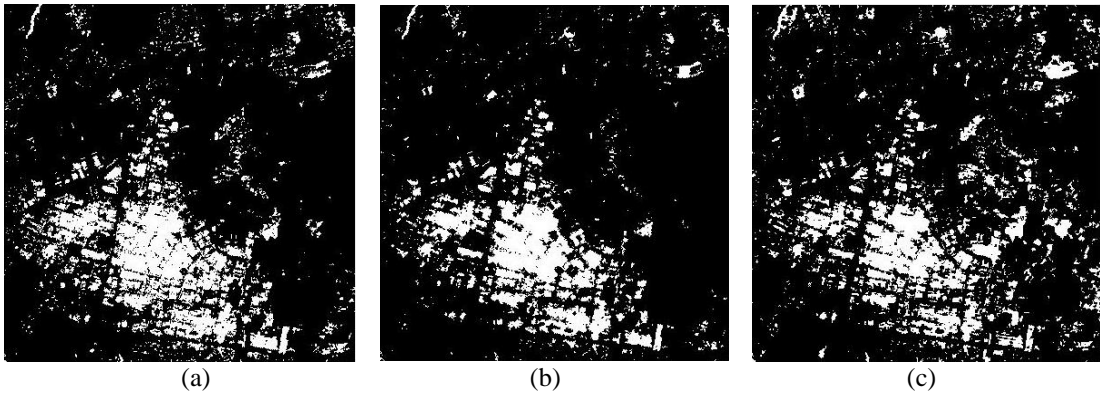
Table 5.7: Accuracy assessment of Roads using Closing

Target	Spatial Operation	CLOSING			
	Structuring Element	Training	Validation	Testing	Overall
Road	Disk	90.10%	100%	88.20%	92.77%
	Line	93%	94.10%	90.20%	92.43%
	Rectangle	87.80%	95.50%	85.70%	89.67%

Referring *Table 5.7*, disk structuring element performs well for road detection using closing operation with 92.77% overall accuracy, whereas line is equally performing well with an accuracy of 92.43%. The reason might be the construction of roads in the considered image dataset are well fitted with disk in case of opening. Also, it appears that, implementing rectangle operator is having some missing parts of roads within its cross-section.

5.5.4.2 Roof Detection

Rectangle is not able to perform with closing operator, leading to a lot of false alarms and detecting surfaces other than roofs as in *Figure 5.9(c)*. Line outdoes as compared to other structuring elements (Refer *Figure 5.9(b)*). Disk also gives a reasonable accuracy as determined visually from *Figure 5.9(a)*. Line is computationally simpler but still it offers better detection than disk and rectangle.

**Figure 5.10:** Roof Detection using Closing (a) disk (b) line and (c) rectangle**Table 5.8:** Accuracy assessment of Roofs using Closing

Target	Spatial Operation	CLOSING			
	Structuring Element	Training	Validation	Testing	Overall
Roof	Disk	87.20%	81.80%	85.50%	84.83%
	Line	86.40%	95%	84.60%	88.67%
	Rectangle	85.20%	78.90%	80.50%	81.53%

Table 5.8. very well identifies the detection mechanism by using opening morphological operator associated with spectral features. The maximum accuracy is offered by disk in case of roads, whereas line seems to be most suitable for roofs. The other reference shapes generate optimum accuracy but with a confused detection of similar materials.

5.6. Summary

A hybrid approach using spectral and spatial properties of hyperspectral data is successfully explored for urban target detection. Roads and roofs are considered as selected targets for study. The work focuses on morphological operations, particularly, Dilation, Erosion, Opening and Closing with three structuring elements disk, line and rectangle for extraction of roads and roofs. Training file containing an average of spectral signatures and considered morphological operator is fed into ANN followed by its implementation for entire hyperspectral data-cube. The approach makes use of neighbouring pixel information and detects the structure of road and roof surfaces. Opening and Closing operations performed well for AVIRIS-NG Udaipur region, with disk as structuring element. The reason for this may be the shape of roads and roofs which fits in the considered disk size. Hyperspectral remote sensing faces a challenge of uniquely identifying targets on spectral grounds but spatial knowledge is an added advantage.

Overall, the spectral-spatial fusion approach when implemented using machine learning for extraction of roads and roofs appears to show better performance.

Chapter 6

Deep learning strategy for detection of engineered objects

Deep learning-based methods are also evolving for target detection due to their exceptional capabilities to learn from voluminous data, extract useful information and predict for the unknown dataset. In the previous chapter, the analysis involved combination of spectral and spatial attributes of hyperspectral data for which handcrafted features have been fed into machine learning network architecture. The results are promising but it involves human intervention for feature selection and extraction. Also, high dimensionality of the data increases the training time, which may be addressed by using suitable dimensionality reduction measures. Deep learning algorithms are having dense architectures catering the automated feature extraction followed by a fully connected classification/detection layer.

6.1. Introduction

Hyperspectral remote sensing is opening new gateways for extraction of urban objects which has gained prominence during the past decade for maintaining a pace with increasing urbanization. Fernando *et al* implemented Gaussian Synapse artificial neural network (ANN) for detection and unmixing of endmembers within hyperspectral images (López, Crespo and Duro 2009). Kernel based target detection techniques have been very popular in extraction of sparse targets, as they can address the issues like curse of dimensionality, less labelled information, atmospheric noise *etc.* Wang and Duan have addressed these research issues by developing an SVM based approach jointly employing spatial, spectral and hierarchical structure information and integrated into the classifier with multiple kernels, on standard datasets (Yi and Duan 2018).

Autoencoders (Windrim, *et al.* 2019), Recurrent Neural Networks (RNN) (Hang, *et al.* 2019) (Mou, Ghamisi and Zhu 2017) , Convolution Neural Networks (CNN) (Hu, *et al.* 2015), Generative Adversarial Networks (GAN) (Shi, Liu and Li. 2017), as part of deep learning approaches have also been exploited in near past for hyperspectral remote sensing.

This part of work presents an alternate method for detection of roads and roofs as engineered surfaces, also referred as urban targets, using convolution neural network in hyperspectral data. The work highlights a brief taxonomy about vertex component analysis which has been used as ground truth image generator instead of spectral unmixing of mixed pixel targets. Convolution neural network has been used as a deep learning measure due to its high prediction capability and its effectiveness over conventional target detection approaches. Principal component Analysis (PCA) is also used for dimensionality reduction because of its simplicity and reduction of implementation time. The work is likely to assist in city planning, sustainable development and various other governmental and non-governmental works related to urban growth.

6.2. Problem Statement

With the advent of high-end equipment and advanced techniques, a lot of data may be captured, with supporting storage capabilities and processing features (Kruse, *et al.* 2000). Multitude of methods use machine learning as foundation, which is continuously evolving field in itself, instigating deep learning approach which works on automated feature extraction, making use of in-depth architectures and capability to deliver end-to-end detection from image to target. However, urban target detection using deep learning approaches in hyperspectral remote sensing, suffers from multiple challenges, mentioned in *Table 6.1*.

Table 6.1: Challenges and research gaps

S No.	Domain	Challenges and Research Gaps
1.	Urban Target Detection	1.1. Major research is focused on natural targets such as vegetation, soil, minerals. 1.2. Small size of urban targets such as roofs, pavements <i>etc.</i> 1.3. Higher within class variability and less inter class variability 1.4. Heterogeneity within urban environment
2.	Hyperspectral remote sensing	2.1. Curse of dimensionality 2.2. Non-availability of corresponding ground truth 2.3. Interference of multiple factors (sensor, scene related and atmospheric factors) 2.4. Spectral variability 2.5. Unavailability of standard datasets
3.	Deep learning approach	3.1. Complex and time-consuming training process 3.2. High computation complexity 3.3. Overfitting of developed model 3.4. Selection of hyper-parameters for high performance 3.5. Blackbox nature of training procedure 3.6. Lack of labelled or known samples

In this chapter, it is proposed to address a subset of aforementioned gaps, such as, (i) heterogeneity in urban cover which makes it difficult to select the exhaustive training dataset to make the network learn; (ii) High number of spectral bands with redundant information; (iii) spectral variability due to locational changes, as the features are selected irrespective of the geographical details; (iv) lack of labelled data to make the architecture learn complex features. Therefore, the novelty of the work lies in the idea of generating the ground reference for an AVIRIS-NG image dataset in first stage followed by dimensionality reduction as second stage and later on extraction of urban surfaces particularly roads and roofs as last stage. The approach used for the study appears to be well suited for urban target detection using hyperspectral data.

6.3. Study Area and Data

The Hyperspectral data analysis is acquired as part of Airborne Visible and Infrared Imaging Spectrometer – Next Generation (AVIRIS-NG) data collection campaign held in February 2016. Level 2 (derived geospatial variables at same resolution and location as Level 1 source data) spatial subset of 400 lines and 400

samples, which constitutes maximum urban area has been selected manually for conducting the set of experiments. For more details, *Chapter 4, Subsection 4.3* can be referred.

6.4. Methodology and Implementation

Removal of bad bands: As part of pre-processing, Level 2 (derived geospatial variables at same resolution and location as Level 1 source data) AVIRIS-NG data having 425 bands is processed and bands severely affected by atmospheric gases and water vapours are removed. A total of 53 bands ranging from 1348-1433 nm in near infrared (NIR) region and 1778-1954 nm in short wave infrared (SWIR) region are not considered for further analysis of hyperspectral imagery. After removal of bad bands, the implementation is carried out on 372 bands.

Selection of endmembers: According to National Geographic Society, urban areas are very developed, meaning there is a density of human structures such as houses, commercial buildings, roads, bridges, and railways. Therefore, a subset of existing infrastructure, that is roads and roofs are chosen as engineered surface targets to be detected. The pure endmembers are selected, considering the V-I-S (Vegetation- impervious surface- soil) model, vegetation and soil are taken as background while road and roofs as targets, therefore other details are masked out leaving only built-up area (Ridd 1995), (Phinn, *et al.* 2002).

Creation of Training File: A training file of size 1600 samples derived from ground data and image is employed for making the network to learn. Wherein, 400 spectra each constitute the reflectance values of roof, road, vegetation and soil respectively. The Training and Testing sets are categorised as 75% and 25% of the total samples individually, where Training set constitutes 1200 and testing set contains 400 known samples. While implementing the algorithm for a

particular target (road or roof), all pixels belonging to other category are treated as background or non-target.

Abundance fractions: The spectral signatures of the endmembers may be chosen from the standard digital spectral libraries, (such as USGS), captured from the field, processed in laboratory or derived from the imagery. The abundance fractions are generated using Dirichlet distribution (Nascimento and Bioucas-Dias 2011), given by Equation 6.1:

$$p(\alpha_1, \alpha_2, \dots, \alpha_p) = \frac{\tau(\mu_1 + \mu_2 + \dots + \mu_p)}{\tau(\mu_1)\tau(\mu_2)\dots\tau(\mu_p)} \times \alpha_1^{\mu_1-1} \alpha_2^{\mu_2-1} \dots \alpha_p^{\mu_p-1} \quad (6.1)$$

Where $0 \leq \alpha_i \leq 1$, $\sum_{i=1}^p \alpha_i = 1$, $E[\alpha_i] = \mu_i / \sum_{k=1}^p \mu_k$ is the expected value of the i^{th} endmember fraction, and $\tau(\cdot)$ denotes the gamma function. Parameter γ is Beta (β_1, β_2) distributed, constructing equation 6.2:

$$p(\gamma) = \left(\frac{\tau(\beta_1 + \beta_2)}{\tau(\beta_1)\tau(\beta_2)} \right) \gamma^{\beta_1-1} (1 - \gamma)^{\beta_2-1} \quad (6.2)$$

Ground Reference Generation: The mean spectral signature is generated for each feature and assumed as pure endmember for generation of ground reference image of the scene under investigation, as shown in *Figure 6.1(a)*. The five-class ground reference displays roads (red), roofs (yellow), vegetation (green), soil (brown) and water (masked in black). The abundance values of the considered endmembers are generated using Dirichlet distribution followed by VCA (mentioned in *Chapter 2, Subsection 2.6.5.2.*) for assigning the label to particular classes. As engineered surfaces, particularly roads and roofs are to be extracted, therefore ground reference with only built-up area is generated for implementation of CNN (refer *Figure 6.1(b)*). Also, ground reference image is georeferenced and overlayed on Google Earth imagery, validated against 59 and

75 locations belonging to roads and roofs respectively (collected during field data acquisition).

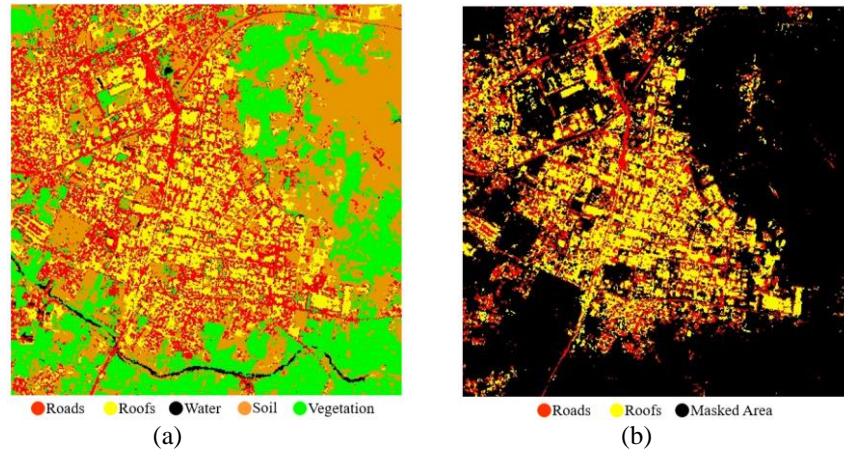


Figure 6.1: (a) Ground Reference generated using VCA for road, roof, vegetation and soil (b) Ground Reference for engineered surfaces (roads and roofs)

Dimensionality reduction using PCA: Higher dimensionality of hyperspectral satellite imagery may lead to computation burden in terms of time and space complexity. PCA transforms the data and reduces it to components contributing maximum for the detection accuracy. Also, neighbouring bands of hyperspectral imagery are highly correlated and often redundant, so optimum combination of bands accounting for variation in terms of target detection are identified. For the proposed work, the number of components is confined to 30, 40 and 50 as the information content is indirectly proportional to the number of principal components because most of the information is comprised in initial bands (Rodarmel and Shan 2002).

Architecture of CNN: For extraction of roads and roofs, supervised CNN is implemented that utilizes spectral data generated from AVIRIS-NG hyperspectral imagery. The complete stage constitutes a convolution layer, non-linear activation operation and a drop-out layer, which is replicated again to formulate a deep network, followed by fully connected layer. The user defined

filter is convolved over a fragment of input data, for identifying features from the previous layers to yield the detected targets. The network is made to learn these features with the supporting non-linear operation, here Rectified Linear Unit (ReLU) trailed by drop-out layer which summarises the output of multiple neurons. Drop-out layer is active during training process while inactive during evaluation acting as a regularization technique. It reduces, (i) overfitting of the network, (ii) superfluous feature dependencies and (iii) spatial size of the output generated. The dropout value is varied with respect to the regularization required, for the initial stage it is set as 0.25 and 0.5 for the later stage.

In order to ensure parallel processing, the image data is alienated into three-dimensional patches of size ' n ' (where $n = 5, 7$ and 9) which are clustered together in form of small batches, acting as initial input to CNN. The layer contains filters of size ' d ' (where $d = 3$), stride ' s ' set as 1 and padding ' p ' of size 2, with ReLu function to be performed. After another replication, the output generated is flattened and sent to the fully connected layer. For the current work, two fully connected layers are taken generating the output with a dropout layer of rate 0.25 and 0.5 respectively.

The labelled spectral data is split in ratio 75:25, where 75% of the complete data constitutes the training file and 25% is the testing ratio. Other hyper parameters encompassing, learning rate is set as 0.0001, momentum as 0.9, epoch as 15. Training parameters like performance error, epochs, momentum, learning rate, *etc.* have been tuned by trial and error in order to improve accuracy of the network. The architecture is explained in *Figure 6.2*.

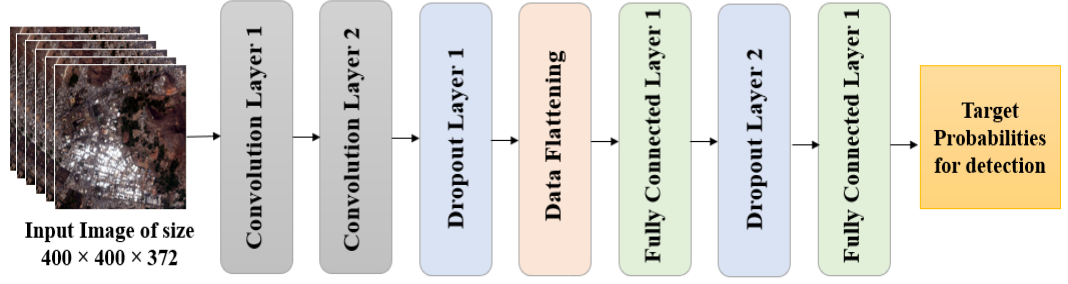


Figure 6.2: CNN Architecture for the proposed approach

Performance Analysis: The performance evaluation metrics used to evaluate the approach are precision, recall and F1 along with binary output images, where bright pixels represent the presence of target (road or roof) and dark pixels depict the non-target or background region. True positive (TP) and true negatives (TN) are the observations that are correctly predicted to minimize false positives (FP) and false negatives (FN). Precision is the ratio of correctly predicted positive targets to the total predicted positive observations. Recall is the ratio of correctly predicted positive observations to the all observations in actual class. F1 Score is the weighted average of Precision and Recall as it helps in balancing the both parameters. The equations supporting them as given from *Equation numbers 6.3 to 6.5* (Davis and Goadrich 2006).

$$Precision = \frac{TP}{TP+FP} \quad (6.3)$$

$$Recall = \frac{TP}{TP+FN} \quad (6.4)$$

$$F1 = 2 * (Recall \times Precision) / (Recall + Precision) \quad (6.5)$$

Implementation: The software used to carry out VCA for generation of ground reference image is MATLAB 2018b (the code is from (MP and Dias 2005)- is reproduced) and Python is used for implementation of CNN using keras library (the code from (Makantasis 2015) is amended for the area of interest). The architecture is implemented using Intel® Core™ i7-8550U CPU with 16 GB

RAM, NVIDIA GeForce MX130. The block diagram of the implementation is shown in *Figure 6.3*.

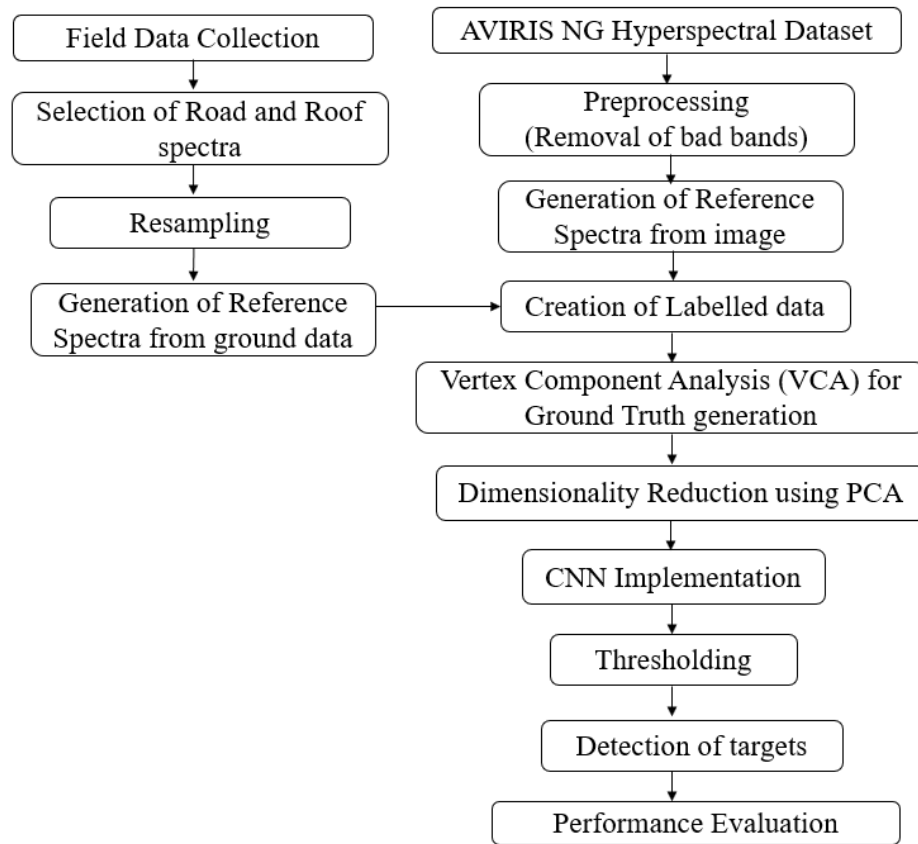


Figure 6.3: Block Diagram of Methodology

6.5. Results and Discussion

The common inferences that may be drawn from the literature is that, challenges like spectral similarity, spectral variability still affect hyperspectral data. In reference to road extraction, deep learning approaches are yet to be explored, for advantages such as, automatic learning from the data. The analysis and approach for detection of roads and roofs is presented in this section along with the accuracy table and the resultant imagery. The white pixels appearing in different images correspond to the presence of targets whereas the black pixels represent non-target or background.

6.5.1. Detection of Roads

The images in *Figure 6.4* in different window sizes show the results obtained in different window size (5,7 and 9) with varying PCA components (30,40 and 50) and the prediction of each pixel has been performed by assigning values as 1 for target and 0 for non-target class.

6.5.1.1. Window Size 5×5

The overall accuracy for considering the window size as 5, results into a balance between precision and recall (*Table 6.2*), the street roads along with major roads are detected in the area considered, whereas some traces of bare soil are also detected. Still, CNN is widely used for image recognition because it is invariant to small rotation and shifts (Hinton 2012). Varying the PCA components from 30, 40 and then to 50 does not bring any noticeable change in the illustrated results in *Figure 6.4 (a, b, c)* and also in accuracy assessment. The F1-score is 0.92 for 30 and 50 components, it reduces to 0.91 for 40 components under the influence of precision and recall value. PCA is linear transformation technique which effectively computes variance from multiple channels to a new set of uncorrelated bands with maximized data variance, therefore a suitable number of PC bands should be determined for an efficient dimensionality reduction of hyperspectral imagery (Sun, Liu and Fu 2017). Since, the variance beyond 30 bands is varying but still remains above 0.90, hence we may opt for minimum number of bands.



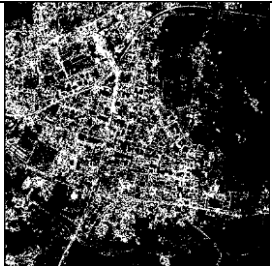



6.5.1.2. Window Size 7×7

For detection of roads, window size of 7×7 with 50 components seems to give the maximum value for performance evaluation parameters (*Refer Table 6.2 and Figure 6.4 (d, e, f)*). The reason articulated for this is that roads belong to linear features and due to spatial resolution of the AVIRIS-NG sensor the roads are best detected in 7×7 window size, whereas there is very less perceptible decrease in accuracy corresponding

to 5×5 and 9×9 window. The complex variations in urban materials make pixel by pixel analysis difficult, therefore such robust and invariant features are required. Unlike Zhang *et al* who took a window size of 3×3 with lowest root mean square error (RMSE) for urban dataset (<https://rslab.ut.ac.ir/data>) using their approach to apply pixel based and cube-based CNN (Zhang, *et al.* 2018).

6.5.1.3. Window Size 9×9

The visual examination of the resultant images indicate that the spectra based detection of roads leads to detection of several additional features having similar spectra (Figure 6.4 (g, h, i)) and this significantly affects detection of road pixels. PCA is introduced to abridge the whole image which reduces the data dimension to an acceptable scale (here, 30, 40 and 50 components). The analysis of the number of PCA components gives another observation that the increase in components do not lead to any improvement in the accuracy primarily because most of the relevant variance is captured in the first few bands itself.

S No	Window Size	PCA Components = 30	PCA Components = 40	PCA Components = 50
1	5×5			
2	7×7			

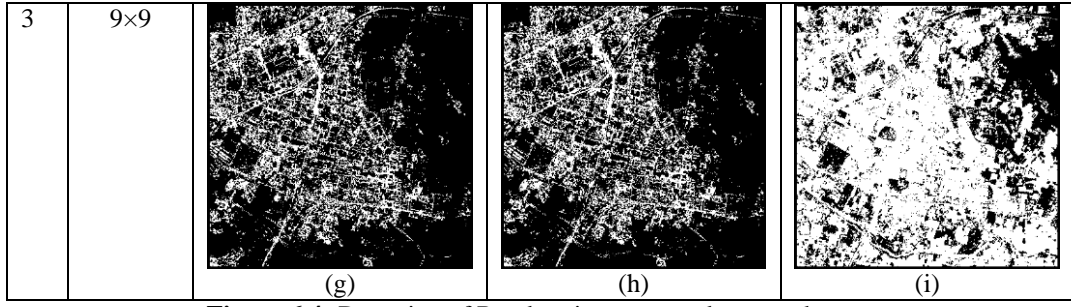


Figure 6.4: Detection of Roads using proposed approach

Table 6.2: Accuracy assessment for road detection using proposed approach

S No	Window Size	PCA Components	Road		
			Precision	Recall	F1
1	5×5	30	0.93	0.90	0.92
		40	0.94	0.89	0.91
		50	0.92	0.91	0.92
2	7×7	30	0.92	0.89	0.90
		40	0.92	0.91	0.92
		50	0.94	0.89	0.92
3	9×9	30	0.90	0.88	0.89
		40	0.90	0.90	0.90
		50	0.34	1.00	0.51

On visual examination, less variation is observed in the resultant images while changing the window size. The proposed CNN based approach has consistent performance but has few pixels of roads confused with soil pixels at certain locations. It detects patches of soil along with extraction of roads on top right side of the images (Figure 6.4). Since the material used for construction of roads may include soil, therefore it is detected at some parts. One of the major challenges in target detection for hyperspectral imagery include presence of targets in different sizes, different orientations and at very close positions (Khan, *et al.* 2017). Also, CNN exploits the advantage of large data samples, which require more computational resources to extract features for better data fitting and higher detection performance (Zhang, *et al.* 2020). Therefore, at the time of implementation, though the training time is compromised but the method effectively improves the detection rate.

6.5.2. Detection of Roofs

The visual analysis of the images illustrated in *Figure 6.5* represents detection of roofs as clusters in urban areas, using CNN and *Table 6.3* shows the corresponding performance evaluation metrics.

6.5.2.1. Window size 5×5

Window size of 5 with 30 components appears to be the most suitable for extraction of roofs for the current dataset used for the study (*Figure 6.5 (a, b, c) and Table 6.3*). Roofs appear in the form of clusters; therefore, smaller size window is able to detect most of them. Also, the computation time for smaller window and a smaller number of components is comparatively low in contrast with other experiments considered. Sun *et al.* have proposed to extract impervious surfaces with 3D – CNN using WorldView-2 and airborne LiDAR data with a Producer's Accuracy (PA) maximum of 91% for combined of impervious surfaces (Sun, *et al.* 2019). In contrast, the maximum F1 value generated for roof detection for this approach and dataset is estimated as 0.93.

6.5.2.2. Window size 7×7

The window size of 7 also shows similar results for detecting roof surfaces on visual examination, as given in *Figure 6.5 (d, e, f)*. Roof being high albedo reflects maximum energy falling on them, creating a confusion with other features such as barren lands, which might get detected additionally in big window sizes.

6.5.2.3. Window size 9×9

The window of size 9 appears to be large for detecting the small roofs when number of components are increased to 50 as demonstrated in *Figure 6.5 (i)*. PCA components 30 and 40 shows marginal difference in detection (*Table 6.3*).









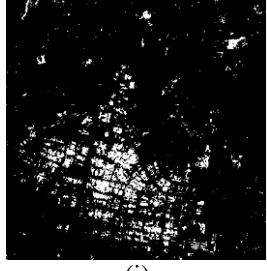
S No	Window Size	PCA Components = 30	PCA Components = 40	PCA Components = 50
1	5×5			
		(a)	(b)	(c)
2	7×7			
		(d)	(e)	(f)
3	9×9			
		(g)	(h)	(i)

Figure 6.5: Detection of roof using proposed approach

Table 6.3: Accuracy Assessment of roof detection using proposed approach

S No	Window Size	PCA Components	Roof		
			Precision	Recall	F1
1	5×5	30	0.93	0.94	0.93
		40	0.91	0.95	0.93
		50	0.93	0.93	0.93
2	7×7	30	0.91	0.92	0.92
		40	0.93	0.93	0.93
		50	0.91	0.96	0.93
3	9×9	30	0.91	0.91	0.91
		40	0.92	0.91	0.92
		50	0.89	0.84	0.82

In this work, a CNN network has been evolved for detection of road and roof pixels which is easy to implement, can be used for large datasets with minimal human intervention, can generate high accuracy and can be used for different datasets without much additional training. However, it may be noted that with increase in window size, computation burden in terms of time complexity also intensifies.

6.6. Summary

This work presents an approach for extraction of engineered surfaces using hyperspectral data. The problem of extraction of roads and roofs has been successfully dealt using deep learning approach. VCA algorithm which is used for spectral unmixing as reported in literature, is used for generating the ground reference which is further supplied to CNN as input. In this work, CNN has been implemented using recently acquired hyperspectral AVIRIS- NG data of Udaipur region in India.

The algorithm has been compared under three categories of window sizes, (i) 5×5 (ii) 7×7 (iii) 9×9 where roads and roofs have been treated as targets. It is observed that increase in the window size (5, 7, 9) often degrades the performance of the target detector. Also varying the number of components from 30, 40 to 50 further decreases the precision and recall value. By visual examination of the results, the highway roads, street roads made up of asphalt, bitumen are mostly detected, whereas unmetalled or soil dominated roads are confused with bare soil. Besides, the spatial resolution of data used in these experiments is 8.1 meters and this might be insufficient for detection of engineered surfaces as their scale is much smaller. A sharp delineating boundary between roads and roofs is therefore not seen/detected in the resultant mages.

Deep learning methods appear to be more attractive and show their tremendous potential in detecting targets with less execution time and high accuracy rate. Their learning ability from labelled data and prediction for unlabelled data make them outperform. Overall, experimentation appears to perform uniformly, for detection of roads and roofs. Apart from this, material used for construction of roads and roofs is also similar, such as concrete, asphalt, bitumen which could be regarded as another reason for lesser detection rate in some cases. Removal of redundant bands is needed to realize a better target detection system. Dimensionality reduction methods, other than

PCA can also be explored for decreasing the computation time for implementation. Also, in traditional spectral matching and machine learning methods, which work on supervised approach with *a priori* knowledge of spectral signatures and derived features which include high amount of involvement of analyst, unlike deep learning techniques that automate the complete process followed by fully connected classification or detection layer.

It is observed that consideration of only spectral aspect leads to confusion in classes made up of similar materials, therefore spatial attributes which exhibit strong dependencies in hyperspectral data should also be considered for enhanced detection. The study is also bounded till detection of roads and roofs only, further their condition with respect to aging can also be determined. The proposed approach assumes targets as full pixel; however, mixed pixels are also encountered during aerial data collection due to sensor configuration. In recent times, many feature selection and extraction techniques have been developed which can be used in association of deep learning measures for real-time processing of data.

Chapter 7

Shape Identification of engineered objects using spectral and shape-based features

Hyperspectral imagery holds spectral and spatial (locational details) attributes making it a rich source of information for applications like target detection, forestry, agriculture, urban areas and many more. As the last chapter focuses on automatic extraction of features to delineate road and roof surfaces, there lies a need to extract defined shapes and boundaries of the considered targets. Associating spatial aspect, such as inclusion of morphological, textural features along with spectral details, often helps in increasing the detection rate. The study provides an insight of extraction of shape-based features fused with the spectral characteristics for detection of urban targets particularly roads and roofs.

7.1. Introduction

The present work focusses on exploitation of shape-based features, based on standard deviation and range of the neighboring pixels for detection of urban targets (roads and roofs). These methods can accommodate spatial information in terms of shape of the target and enhance the desired response by overpowering the background. The analysis is three-fold, at first only spectral features are trained and investigated by variants (Linear, Quadratic, Cubic and Gaussian) of SVM, followed by shape features and lastly, both of them are fused together to increase the detection accuracy. These features are described in succeeding paragraphs:

Spectral Features: A spectral pixel vector x_i constitutes all the pixel values in third domain, $x_{1i}, x_{2i}, \dots, x_{Ni}$ at every corresponding spatial location of hyperspectral data cube, where N is the total number of pixels. For a hyperspectral image having r

rows and c columns, then the number of image vectors present would be $N = r \times c$.

Equation 7.1 represents the hyperspectral data in higher dimension,

$$\{x_i\}_{i=1}^N, x_i \in \mathbb{R}^d \quad (7.1)$$

Where, d is the number of spectral bands. This implies that the dimension of every spectral feature is $1 \times d$, as shown in *Figure 7.1*.

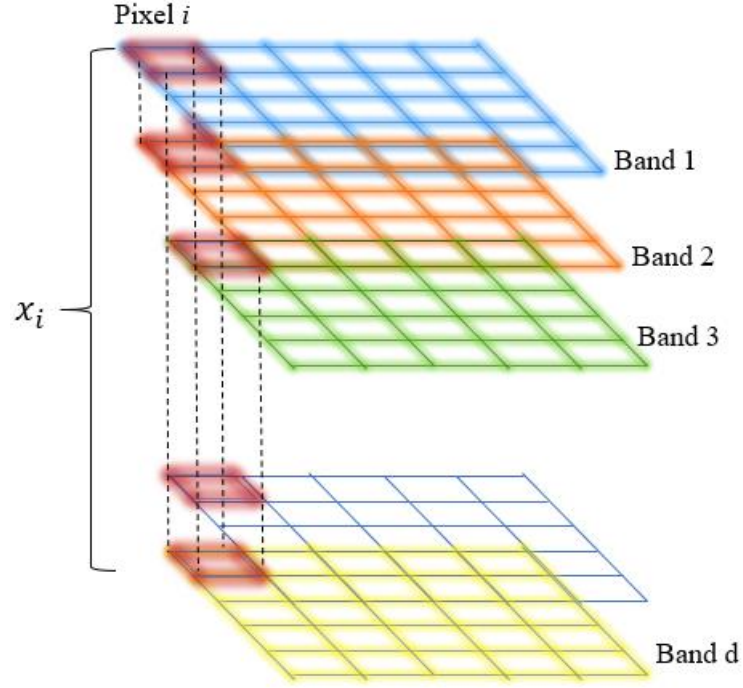


Figure 7.1: Three-dimensional hyperspectral data cube depicting pixel vector

Here, x_i denotes a spectral signature of a particular pixel i , which holds the reflectance value at every wavelength yielding a spectral plot. The techniques that use spectral details derived from pixels are known as spectral or pixel-based methods. SAM is one such approach which computes spectral angle similarity between the reference and the target spectra (Zhang and L. 2014) and other similar techniques are discussed in *Chapter 2, Subsection 2.6.1.2*. These techniques are computationally simple and provide an easy way for extraction of information through spectral component of hyperspectral data.

Shape Features: Shape features are part of the spatial component in hyperspectral imagery, which further includes texture, size, morphological operators calculated with respect to the neighbouring pixels. Han *et al.* proposed shape-size index (SSI) which combines homogeneous areas between one central pixel and its neighbouring pixels using spectral similarity for multispectral images (Youkyung, *et al.* 2012). Grey level co-occurrence matrix (GLCM) (Robert, Shanmugam and Dinstein 1973) is one of the common spatial texture extraction approaches which transforms the grey scale value of an image by various statistical measures like homogeneity, energy, entropy and contrast. Another technique mentioned in literature for performing shape-based analysis is Histogram of Oriented Gradient (HoG) (Navneet and Triggs 2005). Farooq *et al.* used HoG features for automatic grass weed detection and classification in hyperspectral data (Adnan, Jia and Zhou 2019). The methods proposed for the study to extract shape are based on standard deviation and range of the central pixel with the neighboring pixels instead of other geometric shapes which are unable to fit the asymmetric urban targets (roads and roofs). *Table 7.1* gives a brief description about these features, each of them considers a window of a size s , where $s = 3, 5, 7$ and so on.

Table 7.1: Shape extraction features used

S No.	Shape Extraction Feature	Description	Formula
1.	Standard deviation	<ul style="list-style-type: none"> The value of output pixel is the standard deviation of neighborhood window of size $s \times s$ around the corresponding input pixel. Brighter pixels in the output image corresponds to the higher standard deviation thus extracting the shape of the target. The central element of the neighborhood is computed as $\text{floor}((\text{size}(s) + 1)/2)$ 	$\sqrt{\frac{\sum (x_i - x)^2}{s * s - 1}}$ <p>Where, x_i is the individual pixel value of input; x is the mean value of pixels; s is the neighborhood size.</p>
2.	Range	<ul style="list-style-type: none"> The value of output pixel is the range (maximum – minimum) of neighborhood window of size $s \times s$ 	$\delta_E(X) = \{x \in R^D \mid E_x \cap X \neq \emptyset\}$ $\varepsilon_E(X) = \{x \in R^D \mid E_x \subseteq X\}$ $\text{Range} = \delta_E - \varepsilon_E$

<p>s around the corresponding input pixel.</p> <ul style="list-style-type: none"> • Pixels having greater values of difference belongs to other feature class, discriminating the target from the background. • Range is calculated by dilation and erosion morphological attributes. 	<p>Where,</p> <p>δ_E – Dilation with respect to Structuring Element E</p> <p>ε_E – Erosion with respect to Structuring Element E</p> <p>X – Image on which dilation is performed</p> <p>x – Origin where the locus of points is taken</p>
---	--

Fusion of spectral and shape-based features: Using either spectral or spatial component of hyperspectral data does not completely exploit the rich information it stores. Particularly for urban areas, integrating spectral and spatial information is necessary, as spectral component helps in classification of heterogeneous materials and spatial component delineates the shape of roads and roofs. Fauvel *et al.* proposed a method based on fusion of morphological information and original hyperspectral data by concatenating the two vectors into single feature vector followed by classification of urban data using SVM (Mathieu, *et al.* 2008). Fusing spectral and spatial aspect of hyperspectral data is not only limited to classification but mixed pixel characterization is also addressed in the literature (Mahdi, *et al.* 2014). Recently deep learning approaches have also been presented for better classification accuracies as they automatically learn high level features from the image itself (Wenzhi and Du 2016).

SVM and its variants: These can be used to analyse spectral, shape and fused features. The key advantage that SVM has over other machine learning algorithms is that the features can be transfigured using multiple kernel functions (Farid and Bruzzone 2004). The kernel enables the data to be mapped (dot product of two vectors) in preferably higher dimension where it is assumed that, the features may be separated by a linear boundary. This technique enhances the capability of SVM and makes it feasible for multi-class problems also. The computational complexity increases in case of the kernel functions, where the samples are transformed into higher dimensions, and it also

dependent on the number of samples (Savas and Dosis 2019). Each kernel function must be tuned to obtain the best result performance (Zhang and Wu 2012).

By setting different values of degrees for polynomial kernels different number of feature combinations can be considered unlike linear kernel. If degree of the polynomial kernel is set as 1 then this method behaves like linear kernel approach. In data, where it is not possible to have a decision surface defined by the linear equations, then the technique may be extended to allow for non-linear decision surfaces. Further to optimize it, the kernel function is computed to move the training data into a higher-dimensional feature space to find a larger margin for data separation. Numerous kernels are explored in the literature, but it is difficult to choose the one with best generalisation. The selected kernel method and the parameters chosen for the implementation of SVM affects the accuracy rate.

Pal has used five categories of kernel methods (linear, polynomial, Radial Basis Function (RBF), linear spline and sigmoid kernel) to investigate their effect on classification accuracy using remotely sensed data (Mahesh, Factors influencing the accuracy of remote sensing classifications a comparative study 2002). Later, Camps-Valls *et al.* proposed new kernels addressing spatial and spectral characteristics of remotely sensed data for generating the land cover thematic maps (Camps-Valls, *et al.* 2006). Researchers have also used a modified kernel approach that considers the spectral similarity (spectral angle) between support vectors for hyperspectral data (Mercier 2003) (F. a. Melgani 2004).

The linear kernel is used when the samples considered are linearly separable. To consider nonlinear relationship between the features, polynomial kernel may be used as degree controls the flexibility of the classifier/target detector. The Gaussian kernel can be fine, medium and coarse depending upon the distinctions within the classes

depending upon the kernel scale set. The kernel functions used for the current work are tabulated in *Table 7.2* with their description.

Table 7.2: SVM and its variants with kernel functions

S No.	Type of SVM	Variants	Details	Kernel Functions
1.	Linear (Melgani and Bruzzone 2004)	-	A single hyperplane holds the efficiency to classify the two classes, but the optimal decision boundary is required to maximize the margin between them.	$K(x_i, x_j) = x_i^T \cdot x_j$ x_i = feature vector 1 x_j = feature vector 2 x^T = transpose
2.	Polynomial (M. J. Fauvel 2009)	Quadratic	Kernel trick refers to calculating the dot product of feature vectors. Here the degree is 2.	$K(x_i, x_j) = (x_i^T \cdot x_j + 1)^d$
		Cubic	Here the power is increased as 3.	Value of d is 3
3.	Gaussian (M. J. Fauvel 2008)		The value depends upon the distance of any data point to the margin. Highly effective when no knowledge of data is there	$K(x_i, x_j)$ $= \exp\left(-\frac{\ x_i - x_j\ ^2}{2\sigma^2}\right)$ σ = width of kernel

7.2. Problem Statement

Researchers have tried to classify different roof materials using hyperspectral data by creating spectral library of various materials used for urban roofs followed by their detection using multiple supervised approaches, which lacks shape aspect. The shape features used are rectangular or quadratic for smaller buildings which cannot be generalised for complete area under consideration. No standard approach for mapping road surfaces is available. Though some researchers have emphasized extraction of road centreline, but still, it is difficult to differentiate them on spectral grounds. Therefore, in this work, two shape based features are proposed which are based on standard deviation and range of the surrounding pixels to extract roads and roofs along with the spectral features.

7.3. Study area and data

The Hyperspectral data is acquired as part of Airborne Visible and Infrared Imaging Spectrometer – Next Generation (AVIRIS-NG) data collection campaign held in February 2016. This is a joint mission between Jet Propulsion Laboratory (JPL), NASA and Indian Space Research Organization (ISRO) collecting data in 27 regions of India over different types of terrain (forests, agricultural land, urban, waterbodies, snow and glaciers). More details can be found in *Chapter 3 and Chapter 4, Subsection 4.3*.

7.4. Methodology and Implementation

The steps involved in implementing the proposed approach are mentioned in this section.

Pre-processing: In this phase, the atmospherically corrected Level 2 AVIRIS-NG data comprising of 425 spectral bands is processed to get a transformed hypercube having 387 bands. Here, the bands affected by water vapors, atmospheric gases and noise are removed and then the implementation is carried out.

Spectral based features: In order to preserve the of hyperspectral data, no dimensionality reduction methods are applied for the analysis of hyperspectral data. Spectral signature belonging to every class is extracted at pixel level, yielding a feature vector of size $1 \times d$, where d is the number of bands.

Shape based features: Standard deviation and range are chosen as spatial features for detection of considered urban targets, roads and roofs. Both the features work locally on small window sizes exploiting the spatial attribute of hyperspectral data. These features are computed band-wise for detecting the

shapes of prominent targets, later the computation is done at pixel level. *Figure 7.2.* gives a brief idea about the shape feature extraction process.

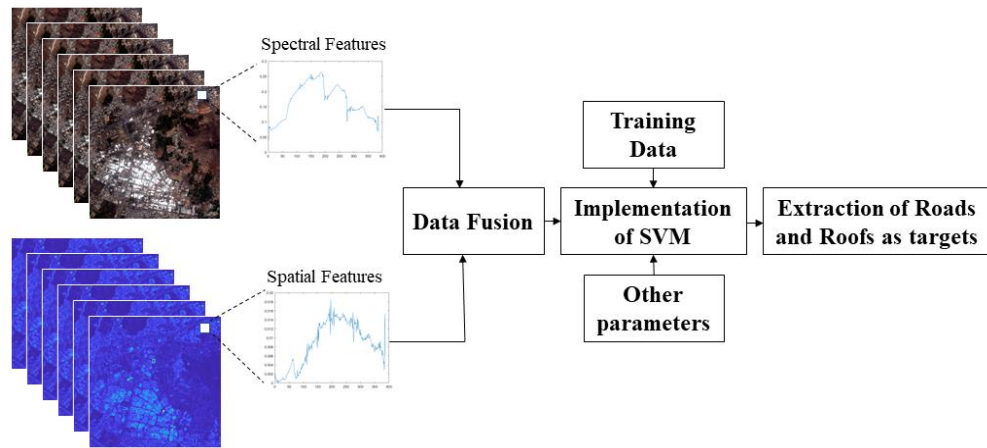


Figure 7.2: Fusion of spectral and spatial features

Training file generation: There are three different training files used for the study comprising of spectral, shape and fused feature vectors belonging to each class considering Vegetation, Impervious surfaces and Soil (VIS Model). Each training file contains 2000 labelled samples of vegetation, imperious surfaces (roads and roofs) and soil surface, where every individual category has 500 observations. The first training file contains only the spectral information, the second training file comprises of the shape attributes and the third one has the average of spectral and shape-based feature considered for a particular pixel. Other pixels encompassing water, bare lands are already masked out by visually interpreting the image data, field examination and validating the geo-locations from Google Earth software.

SVM Implementation: The previously generated training files are set as an input for SVM model for its learning step followed by applying the result to the complete image for detecting the presence of urban targets. Cross-validation is set to avoid overfitting by partitioning the training dataset into k-folds, and value of k is kept as 5.

Performance Evaluation: The experiments are designed to evaluate the results using the spectral, shape and fused features to evaluate the accuracy by taking into account the variants of SVM (Linear, polynomial and gaussian). An exhaustive comparative assessment has been performed between different kernel methods with respect to spectral, spatial and combined features; to extract the urban targets and explore the suitable approach for the same. The flow chart of the approach and the detailed steps are shown in *Figure 7.3*.

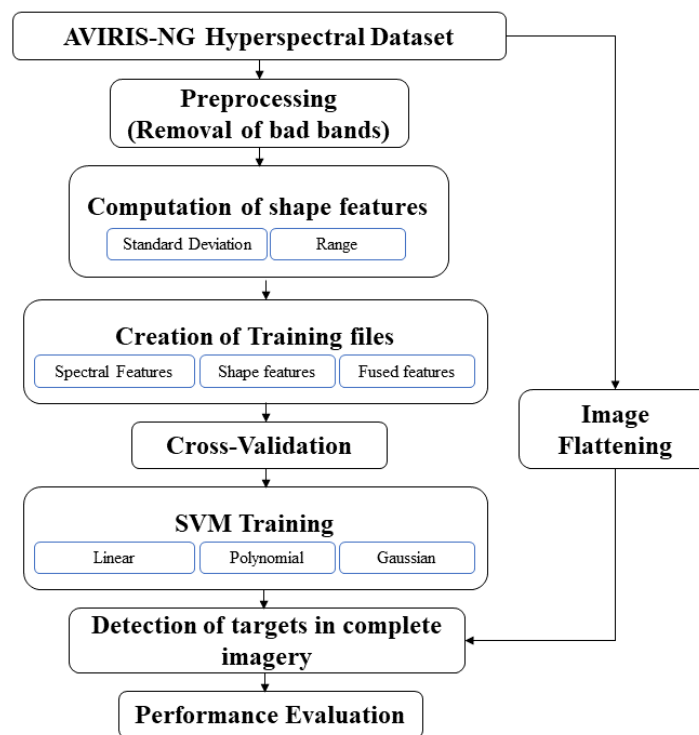


Figure 7.3: Flow chart of the proposed Approach

7.5. Results and Discussion

The approach mentioned above is implemented successfully and the results are presented in this section. The work is an improvement in detection of urban targets using spectral and spatial components of hyperspectral data. This study is an attempt to analyse AVIRIS-NG data collected during the joint campaign and unfurl the treasure the information stored in it. As mentioned, with advent of new materials being used for built-up surfaces paves way for other challenges to be addressed, therefore this work

has been carried out to exploit AVIRIS-NG hyperspectral dataset for urban analysis. This part deals with three set of experiments based on the training files created, that is, Spectral Features, Shape Features and Fused features (spectral and spatial both). Shape features are again computed using two local windowing methods, standard deviation and range. All three training files are then fed into kernel variants of SVM (Linear, polynomial with degree 2 and 3, Gaussian) to generate road and roof extraction results. In the images shown in this section, the white pixels correspond to the presence of targets whereas the black pixels represent background pixels. The software used in this work are ENVI 4.8 and MATLAB 2018b along with a system configuration of 16GB RAM, with Intel i7 processor.

7.5.1. Urban target detection using spectral features

The spectral signatures at multiple confirmed locations belonging to roads and roofs are extracted from the image itself to create the training file. Ground data spectral collection was synchronized with the hyperspectral airborne campaign; therefore, the labelled data is created, taking the geo-locations of urban targets as reference. The resultant images are shown in *Figure 7.4* and the corresponding accuracies are shown in *Table 7.3*.

Table 7.3: Accuracy Assessment using spectral features

Linear SVM	Polynomial SVM		Gaussian SVM		
	Quadratic	Cubic	Fine	Medium	Coarse
89.1%	89.6%	89.8%	88.2%	88.4%	87.9%

When the spectral signatures are given as input, the variation in accuracies by using different kernel methods for SVM vary in the range of 87.9% to 89.8% (*Table 7.3*). Wherever the difference in the spectra of roads and roofs is prominent in the captured training samples, the detection of road and roof pixels are also distinctly accurate. However, wherever there is confusion between the spectra of road and roof,

the detection of road and roof pixels is also poor (*Refer Figure 7.4(c)*). Linear SVM performs well as compared to Gaussian kernel with an accuracy of 89.1%. While increasing the degree of polynomial kernel from 2 to 3, increases the accuracy from 89.6% to 89.8%. Though the differences in the accuracy of the implemented kernel methods seem not to be at a considerable level, the method that provides higher accuracy gains importance. All the models perform equally consistent and later the trained model with maximum accuracy (here, cubic – *Refer Table 7.3*) is used for extraction of roads and roofs from the hyperspectral subset of Udaipur region.

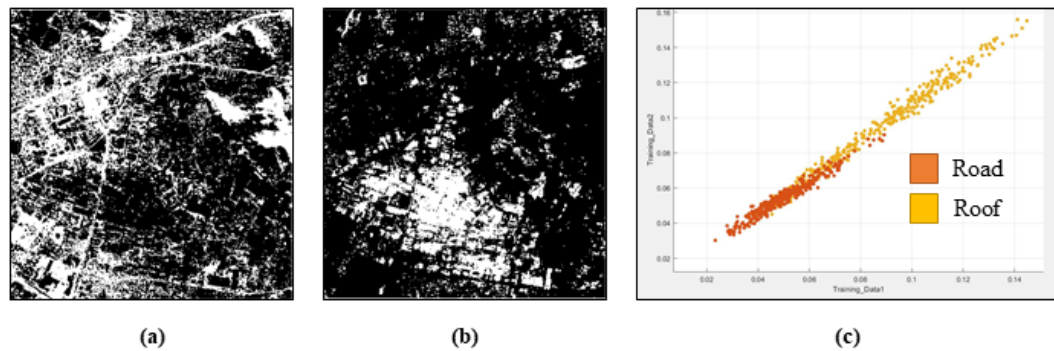


Figure 7.4: Spectral Approach (a) Detection of Roads (b) Detection of Roofs (c) Scatter plot for both urban targets

The immediate observation that can be made by visually interpretation of *Figure 7.4(a)* is that road surfaces are highly similar to bare soil (top-right region of the image), therefore extracting the roads using only spectral features is difficult. In next result, *Figure 7.4(b)* major roof areas are detected but the edges and boundaries are not prominent due to consideration of spectral features only. Certain geo-locations where roads and roofs are composed of similar materials, it is difficult to identify them leading to false alarms. Also, *Figure 7.4(c)* shows the scatter plot of roads and roofs in which a major portion appears to be overlapping, indicating the spectral similarity at material composition level.

7.5.2. Urban target detection using shape features

Multiple spatial features are used depending upon the characteristics of the targets to be detected. Simple mathematical operators such as, standard deviation and range can also be productive and reduce the computational burden while training process. Here the neighbourhood value is chosen to be 3, making a window size of 3×3 , giving 8 neighbours for the central pixel to be detected, where cell padding is also accommodated for the boundary pixels. Simultaneously standard deviation and range are computed for every band and feature vectors are derived from exactly same geo-locations considered for spectral attributes. The results for the same are shown below:

Table 7.4: Accuracy Assessment using shape features

Shape Features	Linear SVM	Polynomial SVM		Gaussian SVM		
		Quadratic	Cubic	Fine	Medium	Coarse
Standard Deviation	39.1%	41.3%	37.4%	38.2%	37.5%	34.3%
Range	38.8%	40.4%	36.9%	39.1%	38.4%	34.6%

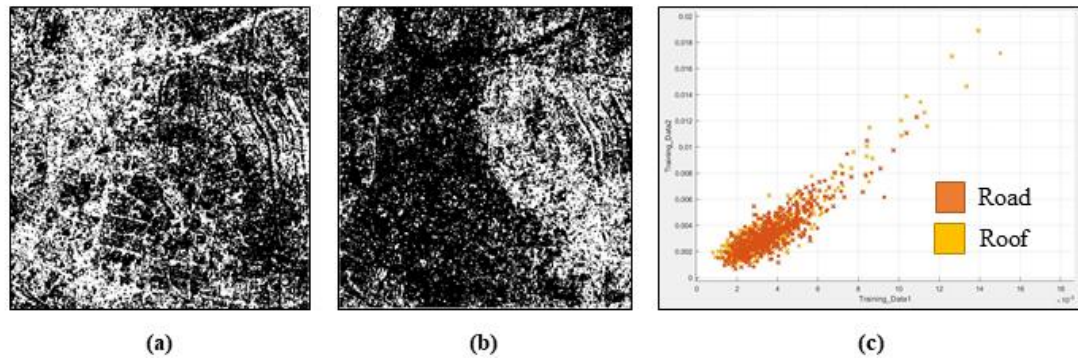


Figure 7.5: Standard Deviation (a) Detection of Roads (b) Detection of Roofs (c) Scatter plot for both urban targets

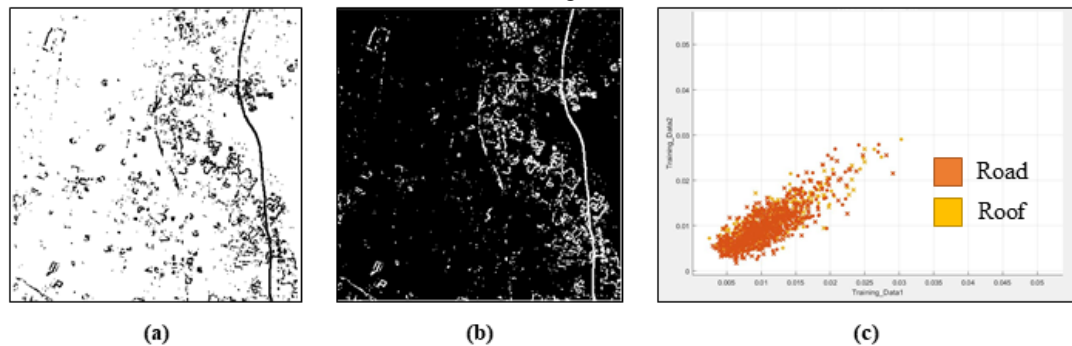


Figure 7.6: Range (a) Detection of Roads (b) Detection of Roofs (c) Scatter plot for both urban targets

The accuracy of shape features is expected to be less, which is also evident from *Table 7.4*. Polynomial kernel SVM gives a marginal detection percentage for both standard deviation and range-based analysis. Also, standard deviation appears to perform slightly better than the range as it is computed on the basis of filter applied on neighbouring pixels. In *Figure 7.5 (a) (b)* and *Figure 7.6 (a) (b)* neither the road nor roof appears to be detected, a very faint boundary is visible for both. Also, the data points for most of the samples are having very high overlap, unable to distinguish them using shape features. In *Figure 7.5(c)* and *Figure 7.6(c)* which display the scatterplot using standard deviation and range respectively depicts the overlapping nature of roads and roof targets. The relationship between the data points appears to be strong, positive and highly correlated. By identifying the patterns in the data, it is clear that shape features are unable to differentiate between the considered targets.

7.5.3. Urban Target detection using fusion of spectral and shape features

Combining the spectral and spatial components to extract the urban targets appears to give good results as compared to spectral or spatial attributes considered individually. The very same inference can be drawn from the literature also, but varying the process and methods to extract spectral or spatial features differs. Spectral features may be transformed using Principal Component Analysis (PCA) (Bakken 2019), Minimum Noise Fraction (MNF) (Luo 2016) *etc.* whereas, spatial features include multiple morphological operations (Benediktsson 2005), texture-based analysis (Seifi Majdar 2017), shape extraction *etc.* Here in this study, in order to preserve the spectral shape of spectral signature no dimensionality reduction method is used. Therefore, the spectral signatures are combined with shape-based features to enhance the detection

percentage. Simply, averaging both the attributes has yielded better results which are shown in *Figure 7.7 and 7.8* and the corresponding results are mapped in *Table 7.5*

Table 7.5: Accuracy assessment using spectral and shape features

Spectral and Shape Features	Linear SVM	Polynomial SVM		Gaussian SVM		
		Quadratic	Cubic	Fine	Medium	Coarse
Standard Deviation	96.5%	97.3%	96.9%	96%	96.7%	95.6%
Range	91.3%	91.5%	89.8%	88.9%	90.6%	88%

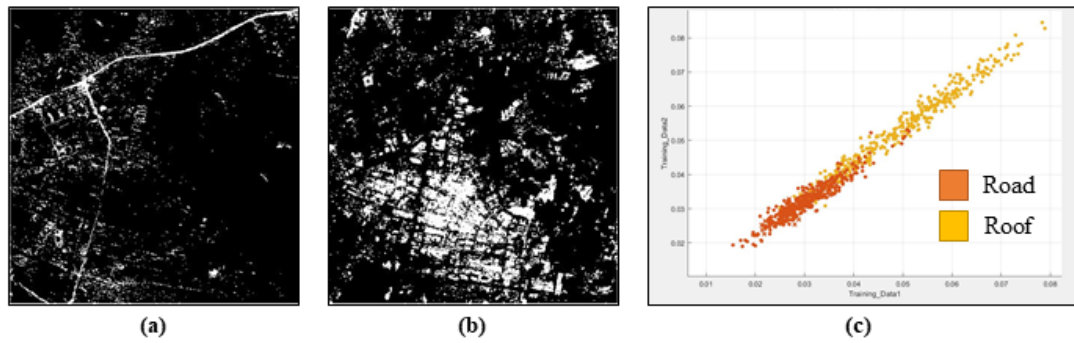


Figure 7.7: Spectral features and Standard deviation (a) Detection of Roads (b) Detection of Roofs (c) Scatter plot for both urban targets

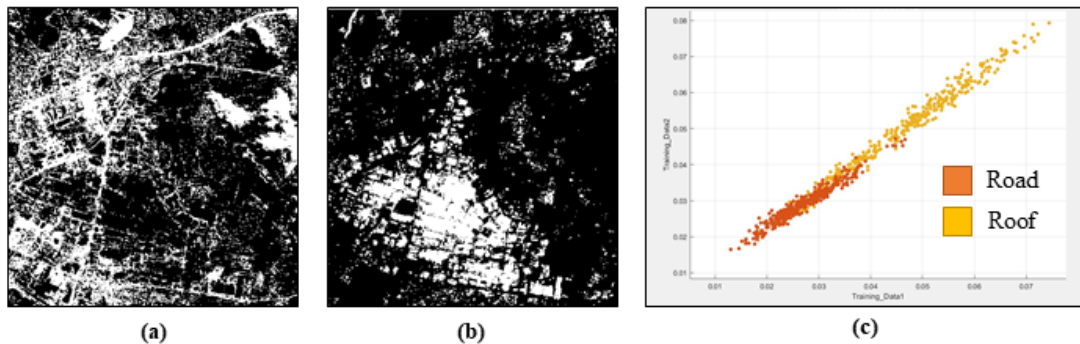


Figure 7.8: Spectral features and Range (a) Detection of Roads (b) Detection of Roofs (c) Scatter plot for both urban targets

By analysing the results shown in *Table 7.5*, spectral features fused with standard deviation gives more accuracy as compared to spectral features combined with range. Amongst linear, polynomial and gaussian kernels, quadratic polynomial gives the highest accuracy of 97.3% when standard deviation is considered as spatial measure. Though Gaussian (fine, medium and coarse) and linear kernel tricks have also offered a consistent accuracy, but polynomial kernel has detected maximum target pixels in stipulated time. The reason articulated for this may be that range being a simple statistical measure works on minimum and maximum values in the neighborhood but standard deviation computes mean value and then on the basis of deviation, decides the

presence and absence of target. Again, polynomial kernel method with degree 2 gives better results as compared to the other types of SVM. The road boundary and cross-section are easily delineated in *Figure 7.7 (a)* and roof clusters are also identified in *Figure 7.7 (b)*. However, in *Figure 7.8 (a) and (b)* where spectral signatures are fused with range; misdetections are witnessed by visual examination of images. Also, the observation that can be drawn from the scatterplots displayed in *Figure 7.7(c)* and *Figure 7.8(c)* is that, despite of high positive correlation between road and roof features, they can be distinguished on the basis of spectral and spatial attributes. However, all the data points of roads and roofs are not appearing to be segregated by a visible boundary but maximum points are drifted apart.

7.6. Summary

A fusion approach by using spectral signatures and shape properties of urban surfaces is successfully applied by using hyperspectral data. The work emphasizes on averaging the spectral attributes with shape-based features for detecting roads and roofs which form major portion of urban landcovers. Training files with (i) spectral (ii) shape and (iii) combination of spectral and shape feature vectors is treated as input for multiple variants of SVM followed by using the best performing model for prediction of target availability. Pixels where target is present are highlighted as bright as compared to the background pixels giving a binary result image. The approach not only exploits the spectral information but also helps in detecting the shape of urban targets. In general, polynomial (quadratic and cubic) kernel trick has outperformed and given the highest results as compared to other methods studied for the work. Apart from this, standard deviation being a two-level statistic approach, which works locally on a small window, produces better results as compared to range. Strong and positive correlation between roads and roofs is inferred by scatterplots, when spectral, shape and fused

features are considered but still the datapoints are not separated by distinct boundary due to similar material used for their construction. Hyperspectral remote sensing already faces a challenge of spectral variability from one location to another, therefore this approach might help to detect linear (roads) and clusters (roofs) features of a landcover working locally on adjoining pixels.

Chapter 8

Shape enhancement using spatial super-resolution

Super resolution mapping techniques have been explored to address mixed pixel, which enable prediction of land-cover patches smaller than the size of image pixel. Elbakary and Alam proposed a method to produce high resolution bands from low resolution imagery based on local correlation values using super resolution reconstruction (Elbakary 2007). Models that enable to represent hyperspectral data as linear combination of small image planes to reconstruct spectrum of observed scene is also another approach mentioned in literature (Akgun 2005). In previous chapter, though the spatial attributes like, standard deviation and range have been considered along with spectral profiles of roads and roofs, but coarse spatial resolution is still a challenge to extract the shape of subpixel targets, therefore the shape derived may be enhanced using the concept of super-resolution.

8.1. Introduction

Atkinson presented a method to find spatial distribution of every endmember present in a pixel by dividing it into sub pixels such that their number is proportional to the fraction of that endmember in original pixel (Atkinson 1997). Super resolution mapping can be achieved in multiple ways as per literature, knowledge-based procedures (Kasetkasem 2005), Hopfield neural network (Nguyen 2005), Linear optimization, Genetic algorithm, neural network predicted wavelet coefficient (L. Y. Li, 2015).

Extracting full pixels of targets along with its fractions or endmember abundance values using the concept of spectral unmixing is often followed by super-resolution techniques in order to locate correct spatial distribution. Therefore, this

category of target detection lies unexplored as most of the approaches reported here, use random allocation of location to subpixels of different endmembers. This recursive procedure not only increases the computational complexity but adds on to CPU time as well, for instance, Pixel Swap Algorithm (P. M. Atkinson 2005). Algorithms like Inverse Euclidean Distance (Arora and Tiwari 2013) are based on a non-random, non-recursive assignment of subpixels to binary end members. Both of these approaches are already explained in *Chapter 2, Subsection 2.6.6*.

8.2. Problem Statement

Targets of interest may be confined to multiple pixels (full pixel) or are a fraction of the pixel (subpixel) resulting into a mixed signal to the sensor. Coarse spatial resolution is also one of the major challenges faced while extraction of urban built-up surfaces using remote sensing methods. AVIRIS-NG hyperspectral data collected during the campaign has been considered for exploring the mixed pixels for extraction of spatial content of urban engineered surfaces. Spectral unmixing is one of the most common solutions to extract the abundance information about the target present in the pixel. However, spectral unmixing fails to provide spatial distribution of the subpixel components of target within the pixel. In case, a target resides fully in one pixel and partially in all the surrounding pixels then recovery of subpixel components of the target in all the surrounding pixels becomes necessary for correct estimation of the shape and size of the concerned target (urban engineered surfaces).

The current work emphasizes extraction of mixed pixel using super resolution technique in order to delineate the boundaries of urban targets particularly roads and roofs. The AVIRIS-NG hyperspectral data has been used for the study. The approach provides an alternative to traditional mixed pixel analysis methods with an added advantage of refining it to fine spatial resolution. Simultaneously, it also presents a

comparative assessment of Atkinson's pixel swap method with inverse Euclidean distance.

8.3. Study area and data

Due to lack of availability of ground truth data for different types of urban engineered surfaces, a set of synthetic data as described below has been generated. In all, two sets of data have been considered for extraction of road and roof surfaces.

8.3.1. Synthetic Data

The synthetic data generated for carrying out the analysis involves three road-like and three roof-like structures with known abundance fractions in different pixels. These have been used to test the super-resolution techniques mentioned in *Section 2.6.6.1 and 2.6.6.2*. Each structure approximates either the shape of a road or a roof and is of size 30×30 for uniformity and ease of computation. The scaling factors considered for analysis are 3, 5 and 7. So, the number of super-resolved pixels become s^2 , where s is the scaling factor and the subpixels generated are 3^2 , 5^2 and 7^2 respectively. For instance, if the value of $s = 5$, image size is 30×30 , then the resultant imagery with subdivisions will be equal to $(m \times s)(n \times s)$, that is 150×150 . This can be down sampled using a filter of size 5×5 , dividing every subpixel by 25. The reference targets corresponding to roads are shown in *Figure 8.1* and for roofs are shown in *Figure 8.2*. The data before down-sampling is used as reference to validate the super-resolved image. Complexity of the synthetic targets approximating the shape of roads and roofs is increased sequentially from target number 1 to target number 3.

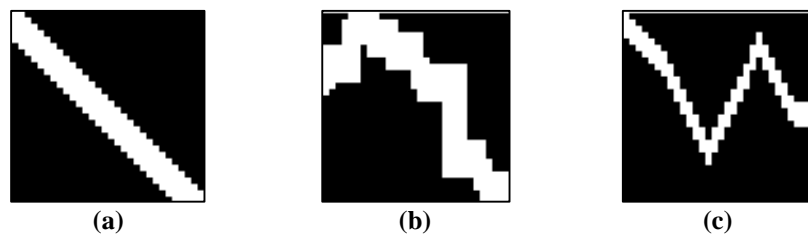


Figure 8.1: Synthetic data for road targets

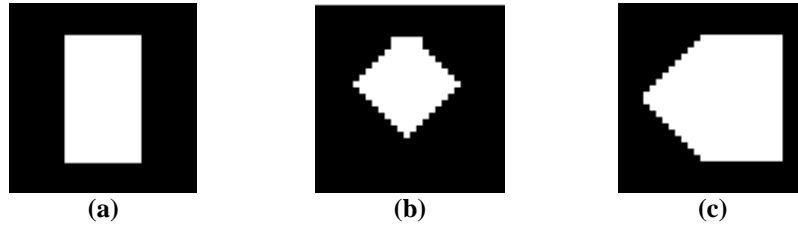


Figure 8.2: Synthetic data for roof targets

8.3.2. AVIRIS-NG Data

The hyperspectral data used for the analysis is acquired as part of AVIRIS-NG data collection campaign. Three targets each of roads and roofs individually are considered from the urban cover of Udaipur, Rajasthan region of India. A spatial RGB subset containing maximum urban coverage is shown in *Figure 8.3*. The road targets are shown with yellow-coloured shapes and the roof targets are shown with blue coloured shapes along with their zoomed layout. The spatial resolution of this data is 8.1 m. The other descriptions of these targets are given in *Table 8.1*.

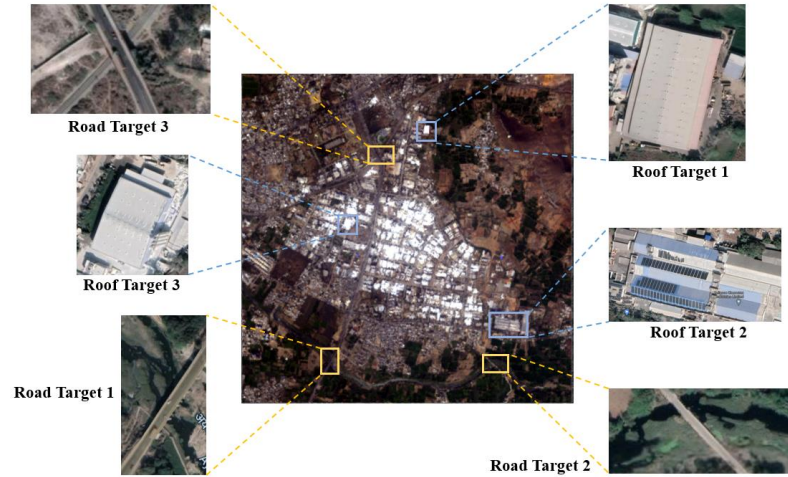








Figure 8.3: Road and Roof targets identified for super-resolution

Table 8.1: Description of road and roof targets selected from AVIRIS-NG hyperspectral Dataset							
<i>S.No.</i>	<i>Target</i>	<i>Name</i>	<i>Lines</i>	<i>Samples</i>	<i>Latitude (decimal)</i>	<i>Longitude (decimal)</i>	<i>Image</i>
1.	Road Target 1	NH48 Highway	37	31	24.566976	73.743191	

2.	Road Target 2	Crossing over Ayad River	48	40	24.565624	73.758564	
3.	Road Target 3	NH48 Highway Khempura	40	40	24.584506	73.749146	
4.	Roof Target 1	Roof from Transport Nagar	32	26	24.586459	73.754064	
5.	Roof Target 2	Uday Pratap Colony	48	28	24.568843	73.760123	
6.	Roof Target 3	ASDC- Golcha Grinding Unit	31	25	24.578880	73.74570	

8.4. Methodology and Implementation

Pre-processing: The data is atmospherically corrected by ISRO and Level 2 reflectance imagery is received with metadata. The complete hypercube is then tested for bad bands and bands affected by noise, water vapours and atmospheric gases are removed to get a transformed data of 387 bands.

Creation of synthetic dataset and other targets: The structures similar to roads and roofs are created to match the urban targets. Three targets belonging to each category are generated for super resolution with scale factor of 3, 5 and 7. For ease of referring synthetic targets, these have been labelled as, (Syn_Category_TargetNumber), that is, Syn_Road_T1, Syn_Road_T2, Syn_Road_T3, Syn_Roof_T1, Syn_Roof_T2 and Syn_Roof_T3. The process of creation of synthetic data has already been described in *Section 8.3*.

Spectral Unmixing: On visual interpretation of the hyperspectral data and considering the parameters of field visit, the urban features identified as

endmembers are roads, roofs, vegetation, soil, and water. Linear spectral unmixing is carried out to determine the relative abundance of aforementioned features on the basis of their spectral characteristics. The reflectance of every pixel in the hyperspectral image is assumed to be a linear combination of every endmember present in it. In the resultant imagery the pixel values are an indicative of the fraction of pixel containing the endmember's composition. For instance, the fraction value of 0.65 inside a particular pixel indicates that the pixel contains 65% of that endmember. Generally, the values lie in the range of 0 to 1 and the process is also validated by calculation of Root Mean Square Error (RMSE).

For unmixing, 100 spectral signatures belonging to each urban feature have been extracted from the image itself and then mean spectra is calculated as a reference endmember (Anita, Raczko and Zagajewski 2020). Later, after performing linear spectral unmixing, abundance maps have been generated. In the next step, the road and roof targets shown in *Figure 8.3* have been extracted by spatial sub-setting from the corresponding abundance maps for input to super-resolution techniques. *Figure 8.4 (a) and (b)* show the results for road and roof surfaces.

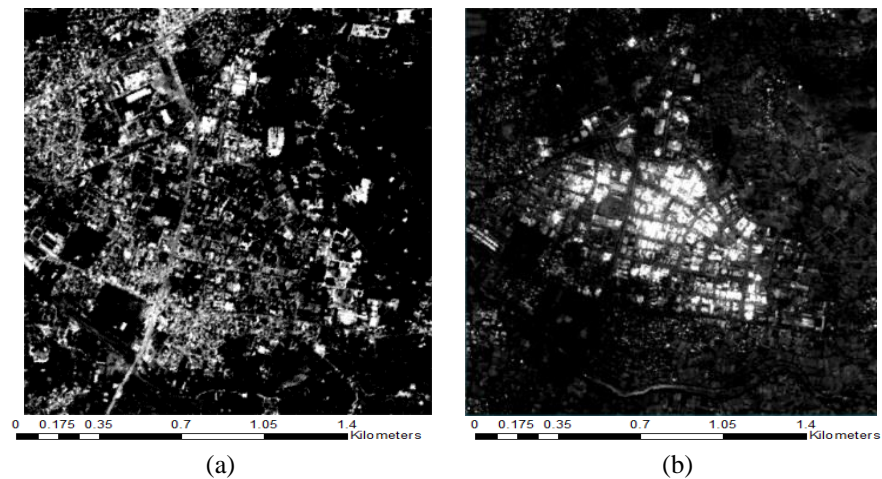


Figure 8.4: Abundance maps of (a)road and (b)roof surfaces generated using spectral linear unmixing

Super resolution using abundance fractions: The abundance fractions are optimized to generate subpixel map of fine spatial resolution, by varying the scale factors. For attaining super resolution, the quantification of subpixels in the given pixel is necessary to define the relationship with its neighborhood, at a given scale factor. Modelling of attractive influence between each subpixel and the consequent neighborhood requires defining an optimum distance function. The details of this function is given in *Chapter 2, Section 2.6.6*.

For the present work, super resolution is performed using two methods (i) Pixel-swap and (ii) Inverse Euclidean approach already explained in *Section 2.6.6*. Mixed pixels exist expansively in hyperspectral data due to sensor configuration and technical specifications. To address mixed pixels, unmixing algorithms can be used, but still the exact spatial location of the endmembers present in the mixed pixel remains unknown, which is resolved by super resolution.

Performance Analysis: Performance Evaluation is done with reference to the synthetic dataset generated. Two parameters are considered to evaluate the accuracy, the first one is the detection rate (percentage) and the other one is CPU time (seconds). For AVIRIS-NG hyperspectral data, the inferences are made on the basis of visual examination and CPU time, due to unavailability of reference data of the same date.

Implementation Background: Spectral linear unmixing is carried out using the software ENVI 4.8 and super resolution techniques are implemented in MATLAB 2018b environment on a system configuration of 16GB RAM, Intel® Core™ i7-8550U CPU and NVIDIA GeForce MX 130 GPU. The flow chart of the same is given in *Figure 8.5*.

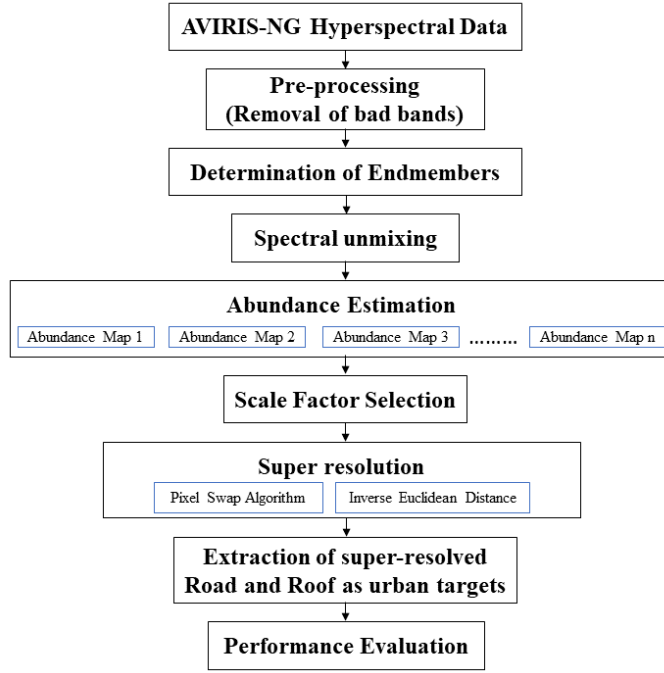


Figure 8.5: Flow chart of the proposed Approach

8.5. Results and Discussion

8.5.1. Super-resolution using synthetic data

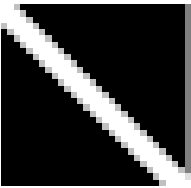


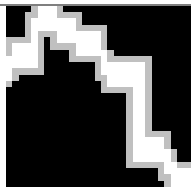


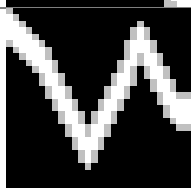


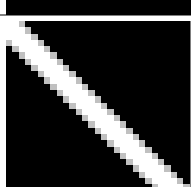
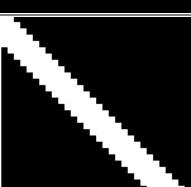
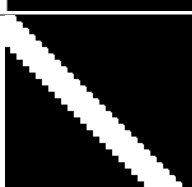
In total six synthetic data have been considered resembling the shapes of road and roof surfaces. The advantage of creation of synthetic data is that the abundance fractions are already known for every pixel, so the detection percentage is determined by percent correct measure. The other performance parameter used for the comparative assessment is CPU cycle time. The detection percentage of Synthetic Road targets based on considered scale factors and the CPU time are tabulated in *Table 8.2* and *Figure 8.6*. The figure shows the results of Pixel Swapping and Inverse Euclidean Distance method along with the original image without any scaling.

Table 8.2: Accuracy Assessment of Synthetic Road Targets using Pixel Swapping and Inverse Euclidean Distance Method

<i>Scale Factor</i>	<i>Synthetic Road Targets</i>	<i>Pixel Swapping Method</i>		<i>Inverse Euclidean Distance</i>	
		<i>Detection percentage (%)</i>	<i>CPU Time (secs)</i>	<i>Detection percentage (%)</i>	<i>CPU Time (secs)</i>
3	<i>Syn_Road_T1</i>	82.1613	8.9064	84.4356	8.7187
	<i>Syn_Road_T2</i>	80.4031	8.4386	83.0665	8.0313
	<i>Syn_Road_T3</i>	56.0821	7.9699	63.8167	7.4375
5	<i>Syn_Road_T1</i>	81.8497	8.0469	82.6743	7.6719

7	<i>Syn_Road_T2</i>	42.6624	9.5000	79.9685	9.8975
	<i>Syn_Road_T3</i>	55.8717	4.5735	50.1680	7.5000
	<i>Syn_Road_T1</i>	81.7338	8.1563	86.0655	8.2031
	<i>Syn_Road_T2</i>	40.3584	7.6719	79.8594	1.2031
	<i>Syn_Road_T3</i>	55.8222	9.2656	46.6349	8.1406

It can be observed from Table 8.2 that the detection range for various road targets using different scale factors is ranging from 42% to 82% for Pixel Swapping method, whereas the Euclidean Inverse method gives a maximum accuracy of 86%. The CPU time is having marginal difference for both the algorithms. A similar trend is observed that with respect to the scale factors, the detection percentage decreases with the increase in scale factors, irrespective of the algorithm used. Apart from this, Syn_Road_T1 performs highest amongst Syn_Road_T2 and Syn_Road_T3 because of its simple structure, for scale factor 3, 5 and 7. Syn_Road_T2 and Syn_Road_T3 resembles the curved roads, where the accuracy decreases due to their complex structures, in case of both algorithms considered.

<i>Scale Factor</i>	<i>Synthetic Road Targets</i>	<i>Abundance map</i>	<i>Pixel Swapping Method</i>	<i>Inverse Euclidean Distance</i>
3	<i>Syn_Road_T1</i>			
	<i>Syn_Road_T2</i>			
	<i>Syn_Road_T3</i>			
5	<i>Syn_Road_T1</i>			

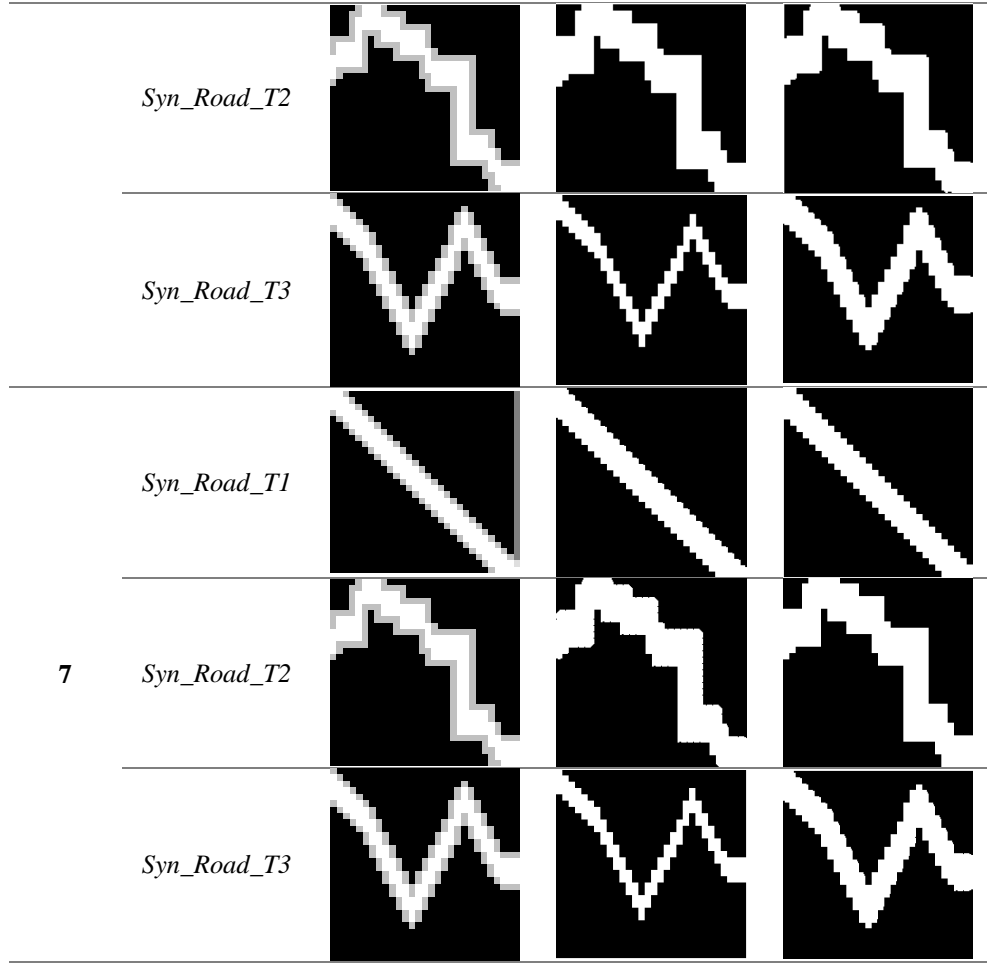


Figure 8.6: Detection of Synthetic Road Targets using Pixel Swapping and Inverse Euclidean Distance Method

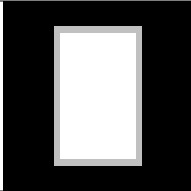
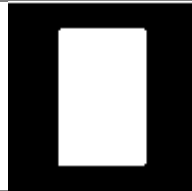

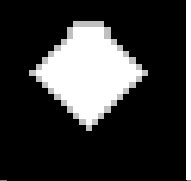


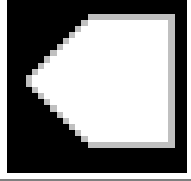


On visually interpreting the results generated for synthetic road targets, in case of Syn_Road_T1 which is a linear road, the detection percentage is higher for all the scale factors (3, 5, and 7) considered, irrespective of the algorithm used. To replicate the real-time road targets, curved shapes are taken as Syn_Road_T2 and Syn_Road_T3. Here, Inverse Euclidean Distance performs better as compared to Pixel Swapping algorithm. *Figure 8.6* demonstrates better performance of Inverse Euclidean method for detection of complex urban targets such as roads.

Table 8.3: Accuracy Assessment of Synthetic Roof Targets using Pixel Swapping and Inverse Euclidean Distance Method

<i>Scale Factor</i>	<i>Synthetic Roof Targets</i>	<i>Pixel Swapping Method</i>		<i>Inverse Euclidean Distance</i>	
		<i>Detection percentage (%)</i>	<i>CPU Time (secs)</i>	<i>Detection percentage (%)</i>	<i>CPU Time (secs)</i>
3	<i>Syn_Roof_T1</i>	80.4343	0.8125	85.5492	10.0156
	<i>Syn_Roof_T2</i>	80.8687	0.7969	81.7212	11.8906
	<i>Syn_Roof_T3</i>	85.5661	0.8281	88.0317	8.1406
5	<i>Syn_Roof_T1</i>	80.2683	0.9688	83.5263	9.8594

7	<i>Syn_Roof_T2</i>	80.7907	1.1015	86.2016	12.2344
	<i>Syn_Roof_T3</i>	82.8168	0.9844	85.4662	9.3750
	<i>Syn_Roof_T1</i>	34.3485	1.1875	80.2231	8.3281
	<i>Syn_Roof_T2</i>	38.3084	1.1119	80.7590	7.3906
	<i>Syn_Roof_T3</i>	53.6865	1.3125	85.4352	5.1563

Similar to the synthetic road targets, synthetic roof targets have been also generated in order to attain super-resolution by varying the scale factors. The first target is a simple rectangular geometric shape named as *Syn_Roof_T1*, whereas the other two targets replicate a pentagon roof structure and are named *Syn_Roof_T2* and *Syn_Roof_T3* for reference. In *Table 8.3*, when detection percentages are compared for both the algorithms, Inverse Euclidian Distance approach is outperforming in detection of sub-pixel targets. The maximum accuracy observed is for *Syn_Roof_T3*, at a scale factor of 3, that is, 88.03%. Again, a trade-off between the accuracy and CPU time is observed, an increased accuracy is obtained at cost of higher CPU time. Also, one another pattern is observed that, for pixel swapping algorithm the detection rate either remains constant or decreases with increase in the scale factor but for the other approach, only a small difference in accuracy is detected.

<i>Scale Factor</i>	<i>Synthetic Road Targets</i>	<i>Abundance map</i>	<i>Pixel Swapping Method</i>	<i>Inverse Euclidean Distance</i>
3	<i>Syn_Roof_T1</i>			
	<i>Syn_Roof_T2</i>			
	<i>Syn_Roof_T3</i>			

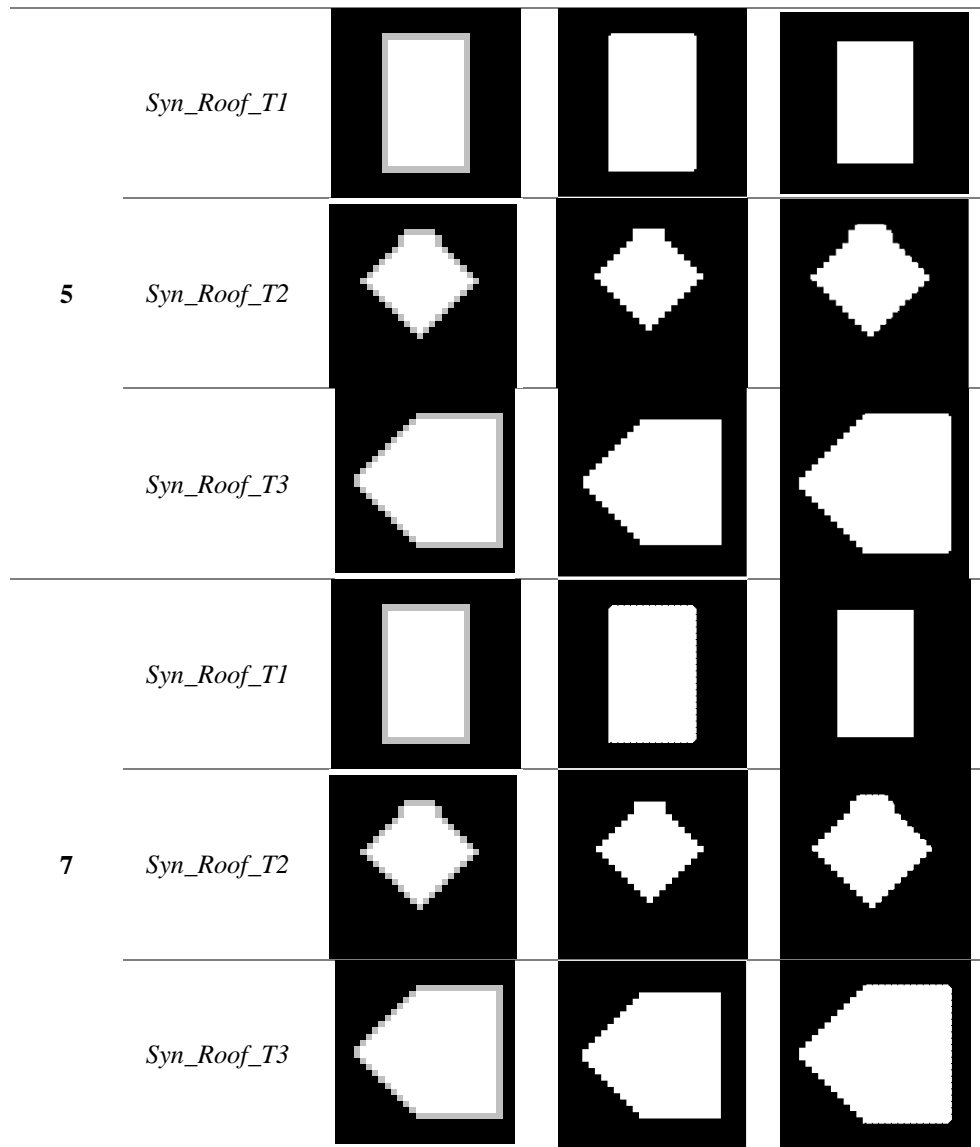


Figure 8.7: Detection of Synthetic Roof Targets using Pixel Swapping and Inverse Euclidean Distance Method


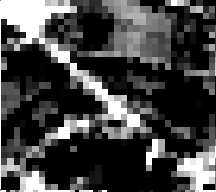



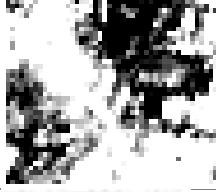
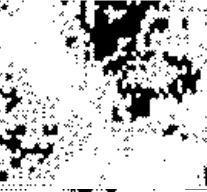



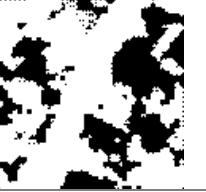

In *Figure 8.7*, by carefully examining the results generated, Pixel Swapping algorithm is not able to detect the corner most pixel of *Syn_Roof_T1*, whereas a complete rectangular structure is obtained at implementation of Inverse Euclidean distance. Also, with an increase in scale factor, a loss of information is detected in terms of boundary pixels.

A common observation from the results discussed above is that the reason for low performance of pixel swapping algorithm is random allocation of subpixels, at the initial stage followed by an iterative process. In this algorithm, in order to super-resolve all the pixels, the pixel positions are translated thereby increasing the difference

between the target classes. However, in case of Inverse Euclidean distance, the attractive influence exerted by surrounding pixels is calculated *ab initio* itself and stored. There is no random initialization of subpixel allocations. During the super resolution process, the stored values are recalled and subpixels of a target are assigned locations based on comparative influence exerted by the surrounding pixels.

8.4.2. Super-resolution using hyperspectral data

The super-resolution using Pixel Swapping and Inverse Euclidean Distance Method is carried out on AVIRIS-NG hyperspectral datasets to extract road and roof targets. The input for both the algorithms is the unmixed results that is the abundance maps of the corresponding targets. The extraction of shapes of targets in hyperspectral data is complicated due to the influence of factors such as, sun's angle, Instantaneous Field of View (IFOV) of the sensor, atmospheric hindrances *etc.* (Dixit and Agarwal 2020). *Figure 8.8* shows the results obtained for detection of roads.

<i>Scale Factor</i>	<i>AVIRIS-NG Road Targets</i>	<i>RGB Image</i>	<i>Abundance map</i>	<i>Pixel Swapping Method</i>	<i>Inverse Euclidean Distance</i>
3	<i>Road Target 1</i>				
	<i>Road Target 2</i>				
	<i>Road Target 3</i>				

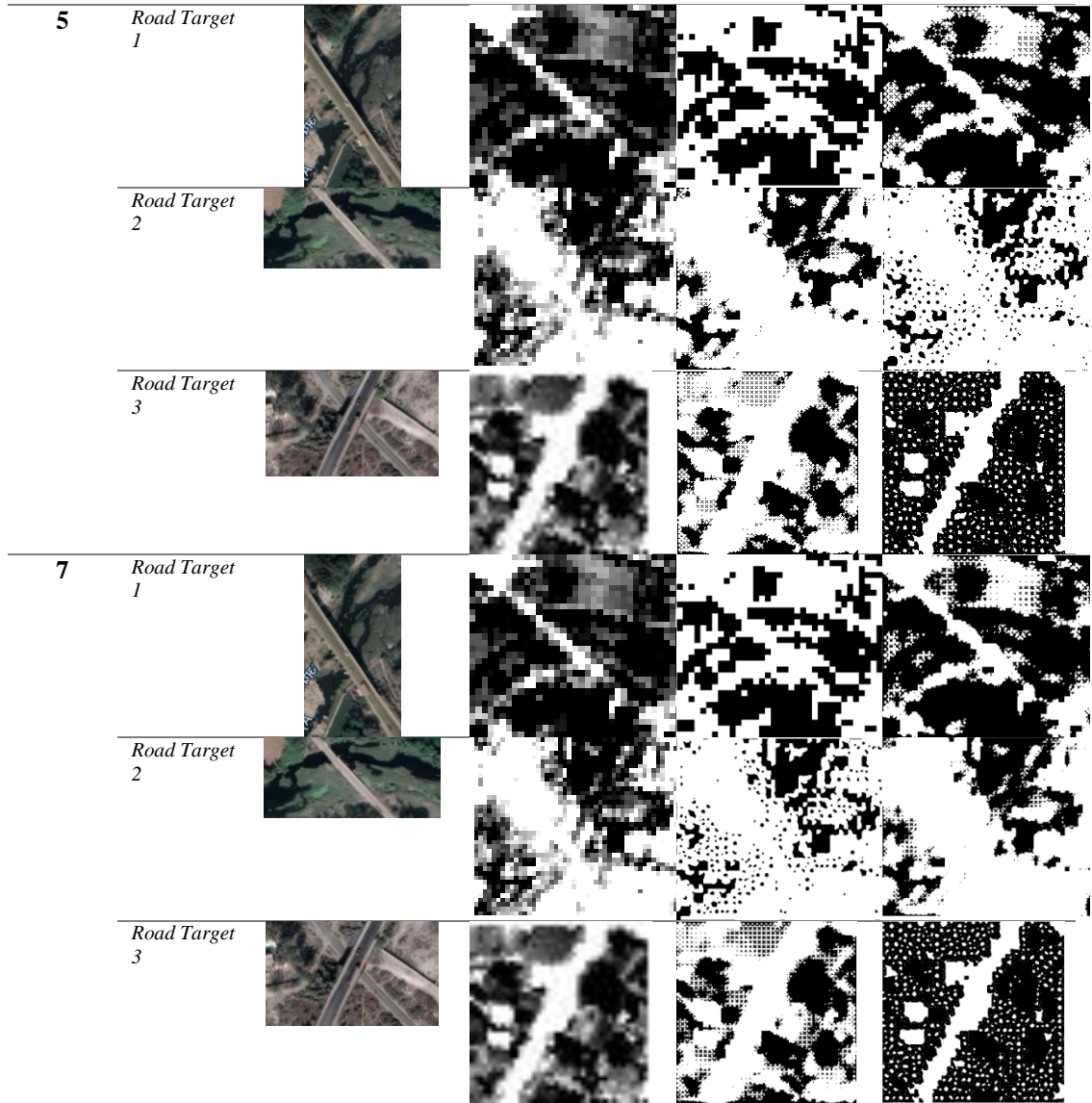


Figure 8.8: Detection of AVIRIS-NG Road Targets using Pixel Swapping and Inverse Euclidean Distance Method

In general, similar inferences as that for synthetic datasets can be drawn for AVIRIS – NG dataset from *Figure 8.8*. In this case, three different road targets have been super resolved, at different scale factors. The abundance maps of these targets are considered as input for super resolution, for which subpixels need to be detected. For Road Target 1, the oblique linear shape in the middle is the road, which is confused with bare soil and some other regions. It only amplifies with the increase in scale factor from 3 to 7. In case of Road Target 2, major region of the road is detected using Euclidean distance but pixel swapping method gives a distorted result. A precise road boundary is extracted for Road Target 3, at every scale factor, using Inverse Euclidean

Distance. The results of super-resolution are highly dependent upon the unmixing of the endmembers present in a scene.


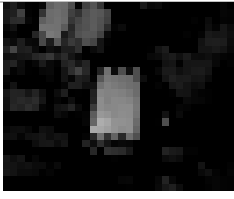











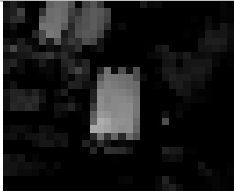

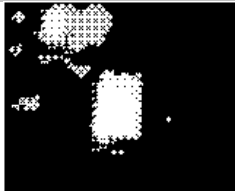



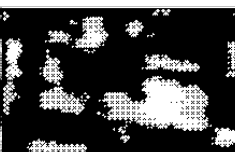





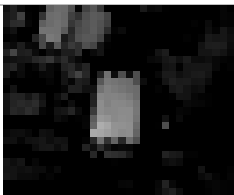
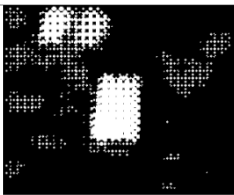
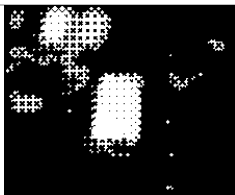




<i>Scale Factor</i>	<i>AVIRIS-NG Road Targets</i>	<i>RGB Image</i>	<i>Abundance Maps</i>	<i>Pixel Swapping Method</i>	<i>Inverse Euclidean Distance</i>
3	<i>Roof Target 1</i>				
	<i>Roof Target 2</i>				
	<i>Roof Target 3</i>				
5	<i>Roof Target 1</i>				
	<i>Roof Target 2</i>				
	<i>Roof Target 3</i>				
7	<i>Roof Target 1</i>				
	<i>Roof Target 2</i>				



Figure 8.9 Detection of AVIRIS-NG Roof Targets using Pixel Swapping and Inverse Euclidean Distance Method

Figure 8.9 shows, the lack of efficiency in detection of subpixels targets for Pixel swapping method in contrast to Inverse Euclidean distance. Different roofs in an urban area are made up of multiple materials such as concrete, asphalt *etc.*, making the extraction process difficult. For roof targets, maximum detection is observed in case of scale factor 3, because of their small size. Further super resolving the targets at a scale of 5 and 7 only degrades the performance in case of both the approaches considered. For Roof target 1, the shape extracted appears to be prominent as compared to other two targets. Due to high slope observed in case of Roof Target 2, only few pixels are extracted.

The pixel swapping method does not attain convergence because of random initialization of subpixel locations. Also, the mathematical formulation includes, a non-linear parameter for calculation of attractiveness function which is again difficult to predict.

8.6. Summary

In this work, two different datasets (Synthetic and hyperspectral) have been examined for detection of urban targets particularly roads and roofs. The problem of subpixel target in hyperspectral remote sensing is addressed by linear spectral unmixing followed by super-resolution. Two techniques namely, Atkinson's Pixel swapping and Inverse Euclidean Distance are implemented for the mentioned data. Further, the shape enhancement is carried out to optimize the results generated by spectral unmixing. The spatial distribution of the abundance fractions obtained after unmixing are optimized

by super-resolution techniques. Performance of Inverse Euclidean distance is measured higher than the Pixel Swapping method by using the synthetic dataset for both roads and roofs, even at higher scale factors. The similar observations are drawn in case of AVIRIS-NG hyperspectral data also. Since the reference data is not available for the real-time satellite imagery, therefore the analysis is done solely on the basis of visual interpretation and field examination of the area considered. Another parameter considered for performance evaluation is CPU time, which is found to be increasing with respect to the scale factor. Therefore, despite of coarse spatial resolution of the sensor, the subpixel targets may be resolved by super-resolution mapping for extraction of complex urban targets.

Chapter 9

Summary and Conclusions

In this study, detection and identification of engineered objects have been carried out under three objectives using hyperspectral data:

- iv. Comparative assessment of spectral target detection algorithms for engineered objects using hyperspectral data.
- v. Development of strategies for detection of engineered objects.
 - c. Spectral - Spatial Urban Target Detection for Hyperspectral Remote Sensing Data using Artificial Neural Network
 - d. Detection of engineered surfaces using deep learning approach
- vi. Mixed pixel analysis and shape identification of engineered objects using hyperspectral data.
 - c. Extraction of urban targets using fusion of spectral and shape features by Support Vector Machine
 - d. Shape enhancement using super-resolution mapping

This chapter highlights the conclusion drawn from this research based on theoretical or experimental contributions made, research contribution and the limitations.

9.1. Conclusions

Some of the major conclusions, drawn with respect to each of the objectives, are summarised here.

- i. The experiments conducted for target detection suggest that roads and roofs can be effectively extracted from the hyperspectral data using both the field reference spectra as well as the scene drawn spectra. However, in all the target detection implementations, it is seen that the reference signature drawn from the

image produces higher detection rate, thereby increasing the accuracy of the algorithm used whereas the field reference spectra due to prevailing effects of background, illumination and resolution yields low detection.

- ii. Regarding angle-based measures, it has been observed that Mahalanobis angle performs well in this category giving maximum accuracy of 87.88% for roads and 85.71% for roofs using image reference signature. This algorithm though reported in the literature has not been found implemented for target detection.
- iii. Machine learning measures, particularly ANN and ELM appear to outperform as compared to other measures. Both roads and roofs are detected with the accuracy range varying from 87.87% - 90.9% for roads and 83.33% – 90.48% for roofs. Machine learning methods appear to be more attractive and show their tremendous potential in detecting targets with less execution time and high accuracy rate. Their learning capability from known data and prediction for unknown data make them outperform among all the algorithms.
- iv. Overall, distance measures appear to be less effective and insensitive to spectral properties of roads and roofs with less accuracy.
- v. Information measures lead to partial detection of roads and roofs as all the techniques depend upon calculation of background covariance matrix.
- vi. Associating the spatial information from the pixels with their spectral pixels helped in delineating the sharp boundary of roads and roofs. Morphological operators, that is, opening and closing performed well for AVIRIS-NG data with disk as structuring element. Morphological operators when used with spectral features improved accuracy.
- vii. VCA algorithm which is used for spectral unmixing as reported in literature, is used for generating the ground reference which is further supplied to CNN as

input, yielding to 0.92 F-score for roads and 0.93, in case of roofs. Therefore, deep learning methods appear to automate the process of feature extraction and lead to better accuracy as compared to machine learning measures for targets having similar spectral composition such as roads and roofs of same material.

- viii. Training files with (i) spectral (ii) shape and (iii) combination of spectral and shape feature vectors, treated as input for multiple variants of SVM, is successfully employed for prediction of urban target availability in the scene. Here, two shape-based features are proposed for the study based on standard deviation and range. Standard deviation being a two-level statistic approach, produces better results as compared to range, for road and roof detection. Fusion appears to produce better detection of shapes of urban engineered surfaces.
- ix. Two techniques namely, Atkinson's Pixel swapping and Inverse Euclidean Distance have been implemented for the mentioned data. The shape attributes from the abundance maps obtained after unmixing are optimized by super-resolution techniques to extract urban targets. Performance of Inverse Euclidean distance appears to be better than Pixel Swapping method for both roads and roofs, even at higher scale factors.

The AVIRIS-NG hyperspectral dataset collected during the joint campaign of ISRO and NASA lies highly unexplored with respect to urban applications. The study is an attempt to detect major engineered surfaces roads and roofs from the urban landcover. During the progression of the research, multiple traditional and modern techniques have been studied for detecting the mentioned targets. One of the major conclusions that can be drawn involves, extensive use of machine and deep learning approaches for large amount of data yielding higher accuracy. Also, inclusion of spatial features such as attribute profiles and shape-based features with spectral

signatures can further help in better detection of targets. Further, aforementioned techniques, consider pure – pixel targets, but due to sensor limitation mixed pixel targets become difficult to detect, therefore concept of super-resolution is also applied to combat the same.

9.2. Research Contributions

The research contributions from the thesis work are as under:

- i. Identification of Mahalanobis angle measure as a robust measure for detection of urban engineered surfaces (roads and roofs) using hyperspectral data.
- ii. The experiments conducted confirmed advantage of machine learning algorithms like ELM over other machine learning measures.
- iii. Improvement in accuracy in extraction of roads and roofs using hyperspectral data by combining spectral features with spatial morphological features.
- iv. Assessment that CNN based deep learning methods have a slight edge over other machine learning methods in extraction of engineered surfaces (roads and roofs).
- v. Usefulness of VCA as a method for ground truth generation.
- vi. Usefulness of standard deviation and range in conjunction with spectral features in characterising shape of urban engineered surfaces (roads and roofs).
- vii. Utility of super-resolution-based methods in mapping of subpixel components in surrounding pixels thereby aiding detection of a target (roads and roofs) by complete recovery of shape.

9.3. Future Scope

This section briefly mentions the future scope of this research, which may be undertaken to investigate further some of the results achieved in this research.

The present work is restricted till only the first level of extraction, as per Anderson's classification (Anderson and James 1976) and subcategories of roads and roofs have not been extracted. Further the research can be carried out to determine the most suitable bands for urban target detection. Only a single category of machine learning and deep learning algorithms with available *a priori* data has been considered, unsupervised and semi-supervised methods can also be implemented. No specific feature selection or extraction technique such as Gray level co-occurrence matrix (GLCM) *etc.* is used, which may be helpful in increasing the current accuracy level.

Apart from CNN, other deep learning approaches such as autoencoders can also be deployed for automatic feature selection process followed by urban target detection. Also, for dimensionality reduction PCA is applied for the study, but effect of other available standard measures can also be employed to analyse the same. Till now, the domain is confined to spatial super-resolution but it may be further extended to spectral super-resolution to transform a coarse resolution data to high resolution imagery. Besides, the attractive influence is modelled using a linear function, a non-linear function may also be considered.

References

- Adnan, Farooq, Xiuping Jia, and Jun Zhou. 2019. "Texture and Shape Features for Grass Weed Classification Using Hyperspectral Remote Sensing Images." *IEEE International Geoscience and Remote Sensing Symposium*. IEEE. 7208-7211.
- Aguayo, Mauricio I., Thorsten Wiegand, Gerardo D. Azócar, Kerstin Wiegand, and Claudia E. Vega. 2007. "Revealing the driving forces of mid-cities urban growth patterns using spatial modeling: a case study of Los Ángeles, Chile." *Ecology and Society* 12 (1).
- Akgun, Toygar, Yucel Altunbasak, and Russell M. Mersereau. 2005. "Super-resolution reconstruction of hyperspectral images." *IEEE Transactions on Image Processing* 14 (11): 1860-1875.
- Angelopoulou, Elli, Sang Wook Lee, and Ruzena Bajcsy. 1999. "Spectral gradient: a material descriptor invariant to geometry and incident illumination." *IEEE International Conference on Computer Vision*. IEEE. 861-867.
- Anita, Sabat-Tomala, Edwin Raczko, and Bogdan Zagajewski. 2020. "Comparison of support vector machine and random forest algorithms for invasive and expansive species classification using airborne hyperspectral data." *Remote Sensing* 12 (3): 516.
- Ann, Bateson, and Brian Curtiss. 1996. "A method for manual endmember selection and spectral unmixing." *Remote Sensing of Environment* 55 (3): 229-243.
- Arindam, Guha. 2020. "Mineral exploration using hyperspectral data." In *Mineral exploration using hyperspectral data*, 293-318. Elsevier.
- Arora, Manoj K., and K. C. Tiwari. 2013. "Subpixel Target Enhancement in Hyperspectral Images." *Defence science journal* 63 (1).
- Atkinson, Peter M. 1997. "Mapping sub-pixel boundaries from remotely sensed images." *Innovations in GIS* 166-180.
- Atkinson, Peter M. 2005. "Sub-pixel target mapping from soft-classified, remotely sensed imagery." *Photogrammetric Engineering & Remote Sensing* 71 (7): 839-846.
- Bakken, Sivert, Milica Orlandic, and Tor Arne Johansen. 2019. "The effect of dimensionality reduction on signature-based target detection for hyperspectral remote sensing." *InCubeSats and SmallSats for remote sensing III*. International Society for Optics and Photonics. 111310L.
- Bannehr, L., Luhmann Th, J. Piechel, T. Roelfs, and A. Schmidt. 2011. "Extracting roof parameters and heat bridges over the city of Oldenburg from hyperspectral, thermal, and airborne laser scanning data." *International Archives of the Photogrammetry, Remote Sensing and Spatial Information Sciences* 38.

- Bazi, Yakoub, Naif Alajlan, Farid Melgani, Haikel AlHichri, Salim Malek, and Ronald R. Yager. 2013. "Differential evolution extreme learning machine for the classification of hyperspectral images." *IEEE Geoscience and Remote Sensing Letters* 11 (6): 1066-1070.
- Benediktsson, Jón Atli, Jón Aevvar Palmason, and Johannes R. Sveinsson. 2005. "Classification of hyperspectral data from urban areas based on extended morphological profiles." *IEEE Transactions on Geoscience and Remote Sensing* 43 (3): 480-491.
- Bhangale, Ujwala M., Kuldeep R. Kurte, Surya S. Durbha, Roger L. King, and Nicolas H. Younan. 2016. "Big data processing using hpc for remote sensing disaster data." *IEEE International Geoscience and Remote Sensing Symposium (IGARSS)*. Beijing, China: IEEE. 5894-5897.
- Bilgin, Gokhan, Sarp Erturk, and Tulay Yildirim. 2008. "Unsupervised classification of hyperspectral-image data using fuzzy approaches that spatially exploit membership relations." *IEEE Geoscience and Remote Sensing Letters* 5 (4): 673-677.
- Bimal, K Bhattacharya, Robert O. Green, Sadasiva Rao, M. Saxena, Shweta Sharma, K. Ajay Kumar, P. Srinivasulu, Shashikant Sharma, D. Dhar, and S. Bandyopadhyay. 2019. "An overview of AVIRIS-NG airborne hyperspectral science campaign over India." *Curr. Sci* 116 (7): 1082-1088.
- Blaschke, Thomas, Geoffrey J. Hay, Maggi Kelly, Stefan Lang, Peter Hofmann, Elisabeth Addink, and Raul Queiroz Feitosa et al. 2014. "Geographic object-based image analysis—towards a new paradigm." *ISPRS journal of photogrammetry and remote sensing* 87: 180-191.
- Boardman, Joseph W., Fred A. Kruse, and Robert O. Green. 1995. "Mapping target signatures via partial unmixing of AVIRIS data."
- Boyu, Feng, and Jinfei Wang. 2018. "Constrained nonnegative tensor factorization for spectral unmixing of hyperspectral images: A case study of urban impervious surface extraction." *IEEE Geoscience and Remote Sensing Letters* 16 (4): 583-587.
- Brun, S. E., and L. E. Band. 2000. "Simulating runoff behavior in an urbanizing watershed." *Computers, Environment and Urban Systems* 24 (1): 5-22.
- Bubner, Timothy Paul, S. K. Kempinger, and V. K. Shettigara. 2001. "An investigation of target detection ability using spectral signatures at hyperspectral resolution." *DEFENCE SCIENCE AND TECHNOLOGY ORGANISATION CANBERRA (AUSTRALIA)*.
- Buddenbaum, H., M. Schlerf, and J. Hill. 2005. "Classification of coniferous tree species and age classes using hyperspectral data and geostatistical methods." *International Journal of Remote Sensing* 26 (24): 5453-5465.
- Burgers, Kate, Yohannes Fessehatsion, Sheida Rahmani, and T. Wittman. J. Seo. 2009. "A comparative analysis of dimension reduction algorithms on hyperspectral data." *LAMDA Research Group* 1-23.

- Camps-Valls, Gustavo, Luis Gomez-Chova, Jordi Muñoz-Marí, Joan Vila-Francés, and Javier Calpe-Maravilla. 2006. "Composite kernels for hyperspectral image classification." *IEEE geoscience and remote sensing letters* 3 (1): 93-97.
- Carvalho, De, O. Abilio, and Paulo Roberto Meneses. 2000. "Spectral correlation mapper (SCM): an improvement on the spectral angle mapper (SAM)." *JPL Airborne Earth Science Workshop*. Pasadena: JPL Publication. 00-18.
- Castrodad, Alexey, Zhengming Xing, John B. Greer, Edward Bosch, Lawrence Carin, and Guillermo Sapiro. 2011. "Learning discriminative sparse representations for modeling, source separation, and mapping of hyperspectral imagery." *IEEE Transactions on Geoscience and Remote Sensing* 49 (11): 4263-4281.
- Chandramouli, C. 2011. *Provisional Population Totals*. New Delhi: Government of India. Ministry of Home Affairs, Census of india, 409-413.
- Chang, Chein-I. 2000. "An information-theoretic approach to spectral variability, similarity, and discrimination for hyperspectral image analysis." *IEEE Transactions on information theory* 46 (5): 1927-1932.
- Charles, Adam S., Bruno A. Olshausen, and Christopher J. Rozell. 2011. "Learning sparse codes for hyperspectral imagery." *IEEE Journal of Selected Topics in Signal Processing* 5 (5): 963-978.
- Chen, Chen, Wei Li, Hongjun Su, and Kui Liu. 2014. "Spectral-spatial classification of hyperspectral image based on kernel extreme learning machine." *Remote sensing* 6 (6): 5795-5814.
- Chen, Fen, Huajun Jiang, Tim Van de Voorde, Sijia Lu, Wenbo Xu, and Yan Zhou. 2018. "Land cover mapping in urban environments using hyperspectral APEX data: A study case in Baden, Switzerland." *International journal of applied earth observation and geoinformation* 71: 70-82.
- Cheng, Yu, Duo Wang, Pan Zhou, and Tao Zhang. 2017. *A survey of model compression and acceleration for deep neural networks*. arXiv preprint arXiv:1710.09282.
- Cheung-Wai, Chan Jonathan, and Desiré Paelinckx. 2008. "Evaluation of Random Forest and Adaboost tree-based ensemble classification and spectral band selection for ecotope mapping using airborne hyperspectral imagery." *Remote Sensing of Environment* 112 (6): 2999-3011.
- Chi, Mingmin, Qian Kun, Jón Atli Benediktsson, and Rui Feng. 2009. "Ensemble classification algorithm for hyperspectral remote sensing data." *IEEE Geoscience and Remote Sensing Letters* 6 (4): 762-766.
- Chisense, C., M. Hahn, and J. Engels. 2012. "Classification of roof materials using hyperspectral data." *International Archives of the Photogrammetry, Remote Sensing and Spatial Information Sciences* 39 (B7): 103.
- Cisz, Adam P, and John R. Schott. 2005. "Performance comparison of hyperspectral target detection algorithms in altitude varying scenes." *In Algorithms and Technologies for*

- Multispectral, Hyperspectral, and Ultraspectral Imagery*. International Society for Optics and Photonics. 839-849.
- Corinna, Cortes, and Vladimir Vapnik. 1995. "Support-vector networks." *Machine learning* 20 (3): 273-297.
- Da, L. I. U., and L. I. Jianxun. 2018. "Spectral-spatial target detection based on data field modeling for hyperspectral data." *Chinese Journal of Aeronautics* 31 (4): 795-805.
- Dalal, Navneet, and Bill Triggs. 2005. "Histograms of oriented gradients for human detection." *IEEE computer society conference on computer vision and pattern recognition*. 886-893.
- Dalla Mura, Mauro, Jón Atli Benediktsson, Björn Waske, and Lorenzo Bruzzone. 2010. "Morphological attribute profiles for the analysis of very high resolution images." *IEEE Transactions on Geoscience and Remote Sensing* 48 (10): 3747-3762.
- Davis, Jesse, and Mark Goadrich. 2006. "The relationship between Precision-Recall and ROC curves." *Proceedings of the 23rd international conference on Machine learning*. 233-240.
- Dengsheng, Lu, and Weng Qihao. 2005. "Urban classification using full spectral information of Landsat ETM+ imagery in Marion County Indiana." *Photogrammetric Engineering & Remote Sensing* 71 (11): 1275-1284.
- Dimitris, Manolakis, Marden David, and A Shaw Gary. 2003. "Hyperspectral image processing for automatic target detection applications." *Lincoln laboratory journal* 14 (1): 79-116.
- DiPietro, R S, D Manolakis, R Lockwood, T. Cooley, and J Jacobson. 2010. "Performance evaluation of hyperspectral detection algorithms for subpixel objects." *Algorithms and technologies for multispectral, hyperspectral, and ultraspectral imagery XVI*. International Society for Optics and Photonics. 76951W.
- Dixit, Ankur, and Shefali Agarwal. 2020. "Super-resolution mapping of hyperspectral data using Artificial Neural Network and wavelet." *Remote Sensing Applications: Society and Environment* 20: 100374.
- Dora, B. Heras, Argüello Francisco, and Quesada-Barriuso Pablo. 2014. "Exploring ELM-based spatial-spectral classification of hyperspectral images." *International Journal of Remote Sensing* 35 (2): 401-423.
- Du, Qian, Nareenart Raksuntorn, Nicolas H. Younan, and Roger L. King. 2008. "End-member extraction for hyperspectral image analysis." *Applied Optics* 47 (28): F77-F84.
- Du, Yingzi, Chein-I. Chang, Hsuan Ren, Chein-Chi Chang, James O. Jensen, and Francis M. D'Amico. 2004. "New hyperspectral discrimination measure for spectral characterization." *Optical engineering* 43 (8): 1777-1786.
- Duran, Olga, and Maria Petrou. 2005. "A time-efficient clustering method for pure class selection." *IEEE International Geoscience and Remote Sensing Symposium IGARSS'05*. IEEE. 4.

- Elbakary, Mohamed, and Mohammad S. Alam. 2007. "Super-resolution reconstruction of hyperspectral images." *Optical Pattern Recognition*. International Society for Optics and Photonics. 65740C.
- Ershad, Ali Mr. 2020. "Urbanisation in India: Causes, Growth, Trends, Patterns, Consequences & Remedial Measures." Academic.
- Falcone, James A., and Richard Gomez. 2005. "Mapping impervious surface type and sub-pixel abundance using hyperion hyperspectral imagery." *Geocarto International* 20 (4): 3-10.
- Fan, Wenyi, Baoxin Hu, John Miller, and Mingze Li. 2009. "Comparative study between a new nonlinear model and common linear model for analysing laboratory simulated- forest hyperspectral data." *International Journal of Remote Sensing* 30 (11): 2951-2962.
- Farid, Melgani, and Lorenzo Bruzzone. 2004. "Classification of hyperspectral remote sensing images with support vector machines." *IEEE Transactions on geoscience and remote sensing* 42 (8): 1778-1790.
- Farooq, Adnan, Xiuping Jia, and Jun Zhou. 2019. "Texture and Shape Features for Grass Weed Classification Using Hyperspectral Remote Sensing Images." *IEEE International Geoscience and Remote Sensing Symposium*. IEEE. 7208-7211.
- Farrell, Michael D, and Russell M. Mersereau. 2005. "On the impact of PCA dimension reduction for hyperspectral detection of difficult targets." *IEEE Geoscience and Remote Sensing Letters* 2 (2): 192-195.
- Fauvel, Mathieu, Jocelyn Chanussot, and Jon Atli Benediktsson. 2009. "Kernel principal component analysis for the classification of hyperspectral remote sensing data over urban areas." *EURASIP Journal on Advances in Signal Processing* 1-14.
- Fauvel, Mathieu, Jón Atli Benediktsson, Jocelyn Chanussot, and Johannes R. Sveinsson. 2008. "Spectral and spatial classification of hyperspectral data using SVMs and morphological profiles." *IEEE Transactions on Geoscience and Remote Sensing* 46 (11): 3804-3814.
- Fauvel, Mathieu, Yuliya Tarabalka, Jon Atli Benediktsson, Jocelyn Chanussot, and James C. Tilton. 2012. "Advances in spectral-spatial classification of hyperspectral images." *Proceedings of the IEEE*. 652-675.
- Faxian, Cao, Zhijing Yang, Jinchang Ren, Weizhao Chen, Guojun Han, and Yuzhen Shen. 2019. "Local block multilayer sparse extreme learning machine for effective feature extraction and classification of hyperspectral images." *IEEE Transactions on Geoscience and Remote Sensing* 57 (8): 5580-5594.
- Fen, Chen, Huajun Jiang, Tim Van de Voorde, Sijia Lu, Wenbo Xu, and Yan Zhou. 2018. "Land cover mapping in urban environments using hyperspectral APEX data: A study case in Baden, Switzerland." *International journal of applied earth observation and geoinformation* 70-82.

- Gakhar, Shalini, and Kailash Chandra Tiwari. 2021. "Spectral-spatial urban target detection for hyperspectral remote sensing data using artificial neural network." *The Egyptian Journal of Remote Sensing and Space Science* 24 (2): 173-180.
- Gamba, Paolo, Fabio Dell'Acqua, and Belur V. Dasarathy. 2005. "Urban remote sensing using multiple data sets: Past, present, and future." *Information Fusion* 6 (4): 319-326.
- Geoffrey, E. Hinton, and Ruslan R. Salakhutdinov. 2006. "Reducing the dimensionality of data with neural networks." *science* 313 (5786): 504-507.
- Giannandrea, AnneMarie, Nina Raqueno, David W. Messinger, Jason Faulring, John P. Kerekes, Jan van Aardt, and Kelly Canham et al. 2013. "The SHARE 2012 data campaign." In *Algorithms and Technologies for Multispectral, Hyperspectral, and Ultraspectral Imagery XIX*. International Society for Optics and Photonics. 87430F.
- Gómez-Chova, Gustavo Luis, Camps-Valls, Jordi Munoz-Mari, and Javier Calpe. 2008. "Semisupervised image classification with Laplacian support vector machines." *IEEE Geoscience and Remote Sensing Letters* 5 (3): 336-340.
- Goodfellow, Ian, Yoshua Bengio, and Aaron Courville. 2016. *Deep Learning (Adaptive Computation and Machine Learning series)*.
- Gu, Yanfeng, Ye Zhang, and Junping Zhang. 2008. "Integration of spatial-spectral information for resolution enhancement in hyperspectral images." *IEEE transactions on geoscience and remote sensing* 46 (5): 1347-1358.
- Guang-Bin, Huang, Zhu Qin-Yu, and Siew Chee-Kheong. 2006. "Extreme learning machine: Theory and applications." *Neurocomputing* 70 (1-3): 489-501.
- Gumley, Liam E. 2001. *Practical IDL programming*. Elsevier.
- Guo, Li, Nesrine Chehata, Clément Mallet, and Samia Boukir. 2011. "Relevance of airborne lidar and multispectral image data for urban scene classification using Random Forests." *ISPRS Journal of Photogrammetry and Remote Sensing* 66 (1): 56-66.
- Han, Youkyung, Hyejin Kim, Jaewan Choi, and Yongil Kim. 2012. "A shape-size index extraction for classification of high resolution multispectral satellite images." *International journal of remote sensing* 33 (6): 1682-1700.
- Hang, Renlong, Qingshan Liu, Danfeng Hong, and Pedram Ghamisi. 2019. "Cascaded recurrent neural networks for hyperspectral image classification." *IEEE Transactions on Geoscience and Remote Sensing* 57 (8): 5384-5394.
- Haralick, Robert M., Karthikeyan Shanmugam, and Hak Dinstein. 1973. "Textural features for image classification." *IEEE Transactions on systems, man, and cybernetics* 6: 610-621.
- Haut, Juan Mario, Mercedes E. Paoletti, Javier Plaza, Antonio Plaza, and Jun Li. 2019. "Visual attention-driven hyperspectral image classification." *IEEE Transactions on Geoscience and Remote Sensing* 57 (10): 8065-8080.

- Hegde, Gaurav, J. Mohammed Ahamed, R. Hebbar, and Uday Raj. 2014. "Urban land cover classification using hyperspectral data." *The International Archives of Photogrammetry, Remote Sensing and Spatial Information Sciences* 8 (8): 751-754.
- Hendriks, CL Luengo, and Lucas J. van Vliet. 2003. "Discrete morphology with line structuring elements." *International Conference on Computer Analysis of Images and Patterns*. Springer. 722-729.
- Heras, Dora B., Francisco Argüello, and Pablo Quesada-Barriuso. 2014. "Exploring ELM-based spatial-spectral classification of hyperspectral images." *International Journal of Remote Sensing* 35 (2): 401-423.
- Herold, Martin, Dar A. Roberts, Margaret E. Gardner, and Philip E. Dennison. 2004. "Spectrometry for urban area remote sensing—Development and analysis of a spectral library from 350 to 2400 nm." *Remote sensing of environment* 91 (3-4): 304-319.
- Herold, Martin, Noah C. Goldstein, and Keith C. Clarke. 2003. "The spatiotemporal form of urban growth: measurement, analysis and modeling." *Remote sensing of Environment* 86 (3): 286-302.
- Hinton, Geoffrey E. 2012. "A practical guide to training restricted Boltzmann machines." *Neural networks: Tricks of the trade* 599-619.
- Hively, W. Dean, Gregory W. McCarty, James B. Reeves, Megan W. Lang, Robert A. Oesterling, and Stephen R. 2011. "Use of airborne hyperspectral imagery to map soil properties in tilled agricultural fields." *Applied and Environmental Soil Science*.
- Homayouni, Saeid, and Michel Roux. 2004. "Hyperspectral image analysis for material mapping using spectral matching." *In ISPRS Congress Proceedings*. ISPRS. 28.
- Hu, Wei, Yangyu Huang, Li Wei, Fan Zhang, and Hengchao Li. 2015. "Deep convolutional neural networks for hyperspectral image classification." *Journal of Sensors*.
- Huali, Li, and Liangpei Zhang. 2011. "A hybrid automatic endmember extraction algorithm based on a local window." *IEEE transactions on geoscience and remote sensing* 49 (11): 4223-4238.
- Huang, Guang-Bin, Qin-Yu Zhu, and Chee-Kheong Siew. 2006. "Extreme learning machine: theory and applications." *Neurocomputing* 70 (1-3): 489-501.
- Huang, Hong, Guangyao Shi, Haibo He, Yule Duan, and Fulin Luo. 2019. "Dimensionality reduction of hyperspectral imagery based on spatial-spectral manifold learning." *IEEE Transactions on Cybernetics* 50 (6): 2604-2616.
- Hughes, Gordon. 1968. "On the mean accuracy of statistical pattern recognizers." *IEEE transactions on information theory* 14 (1): 55-63.
- Huqqani, Ilyas A., and Khurram Khurshid. 2014. "Comparative study of supervised classification of urban area hyperspectral satellite imagery." *Journal of Space Technology* 4 (1): 7-14.

- Hycza, Tomasz, Krzysztof Stereńczak, and Radomir Bałazy. 2018. "Potential use of hyperspectral data to classify forest tree species." *New Zealand Journal of Forestry Science* 48 (1): 18.
- Igamberdiev, Rahmatulla M., Goerres Grenzdoerffer, Ralf Bill, Hendrik Schubert, Martin Bachmann, and Bernd Lennartz. 2011. "Determination of chlorophyll content of small water bodies (kettle holes) using hyperspectral airborne data." *International journal of applied earth observation and geoinformation* 13 (6): 912-921.
- Imani, Maryam. 2019. "Difference-based target detection using Mahalanobis distance and spectral angle." *International journal of remote sensing* 40 (3): 811-831.
- Jacobs, Jane. 2016. *The death and life of great American cities*. 2016.
- James, Falcone A., and Gomez Richard. 2005. "Mapping impervious surface type and sub-pixel abundance using hyperion hyperspectral imagery." *Geocarto International* 20 (4): 3-10.
- Jensen, John R. 1996. *Introductory digital image processing: a remote sensing perspective*. Prentice-Hall Inc.
- Jiaojiao, Li, Qian Du, Wei Li, and Yunsong Li. 2015. "Optimizing extreme learning machine for hyperspectral image classification." *Journal of Applied Remote Sensing* 9 (1): 097296.
- Jin, Chen, Xiuping Jia, Wei Yang, and Bunkei Matsushita. 2009. "Generalization of subpixel analysis for hyperspectral data with flexibility in spectral similarity measures." *IEEE transactions on geoscience and remote sensing* 47 (7): 2165-2171.
- Jun, Goo, and Joydeep Ghosh. 2008. "An efficient active learning algorithm with knowledge transfer for hyperspectral data analysis." *IEEE International Geoscience and Remote Sensing Symposium*. IEEE. I-52.
- Junshi, Xia, Jocelyn Chanussot, Peijun Du, and Xiyan He. 2015. "Rotation-based support vector machine ensemble in classification of hyperspectral data with limited training samples." *IEEE Transactions on Geoscience and Remote Sensing* 54 (3): 1519-1531.
- Kadhim, Nada, Monjur Mourshed, and Michaela Bray. 2016. "Advances in remote sensing applications for urban sustainability." *Euro-Mediterranean Journal for Environmental Integration* 1-22.
- Kantakumar, Lakshmi N., Shamita Kumar, and Karl Schneider. 2016. "Spatiotemporal urban expansion in Pune metropolis, India using remote sensing." *Habitat international* 51: 11-22.
- Kasetkasem, Teerasit, Manoj K. Arora, and Pramod K. Varshney. 2005. "Super-resolution land cover mapping using a Markov random field based approach." *Remote Sensing of Environment* 96 (3-4): 302-314.
- Kawaguchi, Shuji, and Ryuei Nishii. 2007. "Hyperspectral image classification by bootstrap AdaBoost with random decision stumps." *IEEE Transactions on Geoscience and Remote Sensing* 45 (11): 3845-3851.

- Kerekes, JP, and DS Goldberg. 2013. "Hyperspectral image quality for unmixing and subpixel detection applications." *Image Quality and System Performance X* (4): 865304.
- Keshava, Nirmal, and John F. Mustard. 2002. "Spectral unmixing." *IEEE signal processing magazine* (19) 1: 44-57.
- Khan, Muhammad Jaleed, Adeel Yousaf, Nizwa Javed, Shifa Nadeem, and Khurram Khurshid. 2017. "Automatic target detection in satellite images using deep learning." *Journal of Space Technology* 7 (1): 44-49.
- Khodadadzadeh, Mahdi, Jun Li, Antonio Plaza, Hassan Ghassemian, José M. Bioucas-Dias, and Xia Li. 2014. "Spectral-spatial classification of hyperspectral data using local and global probabilities for mixed pixel characterization." *IEEE Transactions on Geoscience and Remote Sensing* 52 (10): 6298-6314.
- Ko, K. 1996. "A hybrid road identification system using image processing technique and back-propagation neural networks." Master's Thesis.
- Koltunov, A., and E. Ben- Dor. 2001. "A new approach for spectral feature extraction and for unsupervised classification of hyperspectral data based on the Gaussian mixture model." *Remote Sensing Reviews* 20 (2): 123-167.
- Kruse, F. A., J. W. Boardman, A. B. Lefkoff, J. M. Young, K. S. Kierein-Young, T. D. Cocks, R. Jensen, and P. A. Cocks. 2000. "HyMap: an Australian hyperspectral sensor solving global problems-results from USA HyMap data acquisitions." *InProc. of the 10th Australasian Remote Sensing and Photogrammetry Conference*. 18-23.
- Kruse, Fred A, A B Lefkoff, J W Boardman, K B Heidebrecht, A T Shapiro, P J Barloon, and AFH Goetz. 1993. "The spectral image processing system (SIPS)—interactive visualization and analysis of imaging spectrometer data." *Remote sensing of environment* 44 (2-3): 145-163.
- Kumar, Tanumi, Sushma Panigrahy, Prasanna Kumar, and Jai Singh Parihar. 2013. "Classification of floristic composition of mangrove forests using hyperspectral data: case study of Bhitarkanika National Park." *Journal of Coastal Conservation* 17 (1): 121-132.
- Kuo, Bor-Chen, Hsin-Hua Ho, Cheng-Hsuan Li, Chih-Cheng Hung, and Jin-Shiuh Taur. 2013. "A kernel-based feature selection method for SVM with RBF kernel for hyperspectral image classification." *IEEE Journal of Selected Topics in Applied Earth Observations and Remote Sensing* 7 (1): 317-326.
- Kuras, Agnieszka, Brell Maximilian, Rizzi Jonathan, and Burud Ingunn. 2021. "Hyperspectral and Lidar Data Applied to the Urban Land Cover Machine Learning and Neural-Network-Based Classification: A Review." *Remote Sensing* 13 (7): 3393.
- Landgrebe, David A. 2003. *Signal theory methods in multispectral remote sensing*. Vol. 24. John Wiley & Sons.
- Lemp, Dirk, and Uwe Weidner. 2005. "Improvements of roof surface classification using hyperspectral and laser scanning data." *ISPRS Joint Conf.: 3rd Int. Symp. Remote Sens. Data Fusion Over Urban Areas*. 14-16.

- Li, Jiaojiao, Bobo Xi, Yunsong Li, Qian Du, and Keyan Wang. 2018. "Hyperspectral classification based on texture feature enhancement and deep belief networks." *Remote Sensing* 10 (3): 396.
- Li, Linyi, Yun Chen, Tingbao Xu, Rui Liu, and Kaifang Shi and Chang Huang. 2015. "Super-resolution mapping of wetland inundation from remote sensing imagery based on integration of back-propagation neural network and genetic algorithm." *Remote Sensing of Environment* 164: 142-154.
- Li, Miao, Shuying Zang, Bing Zhang, Shanshan Li, and Changshan Wu. 2014. "A review of remote sensing image classification techniques: The role of spatio-contextual information." *European Journal of Remote Sensing* 47 (1): 389-411.
- Li, Shanshan, Bing Zhang, Lianru Gao, and Xu Sun. 2009. "Small objects detection of hyperspectral image in urban areas." *Joint Urban Remote Sensing Event*. IEEE. 1-5.
- Li, Wei, Saurabh Prasad, James E. Fowler, and Lori Mann Bruce. 2011. "Locality-preserving dimensionality reduction and classification for hyperspectral image analysis." *IEEE Transactions on Geoscience and Remote Sensing* 50 (4): 1185-1198.
- Li, Yanyi, Jian Wang, Tong Gao, Qiwen Sun, Liguang Zhang, and Mingxiu Tang. 2020. "Adoption of Machine Learning in Intelligent Terrain Classification of Hyperspectral Remote Sensing Images." *Computational Intelligence and Neuroscience*.
- Liao, Wenzhi, Jocelyn Chanussot, Mauro Dalla Mura, Xin Huang, Rik Bellens, Sidharta Gautama, and Wilfried Philips. 2017. "Taking optimal advantage of fine spatial resolution: Promoting partial image reconstruction for the morphological analysis of very-high-resolution images." *IEEE Geoscience and Remote Sensing Magazine* 5 (2): 8-28.
- López, Peña Fernando, Juan Luís Crespo, and Richard J. Duro. 2009. "Unmixing low-ratio endmembers in hyperspectral images through Gaussian synapse ANNs." *IEEE Transactions on Instrumentation and Measurement* 59 (7): 1834-1840.
- Lou, Q. S., Lei Chen, Ping WANG, Chen ZHANG, and Jian XIE. 2008. "The application and prospecting of the hyperspectral remote sensing technology in marine research." *Trans Oceanol Limnol* 3: 168-173.
- Lu, Dengsheng, and Weng Qihao. 2007. "A survey of image classification methods and techniques for improving classification performance." *International Journal of Remote Sensing* 28 (5): 823-870.
- Lulla, Vijay. 2010. "Neural network classification of hyperspectral imagery for urban environments: a case study." PhD diss.
- Luo, Guangchun, Guangyi Chen, Ling Tian, Ke Qin, and Shen-En Qian. 2016. "Minimum noise fraction versus principal component analysis as a preprocessing step for hyperspectral imagery denoising." *Canadian Journal of Remote Sensing* 42 (2): 106-116.
- Lynch, Philip, Blesius Leonhard, and Hines Ellen. 2020. "Classification of urban area using multispectral indices for urban planning." *Remote Sensing* 12 (15): 2503.

- Ma, Xiaofeng, Yutang Hong, and Yongze Song. 2020. "Super resolution land cover mapping of hyperspectral images using the deep image prior-based approach." *International Journal of Remote Sensing* 41 (7): 2818-2834.
- Mahdi, Khodadadzadeh, Jun Li, Antonio Plaza, Hassan Ghassemian, José M. Bioucas-Dias, and Xia Li. 2014. "Spectral-spatial classification of hyperspectral data using local and global probabilities for mixed pixel characterization." *IEEE Transactions on Geoscience and Remote Sensing* 52 (10): 6298-6314.
- Maher, Raju Sahebrao, Dnyaneshwar S. Panchal, Sangramsing Kayte, and Dr Mukta Dhopeshwarkar. 2015. "Automatic Identification of Varies Stages of Diabetic Retinopathy Using Retinal Fundus Images." *International Journal of Advanced Research in Computer Science and Software Engineering* 5 (9).
- Mahesh, Pal. 2002. "Factors influencing the accuracy of remote sensing classifications a comparative study." PhD diss, University of Nottingham.
- Mahesh, Pal, E Maxwell Aaron, and A. Warner Timothy. 2013. "Kernel-based extreme learning machine for remote-sensing image classification." *Remote Sensing Letters* 4 (9): 853-862.
- Makantasis, Konstantinos, Konstantinos Karantzas, Anastasios Doulamis, and Nikolaos Doulamis. 2015. "Deep supervised learning for hyperspectral data classification through convolutional neural networks." *IEEE*. 4959-4962.
- Maktav, D., F. S. Erbek, and C. Jürgens. 2005. "Remote sensing of urban areas." *International journal of remote sensing* 26 (4): 655-659.
- Manolakis, Dimitris G, Ronald B Lockwood, and Thomas W Cooley. 2016. *Hyperspectral imaging remote sensing: physics, sensors, and algorithms*. Cambridge University Press.
- Manolakis, Dimitris G., Christina Siracusa, David Marden, and Gary A. Shaw. 2001. "Hyperspectral adaptive matched-filter detectors: Practical performance comparison." *Algorithms for Multispectral, Hyperspectral, and Ultraspectral Imagery*. International Society for Optics and Photonics. 18-33.
- Manolakis, Dimitris, Christina Siracusa, and Gary Shaw. 2001. "Hyperspectral subpixel target detection using the linear mixing model." *IEEE transactions on geoscience and remote sensing* 39 (7): 1392-1409.
- Manolakis, Dimitris, David Marden, and Gary A Shaw. 2003. "Hyperspectral image processing for automatic target detection applications." *Lincoln laboratory journal* 14 (1): 79-116.
- Manolakis, Dimitris, David Marden, and Gary A. Shaw. 2003. "Hyperspectral image processing for automatic target detection applications." *Lincoln laboratory journal* 14 (1): 79-116.
- Manolakis, Dimitris, Ronald Lockwood, Thomas Cooley, and John Jacobson. 2009. "Is there a best hyperspectral detection algorithm?." In *Algorithms and technologies for multispectral, hyperspectral, and ultraspectral imagery*. International Society for Optics and Photonics. 733402.

- Maryam, Imani. 2019. "Difference-based target detection using Mahalanobis distance and spectral angle." *International journal of remote sensing* 40 (3): 811-831.
- Mas, Jean F., and Juan J. Flores. 2008. "The application of artificial neural networks to the analysis of remotely sensed data." *International Journal of Remote Sensing* 29 (3): 617-663.
- Mathieu, Fauvel, Jón Atli Benediktsson, Jocelyn Chanussot, and Johannes R. Sveinsson. 2008. "Spectral and spatial classification of hyperspectral data using SVMs and morphological profiles." *IEEE Transactions on Geoscience and Remote Sensing* 46 (11): 3804-3814.
- Maxwell, A.E., T.A Warner, and F Fang. 2018. "Implementation of machine-learning classification in remote sensing: An applied review." *International Journal of Remote Sensing* 39 (9): 2784-2817.
- Mei, Shaohui, Jingyu Ji, Junhui Hou, Xu Li, and Qian Du. 2017. "Learning sensor-specific spatial-spectral features of hyperspectral images via convolutional neural networks." *IEEE Transactions on Geoscience and Remote Sensing* 55 (8): 4520-4533.
- Melgani, Farid and Bruzzone, Lorenzo. 2004. "Classification of hyperspectral remote sensing images with support vector machines." *IEEE Transactions on geoscience and remote sensing* 42 (8): 1778-1790.
- Mercier, Grégoire and Marc Lennon. 2003. "Support vector machines for hyperspectral image classification with spectral-based kernels." *International Geoscience and Remote Sensing Symposium. Proceedings*. IEEE. 288-290.
- Merrill, K Ridd. 1995. "Exploring a VIS (vegetation-impervious surface-soil) model for urban ecosystem analysis through remote sensing: comparative anatomy for cities." *International journal of remote sensing* 16 (12): 2165-2185.
- Mohammadi, M. 2012. "Road classification and condition determination using hyperspectral imagery." *Int. Arch. Photogramm. Remote Sens* B7.
- Mou, Lichao, Pedram Ghamisi, and Xiao Xiang Zhu. 2017. "Deep recurrent neural networks for hyperspectral image classification." *IEEE Transactions on Geoscience and Remote Sensing* 55 (7): 3639-3655.
- Mourshed, Monjur, Antonio Bucchiarone, and Fahmida Khandokar. 2016. "SMART: A process-oriented methodology for resilient smart cities." *IEEE International Smart Cities Conference*. IEEE. 1-6.
- MP, Nascimento José, and José MB Dias. 2005. "Vertex component analysis: A fast algorithm to unmix hyperspectral data." *IEEE transactions on Geoscience and Remote Sensing* 43 (4): 898-910.
- Muad, Anuar M., and Giles M. Foody. 2012. "Impact of land cover patch size on the accuracy of patch area representation in HNN-based super resolution mapping." *IEEE Journal of Selected Topics in Applied Earth Observations and Remote Sensing* 5 (5): 1418-1427.

- Nada, Kadhim, Monjur Mourshed, and Michaela Bray. 2016. "Advances in remote sensing applications for urban sustainability." *Euro-Mediterranean Journal for Environmental Integration* 1 (1): 1-22.
- Naeini, A. Alizadeh, M. Babadi, and S. Homayouni. 2017. "ASSESSMENT OF NORMALIZATION TECHNIQUES ON THE ACCURACY OF HYPERSPECTRAL DATA CLUSTERING." *International Archives of the Photogrammetry, Remote Sensing & Spatial Information Sciences* 42.
- Nascimento, José MP, and José M. Bioucas-Dias. 2011. "Hyperspectral unmixing based on mixtures of Dirichlet components." *IEEE Transactions on Geoscience and Remote Sensing* 50 (3): 863-878.
- Navneet, Dalal, and Bill Triggs. 2005. "Histograms of oriented gradients for human detection." *IEEE computer society conference on computer vision and pattern recognition*. 886-893.
- Nguyen, Minh Q., Peter M. Atkinson, and Hugh G. Lewis. 2005. "Superresolution mapping using a Hopfield neural network with LIDAR data." *IEEE Geoscience and Remote Sensing Letters* (2) 3: 366-370.
- Nicolas, Le Roux, and Yoshua Bengio. 2010. "Deep belief networks are compact universal approximators." *Neural computation* 22 (8): 2192-2207.
- Nidamanuri, Rama Rao, and Bernd Zbell. 2010. "A method for selecting optimal spectral resolution and comparison metric for material mapping by spectral library search." *Progress in Physical Geography* 34 (1): 47-58.
- Nirmal, Keshava. 2004. "Distance metrics and band selection in hyperspectral processing with applications to material identification and spectral libraries." *IEEE Transactions on Geoscience and remote sensing* 42 (7): 1552-1565.
- Nobuyuki, Otsu. 1979. "A threshold selection method from gray-level histograms." *IEEE transactions on systems, man, and cybernetics* (9) 1: 62-66.
- Oke, T. R., and H. A. Cleugh. 1987. "Urban heat storage derived as energy balance residuals." *Boundary-Layer Meteorology* 39 (3): 233-245.
- Pal, M. 2006. "Support vector machine- based feature selection for land cover classification: a case study with DAIS hyperspectral data." *International Journal of Remote Sensing* 27 (14): 2877-2894.
- Pal, Mahesh. 2009. "Extreme- learning- machine- based land cover classification." *International Journal of Remote Sensing* 30 (14): 3835-3841.
- Pandey, Dwijendra, and K. C. Tiwari. 2020. "Feature identification and extraction of urban built-up surfaces and materials in AVIRIS-NG hyperspectral imagery." *Geocarto International* 1-22.
- Paoletti, M. E., J. M. Haut, J. Plaza, and A. Plaza. 2019. "Deep learning classifiers for hyperspectral imaging: A review." *ISPRS Journal of Photogrammetry and Remote Sensing* 158: 279-317.

- Parshakov, Ilia, Craig Coburn, and Karl Staenz. 2014. "Z-Score distance: A spectral matching technique for automatic class labelling in unsupervised classification." *IEEE Geoscience and Remote Sensing Symposium*. IEEE. 1793-1796.
- Patino, Jorge E., and Juan C. Duque. 2013. "A review of regional science applications of satellite remote sensing in urban settings." *Computers, Environment and Urban Systems* 37: 1-17.
- Pei, Chengkai, and Jin Fu. 2007. "Status and prospect of hyperspectral remote sensing technique in rock and mineral identification." *World Nuclear Geoscience* 24 (1): 32-38.
- Peijun, Du, Kun Tan, and Xiaoshi Xing. 2012. "A novel binary tree support vector machine for hyperspectral remote sensing image classification." *Optics Communications* 285 (13-14): 3054-3060.
- Peña, Fernando López, Juan Luís Crespo, and Richard J. Duro. 2009. "Unmixing low-ratio endmembers in hyperspectral images through Gaussian synapse ANNs." *IEEE Transactions on Instrumentation and Measurement* 59 (7): 1834-1840.
- Peña-Barragán, José M., Moffatt K. Ngugi, Richard E. Plant, and Johan Six. 2011. "Object-based crop identification using multiple vegetation indices, textural features and crop phenology." *Remote Sensing of Environment* 115 (6): 1301-1316.
- Peng, Bing, Wei Li, Xiaoming Xie, Qian Du, and Kui Liu. 2015. "Weighted-fusion-based representation classifiers for hyperspectral imagery." *Remote Sensing* 7 (11): 14806-14826.
- Peng, Jian, Hong Shen, and Jian Sheng Wu. 2013. "Soil moisture retrieving using hyperspectral data with the application of wavelet analysis." *Environmental earth sciences* 69 (1): 279-288.
- Philip, E. Dennison, and Dar A. Roberts. 2003. "Endmember selection for multiple endmember spectral mixture analysis using endmember average RMSE." *Remote sensing of environment* 87 (2-3): 123-135.
- Phinn, S., M., P. Scarth Stanford, A. T. Murray, and P. T. Shyy. 2002. "Monitoring the composition of urban environments based on the vegetation-impervious surface-soil (VIS) model by subpixel analysis techniques." *International Journal of Remote Sensing* 23 (20): 4131-4153.
- Plaza, Antonia, and CI Chang. 2006. "Impact of initialization on design of endmember extraction algorithms." *IEEE Transactions on Geoscience and Remote Sensing* 44 (11): 3397-3407.
- Plaza, Antonio, Pablo Martínez, Rosa Pérez, and Javier Plaza. 2004. "A quantitative and comparative analysis of endmember extraction algorithms from hyperspectral data." *IEEE transactions on geoscience and remote sensing* 42 (3): 650-663.
- Plaza, Javier, Antonio Plaza, Rosa Perez, and Pablo Martinez. 2009. "On the use of small training sets for neural network-based characterization of mixed pixels in remotely sensed hyperspectral images." *Pattern Recognition* 42 (11): 3032-3045.

- Pu, Hongbin, Dan Liu, Jia-Huan Qu, and Da-Wen Sun. 2017. "Applications of imaging spectrometry in inland water quality monitoring—a review of recent developments." *Water, Air, & Soil Pollution* 228 (4): 131.
- Q, Man, Dong P, Guo H, Liu G, and Shi R. 2014. "Light detection and ranging and hyperspectral data for estimation of forest biomass: a review." *Journal of Applied Remote Sensing* 8 (1): 081598.
- Qin, Mengjiao, Linshu Hu, Zhenhong Du, Yi Gao, Lianjie Qin, Feng Zhang, and Renyi Liu. 2020. "Achieving Higher Resolution Lake Area from Remote Sensing Images Through an Unsupervised Deep Learning Super-Resolution Method." *Remote Sensing* 12 (12): 1937.
- Ramón, Moreno, Francesco Corona, Amaury Lendasse, Manuel Graña, and Lênio S. Galvão. 2014. "Extreme learning machines for soybean classification in remote sensing hyperspectral images." *Neurocomputing* 128: 207-216.
- Ranjan, Sameer, Deepak Ranjan Nayak, Kallepalli Satish Kumar, Ratnakar Dash, and Banshidhar Majhi. 2017. "Hyperspectral image classification: A k-means clustering based approach." *4th International Conference on Advanced Computing and Communication Systems (ICACCS)*. IEEE. 1-7.
- Ren, Hsuan, Qian Du, Chein-I. Chang, and James O. Jensen. 2003. "Comparison between constrained energy minimization based approaches for hyperspectral imagery." *Workshop on Advances in Techniques for Analysis of Remotely Sensed Data*. IEEE. 244-248.
- Ren, Hsuan, Qian Du, Jing Wang, Chein-I. Chang, James O. Jensen, and Janet L. Jensen. 2006. "Automatic target recognition for hyperspectral imagery using high-order statistics." *IEEE Transactions on Aerospace and Electronic Systems* 42 (4): 1372-1385.
- Ridd, Merrill K. 1995. "Exploring a VIS (vegetation-impervious surface-soil) model for urban ecosystem analysis through remote sensing: comparative anatomy for cities." *International journal of remote sensing* 16 (12): 2165-2185.
- Robert, M Haralick, Karthikeyan Shanmugam, and Hak Dinstein. 1973. "Textural features for image classification." *IEEE Transactions on systems, man, and cybernetics* 6: 610-621.
- Robila, S. A. 2005. "Using spectral distances for speedup in hyperspectral image processing." *International Journal of Remote Sensing* 26 (24): 5629-5650.
- Robila, Stefan. 2005. "An investigation of spectral metrics in hyperspectral image preprocessing for classification." In *Geospatial goes global: from your neighborhood to the whole planet, ASPRS Annual Conference*. Baltimore, Maryland. 7-11.
- Rodarmel, Craig, and Jie Shan. 2002. "Principal component analysis for hyperspectral image classification." *Surveying and Land Information Science* 62 (2): 115-122.
- Roux, Nicolas Le, and Bengio Yoshua. 2008. "Representational power of restricted Boltzmann machines and deep belief networks." *Neural computation* 20 (6): 1631-1649.
- Savas, Caner, and Fabio Dovis. 2019. "The impact of different kernel functions on the performance of scintillation detection based on support vector machines." *Sensors* 19 (23): 5219.

- Schueler, Thomas R., Lisa Fraley-McNeal, and Karen Cappiella. 2009. "Is impervious cover still important? Review of recent research." *Journal of Hydrologic Engineering* 14 (4): 309-315.
- Segl, Karl, U. Heiden, M. Mueller, and Hermann Kaufmann. 2003. "Endmember detection in urban environments using hyperspectral HyMap data." *In Third EARSeL Workshop on Imaging Spectroscopy*.
- Seifi Majdar, Reza, and Hassan Ghassemian. 2017. "A probabilistic SVM approach for hyperspectral image classification using spectral and texture features." *International Journal of Remote Sensing* 38 (15): 4265-4284.
- Senchuri, Rabin, Agnieszka Kuras, and Ingunn Burud. 2021. "Machine Learning Methods for Road Edge Detection on Fused Airborne Hyperspectral and LIDAR Data." *11th Workshop on Hyperspectral Imaging and Signal Processing: Evolution in Remote Sensing (WHISPERS)*. IEEE. 1-5.
- Shackelford, Aaron K., and Curt H. Davis. 2003. "A hierarchical fuzzy classification approach for high-resolution multispectral data over urban areas." *IEEE transactions on geoscience and remote sensing* 41 (9): 1920-1932.
- Shafri, Helmi ZM, Ebrahim Taherzadeh, Shattri Mansor, and Ravshan Ashurov. 2012. "Hyperspectral remote sensing of urban areas: an overview of techniques and applications." *Research Journal of Applied Sciences, Engineering and Technology* 4 (11): 1557-1.
- Shanmugam, S., and P. SrinivasaPerumal. 2014. "Spectral matching approaches in hyperspectral image processing." *International journal of remote sensing* 35 (24): 8217-8251.
- Shao, Zhenfeng, and Lei Zhang. 2014. "Sparse dimensionality reduction of hyperspectral image based on semi-supervised local Fisher discriminant analysis." *International journal of applied earth observation and geoinformation* 122-129.
- Shaohui, Mei, Mingyi He, Yifan Zhang, Zhiyong Wang, and Dagan Feng. 2011. "Improving spatial-spectral endmember extraction in the presence of anomalous ground objects." *IEEE transactions on geoscience and remote sensing* 49 (11): 4210-4222.
- Shi, Qian, Xiaoping Liu, and Xia Li. 2017. "Road detection from remote sensing images by generative adversarial networks." *IEEE access* 25486-25494.
- Shi, W, Z Miao, and J Debayle. 2013. "An integrated method for urban main-road centerline extraction from optical remotely sensed imagery." *IEEE Transactions on Geoscience and Remote Sensing* 52 (6): 3359-3372.
- Shi, Zhenwei, Xinran Yu, Zhiguo Jiang, and Bo Li. 2013. "Ship detection in high-resolution optical imagery based on anomaly detector and local shape feature." *IEEE Transactions on Geoscience and Remote Sensing* 52 (8): 4511-4523.

- Shirish, K Shevade, S. Sathiya Keerthi, Chiranjib Bhattacharyya, and Karaturi Radha Krishna Murthy. 2000. "Improvements to the SMO algorithm for SVM regression." *IEEE transactions on neural networks* 11 (5): 1188-1193.
- Shwartz-Ziv, Ravid, and Naftali Tishby. 2017. *Opening the black box of deep neural networks via information*. arXiv preprint arXiv:1703.00810 .
- Stefanou, Marcus S., and John P. Kerekes. 2009. "Image-derived prediction of spectral image utility for target detection applications." *IEEE Transactions on Geoscience and Remote Sensing* 48 (4): 1827-1833.
- Stein, Stephen E, and Donald R. Scott. 1994. "Optimization and testing of mass spectral library search algorithms for compound identification." *Journal of the American Society for Mass Spectrometry* 5 (9): 859-866.
- Storper, Michael, and Allen J. Scott. 2009. "Rethinking human capital, creativity and urban growth." *Journal of economic geography* 9 (2): 147-167.
- Su, Hongjun, Yao Yu, Qian Du, and Peijun Du. 2020. "Ensemble learning for hyperspectral image classification using tangent collaborative representation." *IEEE Transactions on Geoscience and Remote Sensing* 58 (6): 3778-3790.
- Su, Jinya, Dewei Yi, Cunjia Liu, Lei Guo, and Wen-Hua Chen. 2017. "Dimension reduction aided hyperspectral image classification with a small-sized training dataset: experimental comparisons." *Sensors* 17 (12): 2726.
- Sun, Qiaoqiao, Xuefeng Liu, and Min Fu. 2017. "Classification of hyperspectral image based on principal component analysis and deep learning." *7th IEEE international conference on electronics information and emergency communication (ICEIEC)*. 356-359.
- Sun, Zhongchang, Xiangwei Zhao, Mengfan Wu, and Cuizhen Wang. 2019. "Extracting urban impervious surface from worldView-2 and airborne LiDAR data using 3D convolutional neural networks." *Journal of the Indian Society of Remote Sensing* 47 (3): 401-412.
- Svensén, Markus, and Christopher M. Bishop. 2007. *Pattern recognition and machine learning*.
- Tamilarasi, R., and S. Prabu. 2021. "Automated building and road classifications from hyperspectral imagery through a fully convolutional network and support vector machine." *The Journal of Supercomputing* 1-19.
- Teng, A. G., and F. Gao. 2009. "Progress of hyperspectral technology application research in agriculture." *Jiangsu Agric Sci* 8-11.
- Thanh Noi, Phan, and Martin Kappas. 2018. "Comparison of random forest, k-nearest neighbor, and support vector machine classifiers for land cover classification using Sentinel-2 imagery." *Sensors* 18 (1): 18.
- Tiwari, Kailash C., Manoj Kumar Arora, Dharmendra P. Singh, and Deepti Soni Yadav. 2013. "Military target detection using spectrally modeled algorithms and independent component analysis." *Optical Engineering* 52 (2): 026402.

- Townshend, J. R., C. Huang G., S. N. V. Kalluri, R. S. Defries, S. Liang, and K. Yang. 2000. "Beware of per-pixel characterization of land cover." *International Journal of remote sensing* 21 (4): 839-843.
- Truslow, Eric, Dimitris Manolakis, Michael Pieper, Thomas Cooley, and Mike Brueggeman. 2013. "Performance prediction of matched filter and adaptive cosine estimator hyperspectral target detectors." *IEEE Journal of Selected Topics in Applied Earth Observations and Remote Sensing* 7 (6): 2337-2350.
- United Nations, Department of Economic and Social Affairs, Population Division. 2015. "Population 2030: Demographic challenges and opportunities for sustainable development planning." Report, New York.
- Wang, Jing, and Chein-I. Chang. 2006. "Independent component analysis-based dimensionality reduction with applications in hyperspectral image analysis." *IEEE transactions on geoscience and remote sensing* 44 (6): 1586-1600.
- Weng, Qihao. 2012. "Remote sensing of impervious surfaces in the urban areas: Requirements, methods, and trends." *Remote Sensing of Environment* 117: 34-49.
- Wenzheng, Wang, Zhao Baojun, Tang Linbo, Zhou Shichao, and Feng Fan. 2019. "Fusion-based spectral matching method for hyperspectral target detection." *The Journal of Engineering* 20: 6741-6744.
- Wenzhi, Zhao, and Shihong Du. 2016. "Spectral-spatial feature extraction for hyperspectral image classification: A dimension reduction and deep learning approach." *IEEE Transactions on Geoscience and Remote Sensing* 54 (8): 4544-4554.
- West, Jason E., David W. Messinger, Emmett J. Ientilucci, John P. Kerekes, and John R. Schott. 2005. "Matched filter stochastic background characterization for hyperspectral target detection." In *Algorithms and Technologies for Multispectral, Hyperspectral, and Ultraspectral Imagery*. International Society for Optics and Photonics. 1-12.
- Windrim, Lloyd, Rishi Ramakrishnan, Arman Melkumyan, Richard J. Murphy, and Anna Chlingaryan. 2019. "Unsupervised feature-learning for hyperspectral data with autoencoders." *Remote Sensing* 11 (7): 864.
- Winter, Michael E. 1999. "N-FINDR: An algorithm for fast autonomous spectral end-member determination in hyperspectral data." *Imaging Spectrometry* (International Society for Optics and Photonics) 3753: 266-275.
- Xiaoai, Dai, Junying Cheng, Yu Gao, Shouheng Guo, Xingping Yang, Xiaoqian Xu, and Yi Cen. 2020. "Deep Belief Network for Feature Extraction of Urban Artificial Targets." *Mathematical Problems in Engineering*.
- Yanzi, Shi, Jie Lei, Yaping Yin, Kailang Cao, Yunsong Li, and Chein-I. Chang. 2019. "Discriminative feature learning with distance constrained stacked sparse autoencoder for hyperspectral target detection." *IEEE Geoscience and Remote Sensing Letters* 16 (9): 1462-1466.

- Yi, Wang, and Hexiang Duan. 2018. "Classification of hyperspectral images by SVM using a composite kernel by employing spectral, spatial and hierarchical structure information." *Remote Sensing* 10 (3): 441.
- Youkyung, Han, Hyejin Kim, Jaewan Choi, and Yongil Kim. 2012. "A shape-size index extraction for classification of high resolution multispectral satellite images." *International journal of remote sensing* 33 (6): 1682-1700.
- Yushi, Chen, Zhouhan Lin, Xing Zhao, Gang Wang, and Yanfeng Gu. 2014. "Deep learning-based classification of hyperspectral data." *IEEE Journal of Selected topics in applied earth observations and remote sensing* 7 (6): 2094-2107.
- Zhang, Bing, Jianwei Gao, Lianru Gao, and Xu Sun. 2013. "Improvements in the ant colony optimization algorithm for endmember extraction from hyperspectral images." *IEEE Journal of Selected Topics in Applied Earth Observations and Remote Sensing* 6 (2): 522-530.
- Zhang, Bing, Wei Yang, Lianru Gao, and Dongmei Chen. 2012. "Real-time target detection in hyperspectral images based on spatial-spectral information extraction." *EURASIP journal on advances in signal processing* 1: 1-15.
- Zhang, Caiyun, and Fang Qiu. 2012. "Hyperspectral image classification using an unsupervised neuro-fuzzy system." *Journal of Applied Remote Sensing* 6 (1): 063515.
- Zhang, Gaigai, Shizhi Zhao, Wei Li, Qian Du, Qiong Ran, and Ran Tao. 2020. "HTD-net: A deep convolutional neural network for target detection in hyperspectral imagery." *Remote Sensing* 12 (9): 1489.
- Zhang, Hao, Heng-jia Song, and Bo-chun Yu. 2011. "Application of hyper spectral remote sensing for urban forestry monitoring in natural disaster zones." *International Conference on Computer and Management (CAMAN)*. IEEE. 1-4.
- Zhang, Xiangrong, Yujia Sun, Jingyan Zhang, Peng Wu, and Licheng Jiao. 2018. "Hyperspectral unmixing via deep convolutional neural networks." *IEEE Geoscience and Remote Sensing Letters* 15 (11): 1755-1759.
- Zhang, Xiya, and Peijun Li. L. 2014. "Lithological mapping from hyperspectral data by improved use of spectral angle mapper." *International Journal of Applied Earth Observation and Geoinformation* 95-109.
- Zhang, Yudong, and Lenan Wu. 2012. "Classification of fruits using computer vision and a multiclass support vector machine." *sensors* 12 (9): 12489-12505.
- Zhang, Yuxiang, Bo Du, Liangpei Zhang, and Shugen Wang. 2015. "A low-rank and sparse matrix decomposition-based Mahalanobis distance method for hyperspectral anomaly detection." *IEEE Transactions on Geoscience and Remote Sensing* 54 (3): 1376-1389.
- Zhao, Wenzhi, and Du Shihong. 2016. "Spectral-spatial feature extraction for hyperspectral image classification A dimension reduction and deep learning approach." *IEEE*

- Zhao, Wenzhi, Zhou Guo, Jun Yue, Xiuyuan Zhang, and Liquan Luo. 2015. "On combining multiscale deep learning features for the classification of hyperspectral remote sensing imagery." *International Journal of Remote Sensing* 36 (13): 3368-3379.
- Zhilei, Lin, and Luming Yan. 2016. "A support vector machine classifier based on a new kernel function model for hyperspectral data." *GIScience & Remote Sensing* 53 (1): 85-101.

Create Material and Terrain Spectral Data

THEME *

Material and Terrain ▼ - Select a value - ▼

NAME OF THE SITE *

Date and Time of Acquisition

09/19/2021 - 19:56:29

Format: 09/19/2021 - 19:56:29

SOIL SPECTRAL NO

[Location details](#)

Geolocation (Decimal Degrees)

LATITUDE

LONGITUDE

ALTITUDE

 meter

LOCALITY

DISTRICT

STATE

[Environmental Information](#)

ATMOSPHERIC CONDITION

WIND DIRECTION

- None - ▼

WIND SPEED

meter/sec

CLOUD TYPE

- None - ▼

CLOUD COVER

%

TEMPERATURE

degree Celsius

RELATIVE HUMIDITY

SUN ALTITUDE

degree

[Instrument Information](#)

INSTRUMENT ID

FORE OPTICS

- None - ▼

SENSOR TYPE

- None - ▼

CALIBRATION DETAILS

<div></div>

[Measurement Information](#)

SPECTRAL SAMPLING

				years
SLOPE		ELECTRICAL CONDUCTIVITY		FACILITY OCCUPANCY
<input type="text"/> %		<input type="text"/> s/m		<input type="text" value="- None -"/>
EROSION		WATER CURRENT		FACILITY TYPE
<input type="text"/> %		<input type="text"/> meter/sec		<input type="text" value="- None -"/>
DRAINAGE PATTERN		Laboratory Test		MATERIAL & TYPE
<input type="text" value="- None -"/>				<input type="text" value="- None -"/>
CATIONS-ANIONS ANALYSIS				
Soil Characteristics		<input type="text"/>		Camouflage
COLOR				OBJECT NAME
<input type="text" value="- None -"/>				<input type="text" value="- None -"/>
TEMPERATURE		CHROMOPHORE DISSOLVED ORGANIC MATTER (CDOM)		COLOUR
<input type="text"/> °C		<input type="text"/>		<input type="text" value="- None -"/>
SOIL TEXTURE				MATERIAL OF OBJECT TO BE CAMOUFLAGE
<input type="text" value="- None -"/>				<input type="text" value="- None -"/>
Laboratory Test				TYPE OF OBJECT
				<input type="text" value="- None -"/>
DENSITY				TYPE OF STRUCTURE
<input type="text"/> kg/m ³				<input type="text" value="- None -"/>
SOIL MOISTURE				SURROUNDING
Gravimetric <input type="text"/> (in % weight)				<input type="text"/>
POROSITY				
<input type="text"/>				
RATING CONE INDEX(RCI)				SURFACE TEMPERATURE
<input type="text"/>				<input type="text"/> °C
<input type="text" value="- None -"/>				SHAPE
				<input type="text" value="- None -"/>

WHITE REFERENCE SOURCE**FORE OPTICS HEIGHT ABOVE TARGET****FORE OPTICS HEIGHT ABOVE GROUND**[Calibration](#)

Date of calibration

MONTH DAY YEAR HOUR MINUTE

CALIBRATION FILE

No

Files must be less than **2 MB**.

Allowed file types: **txt csv xlsx xls dat**.

TERRAIN TYPE**TARGET****GEOMETRY OF OBSERVER
POSITION RELATIVE TO
INCIDENT RADIANCE****WATER BODY TYPE**[Trafficability](#)[Landscape characteristics](#)**LANDFORM****LANDUSE****GEOLOGY****IN NTU****IN SSC****PH**[Built in material](#)**COLOUR****ROUGHNESS OF MATERIAL****SHAPE****SURROUNDING****FACILITY PURPOSE****FACILITY AGE**

STRENGTH

- None - ▼

CONDITION OF SPECTRAL DATA COLLECTION

- None - ▼

[Files to Upload in .txt format](#)

SOLAR IRRADIANCE SPECTRA

No

Files must be less than **1 MB**. Allowed

file types: **png gif jpg jpeg**.

Images must be between **320x200** and **640x480** pixels.

IMAGE OF SPECTRA

No

Files must be less than **1 MB**. Allowed

file types: **png gif jpg jpeg**.

Images must be between **320x200** and **640x480** pixels.

REFLECTANCE SPECTRA

0 file chosen

Files must be less than **1 MB**. Allowed

file types: **txt csv**.

Author's Biography



Shalini Gakhar

Registration Number: **2K17/PhD/IT/09**

Department of Information Technology

Delhi Technological University,

Delhi-110042

Email: shalinigakhar7@gmail.com

Shalini Gakhar received her Bachelor of Technology (B.Tech.) degree from PDM College of Engineering (Affiliated to Maharishi Dayanand University), Haryana, India in the year 2014 and the Master of Technology (M.Tech.) from Centre for Development of Advanced Computing (C-DAC), Noida, India in the year 2016. Presently, she is pursuing her PhD in the Department of Information Technology (IT), Delhi Technological University, Delhi, India. She has also worked as a Junior/Senior Research Fellow (JRF/SRF) in a “Clustered based Networked Project on Imaging Spectrometer and its Applications (NISA)” funded by Department of Science and Technology (DST), Government of India, and as a Research Associate (RA) in “Phenomics of moisture deficit stress tolerance and nitrogen use efficiency in rice and wheat” funded by ICAR-NASF, Government of India. She has co-authored Technical Brochure, “Manual on Drone Remote Sensing” TB-ICN 259-2021 and is an active resource person in many workshops and webinars. Her research interests include urban remote sensing, Hyperspectral Image processing, satellite image interpretation, machine learning and deep learning.